



Universitat Ramon Llull

C.I.F. G. 59069740 Universitat Ramon Llull Fundació Privada. Rgpre. Fund. Generalitat de Catalunya núm. 472 (28-02-90)

DOCTORAL THESIS

Title Tailoring Carbon Nanotubes Properties for Gene Delivery Applications

Presented by Anna Cifuentes Rius

Centre IQS School of Engineering

Department Bioengineering

Directed by Dr. Salvador Borrós

*C. Claravall, 1-3
08022 Barcelona
Tel. 936 022 200
Fax 936 022 249
E-mail: urisc@sec.url.es*

***Al Neto,
per iniciar-me en aquest món***

What we know is a drop, what we don't know is an ocean.

- Isaac Newton

Acknowledgments

En primer lloc, m'agradaria donar les més sinceres gràcies al meu director de tesi, el Dr. Salvador Borrós. Moltes gràcies Chicho per fer-ho possible. Gràcies per brindar-me aquesta oportunitat, per ensenyar-me tant i per l'enorme confiança que has dipositat en mi sempre. Gràcies per totes les experiències i oportunitats que m'has deixat viure a nivell professional (l'estada al MIT, a Austràlia, als milers de congressos...), però sobretot per ser "el tiet" que ha cuidat de mi també personalment. No ho oblidaré. Em sento molt afortunada d'haver pogut compartir aquest camí amb tu. Moltes gràcies, de veritat!

I would like to thank Prof. Kimberly Hamad-Schifferli. I believe I will never get tired to thank you Kim for letting me be part of your group for these awesome 10 months in Boston. Thanks for your confidence and everything you have taught me. The time working with you has been a great learning experience and all the fruitful discussions we have had are of a priceless value for me. I would also like to thank Dr. James Kah and Dr. Zhichuan Xu for their help, support and advice in the lab. Y en especial, a mis queridas flores de laboratorio, Helena y Paula. Gracias por hacer que cada día (y cada café) fuera genial. ¡Os echOU de menOUS! Per suposat, moltes gràcies també a la meva família a Boston, la IQS crew. Marcelix, Pablito, Kuxi, Johnny, DJ,... Sou fantàstics! Molt especialment al Jose, per haver estat l'auxiliar perfecte, passant pel company GEMAT perfecte, per finalment convertir-se en el roommate perfecte! I el que ens queda! Gràcies per tot Joselito (AFMs inclosos)!

I would also like to thank Prof. Andrew Whittaker and Dr. Kristofer Thurecht for giving me the chance to work within their amazing Polymer Chemistry Group at the Australian Institute for Bioengineering and Nanotechnology (AIBN) at UQ. Thanks Kris for your valuable and interesting science discussions. You have taught me not only how to tackle some of the questions we may ask, but most importantly to directly ask the appropriate question. Of course, I would like to thank to all my AIBN mates, especially my favourite aussies, Nick, Nate, Jo and Sam. Thanks for your endless help in the lab and for making my aussie experience much more fun also outside. You guys are great! M'agradaria agrair a l'IQS la concessió de la beca de doctorat que ha permès realitzar aquesta feina durant 3 anys. També a la gent de "la casa" que m'han ajudat a fer una millor feina. Agrair a Dr. Antoni Planas, Dr. Xevi Biarnés i Dra. Magda Faijes per l'ajuda amb l'enzim. També al Dr. Santi Nonell per deixar-me usar el seu preuat fluorímetre. Gràcies Ester (noieta!) per la paciència!

També voldria donar les gràcies a la Dra. Gerogina Hotter, Dra. Anna Sola i Dr. Jose Luís Viñas, de l'Institut d'Investigacions Biomèdiques de Barcelona (IIBB), per l'estreta col·laboració. Gracias Chrysia por facilitarme (y amenizarme) el trabajo en cultivos. També a la Dra. Gemma Gabriel del

Centre Nacional de Microelectrònica (CNM) per la tecnologia compartida. Thanks also to Dr. Sofia Svedhem from Chalmers University of Technology for teaching me all about the QCM-D technology.

I no em puc oblidar de la família GEMAT! Gràcies per fer que aquests anys hagin estat plens de bons moments, que haguem pogut compartir milers de somriures però també els maldecaps. Gràcies als “sèniors” del Lab Vell, Núria, Marina i Pere, per fer-ho tot més fàcil i divertit. Sou l’ànima del grup! Gracias también a ti, Elena, por hacernos el trabajo duro para que todos podamos avanzar. Moltes gràcies a tots els del Biosotano, Oscar, Pri, Greg, Arbu, Casqui..., i també als que ja no hi són Jorge, Toni, Nuri-Mari,... Vull agrair especialment a l’Ana dP i a la Núria Coronas, per ajudar-me de manera molt significativa a tirar endavant aquest projecte. Sobretot a la Inés, per fer-me la “feina bruta” i fer que aquesta última etapa a l’IQS hagi estat molt especial (junt amb les “enxufades”). Joan, gràcies per fer del plasma una tècnica més divertida, y a ti Nat, por hacerme reír constantemente. No puedo imaginarme este tiempo sin ti Majo; gracias por ser la mejor siesa del mundo y compartir tu vitalidad conmigo. Tampoc se que seria de mi sense la meva companya de viatge per excel·lència; gràcies Maria. Tot i que sembla que els nostres camins s’han separat, sé que podré comptar amb tu per sempre. Dr. Lauri-Xurri, gràcies per tot el que has compartit amb mi, per tot el que m’has ensenyat, per tot el que hem viscut juntes, per les aventures infinites, i per tot el q m’has cuidat... Tot plegat és possiblement del millor que m’enduc del doctorat (en serio!). I per descomptat, gràcies a tu, Victor. Gràcies per la paciència, la fe cega, per donar-ho tot i, en definitiva, per ser indispensable.

Voldria agrair a tots aquells que també han contribuït, encara que de forma indirecta, en fer d’aquesta etapa un camí més entranyable. A les nenes, per haver estat amb mi en els bons i mals moments, sempre donant-ho tot i disfrutant al màxim, confiant en el que faig i recolzant-me en tot. A les jaules, per haver crescut i seguir creixent juntes, per fer-me riure en tot moment i per ser unes grans companyes de viatge. Guillem, gràcies per acompanyar-me des de fa ja uns anyets, per fer-me donar el màxim, per valorar-me tant i fer-me sentir especial. Però sobretot, gràcies per suportar aquesta duríssima última etapa del doctorat en un moment ple de canvis en les nostres vides. Sense tu, molta part d’aquest “treball de recerca” no hagués estat possible.

I està clar que si algú mereix tot el meu agraïment és la meva família. Gràcies a tots els avis, no us oblidó; i a tots aquells que heu contribuït a la causa (també a tu i al teu password de la UB, Ma Carme!). Gràcies Maria per ser una amiga amb qui riure i amb qui plorar (i cotillejar!), i a tu Isaac per donar l’optimisme que moltes vegades ens falta. Moltíssimes gràcies als dos per donar-me el millor nebodet del món a qui estimo immensament (Pol, et trobo moltíssim a faltar!). I sobretot, vull agrair als meus pares, per ser els millors pares del món, per haver-m’ho donat tot i recolzat i estimat com ningú. A vosaltres us dec tot el que sóc, on estic i us he de dir que gràcies a vosaltres sóc molt feliç. Per mi, sou i sereu un model a seguir.

Summary

Tailoring Carbon Nanotubes Properties for Gene Delivery Applications

Gene therapy has become an increasing innovative technique to treat disease by the insertion of genes into individual's cells and tissues. The challenge is to efficiently and safely deliver the therapeutic nucleic acid into the target cells and organs. Among the synthetic vectors recently developed, carbon nanotubes are an interesting choice as they have already demonstrated considerable promise as delivery systems due to their high aspect ratio and their capacity to translocate the cell membrane. The problem that arises is their limited solubilization and spontaneous aggregation *in vivo*.

Aiming to engineer new carbon nanotube-based designs for the formation of complexes able to transfect DNA/RNA to cells with a good track of biocompatibility and cell viability, different strategies have been developed. Firstly, the covalent functionalization of carbon nanotubes by plasma techniques has been optimized. This type of modification allows to either achieving highly reactive surfaces able to covalently bind DNA towards a chemical linker or a positively charged nanotube surface enabling the wrapping of the nucleic acid by electrostatic interaction. Secondly, the dispersion of the differently-sized carbon nanotubes by means of a stabilizing agent including a surfactant, an amphiphilic polymer and proteins has been assessed. The chemical nature of the modifying moieties on the carbon nanotube, alongside to other physical properties such as length or diameter, has a direct effect on the dispersibility, cytotoxicity and biodistribution of these systems.

The use of proteins in the nanoparticle functionalization is encouraging due to the formation of the protein corona on its surface. Such complex exhibits high DNA load capacities and allows a tunable payload release by manipulating the corona composition.

Resum

Tailoring Carbon Nanotubes Properties for Gene Delivery Applications

La teràpia gènica s'està convertint en una tècnica innovadora per tal de curar una malaltia mitjançant la inserció de gens dins les cèl·lules i òrgans d'un individu. El repte recau en l'alliberació eficient i segura de l'àcid nucleic terapèutic a les cèl·lules i òrgans objectiu. De tots els vectors sintètics desenvolupats recentment, els nanotubs de carboni són una elecció interessant que ja ha demostrat prometre considerablement com a sistema alliberació, gràcies a la seva proporció amplada-alçada i la seva capacitat de translocar la membrana cel·lular. El problema que sorgeix és la seva limitada solubilització i l'agregació espontània *in vivo*.

Amb l'objectiu de desenvolupar nous dissenys basats en nanotubs de carboni per a la formació de complexos capaços de transfectar ADN a les cèl·lules, amb un bon registre de biocompatibilitat i viabilitat cel·lular, s'han desenvolupat diferents estratègies. En primer lloc, s'ha optimitzat la funcionalització covalent dels nanotubs per mitjà de tècniques de plasma. Aquest tipus de modificació permet aconseguir tan superfícies altament reactives capaces d'unir ADN a través d'una molècula enllaçant, com superfícies carregades positivament que permeten l'envolcall de l'àcid nucleic per interacció electrostàtica. En segon lloc, s'ha avaluat la dispersió de nanotubs de diferents mides per mitjà d'un agent estabilitzant incloent un surfactant, un polímer amfifílic i proteïnes. Aquesta naturalesa química de la superfície del nanotub, juntament amb altres propietats físiques com ara l'allargada o el diàmetre, té un efecte directe en la dispersibilitat, citotoxicitat i biodistribució d'aquest sistemes.

L'ús de proteïnes per funcionalitzar nanopartícules és encoratjador ja que forma la corona de proteïna a la seva superfície. Tals conjugats mostren una elevada capacitat de carregar ADN i permeten la regulació de la seva alliberació mitjançant la manipulació de la composició de corona.

Table of Contents

Acknowledgments	I
Summary	III
Resum	V
Table of Contents	VII
Index of Schemes And Figures	XI
Index of Tables And Equations.....	XIV
List of Abbreviations.....	XV
1. Introduction	1
1.1. Background	3
1.2. Aims	12
1.3. Content of this Dissertation	13
1.4. References.....	15
2. Surface Modification By Plasma Techniques	19
2.1. Introduction	21
2.2. Experimental Section.....	26
2.2.1. Plasma Reactor Employed	26
2.2.2. Procedure of the Plasma Polymerization by PECVD	27
2.2.3. Methodology of the Plasma-Grafting Modification.....	27
2.2.4. Chemical and Topographical Characterization of the Surfaces	28
2.2.5. Functionalization of the Modified Surfaces	28
2.2.6. Fabrication of Microstructured Surfaces	29
2.2.7. Study of the Covalent Immobilization of Protein Monolayers by Quartz Crystal Microbalance with Dissipation (QCM-D)	30
2.2.8. Fabrication of Bioactive Surfaces <i>via</i> Enzyme Immobilization.....	31
2.2.9. Covalent Immobilization of Gene Delivery Viral Vectors.....	34

2.3. Results and Discussion.....	36
2.3.1. ppPFM Thin Film Formation by PECVD.....	36
2.3.2. Development of the Plasma Grafting Modification Approach.....	40
2.3.3. Study of the Protein Immobilization by QCM-D Analysis.....	49
2.3.4. Obtaining Bioactive Surfaces by Enzyme Immobilization.....	56
2.3.5. Immobilization of Viral Gene Delivery Vectors for Substrate-Mediated Transfections.....	64
2.4. Concluding Remarks.....	67
2.5. References.....	68
3. Modification of Carbon Nanotubes by PECVD for Gene Delivery Vectors.....	73
3.1. Introduction.....	75
3.2. Experimental Section.....	79
3.2.1. Employed Carbon Nanotubes (CNTs).....	79
3.2.2. Surface Modification of CNTs by PECVD.....	79
3.2.3. Characterization of the Modified CNTs.....	80
3.2.4. Reactivity of the ppPFM-coated rCNTs.....	82
3.2.5. Cell Viability of the Decorated-rCNTs.....	83
3.2.6. Dispersibility Studies of the ppPFM-modified rCNTs.....	83
3.2.7. Cell Transfection Studies of the DNA Vectors.....	84
3.3. Results and Discussion.....	85
3.3.1. PECVD Modification of rCNTs with ppPFM.....	85
3.3.2. DNA Condensation to the rCNT <i>via</i> Ionic Interaction.....	101
3.4. Concluding Remarks.....	106
3.5. References.....	108
4. Effect of the Physicochemical Properties of CNTs in Biological Applications.....	121
4.1. Introduction.....	123
4.2. Experimental Section.....	128
4.2.1. CNT types Studied.....	128
4.2.2. Shortening Process.....	128
4.2.3. Dispersibility Studies.....	130
4.2.4. Evaluation of the Cell Viability of the Complexes.....	132
4.2.5. Study of the <i>In Vivo</i> Biodistribution of CNTs in Mice.....	133
4.2.6. Evaluation of the pGFP Complexes.....	134

4.3. Results and Discussion	135
4.3.1. Shortening of CNTs	135
4.3.2. Dispersibility of the Different CNTs	142
4.3.3. Effect of the CNT Structure and Surface Modification on Cellular Viability	147
4.3.4. Study of the <i>In Vivo</i> Biodistribution of the CNTs in Mice.....	153
4.3.5. Assessment of the ppAA-Coated CNT Systems for GFP Gene Delivery	158
4.4. Concluding Remarks	162
4.5. References	164
5. Increasing Loading Capacity: Protein Coronas	169
5.1. Introduction	171
5.2. Experimental Section	175
5.2.1. Nanoparticle Preparation	175
5.2.2. Corona Formation.....	176
5.2.3. Nanoparticle and Corona Characterization	177
5.3. Results and Discussion	180
5.3.1. Optimizing the Protein Corona	180
5.3.2. Assessment of the Evolution of Protein Corona	187
5.3.3. Using Gold Nanrods for Selective Triggered Release Applications	193
5.3.4. Protein Corona Formation on CNTs	199
5.4. Concluding Remarks	204
5.5. References	206
6. Conclusions	209
List of Publications and Presentations	214

Index of Schemes

Scheme 1.1. Gene therapy pathway	4
Scheme 1.2. Structure of the (A) single-walled CNTs and (B) multi-walled CNTs	6
Scheme 2.1 ppPFM thin film structure and reaction with amine-terminated molecules.	22
Scheme 2.2. Pulsed plasma polymerization process	23
Scheme 2.3. Grafting process on polymer substrates	24
Scheme 2.4 Schematic diagram of the plasma reactor and its electrical components.	26
Scheme 2.5 Chemical structure of the FTSC (left) and PEG-amine (right).	28
Scheme 2.6. Microcontact printing methodology.	30
Scheme 2.7. Chemical structure of the 1,3-1,4- β -glucane.....	33
Scheme 2.8. DNS chemical reaction.	34
Scheme 2.9. QCM-D technology used in this work.....	49
Scheme 2.10. Conformational changes of BSA	54
Scheme 2.11. 1,3-1,4- β -glucanase structure and immobilization	57
Scheme 3.1. Formation of CNT-based gene delivery vector <i>via</i> ppPFM polymerization.....	78
Scheme 3.2. Obtaining the ppAA-modified CNT-mediated transfection vector.....	78
Scheme 3.3. Fluorescently-labeled rCNTs (F-rCNTs).....	82
Scheme 4.1. Effect of the physicochemical properties of CNTs.....	127
Scheme 4.2. Carbon nanotubes employed in this work	128
Scheme 4.3. Amphyphylic polymer (pHPMA) synthesis	130
Scheme 5.1. Graphical representation of the corona design approach	173

Index of Figures

Figure 1.1. CNTs penetration through the cell membrane	7
Figure 2.1. Silicon master used in this work	29
Figure 2.2. WCA of the ppPFM thin films.....	37
Figure 2.3. AFM analysis of the ppPFM films.....	39
Figure 2.4. Reactivity of the ppPFM layers towards FTSC.....	40
Figure 2.5. AFM 3D images of Ar-plasma treated PS surfaces.....	41
Figure 2.6. AFM study of the gPFM-modified surfaces.....	42
Figure 2.7. WCA values for the 3 steps in the plasma grafting modification	43
Figure 2.8. Microstructuring of the gPFM-modified surfaces	45
Figure 2.9. Microcontact printing on gPFM-modified surfaces	47
Figure 2.10. Assay evolution of the QCM-D parameters for the modified sensors	51
Figure 2.11. Time-evolution of the mass adhered on the modified surfaces	52
Figure 2.12. Analysis of the viscoelastic properties of the BSA monolayer	52
Figure 2.13. QCM-D evolution of the enzyme front the gPFM-modified sensor	58
Figure 2.14 Viscoelastic properties of the immobilized enzymatic layer.....	59

Figure 2.15. Reactivity of the gPFM-modified PS beads	61
Figure 2.16. Immobilized 1,3-1,4- β -glucanase on the PS-gPFM beads	61
Figure 2.17. Activity of the immobilized enzyme	64
Figure 2.18. GFP expression of the seeded cells on the CRS at diferent MOI ratios.....	66
Figure 3.1. WCA of the resulting ppPFM film depending on the t_{PECVD}	85
Figure 3.2. HRTEM images of the rCNT-ppPFM systems	86
Figure 3.3. Length and diameter of the rCNT-ppPFM complexes.....	87
Figure 3.4. X-Ray microanalysis of the HRTEM-imaged rCNT-ppPFM.....	88
Figure 3.5. XPS of the ppPFM-modified rCNTs	89
Figure 3.6. Deconvolution of the XPS specrum for the ppPFM-modified rCNTs	90
Figure 3.7. Fluorescent microscopy images of the functionalized F-rCNTs	91
Figure 3.8. HRTEM images of the rCNTs functionalized with QDs	92
Figure 3.9. X-Ray microanalysis of the QD-functionalized rCNTs.....	93
Figure 3.10. <i>In vitro</i> fluorescence tracking of the F-sCNTs.....	94
Figure 3.11. Dispersion of the ppPFM-modified rCNTs in ethanol	95
Figure 3.12. Dispersibility of rCNT-ppPFM in different solvents.....	95
Figure 3.13. Graphic representation of the Hansen parameters	97
Figure 3.14. XPS analysis of the TPA-functionalized rCNTs.....	98
Figure 3.15. Analysis of the S2p peak of the rCNT-ppPFM-TPA.....	100
Figure 3.16. IR spectrum of the ppAA coating achieved by PECVD	102
Figure 3.17. WCA of (A) the non-modified silicon wafer and (B) coated with ppAA.	102
Figure 3.18. Size and charge of the rCNTs-ppPFM and rCNT-ppAA complexes	104
Figure 3.20. Cell transfection of the rCNT-ppAA+pGFP complexes	105
Figure 4.1. Shortening procedure evaluation of rCNTs by HRTEM	136
Figure 4.2. Average length (μm) of all shortened rCNTs.....	137
Figure 4.3. EDS of the shortened rCNTs.....	138
Figure 4.4. HRTEM images of the (A) naïve fCNTs and (B) the s-fCNTs.....	140
Figure 4.5. Mean of the lengths of the naïve fCNTs and s-fCNTs.....	140
Figure 4.6. EDS of the flexible CNTs before and after shortening	141
Figure 4.7. Zeta potential of the CNTs with different functionalities	143
Figure 4.8. Hydrodynamic diameter of the CNTs with different functionalities.....	143
Figure 4.9. Dispersibility of CNTs with different functionalities	145
Figure 4.10. Concentration of functionalized-CNTs present in solution over time	145
Figure 4.11. Percentage of CNTs dispersed in solution after 1 h of sonication	147
Figure 4.12. Cell viability of CNTs in function of the incubation time.....	148
Figure 4.13. Microscope image (20x) of 3T3 cells incubated with CNTs.....	148
Figure 4.14. Cell viability of the CNTs at different concentrations	149
Figure 4.15. Cytotoxicity of CNTs with different functionalities	150
Figure 4.16. Microscope images of CNT-HS in cells	150
Figure 4.17. Microscope images of CNT-CTAB in cells.....	151
Figure 4.18. Microscope images of CNT-pHPMA in cells.	152
Figure 4.19. Microscope images of CNT-ppAA in cells.....	153
Figure 4.20. Comparison of <i>in vivo</i> biodistribution of the F-CNTs injected in mice.....	155
Figure 4.21. <i>Ex vivo</i> organ biodistribution of the F-CNTs after 24 h of injection	155

Figure 4.22. Semi-quantitative analysis of the organ biodistribution.....	157
Figure 4.23. Agarose gel electrophoresis of different CNT-ppAA+pGFP (w/w) ratios	159
Figure 4.24. Cell viability of the pGFP complexes varying the CNT concentration	160
Figure 4.25. Transfection of 3T3 cells with CNT-ppAA+pGFP complexes	161
Figure 4.26. Transfection of Cos-7 cells with CNT-ppAA+pGFP complexes	161
Figure 5.1. Vials of the NR-coronas.....	180
Figure 5.2. Absorbance spectra of the NR-corona using different type of proteins.....	181
Figure 5.3. Loading from coronas measured by supernatant loss	182
Figure 5.4. Loading of NR-coronas measured by heat displacement	183
Figure 5.5. Size and charge of the NR-coronas	183
Figure 5.6. Characterization of the NR-coronas.....	184
Figure 5.7. Effect of environmental and assembly conditions on loading of DNA.....	185
Figure 5.8. Absorption spectra of NRs after the formation of the protein corona.....	186
Figure 5.9. Time-evolution of the absorption spectra of the NR-coronas	187
Figure 5.10. DNA passive release profiles of NR-coronas	188
Figure 5.11. Passive release of NR-coronas in different buffer concentrations	189
Figure 5.12. Passive release DNA profiles of coronas in an exchange environment	190
Figure 5.13. Leakage of NR-coronas at different exchange environments.....	191
Figure 5.14. Leakage of DNA in blood plasma	192
Figure 5.15. Melting the NR-CTAB and NB-CTAB	194
Figure 5.16. Selective melting of a NR/NB-CTAB mixture.....	194
Figure 5.17. Characterization of NB-coronas.....	195
Figure 5.18. Passive release DNA profiles of NB-coronas	196
Figure 5.19. NRs and NBs synthesized and loaded for triggered release	197
Figure 5.20. Selective release of NR/NB-corona mixture	198
Figure 5.21. Selective melting of NRs and NBs	198
Figure 5.22. HRTEM images of the CNT-coronas.	200
Figure 5.23. Size and charge of the CNT-coronas	200
Figure 5.24. Loading capacities of the CNT-coronas.....	201
Figure 5.25. Size, charge and DNA loadings of the coronas formed with CNT-ppPFM.....	202
Figure 5.26. DNA release from the fCNT-HS-DNA with different exchange conditions.....	203

Index of Tables

Table 2.1. Reactor conditions for the deposition of ppPFM by PECVD.....	27
Table 2.2. Samples prepared for further activity quantification.....	33
Table 2.3. Optimized reactor parameters for the formation ppPFM thin films.....	37
Table 2.4. ToF-SIMS negative ions maps of ppPFM-modified GS substrates.....	38
Table 2.5. Roughness values after being coated with ppPFM by PECVD technique.....	39
Table 2.6. Roughness of a PS surface after Ar-plasma treatment for diferent times.	41
Table 2.7. Roughness of the resulting gPFM-modified surfaces.....	42
Table 2.8. ToF-SIMS negative ions map of a micropatterned PS surface	46
Table 2.9 ToF-SIMS negative ions map of a PS surface functionalized by μ CP.	48
Table 2.10. BSA adopted forms in function of the pH. ^{62,63}	53
Table 2.11. Both calculated footprints and theoretical protein mass of BSA monolayer.....	54
Table 2.12. General properties of the two modification techniques.....	56
Table 2.13. Values for the quantification of immobilized enzyme..	60
Table 2.14. Data to calculate the mass obtained after the 1,3-1,4- β -glucanase and the PS beads are incubated for 1h (Mass 1 h) or 2 h (Mass 2 h)	62
Table 2.15. Activities of 1,3-1,4- β -glucanase.	63
Table 3.1. Plasma conditions used for the ppPFM deposition on CNTs.	80
Table 3.2. PECVD conditions applied for the ppAA deposition on CNTs.....	80
Table 3.3. Solvents used for the dispersibility studies.	83
Table 3.4. Atomic percentages of the TEM-analyzed samples.	88
Table 3.5. Atomic percentage of rCNTs and rCNT-ppPFM.....	90
Table 3.6. Atomic percentage both the ppPFM-modified rCNTs and the subsequently functionalized with TPA.	99
Table 3.7. Summary of the percentage contributions of the different functionalities identified for both samples.....	99
Table 4.1. Concentrations used to disperse the CNTs by non-covalent functionalization.	131
Table 4.2. Relative atomic percentages of the elements found in the samples.	139
Table 4.3. Relative atomic percentages of the fCNTs and s-fCNTs analysed by HRTEM.....	141
Table 4.4. Conditions of the CNT-ppAA+pGFP complexes.....	159

Index of Equations

Equation 2.1.....	22
Equation 2.2.....	22
Equation 2.3.....	31
Equation 2.4.....	31
Equation 3.1.....	96

List of Abbreviations

AA: Allylamine	PDMS: Polydimethylsiloxane
AFM: Atomic Force Microscopy	PECVD: Plasma Enhanced CVD
BSA: Bovine Serum Albumin	PEG: Polyethylene glycol
CNT: Carbon Nanotube	PFM: Pentafluorophenyl methacrylate
CRS: Cell Reprogramming Surface	PhB: Phosphate Buffer
CTAB: Cetyltrimethylammonium bromide	pHPMA: Poly-N-Hydroxypropyl Metacrylamide
CVD: Chemical Vapor Deposition	pGFP: GFP plasmid
DC: Duty Cycle	ppAA: PECVD-polymerized AA
DH: Hydrodynamic Diameter	ppPFM: PECVD-polymerized PFM
DLS: Dynamic Light Scattering	PS: Polystyrene
DMEM: Dubelco's Modified Eagle Medium	PSb: Polystyrene beads
DMSO: Dimethyl Sulfoxide	PSP: Polystyrene plates
DNS: 3,5-dinitrosalicylic acid	P/S: Penicillin Streptomycin
EDS: Energy Dispersive X-Ray Spectroscopy	QCM-D: Quartz Crystal Microbalance with Dissipation
ES: Equine Serum	R_a: Root Mean Square Roughness
EtOH: Ethanol	RF: Radio Frequency
Et₂O: Diethyl Ether	R_{max}: Maximum roughness height
fCNT: Flexible CNT	RMS: Root Mean Square
F-CNT: Fluorescent CNT	RT-PCR: Reverse Transcription-Polymerase Chain Reaction
FTIR: Fourier Transform Infrared Spectroscopy	R_q: Average roughness
fs: femtosecond	SEM: Scanning Electron Microscopy
FTSC: Fluorescein-5-thiocarbamide	siRNA: Small interfering RNA
GFP: Green Fluorescent Protein	SPR: Surface Plasmon Resonance
Gln: 1,3-1,4-β-Glucanase	SWNT: Single-Walled Nanotube
gPFM: Grafted PFM GS: Glass Slide	s-fCNT: Short flexible CNT
HRTEM: High Resolution TEM	s-rCNT: Short rigid CNT
HS: Human Serum	TEM: Transmission Electron Microscopy
IR: Infrared	ToF-SIMS: Time-of-Flight Secondary Ion Mass Spectroscopy
LSPR: Longitudinal SPR	t_{OFF}: Plasma-off time
μCP: Microcontact Printing	t_{ON}: Plasma-on time
MeOH: Methanol	TPA: Thiol-PEG-Amine
MD: Molecular Dynamics	UV-Vis: Ultraviolet-Visible
miRNA: Micro RNA	WCA: Water Contact Angle
MWNT: Multi-Walled Nanotube	W_i: Input Power
m/z: Mass-to-charge	W_{eq}: Equivalent Power
NB: Nanobone	XPS: X-ray Photoelectron Spectroscopy
NP: Nanoparticle	
NR: Nanorod	
PBS: Phosphate Buffered Saline	

Chapter I.

Introduction

1.1. Background

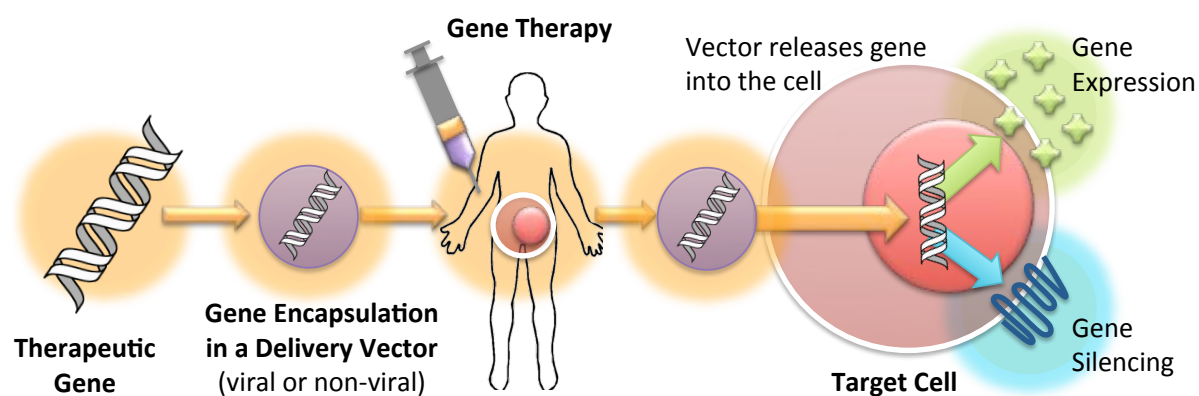
Gene therapy arose as a revolutionary concept in the field of medicine at the end of the 60s and has gained significant importance in the recent years.¹ The principle of gene therapy is to overcome the disorder causing the disease by direct employment of nucleic acids as a medicine. Instead of focusing in erasing the symptoms of the disease such other treatments as drug therapy does, gene therapy propounds dealing with the root of the problem, correcting the errors arising from the defective gene or genes.² Therefore, in this approach, the gene causing the disease is replaced with a healthy copy becoming the only hope of finding a cure for genetic disorders. Similarly, this treatment also consists in a potential tool to face other types of disease enabling the transfection of genes with other beneficial functions such as enhancing the stimulation of the immunological system, inducing the cancer cells death by means of the introduction of a suicide gene, or modifying the genetic information in order to produce proteins with therapeutic properties.

Such strategies have opened up new procedures to combat different types of cancer, hemophilia, cystic fibrosis, Parkinson's and Alzheimer's disease, among others. Although gene therapy by using gene delivery vectors holds a great potential within the future of biomedicine, certain key obstacles need to be overcome before this potential can be fully realized.^{3,4} While this new therapeutic approach has yielded great expectation of benefit, early clinical studies have shown disappointing failures as well as a few hints of success.

Classically, gene therapy has been classified depending on the strategy used to treat the disease:⁵⁻⁹

- Gene supplementation: this approach is based on the supplementation of damaged genes with functional copies of genes to treat diseases caused by recessive mutations.
- Gene augmentation: this procedure consists in the introduction of a new gene (or genes) into the target cells in order to mediate a novel function.
- Gene correction: gene correction therapy or chimeraplasty consists in the substitution of single base pairs in order to correct mutations in the genome.
- Gene silencing: this approach involves the delivery of short double stranded RNA (siRNA) or microRNA (miRNA) sequences to induce post-transcriptional gene knockdown by efficient degradation of specific messenger RNA (mRNA) sequences.

The major historical problem of gene therapy lies in the development of safe and efficient systems, also known as vectors, for the delivery of therapeutic genes to their intended target cells.¹⁰ This goal is formidable and largely predictable since the human body has evolved to protect itself from environmental hazards, notably foreign nucleic acids. The ideal vector for systemic delivery to disseminated diseases should be injected intravenously and able to discern and reach target cells efficiently without premature elimination by components of the bloodstream such as serum proteins, antibodies and cells. Once the vector has reached the target cell, it should also be able to utilize uptake mechanisms and cellular processing machinery and carry out efficient expression of the therapeutic product. Scientists working in gene therapy and gene delivery have classically distinguished two types of delivery vectors – viral vectors and synthetic vectors.¹⁰⁻¹⁴



Scheme 1.1. Gene therapy pathway consisting in the direct delivery of a therapeutic gene or silencing RNA into patients. This type of route involves encapsulating the desired gene in a vector, which delivers the gene to target cells causing a specific expression (protein synthesis, etc) or a gene knockdown.

Many initial efforts in gene therapy have been concentrated on the genetic engineering of viruses to develop efficient vectors for the delivery of therapeutic genes (Scheme 1.1).¹⁴ Nowadays, viral systems are at the edge of fulfilling the short-term requirements for gene therapy. The basis of this success lies in their high transfection efficiency improved by years of evolution. However, the use of many viral vectors is restricted by their limited capacity to carry transgenes, by the cost of large-scale production and by inherent safety risks.^{15,16} Furthermore, viral vectors are often susceptible to neutralization by serum antibodies and complement, coupled with poor target-selectivity or inappropriate infectivity profile.

Thus, synthetic vectors would be the preferred choice in the future, because of their safety and relatively easy manufacturing.^{10,14} However, their low efficiency in delivering genetic material to the

target cells has limited their use as a viable treatment. Nowadays, non-viral methods present some advantages over viral systems, such as a virtually infinite packaging capacity and the lack of significant immunological stimulation, despite the fact that non-viral systems are still in their infancy of development. Typically, nucleic acids have been condensed with cationic and/or hydrophobic carriers in order to form discreet particles.^{17,18} Appropriate formulations of both polyplexes and lipoplexes can be efficient at delivering nucleic acids into target cells *in vitro*, although these vectors face several limitations when administered intravenously.

The progress of material synthesis and the rise of nanotechnology have made possible the synthesis of nanomaterials with tailored properties and specific functions.¹⁹ The development of nanotechnology in the biological area has opened new possibilities in the design of new delivery systems for both small molecules and macromolecules, such as proteins and nucleic acids. Currently, a range of nanometric materials with different shapes and sizes are available as nanocarriers with promising properties to improve the efficiency of gene therapy. Many nanomaterials have been evaluated as transfection carriers due to their low toxicity, biocompatibility and simple modification such as polymeric nanoparticles, dendrimers and inorganic nanoparticles, including gold nanorods and carbon nanotubes.²⁰⁻²⁷

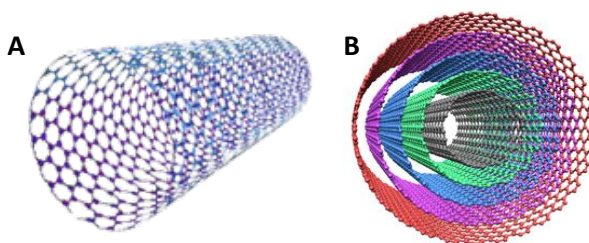
Polymeric nanoparticles (NP) have become a potentially useful tool for the delivery of nucleic acids due to their advanced physical properties, low toxicity and biodegradability, along with their ability to be chemically functionalized with imaging agents and targeted ligands.^{24,25} The most widely used synthetic polymers for gene therapy technology are polyethyleneimine (PEI), poly-(L-Lysine) (PLL) and poly(dimethyl aminoethyl methacrylate) p(DMAEMA), among others. Natural polymers like chitosan, dextran or hyaluronic acid are composed of polysaccharides and are also employed as gene carriers.

Similarly, dendrimers are polymer-based structures composed of repeating units emanating from a central core resulting in completely branched star-like topologies in a symmetrical and ordered fashion.^{20,25} Such unique architecture properties facilitates the synthesis of a broad range of molecules with different functionalities and in a highly tuneable shape and size. When these structures are imperfectly branched or present irregular structures are known as hyperbranched polymers.²⁸ Both types of have emerged as attractive candidates to be used as gene delivery vectors.

Otherwise, inorganic NPs are nanostructures also used as gene vehicles and are characterized by the possibility to be produced in a tuneable shape and variable size.²⁶ They can be made of silica and calcium phosphate, which can be engineered with a certain porosity in order to entrap the specific

molecular payload and protect it from denaturation or degradation.²⁵ Magnetic particles are formed by a magnetic core covered with a functionalizable polymer or metal coating and are also commonly used as gene nanocarriers given their possibility to be driven towards the target cell or tissue by a magnetic field.²⁹ Other frequently employed nanoparticles for gene therapy technology are novel metal nanoparticles mainly made of silver and gold.³⁰ They present unique characteristics such as their highly tuneable optical properties according to their shape, size and composition, their relatively easy synthesis and facile surface functionalization. Gold nanorods (NRs) are especially interesting candidates for their tuneable aspect ratio (AR) that directly changes their longitudinal surface plasmon resonance (LSPR) and thus, their properties.²⁷ Pulsed laser excitation in resonance with their LSPR can induce melting by locally heating the NRs to high temperatures. As a result, NRs with different ARs can be excited independently at different wavelengths allowing their triggered melting and a controlled release of the biomolecule loaded on the NRs.

Among these variety of nanomaterials, carbon nanotubes (CNTs) are an interesting choice as they have already demonstrated considerable promise as delivery systems. Carbon nanotubes were discovered by Iijima in 1991 and can be divided into single-walled (SWNTs) and multi-walled nanotubes (MWNTs) and are characterized by having diameters on the order of a few nanometers and lengths that may exceed 1 μm (Scheme 1.2).^{31,32}



Scheme 1.2. Structure of the (A) single-walled CNTs and (B) multi-walled CNTs.³³

These nanostructures possess highly sought characteristics, such as an easily functionalizable surface *via* different chemistries, high surface area per nanotube unit for high drug/nucleic acid loading, high flexibility and a good track record of biocompatibility. It has been demonstrated that carbon nanotubes (CNTs) can be internalized by variety of cell types thanks to their geometry and relatively long length (200 nm).^{22,34-36} Their high surface area can potentially act as a template for cargo molecules and, thus, to deliver therapeutic and diagnostic small molecules and macromolecules to cells, such as DNA or RNA.³⁵⁻³⁷

Unlike other delivery systems, carbon nanotubes are capable of entering the cell directly through the plasma membrane due to their favorable lipophilicity and size, without the need of endocytotic pathways (Figure 1.1).^{38,39}

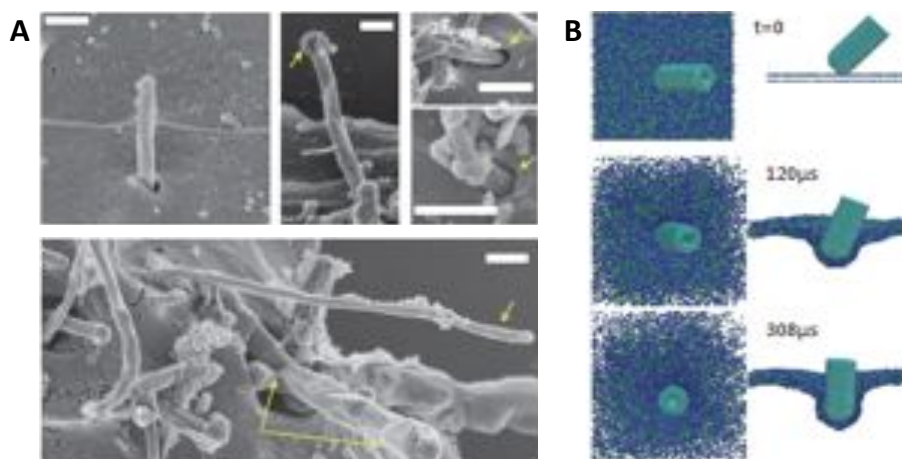


Figure 1.1. CNTs penetration through the cell membrane.³¹ (A) SEM images of the cells after being fixed with osmium tetroxide (scale bars of 300 nm). These images exhibited the threshold of the MWNTs into hepatic fibroblasts *via* passive diffusion through the cell membrane. (B) Molecular simulation of the MWNT penetration into the cell.

Direct intracellular delivery is an attractive feature for the delivery of nucleic acids, since conventional methods can be sometimes inefficient at overcoming biological membranes. In addition, targeting mechanisms, such as cell surface receptor ligands can be incorporated on the surface of carbon nanotubes to enhance target binding to specific tissues or cell types.⁴⁰ However, clinical implementation of carbon nanotubes has been hampered by solubility limitations and spontaneous aggregation *in vivo*, leading to reticuloendothelial system (RES) tropism and subsequent liver accumulation.^{41,42} Chemical surface modification of carbon nanotubes is a prerequisite to achieve homogeneous dispersion in aqueous phase for *in vivo* applications.^{22,34,39} Such dispersion is particularly difficult to achieve as a consequence of the hydrophobic nature of carbon nanotubes, leading to the formation of bundles or aggregates due to strong cohesive force between individual tubes. Accordingly, full exploitation of the benefit of CNTs in biological settings requires their chemical modification in order to facilitate stabilization of individual nanotubes in aqueous dispersions. In addition, modification of nanotubes can provide suitable functional groups to introduce features for superior nucleic acid loading or to promote efficient post-modification or decoration.

The use of carbon nanotubes in biological applications has been hampered by their difficulty to solubilize in aqueous solutions. Existing strategies for proper dispersion of CNTs in aqueous media include covalent modification by various grafting reactions and non-covalent adsorption or wrapping of functional molecules with surfactant nature.^{43,44} Covalent modification treatments have shown to induce a large number of defects onto the graphene structure, which may lead to alteration of its properties. In contrast, non-covalently modified CNTs may suffer ligand/surfactant-exchange reactions with proteins and other components of the biological milieu, leading to the formation of large aggregates.⁴⁵ Furthermore, inadequate density of modifying groups on the surface of CNTs limits the packing of therapeutically active molecules, such as nucleic acids, and the presentation and display of biological targeting ligands, which is a key factor in applications where a high biological specificity is required. Therefore, the development of new coating strategies for bionanotechnology applications of carbon nanotubes requires to be investigated. The proper functionalization of these vectors may lead to the achievement of highly dispersed CNTs and efficiently induce the attachment of the desired genetic material, while simultaneously enhancing the cellular internalization and minimizing the cytotoxicity of the system.

In general, two main modification strategies have been developed for the covalent functionalization of CNTs: (i) amidation and esterification of oxidised CNTs and (ii) addition reactions.

The treatment of CNTs under strong acidic and oxidizing conditions is a common method for the generation of oxygen-containing functional groups. Typically, prolonged heating or sonication of CNTs using strong acids, such as concentrated sulfuric or nitric acid, or mixtures of sulphuric and nitric acid or sulphuric acid and hydrogen peroxide, results in the formation of hydroxyl, carbonyl and especially carboxyl groups on the sidewalls and, predominantly, on the tips of CNTs.^{46,47} Carboxylic acids generated by oxidative methods on the structure of carbon nanotubes can be further modified to produce ester or amide derivatives via reaction with alcohols and amines, respectively. Amidation and esterification reactions can be performed via standard methods, such as activation of carboxylic acids via acid halides or carbodiimide-mediated coupling. Several strategies leading to solubilization of CNTs in organic solvents have been reported, mainly through esterification or amidation reactions between oxidized CNTs and long-chain alcohols or amides, respectively.⁴⁸ The resulting alkyl chains present on the CNTs surface act as solubilizing agents and the derivatized nanotube becomes soluble in most organic solvents. However, most biological applications require the conjugation of rather hydrophilic ligands that promote dispersion of functionalized CNTs in biological media/aqueous solutions. To increase water dispersion, oxidized CNTs have been modified via activation of their carboxylic acids using thionyl chloride or oxalyl

chloride with a wide range of hydrophilic moieties, such as small molecules, hydrophilic polymers, proteins and nucleic acids.⁴⁹⁻⁵¹ Macromolecules, such as proteins and nucleic acids have also been explored as modifying moieties for the solubilisation of CNTs in aqueous solutions or biological media.^{52,53} The same two-step procedure has been also used for the covalent conjugation of DNA strands bearing a nucleophilic primary amine at the 5' and 3' ends.^{54,55} Additionally, biopolymers, such as chitosan, have been covalently grafted to acid-functionalized single- and multi-walled carbon nanotubes via reaction of their acyl chloride derivatives with suitable amines present on this kind of biopolymers.^{56,57} In addition to biopolymers, covalent grafting of hydrophilic polymers is a popular strategy for increasing the water dispersion of CNTs. Pegylation, which consists of the covalent attachment of poly(ethylene glycol) polymer chains to proteins and nanoparticles, is a common strategy used to improve the biocompatibility of such nanostructures.⁵⁸⁻⁶⁰ Similarly, other works have reported CNT-grafting of other highly water-soluble polymers, such as poly(vinyl alcohol) (PVA), poly(m-aminobenzene sulfonic acid) (PABS) or poly(propionylethylenimine-co-ethylenimine) (PPEI-EI), to improve compatibility in biological media.⁶⁰⁻⁶²

In contrast to post-modification of carboxylic groups generated on CNTs by oxidative processes, which take place mainly at the ends and the sidewall defects, functionalization of the sidewalls of CNTs is more difficult to accomplish. The different reactivity towards covalent chemical modification requires the use of higher reactive species. Research on fullerene chemistry has revealed that the curvature of the fullerene molecule drives the reactivity of addition reactions. Increased curvature of the carbon network results in enhanced/increased pyramidalization of the sp²-hybridized C atoms, which makes addition reactions on carbon-carbon double bonds more favourable. However, CNTs consist of graphitic sidewalls that do not present strongly curved regions in comparison to fullerenes. Therefore, functionalization of the sidewalls via addition reactions is less favoured and it is only possible/achieved by reactive species, such as nitrenes, carbenes and radicals. In reality, carbon nanotubes contain defects in their structure and it is likely that addition reactions take place preferentially at such defect sites.^{63,64} Functionalization of both single and multi-wall CNTs via addition reactions to render water solubility has been achieved in both naïve and pre-modified CNTs. The [2+1] cycloaddition of nitrenes is a popular route for derivatizing CNTs in order to improve their solubility and making them more amenable for biological applications. A variety of hydrophilic functional groups, such as crown ethers and poly(ethylene glycol and different types of sugars (glucose, galactose and mannose) have been successfully attached onto CNTs resulting in water soluble conjugates.⁶⁵⁻⁶⁷

A simple method for obtaining water-soluble CNTs was developed by Prato and colleagues.⁶⁸ This method is based on 1,3-dipolar cycloaddition reactions of azomethine ylides generated in situ by thermal condensation of α -aminoacids and aldehydes. 1,3-Cycloaddition on CNTs produces in substituted pyrrolidine fused rings on the surface of carbon nanotubes, which are amenable for further functionalization. The use of hydrophilic α -aminoacids, such as pegylated α -aminoacids, is an interesting approach for obtaining water-soluble CNTs.⁶⁹ Functionalized oligoethylene glycol chains have shown to be particularly suitable for the covalent immobilization of biomolecules such as aminoacids on CNTs.^{70,71}

Another attractive way of functionalizing CNTs is by free-radical addition, which is a widely used one-step method for the derivatization of carbon nanotube sidewalls. In general, carbon radicals generated by various methods, such as photochemically, thermally or via oxidation/reduction reactions, react covalently with CNTs to form conjugates.⁷²⁻⁷⁷

Alternatively, plasma enhanced chemical vapor deposition (PECVD) appears to be an interesting technique in which polymer chains can be grown directly onto the surface of CNTs. This bottom-up approach provides superior surface coverage and involves the covalent attachment of a moiety that initiates polymerization, such as monomers or initiators. During the last decades, plasma polymerization approaches have been optimized as a surface treatment to achieve covalently functionalized surfaces with a high degree of specificity, density of active groups and versatility. Although, PECVD consists in an approach for covalent modification, it allows the modification of all kinds of materials and geometries without affecting their intrinsic properties.⁷⁸⁻⁸⁰ Besides its versatility, this technique involves dry processes and thus avoids the employment of wet chemistry and limits the generation of chemical residues.⁸¹ As a result, PECVD is able to modulate the attachment of the biomacromolecules or genetic material of interest on the CNTs surface and any other surface in a tailored and controlled way.

On the other hand, the feasibility of carbon nanotube coating with surfactants, amphiphilic copolymers and plasma proteins via non-covalent interactions is increasingly attracting attention.⁸²⁻

⁸⁴ All three approaches can render highly efficient surface-engineered carbon nanotubes able to act as nucleic acid carriers with excellent dispersion and colloidal stability in aqueous solution. The coating of carbon nanotubes with hydrophilic copolymers with pendant hydrophilic groups is the basic element to achieve loading of nucleic acids. The performed polymer side-chains with appropriate chemistries can be easily introduced into the amphiphilic polymer structure to increase the packing capacity of the genetic material. Concurrently, it has been recently demonstrated that

the use of swellable proteins around nanoparticles, known as protein corona, can reduce toxicity while increasing loading capacities.^{85,86}

Despite this progress, new delivery approaches need to be explored for systemically administered regulatory RNAs in order to efficiently silence disease-cause genes in a tissue-specific manner at clinically achievable doses to avoid potential off-target effects that may compromise their therapeutic benefit. Recent reports suggest that nanoparticles with controlled geometrical features and appropriate surface modification can present preferential tissue and organ targeting, when administered systemically. Such features are highly desirable, since it implies that rational design of nanoparticles may address basic strategies for maximizing target accumulation, while minimizing non-specific uptake.^{45,87,88} Likewise, physicochemical properties of CNTs including length, diameter, stiffness and chemical functionalization have been proved to play a decisive role in terms of cell internalization and viability.^{41,89} In this scenario, tailoring of the geometrical shape and surface characteristics of these nanocarriers, which may influence the cytotoxicity, pharmacokinetic profile and biodistribution of the resulting delivery systems, demands to be examined.

1.2. Aims

The main objective of this thesis is to develop in-house customized carbon nanotubes capable of efficient delivery of therapeutic nucleic acids with tailored properties and negligible cytotoxic effects.

In particular, the goals of the present thesis can be summarized in the following points:

- To develop, optimize and characterize a covalent surface modification approach in order to produce highly reactive surfaces with increased degree of specificity (Chapter II).
- To achieve functionalized CNT for potential use as gene delivery vectors by both covalent binding and ionic interaction with DNA and evaluate their *in vitro* efficiency (Chapter III).
- To assess the effect of the physicochemical traits including size, chemical functionalization and mechanical properties of the CNTs in their *in vitro* performance in terms of dispersibility and cytotoxicity and elucidate their *in vivo* biodistribution. (Chapter IV).
- To manipulate and optimize protein corona properties round nanoparticles in order to increase the DNA loading capacity and evaluate its release profile (Chapter V).

1.3. Content of this Dissertation

Carbon nanotubes are presented as promising candidates to carry genetic material with a high cargo ratio of genes. Their ability to translocate through plasma membranes as a nanoneedle enables them to be effectively internalized into the target cell. However, these nanoparticles face different problems, as stated before, because they present highly hydrophobic surfaces. Thus, chemical functionalization of CNTs is required not only to attach the desired molecule to its surface, but also to increase the biocompatibility of the resulting conjugate.

Different surface modification approaches are presented in this work to generate appropriate functional groups, enabling the attachment of suitable solubilizing, bioactive or biocompatible species. Plasma polymerization techniques, which provide a covalent functionalization of the CNTs surface, are explored while non-covalently functionalized-approaches are also developed.

First, the amenability of different plasma polymerization approaches is examined. It intends to broaden the horizon of the PECVD technology from the polymer thin film deposition to the fabrication of bioactive surfaces and ultimately, the achievement of cell transfection devices. In this line, Chapter II optimizes two different plasma techniques with the same monomer, understanding the deposition and polymerization processes involved. This previous study investigates the reactivity and properties of the resulting films, and evaluates the modified-surfaces as potential means to achieve smart, bioactive surfaces.

How plasma treatment can be an effective method for the surface functionalization of CNTs is studied in Chapter III. This covalent modification technique allows a high control of the properties and chemistry of the surface coating as demonstrated in Chapter II. Two strategies are assessed in this part of the thesis employing two different monomers. One of them allows the creation of highly reactive layers with a high degree of specificity, enabling the covalent immobilization of suitable chemical groups like thiol-reactive moieties for covalent conjugation with end-modified nucleic acids *via* a cleavable disulfide bond. Alternatively, the deposition of polymer with amine-bearing moieties will lead to a positively charged polymer film able to associate with DNA and RNA through electrostatic interaction. Both approaches are optimized in this study, and the cell viability and transfection efficiency of the resulting vectors are evaluated.

Although the final surface functionalization of the CNTs is a key factor to achieve feasible gene delivery vectors, the physicochemical properties of the CNTs forming the nanocarrier also have a direct influence on its behavior. Chapter IV seeks to explore how these parameters affect the final

cell internalization or cytotoxicity of the resulting complexes. This study evaluates how CNTs of different diameters, lengths and coatings (covalent and non-covalent) interact with cells in terms of cell viability, uptake and biodistribution. Moreover, gene transfection vectors formed with these systems are also tested. This work was mainly performed at the Australian Institute for Bioengineering and Nanotechnology (AIBN) of the University of Queensland (UQ) in Brisbane (Australia) in collaboration with Dr. Thurecht, associate group leader of the Polymer Chemistry Group.

The last part of this thesis is centered in the increase of the loading capacities of the developed carriers. When nanoparticles are introduced to biological fluids, they encounter high concentrations of proteins, which can non-specifically adsorb on the NP surface, forming a protein corona. The corona is large and multilayered, and it has a high capacity for a payload that interacts with the proteins in the corona. Because of this, the corona could be used to improve the carrier loading properties for gene delivery. Thus, Chapter V is focused in the optimization and evaluation of these protein corona loading and release properties. The protein corona studies were assessed and deeply characterized in Prof. Hamad-Shcifferli's Group at the Massachusetts Institute of Technology (MIT) in Cambridge (USA).

1.4. References

- 1 Edelstein, M. L., Abedi, M. R., Wixon, J. & Edelstein, R. M. Gene therapy clinical trials worldwide 1989 - 2004 - an overview. *The Journal of Gene Medicine* **6**, 597-602 (2004).
- 2 Verma, I. M. & Somia, N. Gene therapy - promises, problems and prospects. *Nature* **389**, 239-242 (1997).
- 3 Seymour, L. W. The future of gene therapy in the UK. *Trends in Biotechnology* **24**, 347-349 (2006).
- 4 Trent, R. J. A. & Alexander, I. E. Gene therapy: applications and progress towards the clinic. *Internal Medicine Journal* **34**, 621-625 (2004).
- 5 Broderick, J. A. & Zamore, P. D. microRNA Therapeutics. *Gene therapy* **18**, 1104-1110 (2011).
- 6 Caplen, N. J. Gene Therapy Progress and Prospects. Downregulating gene expression: the impact of RNA interference. *Gene Therapy* **11**, 1241-1248 (2004).
- 7 Doench, J. G., Petersen, C. P. & Sharp, P. A. siRNAs can function as miRNAs. *Genes & Development* **17**, 438-442 (2003).
- 8 Rana, T. M. Illuminating the silence: understanding the structure and function of small RNAs. *Nature Reviews Molecular Cell Biology* **8**, 23-36 (2007).
- 9 Shankar, P., Manjunath, N. N. & Lieberman, J. The prospect of silencing disease using RNA interference. *JAMA* **293**, 1367-1373 (2005).
- 10 Li, S. & Huang, L. Nonviral gene therapy: promises and challenges. *Gene Therapy* **7**, 31-34 (2000).
- 11 Brown, M. D., Schätzlein, A. G. & Uchegbu, I. F. Gene delivery with synthetic (non viral) carriers. *International Journal of Pharmaceutics* **229**, 1-21 (2001).
- 12 Davis, M. E. Non-viral gene delivery systems. *Current Opinion in Biotechnology* **13**, 128-131 (2002).
- 13 Liu, F. & Huang, L. Development of non-viral vectors for systemic gene delivery. *Journal of Controlled Release* **78**, 259-266 (2002).
- 14 Niidome, T. & Huang, L. Gene Therapy Progress and Prospects: Nonviral vectors. *Gene Therapy Progress and Prospects* **9** (2002).
- 15 Kay, M. A., Glorioso, J. C. & Naldini, L. Viral vectors for gene therapy: the art of turning infectious agents into vehicles of therapeutics. *Nature Medicine* **7**, 33-40 (2001).
- 16 Thomas, C. E., Ehrhardt, A. & Kay, M. A. Progress and problems with the use of viral vectors for gene therapy. *Nature Reviews Genetics* **4**, 346-358 (2003).
- 17 Fisher, K. D. *et al.* A versatile system for receptor-mediated gene delivery permits increased entry of DNA into target cells, enhanced delivery to the nucleus and elevated rates of transgene expression. *Gene Therapy* **7**, 1334-1343 (2000).
- 18 Oupicky, D. *et al.* Importance of lateral and steric stabilization of polyelectrolyte gene delivery vectors for extended systemic circulation. *Molecular therapy: the journal of the American Society of Gene Therapy* **5**, 463-472 (2002).
- 19 Tian, H., Chen, J. & Chen, X. Nanoparticles for Gene Delivery. *Small* **9**, 2034-2044 (2013).
- 20 Dufès, C., Uchegbu, I. F. & Schätzlein, A. G. Dendrimers in gene delivery. *Advanced Drug Delivery Reviews* **57**, 2177-2202 (2005).
- 21 Jin, S., Leach, J. C. & Ye, K. in *Micro and Nano Technologies in Bioanalysis* Vol. 544 (eds Robert S. Foote & James Weifu Lee) 547-557 (Humana Press, 2009).
- 22 Lu, F. *et al.* Advances in Bioapplications of Carbon Nanotubes. *Advanced Materials* **21**, 139-152 (2009).
- 23 McBain, S. C., Yiu, H. H. P. & Dobson, J. Magnetic nanoparticles for gene and drug delivery. *International Journal of Nanomedicine* **3**, 169-180 (2008).
- 24 Hosseinkhani, H. *et al.* Biodegradable nanoparticles for gene therapy technology. *Journal of Nanoparticle Research* **15**, 1-15 (2013).
- 25 Pérez-Martínez, F. C., Carrión, B. & Ceña, V. n. The Use of Nanoparticles for Gene Therapy in the Nervous System. *Journal of Alzheimer's Disease* **31**, 697-710 (2012).

- 26 Xu, Z. P., Zeng, Q. H., Lu, G. Q. & Yu, A. B. Inorganic nanoparticles as carriers for efficient cellular delivery. *Chemical Engineering Science* **61**, 1027-1040 (2006).
- 27 Wijaya, A., Schaffer, S. B., Pallares, I. G. & Hamad-Schifferli, K. Selective Release of Multiple DNA Oligonucleotides from Gold Nanorods. *ACS Nano* **3**, 80-86 (2009).
- 28 Tan, J. H. *et al.* Hyperbranched polymers as delivery vectors for oligonucleotides. *Journal of Polymer Science Part A: Polymer Chemistry* **50**, 2585-2595 (2012).
- 29 McBain, S. C., Yiu, H. H. & Dobson, J. Magnetic nanoparticles for gene and drug delivery. *International Journal of Nanomedicine* **3**, 169-180 (2008).
- 30 Conde, J., Doria, G., alo & Baptista, P. Noble Metal Nanoparticles Applications in Cancer. *Journal of Drug Delivery* **2012** (2011).
- 31 Iijima, S. Helical microtubules of graphitic carbon. *Nature* **354**, 56-58 (1991).
- 32 Lin, Y. *et al.* Advances toward bioapplications of carbon nanotubes. *J. Mater. Chem.* **14**, 527-541 (2004).
- 33 Hersam, M. C. Nanotubes keep rolling on. *Nature Nanotechnology* **4**, 465-465 (2009).
- 34 Bianco, A., Kostarelos, K. & Prato, M. Applications of carbon nanotubes in drug delivery. *Current Opinion in Chemical Biology* **9**, 674-679 (2005).
- 35 Lacerda, L., Raffa, S., Prato, M., Bianco, A. & Kostarelos, K. Cell-penetrating CNTs for delivery of therapeutics. *Nano Today* **2**, 38-43, doi:10.1016/s1748-0132(07)70172-x (2007).
- 36 Liu, Z., Winters, M., Holodniy, M. & Dai, H. siRNA Delivery into Human T Cells and Primary Cells with Carbon-Nanotube Transporters. *Angewandte Chemie International Edition* **46**, 2023-2027 (2007).
- 37 Jin, H., Heller, D. A., Sharma, R. & Strano, M. S. Size-Dependent Cellular Uptake and Expulsion of Single-Walled Carbon Nanotubes: Single Particle Tracking and a Generic Uptake Model for Nanoparticles. *ACS Nano* **3**, 149-158 (2009).
- 38 Shi, X., von dem Bussche, A., Hurt, R. H., Kane, A. B. & Gao, H. Cell entry of one-dimensional nanomaterials occurs by tip recognition and rotation. *Nature Nanotechnology* **6**, 714-719 (2011).
- 39 Prato, M., Kostarelos, K. & Bianco, A. Functionalized Carbon Nanotubes in Drug Design and Discovery. *Accounts of Chemical Research* **41**, 60-68 (2008).
- 40 Lin, Y. *et al.* Advances toward bioapplications of carbon nanotubes. *Journal of Materials Chemistry* **14**, 527-541, doi:10.1039/b314481j (2004).
- 41 Liu, Y., Zhao, Y., Sun, B. & Chen, C. Understanding the Toxicity of Carbon Nanotubes. *Accounts of Chemical Research* **46**, 702-713 (2013).
- 42 Yang, S.-T., Luo, J., Zhou, Q. & Wang, H. Pharmacokinetics, Metabolism and Toxicity of Carbon Nanotubes for Biomedical Purposes. *Theranostics* **2**, 271-282 (2012).
- 43 Douroumis, D., Fatouros, D. G., Bouropoulos, N., Papagelis, K. & Tasis, D. Colloidal stability of carbon nanotubes in an aqueous dispersion of phospholipid. *International Journal of Nanomedicine* **2**, 761-766 (2007).
- 44 Singh, P. *et al.* Organic functionalisation and characterisation of single-walled carbon nanotubes. *Chemical Society Reviews* **38**, 2214-2230 (2009).
- 45 Liu, Z. *et al.* Circulation and long-term fate of functionalized, biocompatible single-walled carbon nanotubes in mice probed by Raman spectroscopy. *Proceedings of the National Academy of Sciences* **105**, 1410-1415 (2008).
- 46 Chen, J., Chen, Q. & Ma, Q. Influence of surface functionalization via chemical oxidation on the properties of carbon nanotubes. *Journal of colloid and interface science* **370**, 32-38 (2012).
- 47 Liu *et al.* Fullerene pipes. *Science (New York, N.Y.)* **280**, 1253-1256 (1998).
- 48 Chen, J. *et al.* Solution Properties of Single-Walled Carbon Nanotubes. *Science* **282**, 95-98 (1998).
- 49 Li, H. J., Lu, W. G., Li, J. J., Bai, X. D. & Gu, C. Z. Multichannel Ballistic Transport in Multiwall Carbon Nanotubes. *Physical Review Letters* **95** (2005).
- 50 Matsuura, K., Hayashi, K. & Kimizuka, N. Lectin-mediated supramolecular junctions of galactose-derivatized single-walled carbon nanotubes. *Chemistry Letters*, 212-213 (2003).

- 51 Pompeo, F. & Resasco, D. E. Water Solubilization of Single-Walled Carbon Nanotubes by Functionalization with Glucosamine. *Nano Letters* **2**, 369-373 (2002).
- 52 Huang, W. *et al.* Attaching Proteins to Carbon Nanotubes via Diimide-Activated Amidation. *Nano Letters* **2**, 311-314 (2002).
- 53 Jiang, K. *et al.* Protein immobilization on carbon nanotubes via a two-step process of diimide-activated amidation. *Journal of Materials Chemistry* **14**, 37-39 (2004).
- 54 Weizmann, Y., Chenoweth, D. M. & Swager, T. M. Addressable Terminally Linked DNA,àCNT Nanowires. *Journal of the American Chemical Society* **132**, 14009-14011 (2010).
- 55 Hazani, M., Naaman, R., Hennrich, F. & Kappes, M. M. Confocal Fluorescence Imaging of DNA-Functionalized Carbon Nanotubes. *Nano Letters* **3**, 153-155 (2003).
- 56 Carson, L. *et al.* Synthesis and characterization of chitosan,àcarbon nanotube composites. *Materials Letters* **63**, 617-620 (2009).
- 57 Ke, G. *et al.* Covalent Functionalization of Multiwalled Carbon Nanotubes with a Low Molecular Weight Chitosan. *Biomacromolecules* **8**, 322-326 (2007).
- 58 Harris, J. M. & Chess, R. B. Effect of pegylation on pharmaceuticals. *Nature reviews. Drug discovery* **2**, 214-221 (2003).
- 59 Sano, M., Kamino, A., Okamura, J. & Shinkai, S. Self-Organization of PEO-graft-Single-Walled Carbon Nanotubes in Solutions and Langmuir,àBlodgett Films. *Langmuir* **17**, 5125-5128 (2001).
- 60 Zhao, B., Hu, H., Yu, A., Perea, D. & Haddon, R. C. Synthesis and Characterization of Water Soluble Single-Walled Carbon Nanotube Graft Copolymers. *Journal of the American Chemical Society* **127**, 8197-8203 (2005).
- 61 Riggs, J. E., Guo, Z., Carroll, D. L. & Sun, Y.-P. Strong luminescence of solubilized carbon nanotubes. *Journal of the American Chemical Society* **122**, 5879-5880 (2000).
- 62 Sahoo, N. G. *et al.* Functionalized carbon nanomaterials as nanocarriers for loading and delivery of a poorly water-soluble anticancer drug: a comparative study. *Chemical Communications* **47**, 5235-5237 (2011).
- 63 Aitchison, T. J., Ginic-Markovic, M., Matison, J. G., Simon, G. P. & Fredericks, P. M. Purification, Cutting, and Sidewall Functionalization of Multiwalled Carbon Nanotubes Using Potassium Permanganate Solutions. *The Journal of Physical Chemistry C* **111**, 2440-2446, doi:10.1021/jp066541d (2007).
- 64 Ziegler, K. J. *et al.* Controlled Oxidative Cutting of Single-Walled Carbon Nanotubes. *Journal of the American Chemical Society* **127**, 1541-1547, doi:10.1021/ja044537e (2005).
- 65 Holzinger, M. *et al.* Functionalization of Single-Walled Carbon Nanotubes with (R)-Oxycarbonyl Nitrenes. *Journal of the American Chemical Society* **125**, 8566-8580 (2003).
- 66 Gao, C., He, H., Zhou, L., Zheng, X. & Zhang, Y. Scalable Functional Group Engineering of Carbon Nanotubes by Improved One-Step Nitrene Chemistry. *Chemistry of Materials* **21**, 360-370 (2009).
- 67 Moghaddam, M. J. *et al.* Highly Efficient Binding of DNA on the Sidewalls and Tips of Carbon Nanotubes Using Photochemistry. *Nano Letters* **4**, 89-93 (2004).
- 68 Maggini, M., Scorrano, G. & Prato, M. Addition of azomethine ylides to C60: synthesis, characterization, and functionalization of fullerene pyrrolidines. *Journal of the American Chemical Society* **115**, 9798-9799 (1993).
- 69 Georgakilas, V. *et al.* Organic Functionalization of Carbon Nanotubes. *Journal of the American Chemical Society* **124**, 760-761 (2002).
- 70 Georgakilas, V. *et al.* Amino acid functionalisation of water soluble carbon nanotubes. *Chemical Communications*, 3050-3051 (2002).
- 71 Singh, R. *et al.* Binding and Condensation of Plasmid DNA onto Functionalized Carbon Nanotubes:à Toward the Construction of Nanotube-Based Gene Delivery Vectors. *Journal of the American Chemical Society* **127**, 4388-4396 (2005).
- 72 Bahr, J. L. & Tour, J. M. Highly Functionalized Carbon Nanotubes Using in Situ Generated Diazonium Compounds. *Chemistry of Materials* **13**, 3823-3824 (2001).

- 73 Karousis, N., Ali-Boucetta, H., Kostarelos, K. & Tagmatarchis, N. Aryl-derivatized, water-soluble functionalized carbon nanotubes for biomedical applications. *Materials Science and Engineering: B* **152**, 8-11 (2008).
- 74 Ménard-Moyon, C., Fabbro, C., Prato, M. & Bianco, A. One-Pot Triple Functionalization of Carbon Nanotubes. *Chemistry, A European Journal* **17**, 3222-3227 (2011).
- 75 Peng, H., Alemany, L. B., Margrave, J. L. & Khabashesku, V. N. Sidewall Carboxylic Acid Functionalization of Single-Walled Carbon Nanotubes. *Journal of the American Chemical Society* **125**, 15174-15182 (2003).
- 76 Stephenson, J. J., Hudson, J. L., Leonard, A. D., Price, B. K. & Tour, J. M. Repetitive Functionalization of Water-Soluble Single-Walled Carbon Nanotubes. Addition of Acid-Sensitive Addends. *Chemistry of Materials* **19**, 3491-3498 (2007).
- 77 Yang, Y., Qiu, S., Xie, X., Wang, X. & Li, R. K. Y. A facile, green, and tunable method to functionalize carbon nanotubes with water-soluble azo initiators by one-step free radical addition. *Applied Surface Science* **256**, 3286-3292 (2010).
- 78 Chu, P. K., Chen, J. Y., Wang, L. P. & Huang, N. Plasma-surface modification of biomaterials. *Materials Science and Engineering: R: Reports* **36**, 143-206 (2002).
- 79 Francesch, L., Garreta, E., Balcells, M., Edelman, E. R. & Borrós, S. Fabrication of Bioactive Surfaces by Plasma Polymerization Techniques Using a Novel Acrylate-Derived Monomer. *Plasma Processes and Polymers* **2**, 605-611 (2005).
- 80 Förch, R., Zhang, Z. & Knoll, W. Soft Plasma Treated Surfaces: Tailoring of Structure and Properties for Biomaterial Applications. *Plasma Processes and Polymers* **2**, 351-372 (2005).
- 81 Francesch, L., Borros, S., Knoll, W. & Förch, R. Surface Reactivity of Pulsed-Plasma Polymerized Pentafluorophenyl Methacrylate (PFM) toward Amines and Proteins in Solution. *Langmuir* **23**, 3927-3931 (2007).
- 82 O'Connell, M. J. *et al.* Reversible water-solubilization of single-walled carbon nanotubes by polymer wrapping. *Chemical Physics Letters* **342**, 265-271 (2001).
- 83 Vaisman, L., Wagner, H. D. & Marom, G. The role of surfactants in dispersion of carbon nanotubes. *Advances in Colloid and Interface Science* **128-130**, 37-46 (2006).
- 84 Valenti, L. E., Fiorito, P. A., García, C. D. & Giacomelli, C. E. The adsorption-desorption process of bovine serum albumin on carbon nanotubes. *Journal of Colloid and Interface Science* **307**, 349-356 (2007).
- 85 Kah, J. C. Y., Chen, J., Zubieta, A. & Hamad-Schifferli, K. Exploiting the Protein Corona around Gold Nanorods for Loading and Triggered Release. *ACS Nano* **6**, 6730-6740 (2012).
- 86 Shannahan, J. H. *et al.* Comparison of Nanotube-Protein Corona Composition in Cell Culture Media. *Small* **9**, 2171-2181 (2013).
- 87 Liu, Y. Epithelial to Mesenchymal Transition in Renal Fibrogenesis: Pathologic Significance, Molecular Mechanism, and Therapeutic Intervention. *Journal of the American Society of Nephrology* **15**, 1-12 (2004).
- 88 Moon, H. K., Lee, S. H. & Choi, H. C. In Vivo Near-Infrared Mediated Tumor Destruction by Photothermal Effect of Carbon Nanotubes. *ACS Nano* **3**, 3707-3713 (2009).
- 89 Raffa, V., Ciofani, G., Vittorio, O., Riggio, C. & Cuschieri, A. Physicochemical properties affecting cellular uptake of carbon nanotubes. *Nanomedicine* **5**, 89-97 (2010).

Chapter II.

Surface Modification By Plasma Techniques

Originally published as:

A. Cifuentes and S. Borrós, *Langmuir*, **2013**, 29 (22), pp 6645–6651

D. Horna, J. C. Ramirez, A. Cifuentes, A. Bernad, S. Borrós and M. A. González, *Advanced Healthcare Materials*, **2012**, 1 (2), pp 177-182

A. Cifuentes-Rius, M. Burrial, M. Faijes, A. Planas, S. Borrós, *Biomacromolecules*, **2013** (*in preparation*)

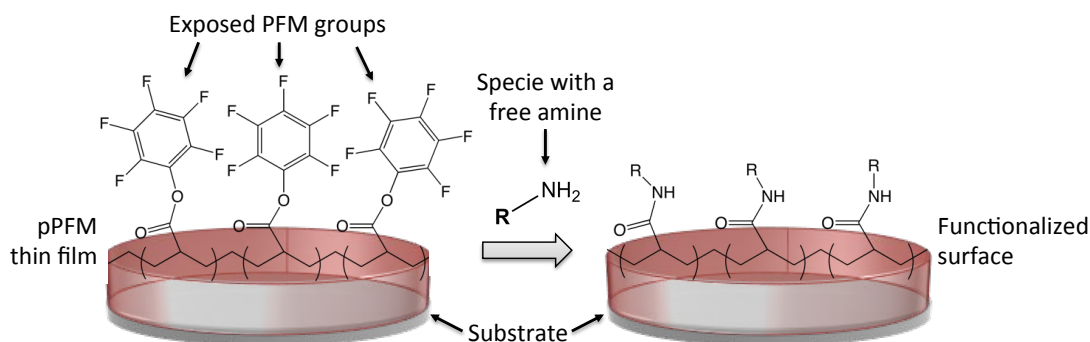
2.1. Introduction

According to the actual needs in the surface functionalization of different materials, in this initial part of this thesis, two distinct plasma polymerization techniques were employed as a surface modification approach. As it has been introduced in Chapter I, carbon nanotubes (CNTs) are one of these above-mentioned materials that demand a suitable functionalization. Pristine CNTs lack appropriate functional groups to enable covalent binding of biocompatible groups, in order to make CNTs compatible with the biological milieu.¹⁻⁵ Therefore, the surface of CNTs requires modification by different chemical synthetic methods to generate appropriate functionalities, enabling covalent attachment of suitable solubilizing, bioactive or biocompatible moieties. Classically, researchers have differentiated CNTs into two zones in terms of their reactivity, i.e. sidewalls and tips.⁶⁻⁸ It has been shown that tips are more prone for modification than sidewalls, and both may be dramatically altered changing the entire CNT morphology.

In this sense, plasma techniques has been proved as a surface modification approach able to homogeneously modify a wide variety of surfaces without affecting their bulk properties of the treated material by the deposition of thin films.⁹⁻¹¹ In the recent years, plasma polymerization approaches have been employed as a previous surface treatment to achieve functionalized surfaces, because of its capacity to modify all kinds of materials, even inert ones, and its ability to do so to all different geometries. Thereof, CNTs may be strategically coated with the adequate polymer, tuning the physical and chemical interaction or conjugation with the molecule of interest. For gene delivery applications, the modification of the CNT surface could lead to the covalent attachment of the genetic material, or facilitate its wrapping around the CNT structure, as it will be discussed in Chapter III. Prior to this, a thorough study is required in order to gain a better understanding in how this technique can be tuned for the generation of tailored surfaces and what these modified surfaces may render.

In our group, the expertise in plasma surface modification allowed the development of polymer thin films by using a monomer that, when polymerized, leads to a reactive group exposed on the surface.^{10,12} This monomer, pentafluorophenyl methacrylate (PFM), is activated by plasma excitation and it is able to form thin films of polymerized PFM (pPFM) on the desired surface. Its exposed ester groups are highly reactive towards amines, which makes it an optimal candidate to achieve extremely active surfaces for selected species (Scheme 2.1).^{10,12-14}

Both parameters, the polymerization technique and the monomer used, have allowed the development of a versatile approach to fabricate all kind of bioactive surfaces, capable to covalently immobilize proteins in a tunable way. In this work, we optimized two techniques, PECVD and plasma grafting of PFM, in order to attach biomolecules in a specific way where its activity is maintained.



Scheme 2.1 pPFM thin film structure and subsequent reaction with amine-terminated molecules.

Plasma enhanced chemical vapor deposition (PECVD), the first technique assessed in this study, enables the modification of wide range of materials by the deposition of polymer thin films on the substrate. The optimization of the working parameters plays an important role to tune the final properties of the polymer layer. Previous work performed in our group on the PECVD-polymerized PFM (ppPFM) have proved that the deposition under pulsed plasma conditions is crucial for the controlled formation of active polymer thin films.^{12,15} This approach can be tuned by the duty cycle (*DC*) applied in the process. The *DC* is defined as the relation between the time in which the plasma is on (t_{ON}) and the total duration of the pulse ($t_{ON} + t_{OFF}$), as can be seen in Equation 2.1.

$$DC = \frac{t_{ON}}{t_{ON} + t_{OFF}}$$

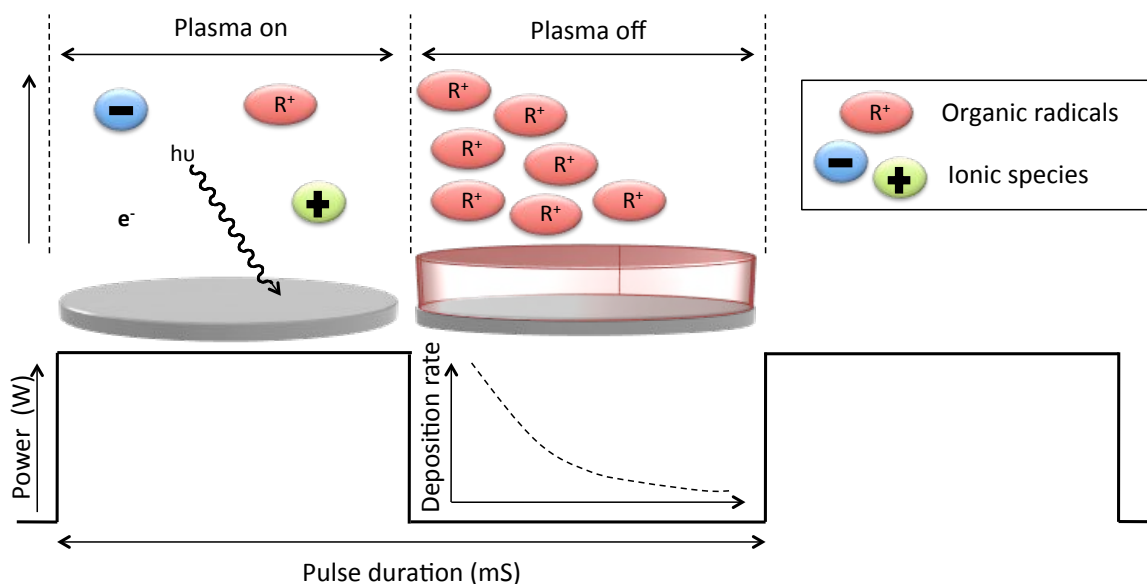
Equation 2.1

Pulsed plasma is characterized for being carried out at a higher W_i maintaining the same equivalent power (W_{eq}) as the continuous plasma. This is possible because the W_{eq} that is actually reaching the sample is dependent on the pulse, being expressed as the product of *DC* and the W_i (Equation 2.2).^{11,15}

$$W_{eq} = W_i \cdot DC$$

Equation 2.2

Scheme 2.2 shows how at t_{ON} , the chemical reactions that take place in the interface are dominated by the reactive species generated during the plasma phase and can be directly compared to the treatment that the surface is receiving when continuous plasma is applied.¹¹

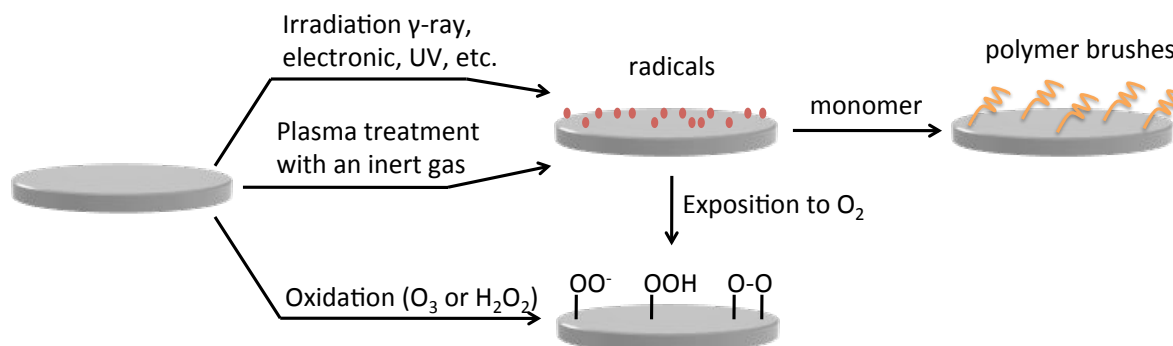


Scheme 2.2. Pulsed plasma polymerization process.¹¹

This reactive species are created by the dissociation of the monomer and the gas present in the chamber to different ions, radicals and electrons. Moreover, a UV radiation is generated due to the relaxation process of the electronically excited species. The treated surface is then submitted to this high reactive atmosphere, resulting in the surface modification, deposition and ablation process. The longer the exposure time of the sample to these conditions, the higher is the effect on the surface. However, when the plasma is off (t_{OFF}), the more reactive species such as ions and electrons tend to disappear due to relaxation processes. Because the organic radicals formed during t_{ON} have a longer lifetime than these other species, they remain on the chamber time long enough to continue the radical polymerization on the surface. As a result, the monomer is exposed to softer conditions, avoiding secondary reactions and retaining a higher reactive functionality.^{11,15} Therefore, using a pulsed plasma polymerization method enables an increased control during the deposition process and a higher reactive functionality is maintained.

Similarly, the plasma grafting approach avoids the monomer exposure to such harsh conditions in order to preserve its chemical integrity when polymerized. In general terms, grafting techniques consist in the modification of the first nanometers of the surface substrate while maintaining the properties of the bulk material. Basically, an energy source used as an initiator creates reactive

radicals on the surface of the polymer, which serve as active sites for a further polymerization of the monomer (Scheme 2.3).¹⁶



Scheme 2.3. Grafting process on polymer substrates.¹⁶

When the active sites are created using a plasma source, the approach is known as plasma grafting, which is also studied and optimized in this thesis. In this case, a polymer substrate is firstly exposed to plasma conditions in the presence of a gas in order to activate its surface. When the monomer of interest interacts with the plasma-activated surface, the polymerization starts and the polymer chain grows from the surface, mainly in a vertical direction. Thus, a controlled and localized modification is achieved and polymer brushes are formed in the resulting pre-activated surface.¹⁷⁻²¹

As said, the first step to achieve the surface modification is creating stable free radicals on the surface. Using an inert gas in plasma treatments creates stable free radicals on the polymer surface.^{20,22,23} It is known that plasma treatments in presence of noble gases induce a hydrogen desorption on the polymeric surface and involve the creation of a high density of active sites. Therefore, there are two differentiated processes that happen at the same time. First, an etching process occurs, in which the first nanometres of the surface are removed. Second, radicals are created due to these mechanical interactions. During the former, the surface is submitted to a cleaning process, whereas in the latter is when the formation of active sites actually takes place. Argon has the lower effect on the surface morphology compared to other noble gases, and because of that, it is the gas used in this work. On the other hand, reactive gases can be also used in this process (O₂ or N₂), but in such cases they interact with the surface forming different chemical groups that may interfere with the following monomer grafting.^{20,23}

In this regard, when modifying by plasma grafting, the actual plasma treatment is only applied in the presence of Ar, when the activation of the surface takes place. After that, the monomer is fed into

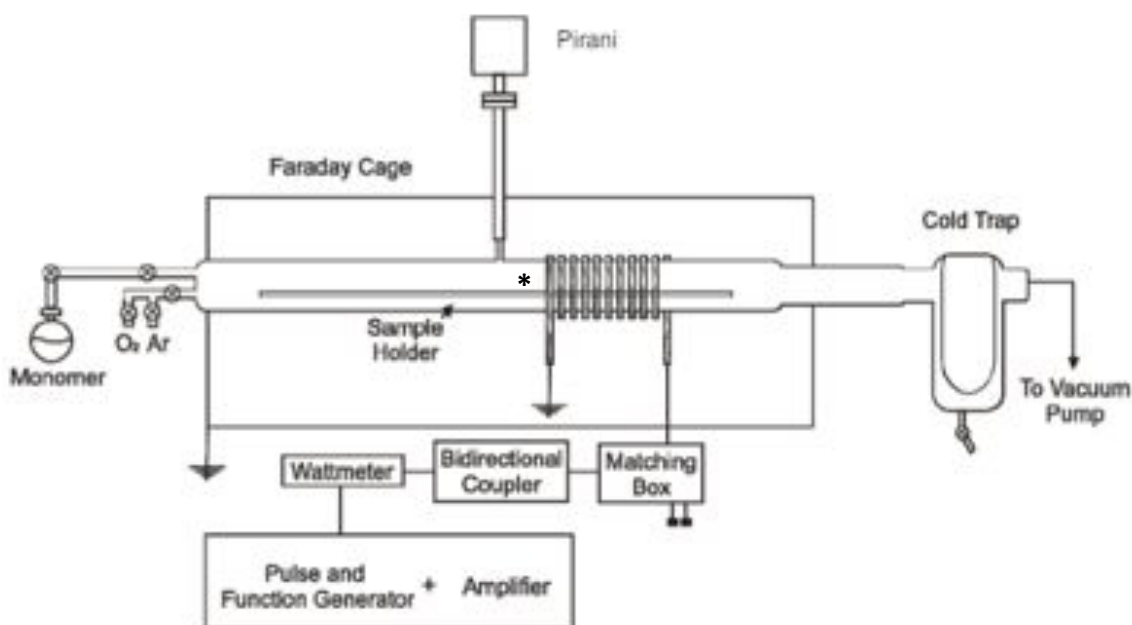
the reactor chamber when the plasma is off. As a result, it is exposed to a non-aggressive environment being able to polymerize under controlled conditions and retaining a major degree of its functionality.

As a result and by tuning the polymerization conditions of the PFM with the two techniques explained above, homogeneous and reactive surfaces are obtained in this part of the work. The immobilization of a protein layer on the treated surfaces is tested and the resulting smart, bioactive surface is analyzed in detail. Each approach differs in the resulting bioactive surface properties and the behavior of the proteins interacting with them, which makes them an extremely interesting tool for immobilizing proteins in a desired way regarding the final application of the material. By these means, we finally aim to gain a complete knowledge of this technique to further modify such a sophisticated material as CNTs in order to turn them into a smart, bioactive gene vector.

2.2. Experimental Section

2.2.1. Plasma Reactor Employed

Both types of plasma modification were carried out in a homebuilt plasma reactor (Scheme 2.4). Plasma treatment was performed by using an excitation frequency of 13.56 MHz. Gases that were fed into the chamber through the system pass through a glass, CO₂/acetone-cooled trap (-78 °C) for the collection of excess reactant before reaching the pump (Edwards RV12 903). An analogical Pirani-type vacuum meter (MKS, USA) was connected near the middle of the reactor chamber to monitor the reaction pressure. In a homebuilt system, the pulse generator controlled the pulsing of the radio frequency (RF) signal, which was amplified by a 150 W amplifier and passed *via* an analogue watt meter and a matching network to a 10-cm-long coil located around the exterior of the reactor. The typical base pressure prior to all experiments was 2×10^{-2} mbar. PFM monomer vapor (Apollo Scientific) heated at 45 °C was introduced until reaching a constant pressure of 1.5×10^{-1} mbar *via* a needle valve. The inner volume of the reactor was approximately 3 L, while the effective plasma volume was about 1.7 L. Substrates were placed just before the cooper coil, marked with an asterisk in Scheme 2.4. In such position, the glow discharge was enough to ensure modification without damaging the formed polymeric film neither the substrate.¹⁵ Moreover, the monomer integrity when contacting the substrate's surface was also guaranteed.



Scheme 2.4 Schematic diagram of the plasma reactor and its electrical components.

2.2.2. Procedure of the Plasma Polymerization by PECVD

Polystyrene strips (Servei Estació, Barcelona; $10 \times 10 \text{ mm}^2$ area; PS) and glass slides (VWR International; 13 mm diameter and 1 mm thick, GS) were modified with PFM by PECVD. The continuous RF input power was varied from 15 to 90 W, and pulsed plasma polymerization (DC tuned between 10/20 and 10/60) was carried out for 5 min (Table 2.1). Then plasma discharge was turned off, and the PFM vapor was introduced at constant flow during 15 min more. After the polymerization process, PECVD-polymerized PFM-samples (ppPFM) were carefully removed from the reaction chamber and stored in N_2 until further use.

Table 2.1. Reactor conditions for the deposition of ppPFM by PECVD.

Sample ID	DC (W/W)	W_i (W)	W_{eq} (W)
O	-	15	15
A1	10/20	15	7.5
A1	10/60	15	2.5
B1	10/20	30	15
B2	10/60	90	15

2.2.3. Methodology of the Plasma-Grafting Modification

Two different substrates were modified. Firstly, PS strips were coated with PFM by plasma grafting in the same plasma reactor as described before. The substrates were previously activated by argon (Carbueros Metálicos 5.0) plasma, which entered the reactor at a constant flow of 45 sccm at a pressure of 7.5×10^{-2} mbar. The continuous RF power setting was carried out at 15 W for 15 min. After surface activation, the plasma was turned off and the Ar gas was closed. The PFM monomer flask was then opened until reaching the desired pressure for 15 min. Secondly, polystyrene beads (Goodfellow, 900 μm diameter; PSb) were modified with PFM by plasma grafting as previously described. The entire procedure was carried out three times shaking the samples in between each treatment in order to achieve a homogeneous modification along the bead surface (PSb-PFM).

When finished, both grafted-PFM (gPFM) substrates were removed from the reaction chamber and stored for further characterization and substrate functionalization.

2.2.4. Chemical and Topographical Characterization of the Surfaces

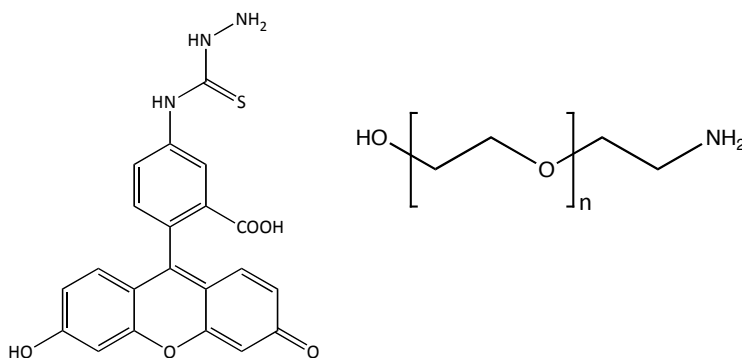
Modified surfaces (ppPFM and gPFM-coated substrates) were characterized by water contact angle (DSA100 Krüss; WCA) and atomic force microscopy (XE 100 Park System; AFM). AFM analysis was performed in tapping mode and the roughness was measured in terms of average roughness (R_a), root mean square (RMS) roughness (R_q) and maximum roughness height (R_{max}). All these analytical techniques were compared to non-modified surfaces.

Time of flight secondary ion mass spectrometry (Ion-ToF GmbH, ToF-SIMS) was also carried out for the ppPFM thin films in order to evaluate the preservation of the PFM groups. This analysis was performed at the *Servei Científicotècnics de la Universitat de Barcelona* (SCT).

2.2.5. Functionalization of the Modified Surfaces

The reactivity of the PFM group towards amines was tested by using as a fluorescent dye, fluorescein-5-tiosemicarbazide (Fluka; FTSC), which allows the tracking of the reaction by fluorescence microscopy. In addition, l'-o-(2-aminoethyl)polietilenglicol (5000 kDa, Sigma-Aldrich; PEG-amine), was also tested on gPFM-surfaces to evaluate the ability of these surfaces to support polymer microstructuration.

Both molecules have a free amine on its structure as can be seen in Scheme 2.5. Therefore, it can react with the PFM groups on the surface confirming the modification, together with the homogeneity and reactivity of the obtained surface. Samples were incubated with FTSC and PEG-amine solutions, 50 mM and 4 mg/mL, respectively for 2 h and under gentle agitation. Covalent functionalization of the surfaces was proved by washing the samples with Milli-Q water in an ultrasonic bath for 30 min. Samples were then dried with N_2 and characterized.



Scheme 2.5 Chemical structure of the FTSC (left) and PEG-amine (right).

Characterization of the Functionalized Surfaces

A fluorescence microscope (AxioVs40 Zeiss Imaging Solutions) allowed the characterization of the fluorescently-modified surfaces. ToF-SIMS was employed to demonstrate successful PEG-amine immobilization on the gPFM-modified surfaces.

2.2.6. Fabrication of Microstructured Surfaces

Patterned surfaces were obtained using a copper grid as a mask. The micropatterning process was carried out by the modification of both substrates GS and PS strips with a copper grid (G50P, Gilder Grid) previously collocated on its surface. The Cu grid was carefully placed on the desired part of the substrate guaranteeing full contact between the surface and the grid. The sample was then treated either by PECVD or plasma grafting, and after modification the Cu grid was removed carefully. Patterned-modified samples were functionalized with FTSC and analyzed by fluorescence microscopy.

Microcontact printing (μ CP) was employed to create a patterned surface after plasma modification was carried out.²⁴⁻²⁶ A polydimethylsiloxane (Sylgard 184 Dow Corning; PDMS) stamp was prepared (8:1 ratio) on a silicon master previously designed by our group (Figure 2.1). The PDMS was poured on the desired part of the master and then cured at 70 °C for 12 h, it was removed from the master, washed in an ultrasonic bath while submerged in ethanol (Panreac) and finally dried with N₂. The hydrophobic PDMS stamp was treated with Ar:O₂ (1:1) plasma to make it more hydrophilic, favoring the interaction with the fluorescent ink.

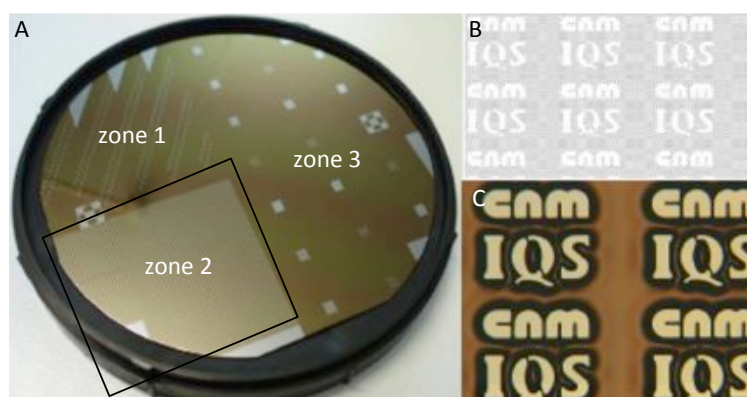
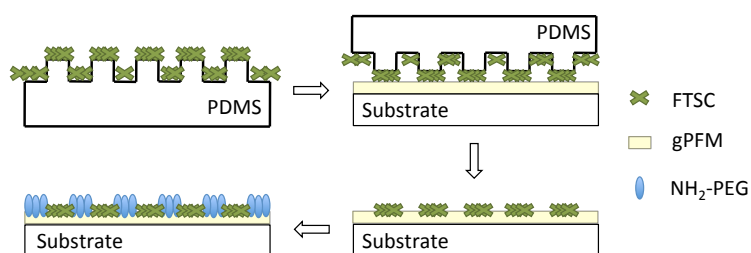


Figure 2.1. Silicon master used in this work. (A) General view of the master with 3 different patterns. (B) Design of the area 2 used in this work and (C) microscope images of the chosen pattern.

The fabricated stamps were incubated in a 0.5 mM FTSC solution for 50 min, protected from light and in an orbital shaker. After drying with N₂, the stamps were immediately and carefully placed on the gPFM-surfaces and were left in contact for 1 min. The fresh microprinted surface was soaked into a 4 mg/mL PEG-amine solution for 15 min (Scheme 2.6). Finally, samples were washed in Milli-Q water under sonication in an ultrasonic bath for 10 min. A control was carried out to a non-modified PS sample.



Scheme 2.6. Microcontact printing methodology.

Stamp and Microstructured Surfaces Characterization

PDMS stamps were imaged by Scanning Electron Microscopy (SEM JSM 5310 equipped with EDS Oxford Link-Isis, Jeol; SEM) after being previously coated with a gold layer, and with a DCM 3D Microscope (Dual Core 3D Measuring Microscope, Leica). Moreover, the hydrophobicity before and after the plasma treatment of the stamps was measured by WCA. Microstructured surfaces obtained by this method were characterized by fluorescence microscopy and ToF-SIMS.

2.2.7. Study of the Covalent Immobilization of Protein Monolayers by Quartz Crystal Microbalance with Dissipation (QCM-D)

QCM-D technology (Q-Sense E1, Sweden) was employed to characterize the immobilization process of the bovine serum albumin (Sigma-Aldrich; BSA) on both types of modified surfaces. This technique has been proven to be suitable for *in situ* dynamic studies of both mass and mechanical properties by monitoring the frequency (f) and the dissipation (D) of an oscillating sensor.²⁷⁻²⁹ The sensor used consists of a piezoelectric quartz crystal sensor (Q-Sense) with polished gold electrodes that has an RMS roughness less than 3 nm, a diameter of 13 mm, and an effective area of 5 mm diameter. An increase in the attached mass on the sensor's surface leads to a decrease in the frequency signal (Δf) according to the Sauerbrey relation (Equation 2.3), which shows that the

adsorbed mass (Δm) is directly proportional to the frequency shift, where the mass sensitivity constant is known as C (17.7 ng/cm·Hz for a 5 MHz sensor) and n (1, 3, 5...) is the overtone number.

$$\Delta m = -\frac{C\Delta f}{n}$$

Equation 2.3

The viscoelastic properties of the film can be inferred from the dissipation signal obtained from the oscillating sensor, and it is defined as the ratio of the dissipated and the stored energy (Equation 2.4).

$$D = \frac{E_{dissipated}}{2\pi E_{stored}}$$

Equation 2.4

The purchased sensors (Q-Sense) were coated with a thin film of gold or PS, and were modified with PFM by the two different techniques analyzed in this study, PECVD and plasma grafting, respectively. When the sensor was placed in the QCM-D chamber, a baseline with phosphate-buffered saline (PAA Laboratories; PBS) was obtained after flowing the solution for 5 min. Then, the 20 $\mu\text{g}\cdot\text{mL}^{-1}$ of BSA solution in PBS was pumped through the sensor for 25 min. The excess of free BSA was removed by a PBS flow for 10 min, and a final cleaning with a 10 mM solution of sodium dodecyl sulfate (Sigma; SDS) ensured that the BSA remaining on the sensor surface was covalently attached.³⁰ The BSA affinity toward the non-modified gold and PS sensors was also checked as a comparative control. All QCM-D measurements were performed at 25 °C and all solutions used were pumped at a flow rate of 50 $\mu\text{L}\cdot\text{min}^{-1}$ after being degassed.

BSA footprints were calculated from the hydrodynamic diameter (D_H) measured by dynamic light scattering (Zetasizer Nano ZS, Malvern Instruments; DLS). Moreover, the radius was also calculated by molecular dynamics (Grmoacs v.4.0, MD). This MD study was carried out in collaboration with the Laboratory of Biochemistry at IQS.

2.2.8. Fabrication of Bioactive Surfaces via Enzyme Immobilization

1,3-1,4- β -Glucanase Synthesis

The enzyme used in this study for the reaction with the gPFM substrates was the 1,3-1,4- β -glucanase (Gln). Its synthesis, purification and quantification was carried out as previously described

and in collaboration with the Laboratory of Biochemistry at IQS.^{31,32} The enzyme was expressed through a bacterial transformation of *E. Coli* cells (BL21 DE3-Star, Novagen) *via* heat-shock transformation with a pD6-2 plasmid. Once the gene was expressed and the enzyme was produced, it was extracted by cellular lysis with a sonicator (SONIFIER 250, Branson), and purified by cationic exchange chromatography (ÄKTA FPLC, Amersham Biosciences UK Limited) with a cationic exchange column (Pharmacia Biotech, HiLoad™ SP Sepharose™ Fast Flow XK 16).

The production of pure 1,3-1,4- β -glucanase was confirmed by sodium dodecyl sulfate polyacrylamide gel electrophoresis (SDS-PAGE) knowing that its molecular weight is 24.4 kDa. The concentration was determined using a UV-Vis Spectrophotometer (Cary 100 UV-Vis Spectrophotometer, Agilent Technologies), knowing that $\epsilon_{280} = 3.53 \times 10^5 \text{ M}^{-1}\cdot\text{cm}^{-1}$ or 14.5 mg/mL·cm).³¹ The purified enzyme was then freeze-dried, stored at -20 °C and dissolved in 50 mM phosphate buffer (Sigma-Aldrich; PhB) pH 7 when used.

Study of the Enzyme Immobilization

Quartz Crystal Microbalance with Dissipation was employed to characterize the immobilization process of the enzyme to a PS sensor modified with gPFM at the same conditions as the PS beads. The baseline was obtained with the PhB 50 mM and a 30 $\mu\text{g/mL}$ of 1,3-1,4- β -glucanase solution was used to study the immobilization. A final cleaning with 10 mM SDS solution and PhB ensures a covalent immobilization of the enzyme to the surface. The viscoelastic properties of the resulting enzymatic layer were studied in detail. The enzyme affinity toward the PS sensor (PS+Gln) was checked as a comparative control. The flow was fixed at 50 $\mu\text{L/min}$ during the whole experiment. Enzyme footprints were also calculated from the DLS (Zetasizer Nano ZS, Malvern Instruments) and MD (Grmoacs v.4.0) data.

Quantification of the Immobilized Enzyme

The amount of enzyme bound to the g-PFM-modified PSb was determined using the Comassie (Bradford) Protein Assay Kit (Thermo Fisher Scientific Inc). Approximately 500 gPFM-treated PS beads (25 mg) were incubated with a 300 nM solution of 1,3-1,4- β -glucanase (500 μL) for different times (from 0 to 2h). After this incubation time, 100 μL of the supernatant was mixed with 900 μL of Bradford reagent and the absorbance of the resulting mixture was measured at 465 nm. Standards solutions of free enzyme ranging from 0 to 300 nM were also prepared and measured with the

samples altogether in order to get the calibration curve that led to the actual quantification of immobilized enzyme.

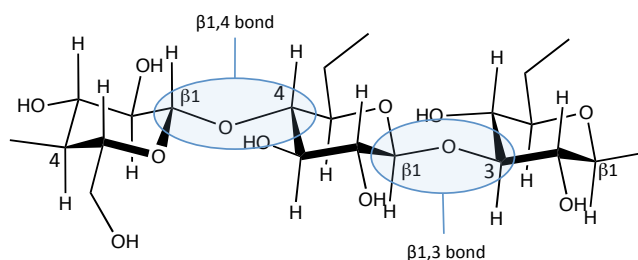
1,3-1,4- β -Glucanase Activity Determination

Immobilization of the enzyme to the gPFM-modified PS-beads was first carried out in a 96 well plate that was previously tested presenting no adsorption in the further working λ . 20 units of PSb-PFM were incubated with 10 nM 1,3-1,4- β -glucanase solution in 50 mM PhB at pH 7. The reaction mixture was left under mild agitation during 2h at 4°C. The total volume of the wells was removed and the PS beads with the immobilized enzyme (PSb-PFM+Gln) were subsequently cleaned with PhB and Milli-Q water. The same procedure was carried out with original PS beads without modification (PS+Gln), as summarized in Table 2.2.

Table 2.2. Samples prepared for further activity quantification of the functionalized PS beads by the DNS method.

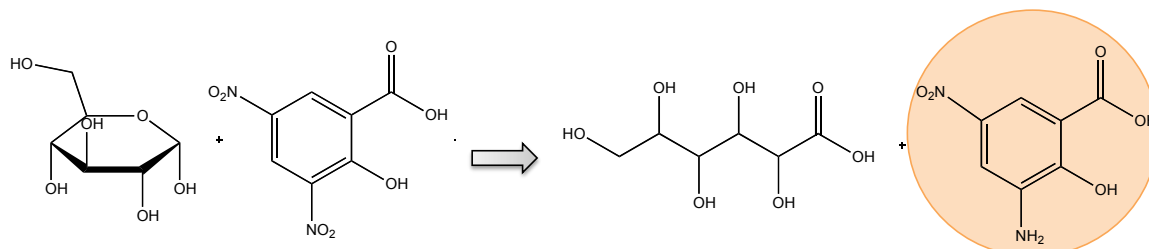
Sample ID	PS Beads Substrate	Plasma Grafting Modification	1,3-1,4- β -glucanase Incubation
PSb	✓	✗	✗
PSb+Gln	✓	✗	✓
PSb-gPFM+Gln	✓	✓	✓
Free Gln	✗	✗	✓

The enzymatic activity of the immobilized enzyme (PSb-gPFM+Gln and PS+Gln) was tested using the DNS method. After several washes with MilliQ water, samples and controls were incubated with the enzyme substrate, a solution of 1,3-1,4- β -glucane (Megazyme) 4 mg/mL in PhB 50 mM and CaCl₂ 0.1 mM, for 5 min at 55 °C (Scheme 2.7).



Scheme 2.7. Chemical structure of the 1,3-1,4- β -glucane.

A fraction of each one of these mixtures was added to the 3,5-dinitrosalicylic acid (DNS) solution, which reacts with the free reducing sugars present producing a color change (Scheme 2.8). The DNS reagent was prepared from a mixture of DNS (Sigma-Aldrich) solution 70 mM in NaOH (Panreac) 1 mM and 1.5 M of potassium tartrate (Sigma) in equal volumes.



Scheme 2.8. DNS chemical reaction.

To obtain the color change required to detect the different amounts of reducing sugar, the samples were boiled at 100 °C for 10 min, cooled down on ice and measured at 540 nm against a blank with Milli-Q instead of enzyme. The activity of the free 1,3-1,4- β -glucanase (10 nM) synthesized was quantified following the same protocol. Simultaneously, a calibration curve made of glucose (Sigma-Aldrich) at a known concentration was required. Solutions from 0 to 4 mM of glucose in PhB 50 mM and pH 7 were prepared and were boiled with the DNS reagent together with the previously described samples.

2.2.9. Covalent Immobilization of Gene Delivery Viral Vectors

Preparation of the Viral Particle Immobilization Platform

Plasma grafting was carried out as described before in the section 2.2.3. As the primary surface, 35 mm polystyrene plates (BD, Franklin Lakes, NJ, USA; PSp) were employed, which were introduced to the reactor used before (Scheme 2.4). Recently modified-PSp were stored in Ar for further adenovirus functionalization.

Production of the Cell Reprogramming Surfaces (CRSs)

PSp modified with gPFM were placed in contact with a solution containing adenoviral supernatant in culture medium (DMEM) at 37 °C for 1 h in an orbital shaker. The medium was removed and the plates were washed with DMEM containing 10% FBS (5 x 50 mL). The concentration of the

adenovirus in solution employed was function to the final number of cells seeded (400000 cells/plate) in order to have a multiplicity of infection (MOI) of 25 and 250. Recombinant adenovirus vectors expressing GFP were provided and produced by the Institut d'Investigacions Biomèdiques de Barcelona (IIBB) group.

Efficiency of CRS Transfection on Macrophages

CRS plates were immediately incubated with mouse macrophages RAW 264.7 (ATCC) for 24 h at 37 °C. A total amount of 400000 cells were seeded on each plate. Classical transfection protocol was developed by IIBB and followed as previously reported.^{33,34}

Measure of the Gene Expression by real-time Reverse Transcription-Polymerase Chain Reaction (RT-PCR)

Total mRNA was extracted from homogenized macrophages culture with TRIzol Reagent (Invitrogen) according to the manufacturer's instructions, and RNA concentrations were calculated from A_{260} determinations. GFP mRNA expression normalized to the housekeeping gene GAPDH was measured by the quantitative RT-PCR method at IIBB facilities. Quantitative RT-PCRs were performed in a Bio-Rad iCycler iQ Real-Time-PCR Detection System. Amplifications were carried out in a 25- μ l-reaction volume with the One Step RT-PCR Kit with SYBR Green (Bio-Rad), according to the manufacturer's instructions. Data were recorded as mean \pm standard error of mean (SEM). The means of different groups were compared using a one-way ANOVA. The Student-Newman-Keuls test was used to evaluate significant differences between groups, significance being set at $P < 0.05$.

2.3. Results and Discussion

2.3.1. ppPFM Thin Film Formation by PECVD

Evaluation of the PECVD Polymerization Parameters

In the PECVD process, the input power (W_i) and the duty cycle (DC) play a crucial role in the final chemical structure of the deposited polymer thin film. Previous research in our group confirmed that the retention of the PFM functionality when polymerized by PECVD could be observed by WCA measurements.¹² Given the hydrophobicity showed by the PFM moieties, the presence of this group in the thin film leads to a hydrophobic surface. Thus, the hydrophobicity of the resulting surface increases with the number of reactive PFM groups oriented towards the surface being the ones accessible on the polymer film. As a result, the quality of the obtained ppPFM coatings can be directly determined from the WCA values measured allowing a direct optimization of the plasma polymerization parameters.

To adjust these polymerization parameters by which the PFM groups remain highly exposed on the surface of the resulting polymer layer, GS substrates were polymerized under different conditions (Table 2.1). When the W_i was fixed at 15 W and the DC was varied from 1 (continuous plasma) to 10/60, the W_{eq} inside the reactor changed, and it affected the resulting polymer layer (Figure 2.2, left) The WCA values of all three samples were higher than the $64.3^\circ \pm 0.4^\circ$ of the control (bare GS), which confirms the formation of a ppPFM film on the surface. It can be observed that the hydrophobicity of the two pulsed-plasma ppPFM layers ($86.3^\circ \pm 1.1^\circ$ and $89.8^\circ \pm 0.4^\circ$) were substantially superior to the $74.2^\circ \pm 2.8^\circ$ obtained under continuous plasma, confirming that softer conditions lead to a higher retention of the PFM group. As mentioned before, continuous plasma involves exposing the surface under such harsh conditions that may damage the polymer thin film. These negative side effects include an increase in temperature, ablation processes and the excess of fragmentation of the monomer resulting in a contamination of the formed layer.³⁵⁻⁴⁰ In addition, it is expected to see an increase in the retention of the PFM functionality on the polymer film with the plasma-off period, since the polymerization process is carried out under mild conditions when a larger t_{OFF} is applied. However, the hydrophobicity obtained at $DC = 10/60$ ($86.3^\circ \pm 1.1^\circ$) was slightly lower the resulting film at $DC = 10/20$ (WCA of $89.8^\circ \pm 0.4^\circ$). These results suggest that, at some point, low DC s do not improve the quality of the reactive thin film. This might be the consequence of the longer plasma-off pulse, causing the total disappearance of the active species generated when

the plasma is on, avoiding the growth of the polymer chain on the surface.¹⁵ Moreover, destabilization of the plasma may occur when the t_{ON}/t_{OFF} ratios are too small, and thus proper formation of the reactive film is hardly favored.

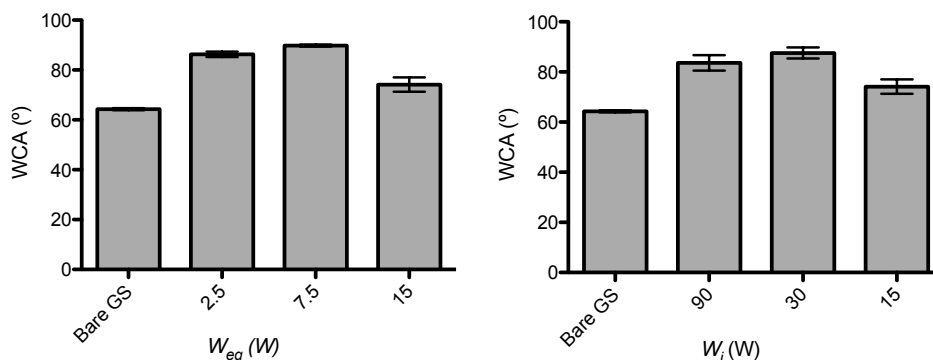


Figure 2.2. WCA of the ppPFM thin films. Values depending on the applied W_{eq} maintaining the W_i constant (left) or varying the W_i set keeping the W_{eq} fixed. Samples were modified by PECVD under the conditions indicated in Table 2.1.

The variation of the W_i in order to ensure the same W_{eq} (15 W) for the same DC studied above allowed the evaluation of the actual effect of the input power. Figure 2.2 (right plot) confirms that different properties of the ppPFM thin film are obtained between the pulsed and the continuous plasma, even though the samples are exposed to same equivalent power during plasma treatment. However, WCA values for the pulsed-ppPFM layers at 90 and 30 W ($83.6^\circ \pm 3.1^\circ$ and $87.6^\circ \pm 2.2^\circ$, respectively) were similar, indistinctly to the variation in the duration of the pulse. This result suggest that as far as pulsed-plasma conditions are applied in order to keep the W_{eq} constant by tuning the input power, the variation in the DC does not influence in the retention of the PFM group on the ppPFM thin films.

As a result of this study, samples modified at the conditions shown in Table 2.3 have proved to retain a higher amount of PFM moieties on the deposited polymer layer and thus, may potentially provide a larger density of actives sites on the surface.

Table 2.3. Optimized reactor parameters for the formation of highly reactive ppPFM thin films

W_i (W)	t_{ON} (ms)	t_{OFF} (ms)	DC (W/W)	W_{eq} (W)
15	10	10	10/20	7.5

Chemical Structure and Surface Topography Determination of the Films

Once plasma conditions have been determined in order to obtain the desired properties on the modified substrates, the newly produced surfaces were characterized by ToF-SIMS (Table 2.4). Such technique gives detailed information about the surface chemistry and the ion maps allow the determination of the chemical content of the sample together with the homogeneity of the coating.

Table 2.4. ToF-SIMS negative ions maps of ppPFM-modified GS substrates. Each map represents a 200 μm^2 area of the surface.

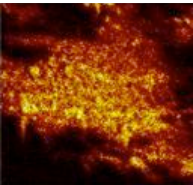
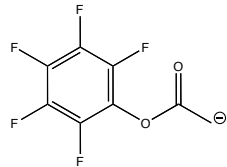
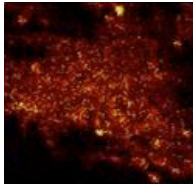
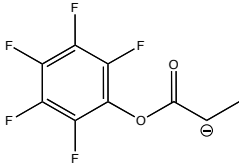
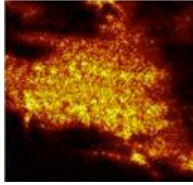
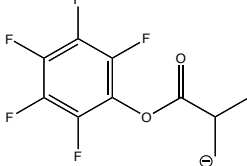
Negative Ion Map	m/z	Intensity (a.u.)	Possible ionic structure	Theoretical m/z
	227.20	567044		227.08
	237.22	134670		237.15
	253.21	577031		253.14

Table 2.4 shows the main peaks of the ToF-SIMS negative ions maps together with the mass-to-charge (m/z) and the fragment association. The x, y, z peaks were assigned to the monomer PFM structure confirming that the PFM group is successfully found in the deposited polymer thin film. The fact that ions with large m/z ratio were detected in the sample is especially interesting because it affirms that the retention of the ester reactive group is successfully achieved when polymerized under the soft conditions of the pulsed plasma. Nevertheless, all ion maps evidence that the achieved coating was not fully homogeneous among the area of study, probably due to plasma conditions.

The roughness of the modified substrates was typically around 25 nm (R_q), whereas the bare PS substrate roughness was nearly 1 nm. These results are probably due to the existing interaction

between the PFM groups during polymerization causing the formation of clusters and thus increasing the final surface roughness when compared to the flat topography of the non-modified samples (Figure 2.3).⁴¹ AFM imaging of the PECVD-modified substrates also reveals that a homogeneous thin film was obtained, as our group reported before.^{10,12}

Table 2.5. Roughness values of the bare PS substrates and after being coated with ppPFM by PECVD technique.

Sample ID	R_q (nm)	R_a (nm)	R_{max} (nm)
Bare PS	1.1	0.8	1.6
ppPFM	25.6	23.1	60.7

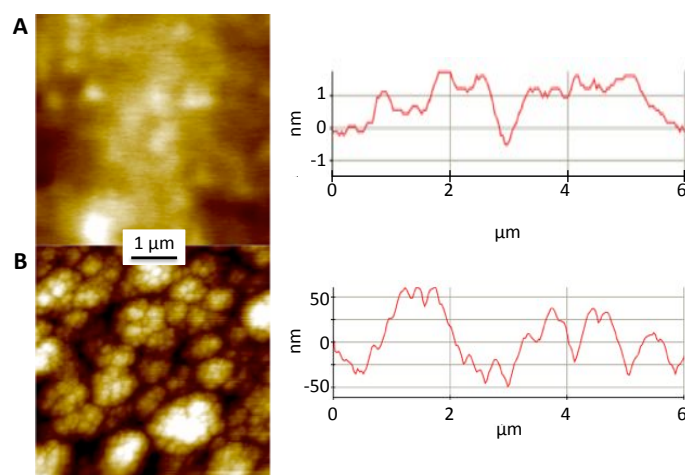


Figure 2.3. AFM analysis of the ppPFM films. AFM image (left) and topographic profile (right) of (A) bare PS and (B) ppPFM thin films obtained by PECVD on PS substrates.

Reactivity and Micropatterning of the ppPFM-Modified Substrates

The modified substrates were also characterized by fluorescence microscopy using FTSC. This is a fluorescent molecule with a free amine on its structure and is able to react with the PFM group on the surface.^{10,13} This method provides a qualitative tracking of the reaction between the activated surface and the amine of interest. Additionally, it confirms the PFM reactivity toward primary amines and shows the homogeneity of the coatings achieved by these techniques. In addition, before the plasma modification, a Cu grid was placed on the surface of the substrate to test the micropatterning viability that this approach may offer (Figure 2.4). The FTSC affinity towards a non-modified PS substrate was also tested as a control in order to ensure that the fluorescence signal achieved for the modified samples was actually due to the covalent attachment of the fluorescent

dye. (Figure 2.4A) Moreover, after several cleaning steps with Milli-Q water, the fluorescence signal remained confirming the covalent union of FTSC on the PS surface (Figure 2.4B).

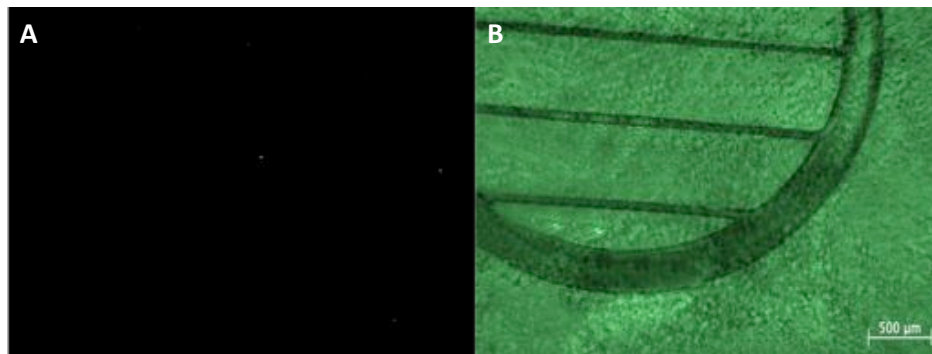


Figure 2.4. Reactivity of the ppPFM layers towards FTSC. Fluorescence images after incubation with FTSC and several washing steps with Milli-Q of a (A) bare PS substrate and (B) a ppPFM-coated PS strips.

It can be seen that the Cu grid was not able to avoid the modification of some covered areas. However, the major fluorescence signal present was on the areas exposed to the previous modification, meaning that the FTSC molecules are able to react with the polymerized PFM mainly on the desired part of the surface. Hence, the use of a grid or an external pattern to cover the substrate in a designed way during modification can be potentially used as a simple method to achieve microstructured surfaces as an alternative to other lithographic approaches.⁵³ Such methodology opens a wide range of possibilities for the design of delivery templates, a patterned substrate able to store a substance and deliver it in a predetermined pattern and to a specific medium, which can be employed also for biological applications, such as in gene delivery.⁵⁴

2.3.2. Development of the Plasma Grafting Modification Approach

Study of the Effects of the Ar-Plasma Activation Treatment

When a material is treated with plasma, an etching effect on the surface occurs that, somehow, may alter its final chemical and physical properties to undesirable changes; especially in terms of roughness and topography.^{23,44-46} Because in the plasma grafting approach the substrate is exposed to an Ar-plasma activation prior to the PFM brushes formation, a fine control of its surface properties is required. The effect in topography and roughness was studied in front of Ar-plasma exposure period-times by AFM (Table 2.6 and Figure 2.5). The input power of the plasma treatment

was fixed at 15 W in order to avoid the increase in temperature or the degradation of the material due to unwanted etching processes.

Table 2.6. Roughness of a PS surface after Ar-plasma treatment for different times.

$t_{Ar-plasma}$ (min)	R_q (nm)	R_a (nm)	R_{max} (nm)
5	0.7	0.6	3.4
15	1.2	0.8	6.3
30	1.5	2.0	9.4

Whereas the RMS roughness (R_q) values showed no remarkable changes in the surface at higher times of treatment compared to the bare PS (data shown in Table 2.5), R_a and R_{max} suggested that larger irregularities in the final topography were created (Table 2.6). AFM images confirm this last statement, where an increase of irregularities was observed due to the formation of active sites on the polymer nature of the substrate (Figure 2.5).

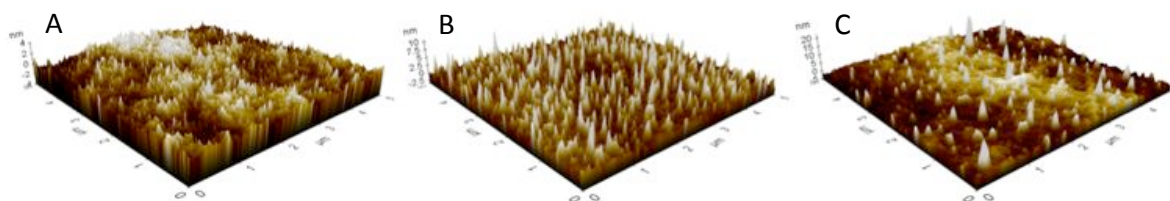


Figure 2.5. AFM 3D images of Ar-plasma treated PS surfaces for (A) 5 min, (B), 15 min and (C) 30 min.

During the first minutes of the Ar-plasma activation process, the surface tends to slightly decrease its roughness as can be seen in the R_q values for the 5-min-treated samples. Such observation confirms that plasma exposition for short times causes a smoothing effect on the surface.¹⁵ However, changes can be noticed as the magnification of irregularities due to etching processes at larger times of plasma exposure (30 min). This increase in roughness may have a negative effect for the subsequent immobilization of proteins favoring its denaturalization.⁴⁷ Because of this, Ar-plasma activation for 15 min seems to be the most suitable time if great amount of active sites want to be achieved without significant alteration in the surface roughness.

Influence of the PFM Exposure after Ar-Plasma Activation

As it has been demonstrated before, during the activation procedure in the first step of the plasma-grafting modification, active sites are generated, and when PFM is exposed, the polymer chain starts

growing from the surface.⁴⁸ AFM images in Figure 2.6 show that this technique forms polymer brushes of PFM. This AFM analysis performed for all samples, exhibit again different topographies between the original PS strip and the modified samples.

To determine the optimal time of PFM exposure after the Ar-plasma treatment, previously activated surfaces were exposed to the monomer for different times (5 to 30 min). Then, the frequency, length and quality of the polymer brushes and the roughness of the final gPFM-modified surfaces were characterized by AFM (Figure 2.6 and Table 2.7, respectively).

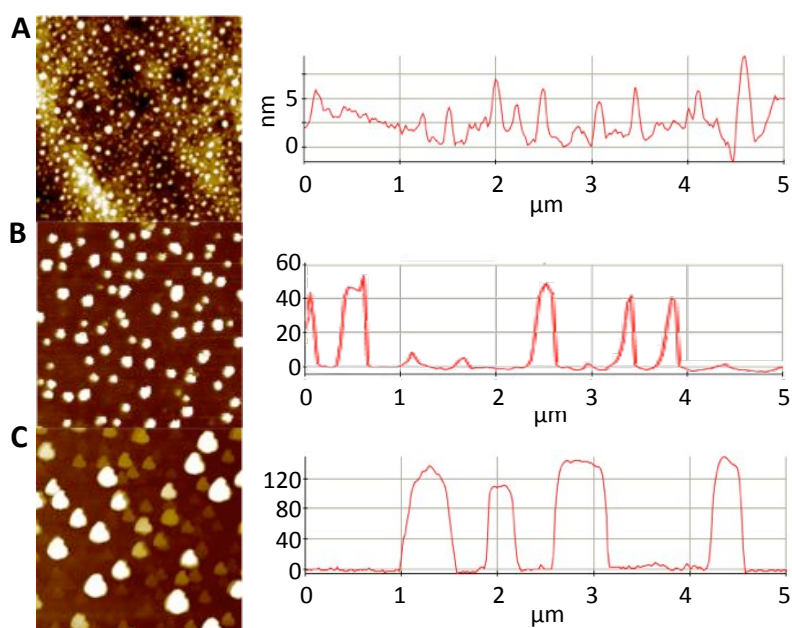


Figure 2.6. AFM study of the gPFM-modified surfaces. AFM mage (left) and topographic profile (right) of Ar-plasma treated PS surfaces after exposure of PFM monomer for (A) 5 min, (B), 15 min and (C) 30 min.

Table 2.7. Roughness of the resulting gPFM-modified surfaces after being exposed to PFM monomer for different times.

$t_{\text{PFM-exposure}}$ (min)	R_q (nm)	R_a (nm)	R_{max} (nm)
5	1.7	1.3	6.9
15	11.4	7.5	53.9
30	57.1	52.3	148.5

Higher roughness was observed at longer PFM-exposure times (30 min) due to more interaction between the PFM radicals. Furthermore, the nuclei present in Figure 2.6 confirm the formation of

PFM brushes growing larger with time. On the other hand, when samples were exposed for less than 15 min, grafting of the PFM could not be ensured. This behavior was consistent with the AFM images taken, where the irregularities observed were higher and thicker reaching around 50 nm height when the PFM was exposed for 15 min, and nearly 150 nm for the 30-min-exposed samples. Moreover, the topography obtained revealed that the formation of PFM clusters seen in the PECVD-modified samples was also taking place for the plasma grafting surface modification approach.

AFM images also exhibit that a higher density of polymer brushes were observed in the 15-min-exposed sample. Thus, an increased reactivity would be expected from the surfaces modified at these conditions. As a result, plasma-grafting parameters were fixed at 15 min of Ar-plasma treatment followed by 15 min of PFM exposure, in order to obtain highly reactive PS surfaces without altering the substrate morphology. Surfaces obtained by this method had a roughness of between 7 and 11 nm, just slightly higher than that of bare PS (1 nm) as expected from the low coverage of the PFM brushes. Briefly, as shown by the topographic values, the grafted surfaces were flatter than the PECVD films.

Evaluation of the gPFM-Modified Surfaces Behavior

Plasma grafting of PFM on PS substrates led to a considerable decrease in contact angle of the original PS (Figure 2.7).

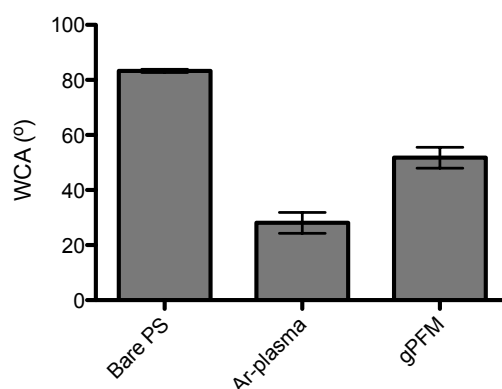


Figure 2.7. WCA values for the 3 steps in the plasma grafting modification. Data from the bare PS substrate, after Ar-plasma activation, and when PFM is exposed and grafted on the surface (gPFM).

The bare PS had a contact angle of $83.3^{\circ} \pm 0.6^{\circ}$, which decreased to $51.8^{\circ} \pm 3.8^{\circ}$ after plasma grafting modification. This was an unexpected value considering the hydrophobicity observed on the PFM

films polymerized by PECVD in section 2.3.1 ($89.8^\circ \pm 0.4^\circ$) and shown in previous publications of our group.^{10,12,49} Nevertheless, when PFM is grafted on the polymeric surface by plasma grafting, it forms a polymer brush layer, as confirmed in the AFM images (Figure 2.6), affecting also its hydrophobicity.

When the surface is activated by plasma in the presence of Ar, an etching effect is produced together with the creation of free radicals.¹⁷ These are needed for the formation of the PFM brushes when the monomer comes into contact with the activated surface and are responsible for the obtaining of a highly hydrophilic surface ($28.1^\circ \pm 3.8^\circ$). However, the PFM grafting is not enough to achieve the hydrophobicity observed for the ppPFM films, probably because the polymeric brushes do not cover the total surface as confirmed by the AFM data. The smaller number of PFM groups present on these surfaces are not enough to substantially decrease the hydrophilicity achieved on the ppPFM-modified surfaces. As a result, the grafted surface may provide less and more spread out active sites for the binding of protein molecules in a more hydrophilic environment, which may avoid remarkable conformational changes of the protein structure.⁵⁰ This fact is especially interesting when an active biomolecule, such as an enzyme, is immobilized on a surface given the importance of maintaining its conformation and ultimately its activity.⁵¹

Functionalization and Microstructuration of the gPFM-Modified Surfaces

Similarly to what has been done for the surfaces polymerized by PECVD and has been previously discussed, the functionality of the gPFM-coated substrates was assessed. Furthermore, the surfaces were micropatterned using a Cu grid. The FTSC molecule was also employed to prove the PFM modification and the different surface nature between the two phases was also analyzed by AFM. Phase imaging analysis by AFM allows the monitorization of nature changes in the same surface, creating a new image where the distinct phases can be differentiated. These variations in the surface nature are due to changes in the inner material traits such as viscoelasticity or mechanical properties, therefore allows the determination of the effects that plasma grafting modification have on the surface.⁵²

Figure 2.8A shows two different phases, one corresponding to the exposed part of the surface that experimented the plasma grafting treatment, and the other belongs to the part covered by the Cu grid. Each phase has its own new properties, and this is why the cantilever is able to change its oscillation response when passes from one to the other, differentiating the areas where PFM molecules have been grafted to the ones protected by the grid. Thus, it can be confirmed that the

modification of the substrate occurred differently along the surface and accordingly to the pattern used.

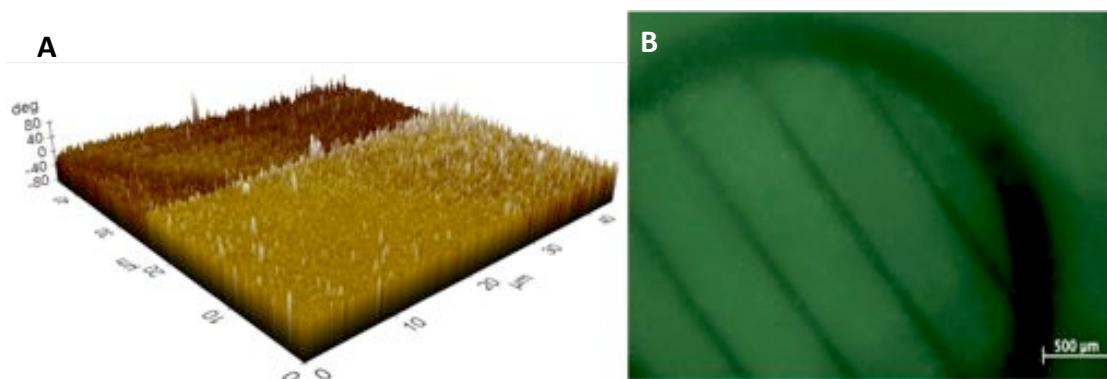
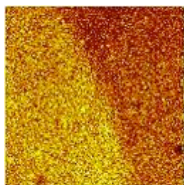
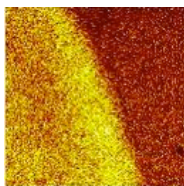
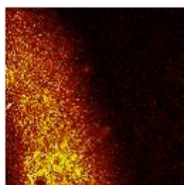
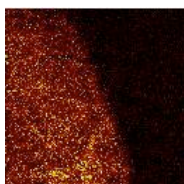
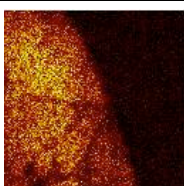
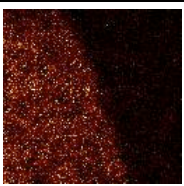


Figure 2.8. Microstructuring of the gPFM-modified surfaces. (A) AFM phase image of the micropatterned surface previous to functionalization. (B) Fluorescence image of FTSC-functionalized gPFM-modified PS.

However, the presence of reactive PFM groups on the exposed areas still needs to be proved, and for this reason the immobilization of the fluorescent dye with a free amine in its structure (FTSC) was carried out. Figure 2.8B demonstrates the successful attachment of the fluorescent molecule *via* the grafted PFM on the PS surface. Likewise, Figure 2.8B allows the distinction of the non-modified areas covered by the Cu grid verifying the achievement of the micropatterned surface also by this method. Covalent union of FTSC was again guaranteed after several washes with Milli-Q water under sonication.

Concurrently, the reactivity of the gPFM-modified and micropatterned with a Cu grid towards a PEG-amine was also tested and analyzed by ToF-SIMS. The most relevant negative ion maps corresponding to the amino-PEG functionalized surfaces are presented in Table 2.8. This map imaging technique allowed the differentiation of the two main areas, belonging to the transition between the coverage of the Cu grid and the plasma-grafting exposed part (Table 2.8). Therefore, a more intense signal was recorded in the gPFM regions where the PEG-amine was immobilized, whereas no functionalization was detected in the grid-protected area. It can be noticed that PEG typical signals of m/z 25 and 43 were also observed in the non-exposed parts despite being less intense, probably due to the low coverage of the Cu grid in these near frontier areas. Nonetheless, these parts did not show high m/z signals, which typically belong to larger molecular PEG fractions and thus it can be considered as a low contamination effect. Moreover, these signals also corroborate the proper functionalization of the micropatterned surface with PEG-amine.

Table 2.8. ToF-SIMS negative ions map of a micropatterned PS surface previously modified by plasma grafting and functionalized with PEG-amine.

Negative Ion Map	m/z	Intensity (a.u.)	Possible ionic structure	Theoretical m/z
	25.00	607910	C_2H^\ominus	25.00
	43.00	618658	$C_2H_3O^\ominus$	43.00
	61.99	211658	<chem>HOCC[O-]</chem>	61.05
	79.96	114161	<chem>HOCCOCC[O-]</chem>	80.09
	96.96	241213	<chem>HOCCOCCOCC[O-]</chem>	97.09
	123.01	59544	<chem>HOCCOCCOCCOCC[O-]</chem>	123,02

Regardless, this approach is only feasible for the immobilization of one type of molecule in a specific way because it offers basically two zones: one able to be functionalized, while the other remains unmodified. Yet, some applications may need to have two different types of molecules or proteins attached on the surface.²⁴ Among the already existing methods to achieve these types of engineered surfaces, μ -contact printing (μ CP) has gained increasing popularity in the last decades for being a simple, clean and fast micropatterning tool.^{24-26,55} Its main advantage is the possibility to produce

extremely detailed patterns with the desired design depending on the application.²⁴ In this work, a silicon master was designed with the initials of *Institut Químic de Sarrià* (IQS) and *Centre Nacional de Microelectrònica* (CNM), the centres in collaboration for this project, and was used to fabricate the PDMS stamps. These stamps were employed to produce a patterned surface on the gPFM-modified substrates (Figure 2.9).

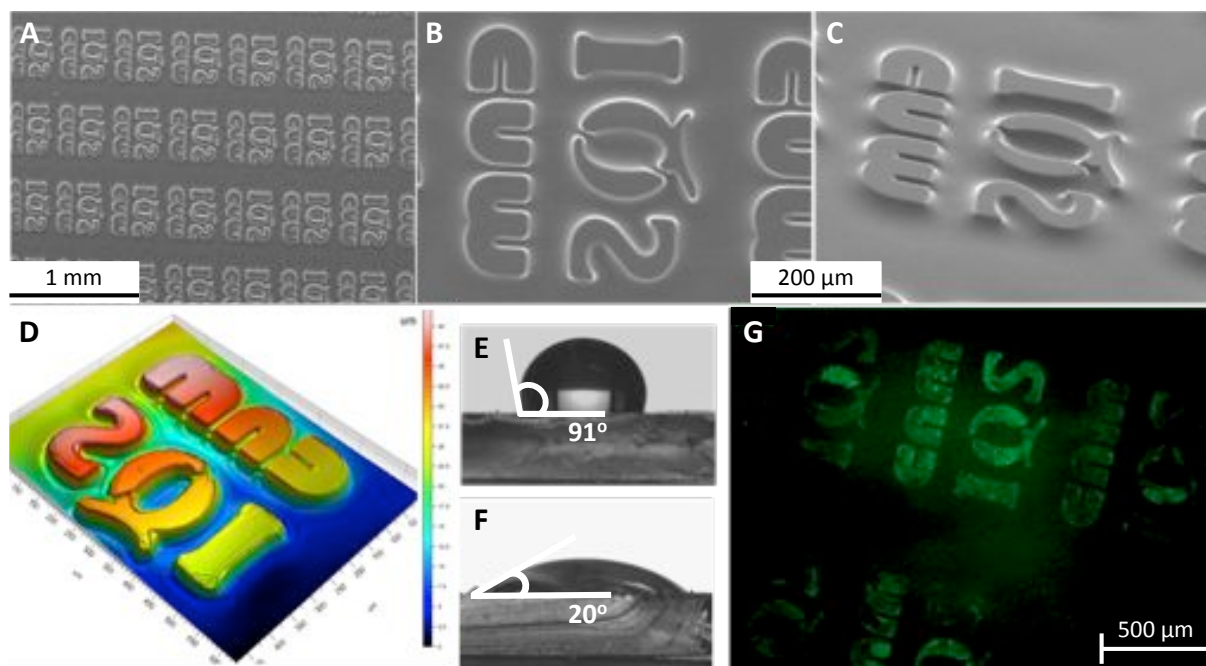
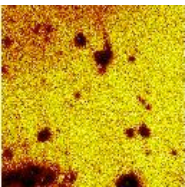
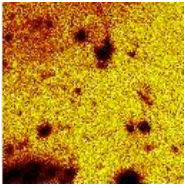
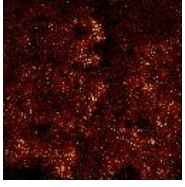
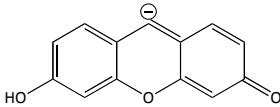
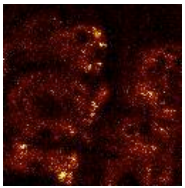
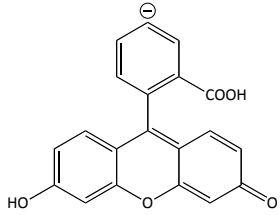
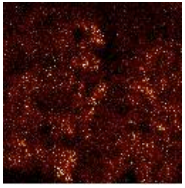
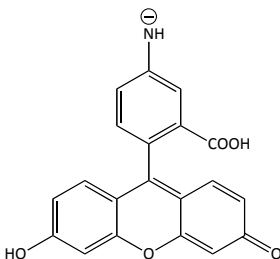


Figure 2.9. Microcontact printing on gPFM-modified surfaces. (A) General, (B) in detail and (C) 3D SEM images of the recently produced PDMS stamp, and (D) stamp viewed in 3D with a confocal microscope. WCA of the PDMS stamp (A) before and (B) after plasma treatment with Ar:O₂ (1:1) at 10 W and for 10 min. (G) Final fluorescence image of the patterned gPFM-modified PS surface by μ CP.

SEM and confocal microscopy were used to corroborate the successful fabrication of a homogeneous stamp, as presented in Figure 2.9A to D. Furthermore, the PDMS silicone was turned hydrophilic by a O₂:Ar plasma treatment and confirmed by WCA, which proved that the stamp was converted from its hydrophobic nature (Figure 2.9E) to hydrophilic (Figure 2.9F) with higher degree of wettability. As a result, the PDMS stamp could be soaked into the FTSC-water solution and subsequently used to pattern the plasma-grafting modified surfaces. Figure 2.9G exhibits the result of the patterned surface by this technique and using the described PDMS stamp. The fluorescent microscope image confirms the functionalization of gPFM-modified surfaces when they come in contact with the fluorescent dye adsorbed on the stamp.

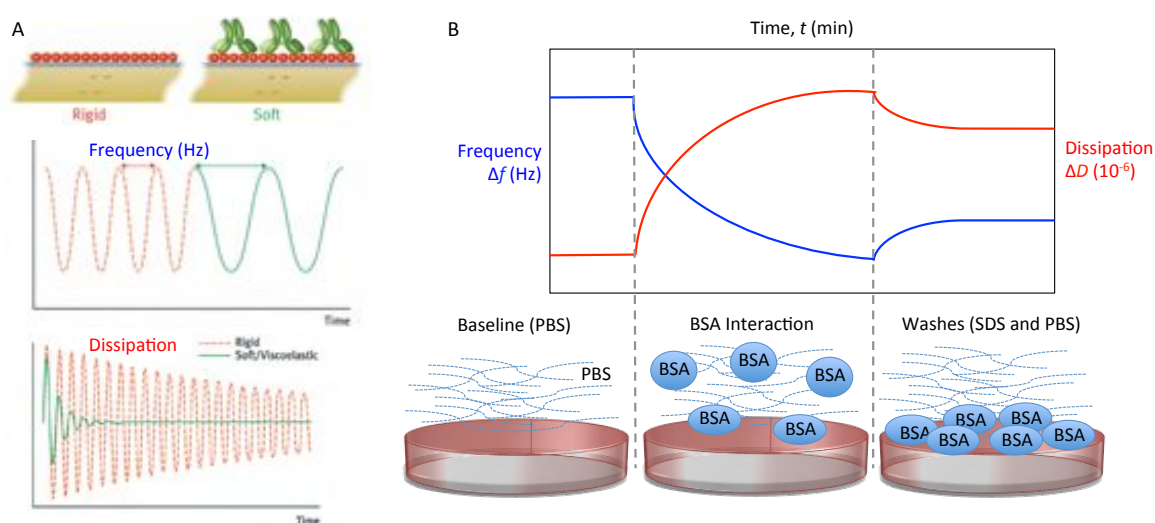
The deactivation of the remaining PFM groups on the surface was carried out with the immobilization of the PEG-amine molecule, and the success of this process was tested by ToF-SIMS. Conclusive results are shown in Table 2.9, where not only the PEG-amine typical signals (m/z 25 and 43), but also the presence of the fractions corresponding to FTSC molecule were found on the functionalized surfaces. Besides that, these FTSC fractions (m/z 211.19, 331.13 and 346.79) were clearly detected in the image maps revealing the pattern formed by μ CP and supporting the fluorescence microscope image described before (Figure 2.9G). Hence, this work corroborates that producing this kind of surfaces on gPFM-treated surfaces is also possible and therefore a wide range of applications are potentially opened to this modification technique.

Table 2.9 ToF-SIMS negative ions map of a PS surface functionalized with FTSC and PEG-amine by μ CP.

Negative Ion Map	m/z	Intensity (a.u.)	Possible ionic structure	Theoretical m/z
	25.00	783175	C_2H^\ominus	25.00
	43.00	682966	$C_2H_3O^\ominus$	43.00
	211.03	77588		211.19
	331.13	129163		331.29
	346.79	79004		346.31

2.3.3. Study of the Protein Immobilization by QCM-D Analysis

First experiments proved the reactivity of these PFM-modified surfaces in front of amines present in small molecules, such as the fluorescent FTSC dye. However the attachment of biomacromolecules on the surface is required to achieve bioactive surfaces.⁴³ Noteworthy, as it will be discussed in Chapter V, understanding the protein immobilization on surfaces is of a great interest, especially in the use of nanoparticles like CNTs with final biological applications. When nanoparticles are introduced into a biologic environment, protein absorption on their surface certainly occurs and forms what is known as protein corona.⁵⁶ This opsonization process may dramatically affect the nanoparticle properties, inducing its aggregation or masking the attached linkers and receptors and thus, elucidating its behavior is gaining attention.⁵⁷⁻⁵⁹ As a result, the capacity to immobilize proteins on the modified surfaces by both techniques and how these biological species interact with the surface needs to be evaluated. QCM-D is a well-suited technique for this purpose and was therefore chosen to develop this study.^{27,29} This technology measures the frequency (f) and dissipation (D) from the oscillatory movement of a quartz sensor and monitors the time-evolution of these parameters when the sensor is in contact with the solution of interest (Scheme 2.9A). A frequency shift indicates a variation in mass adhered to the sensor surface; a decrease in frequency means that the sensor oscillates slower due to an increase of the real mass on it. The dissipation parameter gives information about the viscoelastic properties of the formed layer on the sensor; softer coatings lead to an increase of the oscillation damping which is traduced as an increase in dissipation.



Scheme 2.9. QCM-D technology used in this work. (A) The QCM-D principle showing the differences responses in frequency and dissipation for rigid and soft layers.⁶⁰ (B) Evolution of the QCM-D parameters for protocol studied in this work.

To study the protein immobilization on solid surfaces, a methodology needs to be standardized in order to carry out same conditions for all substrates (Scheme 2.9B). The method was conducted as follows. First, the signal was stabilized and then a baseline was acquired, which was used for further quantifications. Afterwards, the BSA solution was entered to the chamber and the interaction with the sensor began, resulting in a decrease in frequency. This phenomenon was usually accompanied by an increase of dissipation, due to the formation of a protein layer on the surface. Several washing steps with PBS and SDS were followed to ensure covalent attachment of the protein on the surface and the consequent removal of the unspecific interactions. The assay finished with a final pass of PBS through the chamber, which allowed the comparison between these final values and the baseline. In general, SDS is a detergent frequently employed to unfold proteins for gel fractionation and to remove proteins physically adsorbed on surfaces. Yin *et al.* demonstrated that the SDS cleaning process in a QCM-D assay is a valid method to ensure covalent anchoring of the horseradish peroxidase (HRP) protein on acetylene plasma polymerized surfaces, confirming the formation of a protein monolayer.⁵⁹ The washing procedure using SDS performed was based in this report.

The immobilization of BSA on the ppPFM and gPFM-modified surfaces was *in situ* monitored using the QCM-D technology and following the protocol described before (Figure 2.10). This procedure was also performed on naïve gold and PS sensors to probe if the BSA showed strong unspecific binding with the bare substrate and if its removal was successfully achieved with the cleaning protocol (Figure 2.10 bottom). Note that both sensors were coated whether with a carbonaceous material such the PS in accordance to the further conjugation of proteins on CNTs (Chapter IV and V), or with gold, which will allow the verification of the protein interaction with gold nanorods in Chapter V. Only subtle changes in ΔD were observed on BSA-coated surfaces *via* both PECVD and plasma grafting modification techniques (Figure 2.10 top, red line). However, it indeed caused a significant frequency shift (Δf), which could be directly correlated to the increase in mass on the sensor's surface as a result of the attachment of the BSA (Figure 2.10 top, blue line). Nevertheless, this frequency profile varied depending on the surface modification previously carried out. This is the main reason why a deeper insight into the frequency signal was performed.

When the BSA came into contact with both modified quartz crystal sensors, the result was expressed as a shift in their resonance frequencies. It can be seen how the frequency decreased rapidly in the PECVD-modified sensor and how, after 30 min, the signal was stabilized at around -17 Hz (Figure 2.10A top, blue line). In contrast, the frequency variation on the crystal modified by plasma grafting was much slower, suggesting that it was capable of immobilizing less than a half of the protein (-7 Hz aprox.) when compared to PECVD (Figure 2.10B top, red line). These results confirm that greater

amounts of active PFM and thus higher reactivity are achieved when PECVD is used. Therefore, the final application of the modified surface is crucial to determine which of the plasma treatments should be carried out. This has to be pointed out, as it will be explained later, because the different reactivity of the surfaces towards proteins may in some cases cause a conformational change on the protein structure, probably affecting its final activity.⁵⁰

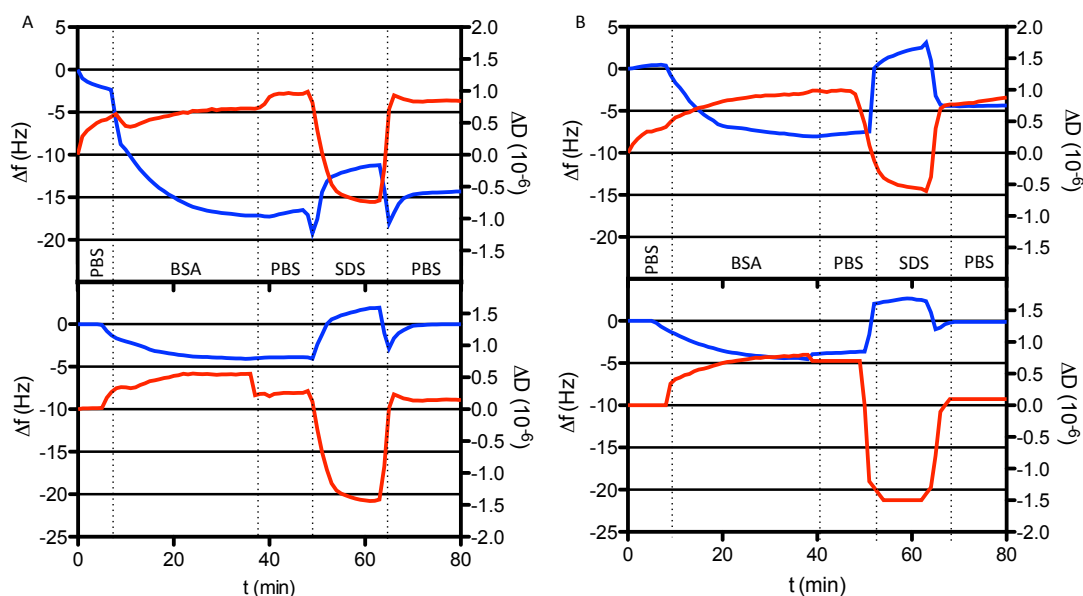


Figure 2.10. Assay evolution of the QCM-D parameters for the modified sensors. Evolution of the frequency (blue) and dissipation (red) for (A) PECVD and (B) plasma-grafting modified sensors. Plots on the bottom correspond to naïve (A) gold and (B) PS sensors, exposed to the same protocol.

A final cleaning with SDS and PBS removed all the unbounded BSA, which ensured that a protein monolayer was obtained and unspecific interaction was removed from the surface.³⁰ The frequency data obtained was then analyzed and converted to the consequent mass value by using Equation 2.3 (Figure 2.11). This equation is valid only for rigid layers as is the case for the study carried out after obtaining an almost negligible variation in the dissipation signal for both surfaces.

The surface coated with ppPFM by PECVD was able to immobilize 210 ng/cm^2 , while the grafted PFM could covalently bind only 115 ng/cm^2 . This difference can be attributed to the different densities of active sites present on the modified surfaces, as has been previously discussed. During the plasma-grafting process, when the polymer brushes are formed, fewer molecules of free PFM are available to react with the proper amine. Instead, the polymeric film obtained *via* the PECVD process is much more reactive, resulting in a greater amount of covalent linking sites able to react with the protein. Thus, the protein layer formed by PECVD modification is more dense than the obtained when the

plasma-grafting technique is carried out. However, this greater attachment to the surface achieved with the ppPFM films and the high hydrophobicity may affect the protein structure and cause its denaturalization, which could affect its activity.

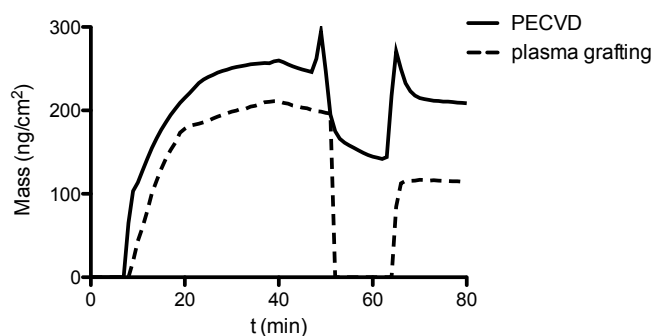


Figure 2.11. Time-evolution of the mass adhered on the modified surfaces.

Viscoelastic Properties of the Obtained Protein Layer Assessment

An alternative method to analyze the data obtained by the QCM-D is to study the variation of the dissipation *versus* the frequency shift (Figure 2.12A).^{27,28,61}

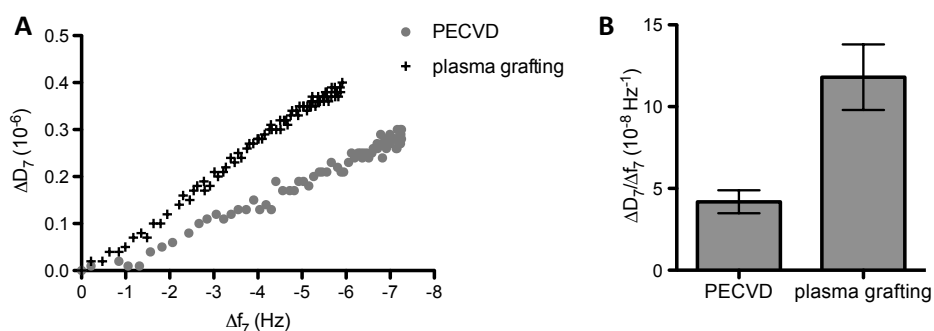


Figure 2.12. Analysis of the viscoelastic properties of the BSA monolayer. (A) Plot of the variation of the dissipation (ΔD) vs. the frequency shift (Δf) showing a higher increase in the viscoelastic properties per mass unit attached on the gPFM-modified surface. (B) The final value of the $\Delta D/\Delta f$ ratio confirmed that the protein layer formed by PECVD was more rigid and thus had lower water content.

By this method, the parameter time is eliminated from the plot and a direct comparison of the energy dissipation (ΔD) per unit mass attached to the surface (Δf) is possible. According to this relation, the influence that the protein absorption has on the damping of the sensor oscillation due to viscoelastic effects can be immediately determined. Then, the viscoelastic properties of the protein layer formed and the conformation of how the protein is immobilized on the surface can be

deduced. Results show that the variation of the viscoelasticity per mass unit of adsorbed protein was higher when the BSA reacted with the PFM brushes obtained by the plasma-grafting modification. This behavior would suggest that the formed protein layer in these surfaces is less rigid than the BSA anchored on the ppPFM, resulting in a more viscoelastic film.

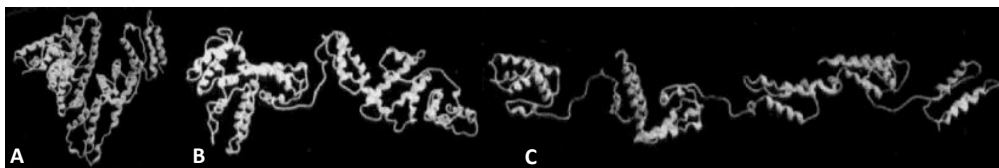
To gain a deeper understanding of the viscoelastic properties of the protein layer obtained by these two techniques, its water content was explored. The trapped water on the formed protein layer can be determined by the final value of the $\Delta D/\Delta f$ relation, which decreases with the rigidity of the protein film (Figure 2.12B). In other words, the lower this value is, the lower water content the BSA adsorbed layer has and, thus offers a less viscoelastic behavior. However, it has to be considered that this tool does not give quantitative values of the water present on the film but still gives satisfactory information about the system in order to make the appropriate approximations in terms of viscoelastic properties. By plotting the two values corresponding to both modification techniques (PECVD and plasma grafting) discussed here, it could be seen that the rigidity of the BSA layer formed on the gPFM sensors was significantly lower than when the protein is attached to the ppPFM film (Figure 2.12B). This data confirms the more viscoelastic behavior of the protein layer obtained by plasma grafting, whereas the formed on the PECVD-modified sensors is more dense and rigid.⁶¹ Moreover, the lack of water retention in the BSA structure achieved on the ppPFM-modified surfaces may also induce a conformational change of the protein.

Study of the BSA Conformation Acquired When Attached to the Modified Surfaces

As previously mentioned, protein immobilization on a surface is likely to cause a conformational change in its structure.⁵⁰ It is known that the BSA has a high affinity towards hydrophobic surfaces, which may induce its deformation due to the exposure of its hydrophobic domains located inside its structure.⁶² As a result, BSA's structure can evolve from the native form (N form) corresponding to the folded form and found under normal conditions, to the expanded form (E form), which is totally denaturalized and inactive. However, between these two, there is a third form called fast (F form) in which the two main domains of the protein are partially unfolded, but it preserves part of its activity (Table 2.10 and Scheme 2.10).^{62,63}

Table 2.10. BSA adopted forms in function of the pH.^{62,63}

	E	↔ F	↔ N	↔ B	↔ A
Name	Expanded	Fast	Normal	Basic	Aged
Transition pH	2,7	4,3	8	10	-



Scheme 2.10. Conformational changes of BSA. It can evolve from (A) the globular native structure to (B) the fast and (C) expanded form.⁶³

Given the differences of hydrophobicity seen on both surfaces studied here, it is particularly interesting to analyze the final conformational structure by which the BSA is attached to each type of surface. To do so, a calculus of a protein monolayer by using its footprint is required (Table 2.11). Each possible form adopted by the BSA has known dimensions described elsewhere, including the native form, which was measured by molecular dynamics (MD) and dynamic light scattering (DLS).^{62,63} Both measurements include the water content of the protein by giving the hydrodynamic diameter (around 10 nm).

Table 2.11. Both calculated footprints and theoretical protein mass that is expected to be immobilized for each type of BSA conformation.

	N form	F form	E form
Footprint (nm²)	80	43	36
Theoretical Mass (ng/cm²)	140	258	302

It has to be considered that it is unlikely to obtain a full coating of the protein on the surface because of the fact that the first contact of the biomolecule with it is totally random. Therefore, because it is an irreversible interaction, some dead spots might be produced, where any protein would be able to access. However, to avoid that, the BSA concentration used in this experience was high enough to ensure the maximum coverage of protein on the modified surfaces.

Having said that, it is statistically difficult to obtain a protein layer formed mainly by BSA in the E form because it would mean that the immobilization yield obtained on both modified surfaces (PECVD and plasma grafting) regarding the theoretical mass calculated would be much lower than the predicted given its highly reactive PFM chemistry.^{10,12}

On the PECVD-modified surfaces, the difference between the theoretical mass obtained if a BSA monolayer is attached to the surface and the actual mass detected by the QCM-D technology is only in its N form is around 30%. That would suggest that the rest of the mass that was quantified

experimentally could be attributed to water content of the protein layer. This amount of water trapped on a protein coating is typically expected when viscoelastic proteins such as a mussel adhesive protein (Melp-1) is used.⁶⁴ This is not the case when using BSA for immobilization, which usually forms rigid layers with low water contents.²⁷ Thus, these results suggest that the BSA undergoes a conformational change when it reacts with the ppPFM deposited by PECVD, most likely to the F form. The large number of accessible lysine groups, the amino acid in charge of reacting with the PFM labile group and present in a large quantity in the BSA structure, may cause the partial unfolding of the protein as a result of the different tensions created around its structure during the immobilization process.⁶⁵ This phenomenon is also favored by the hydrophobic nature of the ppPFM coating previously discussed, which may induce to a conformational change.⁵⁰ Both effects are especially crucial when protein units are first immobilized on the surface, but as soon as different BSA molecules cover it, the hydrophobic forces decrease together with the free PFM groups able to interact with Lys. In this environment, the interaction of BSA with the surface is weaker and the unfolding of its structure is less probable, so in the end the N form can be immobilized as well. The average mass considering the theoretical mass calculated by assuming that half of the protein is immobilized in its F form and the other half is anchored in its native structure (N form) is 200 ng/cm², which differs from the experimentally obtained mass by only 5%. This percentage of extra mass monitored by the QCM-D technology can be attributed to the water content of the layer, meaning that the protein coverage of the surface is near to its totality.

As it has been said, the obtained mass of immobilized BSA on the surfaces modified by plasma grafting was approximately 115 ng/cm². This value is lower than the three calculated by the different footprints depending on the form in which BSA is attached to the surface (Table 2.11), which confirms that the density of active sites is lower than the formed by PECVD. For that reason, the amount of immobilized protein does not cover the entire surface. However, the attachment of the BSA in F or E form is ruled out by the low yield that the gPFM reactivity would offer. In that case, it can be assumed that the BSA is immobilized to the surface in its native conformation. The less hydrophobic environment that the plasma grafting confers to the modified surface may favor this behavior, also causing a more viscoelastic layer capable of trapping a greater amount of water on its structure, as has been previously demonstrated. However, because the value of the native BSA radius was obtained by DLS and so the solvating water around the molecule was also measured (hydrodynamic diameter), the difference could be due to the real amount of trapped water on the protein layer, which seems to be higher considering the viscoelasticity shown. However, it might be plausible that BSA might suffer a deformation of its native structure without resulting in a notable

conformational change when it approaches to the modified surface. If so, the footprint used to calculate the theoretical mass would not fully adjust to the real dimensions during the immobilization process.

Therefore, the use of each surface-modification technique can be used depending on its final application, regarding the amount of protein immobilized on it and its conformation structure

2.3.4. Obtaining Bioactive Surfaces by Enzyme Immobilization

It has been demonstrated that each technique offers different properties to the final protein monolayer, depending on the crucial function that the biomaterial is asked to develop. If full coverage of the surface is needed and the activity of the biomacromolecule immobilized is not important, then PECVD would be the preferred option. One clear example would be when a chemical linker wants to be attached in a high density on a surface, as it will be discussed in Chapter III. In such case, a PEG-amine molecule is immobilized on the CNTs surface *via* the PFM functionality previously deposited by PECVD. However, plasma grafting would be more suitable when bioactive proteins or molecules such as enzymes have to be immobilized without suffering any conformational changes. Hence, in the production of bioactive surfaces, where the activity of the attached biomolecule plays a crucial role in the final application, plasma grafting happens to be the most suitable option given the properties that offers as early discussed (Table 2.12)

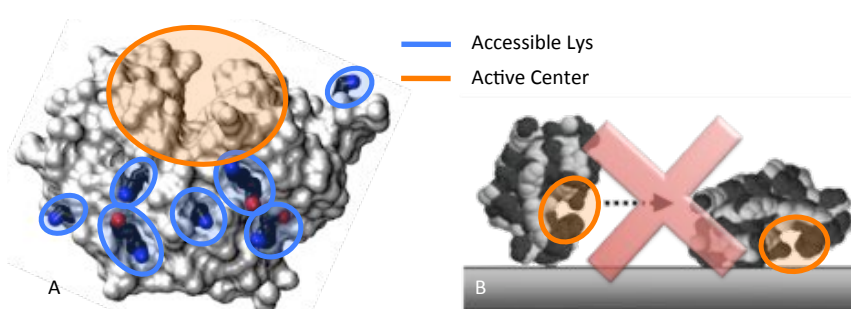
Table 2.12. General properties of the two modification techniques, PECVD and plasma grafting.

	Properties	PECVD	Plasma Grafting
Modified Surface	Obtained Coating	ppPFM thin film	gPFM brushes
	Nature	Hydrophobic	Hydrophilic
	Roughness (R_q)	28.6 nm	11.4 nm
Protein Layer	Attached mass	210 ng/cm ²	115 ng/cm ²
	BSA Form anchored	F + N Form	N Form
	Water content	Low	High
	Nature	Rigid	More viscoelastic

This study seeks to confirm that the biomacromolecule of interest remains active once attached on gPFM-modified surfaces. For this reason, the immobilization of the enzyme 1,3-1,4- β -glucanase (Gln) was performed and its activity once anchored was quantified. This enzyme offers a high thermal and

pH stability, making it the perfect candidate to be used as a proof of concept for the production of bioactive surfaces by this method.^{66,67} Furthermore, because it presents a strict specificity towards the β -1,3 and β -1,4 bonds in the β -glucane structure, it becomes of a remarkable value in food technology applications.

This enzyme, not only meets the described advantages, but also possesses an interesting structure, which leaves its active centre exposed once immobilized on the gPFM-modified surfaces. A molecular dynamic study (Gromacs v.4.0) carried out by the Laboratory of Biochemistry at *Institut Químic de Sarrià* (IQS) revealed that the lysine groups present in the 1,3-1,4- β -glucanase structure that act as the linking sites, are mainly located in the opposite side of the active centre (Scheme 2.11A). Therefore, the active part of the enzyme remains accessible for the substrate, avoiding its inactivation, as it is presented in Scheme 2.11B. Furthermore, it is ensured that the amino acid residues essential for the catalytic activity are not involved in the covalent linkage to the support.



Scheme 2.11. 1,3-1,4- β -glucanase structure and immobilization. (A) Model of the 1,3-1,4- β -glucanase structure obtained by molecular dynamics, showing the active center (orange) and the accessible lysines (blue). (B) Possible absorption of the enzyme LamA, with similar structure as the enzyme studied here, where the active center becomes inaccessible for the substrate can be avoided.⁶⁶

The attachment of enzymes to the appropriate surface ensures that they stay where their activity is required. This immobilization enhances the concentration at the proper location and it may also protect the enzyme from being destroyed. Thus, achieving a stable linkage between the enzyme and the substrate has become increasingly interesting for its technical utility in the biotechnology field.⁶⁸

Understanding the 1,3-1,4- β -Glucanase Immobilization

Plasma-grafting modification technique fulfills the requirements discussed before therefore PS sensors were used. Again, QCM-D technology allowed the analysis of the interaction of the 1,3-1,4- β -glucanase and the PFM-grafted PS. Same protocol basis applied for the BSA immobilization studies

performed before were carried out with the enzyme of interest. The non-specific interaction towards the PS sensor was also tested (Figure 2.13.).

In the two cases, the sensor was stable during the baseline with phosphate buffer (PhB), while both parameters, dissipation and especially frequency, significantly changed when the 1,3-1,4- β -glucanase comes in contact with the surface. However, only subtle changes in ΔD were again observed, meaning that the formed layer was rigid. For the non-modified sensor, the decrease in frequency was smooth and modest compared to the gPFM-treated surface. In the former, the frequency was stabilized around -5 Hz whereas it reached -15 Hz for the modified sensor. This result suggests that the enzyme clearly shows a higher affinity to the PFM brushes than to the bare PS. Nonetheless, the unspecific adsorption of the 1,3-1,4- β -glucanase to the PS cannot be entirely removed with this protocol, despite being effective for the BSA, and the amount adsorbed has to be taken into account for further QCM-D quantifications.

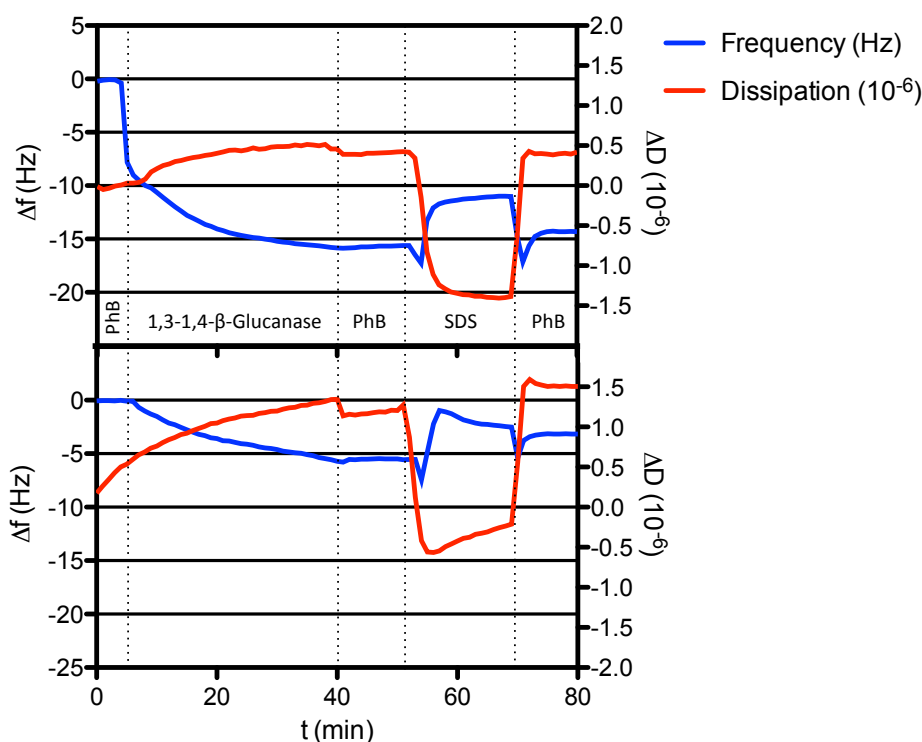


Figure 2.13. QCM-D evolution of the enzyme front the gPFM-modified sensor. Frequency (Δf) and dissipation (ΔD) shift as function of time of the 1,3-1,4- β -glucanase immobilization carried out on a gpFM modified sensor (upper plot) and the bare PS sensor (lower plot).

To confirm the rigidity of the obtained enzymatic layer, the dissipation energy (ΔD) as function as the adhered mass (Δf) on both gPFM-treated and non-modified sensors was analyzed (Figure 2.14A).

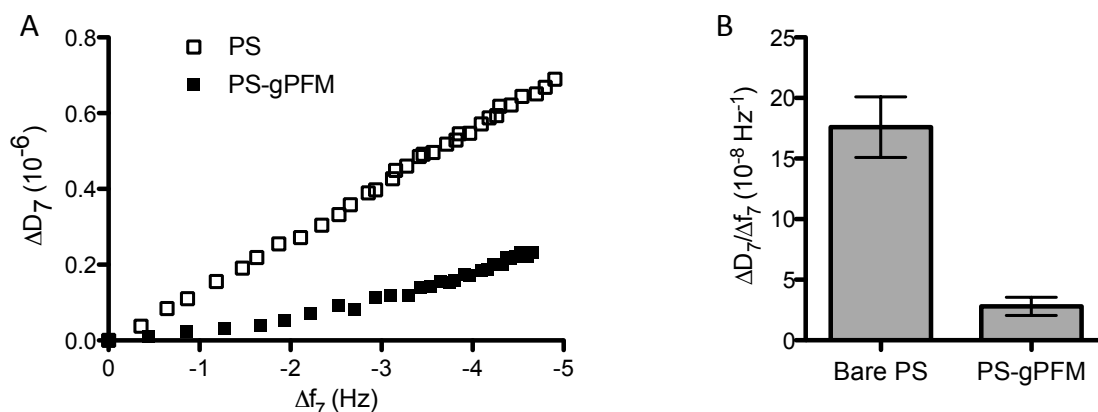


Figure 2.14 Viscoelastic properties of the immobilized enzymatic layer. (A) Evolution of the $\Delta D/\Delta f$ ratio, showing a higher increase in the viscoelastic properties per mass unit of enzyme attached on the gPFM-modified surface than when is adhered by unspecific interactions. (B) Final $\Delta D/\Delta f$ ratio value confirmed that the enzymatic layer formed by covalent immobilization was more rigid and thus had lower water content.

This plot reveals that the covalent attachment of the enzyme through the PFM brushes led to a less viscoelastic, thus more rigid, layer than the one formed due to unspecific interactions with the PS surface. This behavior was confirmed by the final value of the $\Delta D/\Delta f$ ratio (Figure 2.14B) where the enzymatic coating was significantly more rigid for the gPFM-modified sensor, resulting in a layer with lower water content.

As previously done for the BSA attachment studies and because the formed enzymatic layer could be considered rigid, the final adhered mass was quantified by using Equation 2.3. Furthermore, the 1,3-1,4- β -glucanase's footprint was acquired from the D_H value measured by DLS and the theoretical mass of a 1,3-1,4- β -glucanase adhered monolayer was calculated. Altogether are presented in Table 2.13. Any conformational changes that this enzyme may suffer are still unknown, thus the theoretical quantification was carried out considering as if it was immobilized in its native structure. The amount of 1,3-1,4- β -glucanase covalently attached to the PS sensor modified with PFM by plasma grafting, was approximately 260 ng/cm^2 , whereas the bare PS was able to adhere around 80 ng/cm^2 . This last result confirms that the SDS cleaning was not enough to remove the unspecific attached enzyme on a PS substrate, which was not a surprising behavior due to the high affinity that this type of enzymes have on hydrophobic surfaces.⁶⁶ Koutsopoulos *et al.* achieved the immobilization of a 1,3-1,4- β -glucanase enzyme (endo-1,3- β -glucanase) on a highly hydrophobic surface such as Teflon in a 78% of surface coverage and proved that the interaction to this substrate was irreversible. Therefore, it could be expected to obtain a non-specific and permanent adhesion of the 1,3-1,4- β -glucanase also on the PS substrates used in this study. Nevertheless, how the activity

of this attached enzyme could be affected has to be analyzed. In the preceding Koutsopoulos' work, the presence of unstructured domains of the endo-1,4- β -glucanase was detected once immobilized on their Teflon surfaces, hence its activity may have been clearly altered.

Table 2.13. Values for the quantification of immobilized enzyme. Hydrodynamic diameter of the 1,3-1,4- β -glucanase measured by DLS, the subsequent value for its footprint, and the theoretical and experimentally obtained mass of a 1,3-1,4- β -glucanase adhered monolayer on both, treated (PS-gPFM) and naïve (PS) sensors.

D_H (nm)	Footprint (nm ²)	Theoretical Mass (ng/cm ²)	PS-gPFM (ng/cm ²)	PS (ng/cm ²)
4.8	18	217	260	80

Considering the mass of this unspecific adhered 1,3-1,4- β -glucanase on the PS sensor as the baseline and subtracting it from the 260 ng/cm² of enzyme covalently attached on the gPFM-modified surface, the final amount of immobilized 1,3-1,4- β -glucanase was calculated to be 180 ng/cm². Such value differed between 20 and 25% from the theoretical mass obtained, meaning that the plasma grafting technique was able to immobilize around 80-85% of the 1,3-1,4- β -glucanase. These results are consistent with immobilization rate obtained in previous studies with the BSA, illustrating the homogeneity of this modification and the applicability to different kind of proteins.

Surface Modification of the Substrates Analysis

Surface modification of flat surfaces has been commonly employed due to its easiness and as a proof of concept. However, the modification of spherical particles has been considered given the industrial application that this methodology may render. These types of material exhibit a high specific surface area, which make them ideal to be used in bioreactors and could easily be separated from the reaction media.⁶⁹ Therefore, PS beads (PSb) were modified with PFM by the plasma grafting approach at the previously optimized and analyzed conditions.

After the PFM grafting, PS-gPFM substrates were functionalized with FTSC. Figure 2.15 shows the tracking of this immobilized fluorescent molecule. gPFM-modified PS beads exhibited homogeneous fluorescence around the spherical surface (Figure 2.15B), in contrast to the bare PSb samples (Figure 2.15BA). Hence, the technology developed in this work together with the reactor used is able to also produce reactive spherical particles *via* the PFM grafting on its surface.

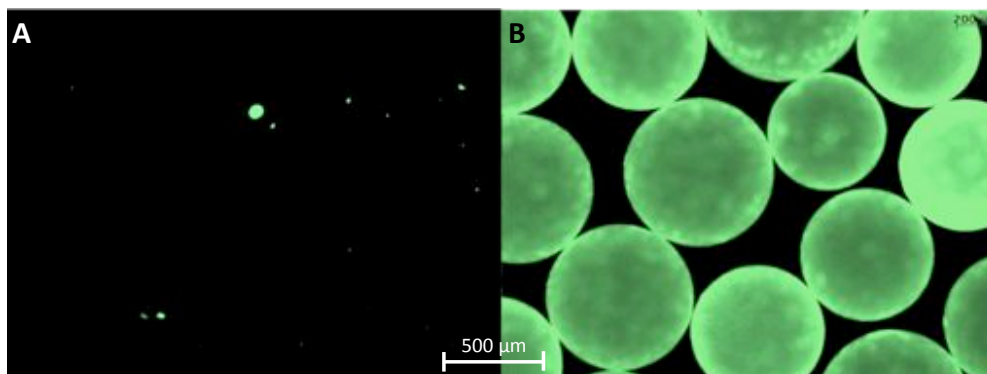


Figure 2.15. Reactivity of the gPFM-modified PS beads. Fluorescence image of the (A) bare PS beads and (B) the PS-gPFM after incubating with the fluorescent dye FTSC.

Quantification of the Immobilized Enzyme on the gPFM-Modified Substrates

After the immobilization studies of the 1,3-1,4- β -glucanase on gPFM-treated flat surfaces and the corroboration of the successful modification also on PS beads, the attachment of the enzyme on the new modified spherical substrate was analyzed. Substrates were incubated with the enzyme at different times (from 0 to 2 h) and the enzyme remaining in the solution was quantified by the Bradford method. Thus, by measuring the 1,3-1,4- β -glucanase not bound on the PS-gPFM beads, the quantity of immobilized enzyme could be determined and plotted in function of time (Figure 2.16).

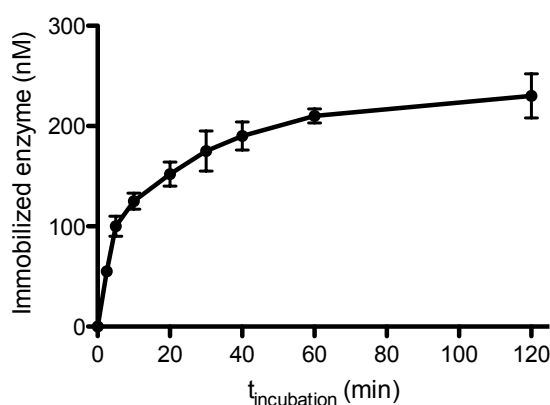


Figure 2.16. Immobilized 1,3-1,4- β -glucanase on the PS-gPFM beads in function of the incubation time.

The 70% (210 nM) of the added 1,3-1,4- β -glucanase was immobilized after 1 h of incubation, and only a 5% more of enzyme was attached after a total time of 2 h. Knowing the surface area of the PS beads (SA_{PS}) that was calculated and the total amount of used particles was considered, the final surface (SA_{total}) area where the 1,3-1,4- β -glucanase could be attached was estimated (Table 2.14).

Table 2.14. Data to calculate the mass obtained after the 1,3-1,4- β -glucanase and the PS beads are incubated for 1h (Mass 1 h) or 2 h (Mass 2 h)

SA_{PS} (mm^2)	PS beads units	SA_{total} (cm^2)	Mass 1 h (ng/cm^2)	Mass 2 h (ng/cm^2)	Theoretical Mass (ng/cm^2)
2.5	500	12.7	198 ± 6	217 ± 20	217

These results showed that the total coverage of the PSb-gPFM after 2 h of incubation was accomplished (Table 2.14). The mass of 1,3-1,4- β -glucanase covalently attached on the particle substrates fit with the theoretical mass calculated before for the QCM-D analysis, assuming that an enzyme monolayer was immobilized. Therefore, not only the total immobilization of the 1,3-1,4- β -glucanase on the PSb but also the achievement of a homogeneous and complete modification could be reaffirmed.

The difference observed with the QCM-D analysis, where the enzyme covering was around 80-85% from the theoretical mass calculated, can be attributed to the experimental differences of each procedure. For the QCM-D assay, a constant flow of enzyme solution passed through the modified surface and a random interaction with the PFM is more likely to occur. On the other hand, when the 1,3-1,4- β -glucanase was incubated with the gPFM-treated PS beads, the enzyme remained in solution with the substrates for longer times. In such conditions, the interaction enzyme-substrate and thus the capacity of reacting can be significantly increased, especially for small biomacromolecules like the 1,3-1,4- β -glucanase. Furthermore, in the QCM-D methodology a SDS cleaning ensured a total removal of the unspecific attached proteins. This washing step was not carried out for the functionalized PS beads in order to avoid the enzyme denaturalization. Therefore, QCM-D technology is still presented as a reliable and interesting tool for protein layer quantification and characterization if these limitations are taken into account.

Measurement of the Enzyme Activity of the Produced Bioactive Surfaces

As previously discussed, immobilized proteins on solid surfaces may suffer from conformational changes that can affect its final activity. This fact is especially undesirable when enzymes are anchored on substrates since their major function is still required. Therefore, once the 1,3-1,4- β -glucanase was immobilized on the modified substrates developed in this work (PS-gPFM), the resulting bioactive PS beads were asked to maintain the enzymatic activity.

The free 1,3-1,4- β -glucanase's activity was measured together with the functionalized PS beads (PSb+Gln and PSb-gPFM+Gln) by the DNS method. This assay quantifies the reducing sugar present after the enzyme has been incubated with its substrate, the 1,3-1,4- β -glucane (Scheme 2.8.). The 1,3-1,4- β -glucanase is the responsible for the cleavage of the 1,3-1,4- β -glucane, generating a determined amount of reducing sugars that can be directly related to the activity of the enzyme. The produced reducing sugars react with the DNS reagent yielding the colored subsequent product detectable at a 540 nm absorbance. Altogether with a standard curve made with different concentrations of glucose allowed the determination of the reducing sugars concentration and then, the enzymatic activity was calculated. After 10 min of reaction, the free 1,3-1,4- β -glucanase was able to hydrolyse the 1,3-1,4- β -glucane producing a total amount of 3 mM of reducing sugars, which corresponds to an activity of approximately 30 μmol of reducing sugars per nmol of 1,3-1,4- β -glucanase and minute.³¹ The same assay realized to the functionalized PS beads and a control lead to the results shown in Table 2.15 and plotted in Figure 2.17.

Table 2.15. Activities obtained for the different substrates and the free 1,3-1,4- β -glucanase.

Sample ID	Immobilized Enzyme from the Total Added (%)	Activity (μmol reducing sugars \cdot nmol 1,3-1,4- β -glucanase ⁻¹ \cdot min ⁻¹)	Relative Activity (%)
PSb+Gln	50	7	22
PSb-gPFM+Gln	80	16	54
Free Gln	100	30	100

When the 1,3-1,4- β -glucanase was non-specifically bounded to the PSb (PSb+Gln), the activity achieved for these substrates was only around 20% of the observed for the free enzyme. The obtained enzymatic activity for the PSb+Gln samples was calculated considering that 50% of the added enzyme during the incubation process with the bare PS beads was actually attached on the substrate and it was not removed after washing with MilliQ (as it is inferred from the QCM-D data in Figure 2.13). Results show a substantial decrease of the activity of the PS substrates functionalized with the 1,3-1,4- β -glucanase in a non-specific way. This can be caused by several factors. First, the enzyme is prone to denaturalize when interacts with the hydrophobic bare PSb.^{66,69} Second, and most important, the unspecific attachment on the surface may lead to the inaccessibility of its active centre.⁶⁶ On the contrary, this fact was probably avoided when the enzyme was immobilized *via* the grafted PFM. This is likely to be the main reason why the activity was considerably increased for the

PS beads modified with PFM by plasma grafting and subsequently functionalized with the 1,3-1,4- β -glucanase. The covalently functionalized substrates exhibited an activity in excess of 50% of the obtained for the free enzyme. This value was obtained considering that 80% of the total enzyme added during the incubation process was considered actually attached, as demonstrated before in the QCM-D analysis.

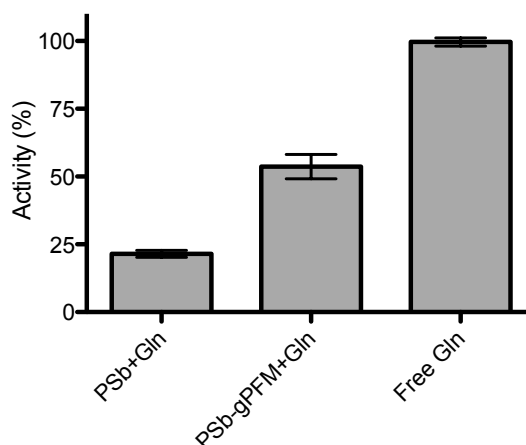


Figure 2.17. Activity of the immobilized enzyme. Relative activity of the 1,3-1,4- β -glucanase immobilized to the PS substrates unspecifically or through the PFM bound compared to the activity obtained for the free enzyme.

These results suggest that part of the enzyme's activity has been also lost during the attachment on the grafted substrate, but a higher control of the enzyme immobilization process has been clearly achieved compared to the non-specific interaction. Hence, this technique entails promising advances for the production of immobilized enzyme systems without affecting its final activity, resulting in the formation of bioactive surfaces. Additionally, this study provides a step forward in the creation of these smart, bioactive surfaces in complex substrates like particles, which are of special interest in many bioengineering applications, as will be deeply evaluated in Chapter III.

2.3.5. Immobilization of Viral Gene Delivery Vectors for Substrate-Mediated Transfections

Last section proved that plasma grafting is a versatile approach to produce bioactive surfaces. Depending on the final application, the immobilization of the desired biomacromolecule can be achieved and its activity can be maintained almost entirely. As exposed in Chapter I, this thesis aims to take advantage of these plasma techniques in order to produce CNTs vectors to efficiently deliver

a therapeutic silencing nucleic acid to target cells. This vector should be injected intravenously and able to discern and reach target cells efficiently without premature elimination by components of the bloodstream, such as proteins antibodies and cells, as it will be further discussed in the following chapters (Chapter III, IV and V).

However, safety issues in the *in vivo* use of gene therapy stem from the little control over the location of transduction sites, once vectors are administered in the body. Under these conditions, the administered vectors can travel beyond the site of administration, leading to uncontrolled accumulation and transduction of non-target tissues and organs.⁷⁰⁻⁷³ Although *in vivo* gene delivery, such as functionalized-CNTs, for systemic applications is expected to overcome these limitations in the near future, which is the challenge of this work, other gene therapy strategies may hold great promise in specific therapeutic situations.⁷⁴ Localized gene delivery from surfaces is a growing area of research, because of its advantage in delivering nucleic acids directly at the site of interest. Such localized gene delivery method, also known as substrate-mediated, reverse transfection or solid-phase transfection, has promising applications in tissue engineering, medical implants and *in vitro* transfection protocols. In these settings, gene deliver vectors are tethered on the surface of suitable substrates, such as tissue culture material for *in vitro* applications or medical implants for *in vivo* approaches, and placed directly and in sustained contact with target cells. Surface immobilization of gene delivery vectors may improve cell binding and internalization, requiring lower doses of nucleic acids. Substrate-mediated gene delivery permits to concentrate nucleic acids at the site of interest, resulting in improved transfection efficiency.⁷⁴⁻⁷⁶ In contrast to systemic delivery, substrate-mediated delivery minimizes distribution to non-targeted tissues, as well as reducing the potential of immune and toxicity responses.^{77,78} Classically, SAMs have been the preferred choice to design substrate-mediated delivery systems due to their ease of fabrication and a wide spectrum of possible surface chemistries. However, SAMs are limited to specific substrates (e.g. thiols on Au surfaces) and in most cases are restricted to certain metal surfaces, which may be incompatible with some biomedical applications.⁷⁹

To address limitations with present strategies for vector immobilization, plasma grafting appears to be a feasible method to achieve complete surface functionality and enhance immobilization specificity. In this line, a preliminary study was carried out, in which an adenoviral vector encoding GFP was attached on PFM-grafted PS plates (PSP). After extensive washing, these cell reprogramming surfaces (CRS) were seeded with mouse macrophages (RAW 264.7). Two different concentrations of virus particles were used to transfect the same amount of cells (400,000 cells/plate) obtaining a multiplicity of infection (MOI) of 25 and 250. Transfection of GFP by these

CRSs was compared with the classical transfection protocol developed by the Institut d'Investigacions Biomèdiques de Barcelona (IIBB) with adenoviral supernatant encoding the same gene.^{33,34} Quantitative RT-PCR of the samples allowed the determination of the RNA amount transfected to the macrophages of both virus-functionalized surfaces (Figure 2.18).

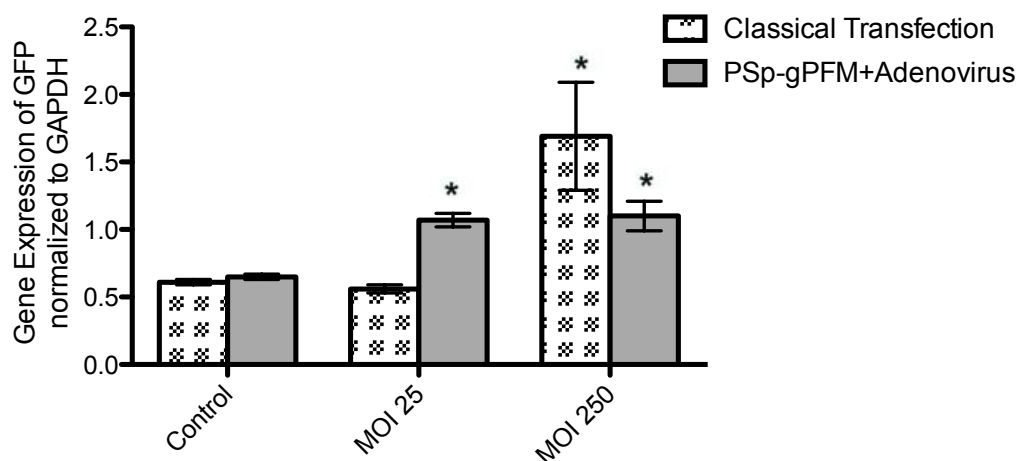


Figure 2.18. GFP expression of the seeded cells on the CRS at different MOI ratios. Quantification assessed by quantitative RT-PCR in macrophages. Data was collected after following classical adenoviral supernatant protocol or using the created CRSs. Gene expression normalized to GAPDH is represented as mean \pm SEM. *P < 0.05 versus Control.

Figure 2.18 shows that the GFP transfection achieved for the CRSs at low MOI (25) was significantly higher than employing the traditional protocol at same ratio of infectious virus particles to infection target cells. However, the transfection at higher MOI (250) increased being superior to the achieved by the CRSs. In fact, the same transfection efficiency was observed for both ratios when using the modified-PSp. This is due to the fact that both plates probably have the same number of attached virus particles, independently to the adenovirus concentration initially used. When PSp are modified by plasma grafting, a certain amount of active sites are created, as demonstrated before. Therefore, a limited quantity of virus particles can be covalently immobilized regardless of the total amount present. As a result, the obtained CRSs incubated with different concentrations of adenovirus have similar density of attached gene delivery agents after several washing steps. Not surprisingly, then, the transfection efficiency of both virus-functionalized surfaces is kept constant, whereas for the traditional protocol, the production of GFP increases with the quantity of adenovirus used. Hence, the use of these CRSs improves the transfection efficiency at low infectious agent to infection target ratios. These results open the door to new methods for gene delivery applications using plasma treatments for the immobilization of viral but also synthetic nucleic acid vectors.

2.4. Concluding Remarks

We have developed two different approaches to the immobilization of biomacromolecules, depending on the final application of the functionalized material. PECVD and plasma grafting create highly reactive surfaces towards amines and can be used to produce micropatterned surfaces. The resulting surfaces vary in properties such as roughness, hydrophobicity and reactivity, which lead to different behavior in front of the biomolecule of interest. The effect of this kind of characteristics on the material-protein interface has been deeply analyzed studying the interaction of the BSA protein with these two surfaces, PECVD-polymerized and plasma-grafted PFM, by QCM-D technology. Both allow the covalent union of BSA proteins in different ranges (200 and 100 ng/cm⁻², respectively).

Although the immobilization rate is lower, plasma grafting forms more hydrophilic and flat surfaces than PECVD, which is crucial for the immobilization of active molecules like proteins and enzymes. In such conditions, the bioactive molecule can be attached on the surface without suffering any remarkable structural change. As a result, for the production of bioactive surfaces, plasma grafting would be the most suitable technique. This is why this work has also demonstrated that grafted PFM can immobilize the 1,3-1,4- β -glucanase on PS beads maintaining 60% of its natural activity, becoming a step forward in the production of bioactive surfaces *via* the PFM group. Furthermore, complex materials such as PS beads have been successfully modified using the described home-built reactor. Therefore, this approach opens the possibility to functionalize other non-flat type of materials in the working reactor like powder CNTs. In addition, it has been demonstrated that tailored reactive surfaces allow the controlled covalent immobilization of gene delivery agents on a solid-matrix, generating efficient CRSs over which cells to be reprogrammed can be seeded and successfully transfected.

On the other hand, by PECVD, a more hydrophobic surface is achieved due to the PFM film layer, which causes a greater conformational change when BSA is anchored. However, the greater number of exposed PFM groups obtained by this method compared to the PFM brushes formed with plasma grafting results in a higher capacity of BSA immobilization. The higher density of reactive groups is especially interesting when superior coverage of the surface is desired. This could be the case when a chemical linker is needed between the modified surface and the molecule of interest to be immobilized. Then, the maximum functionalization of the surface possible is desired and thus, PECVD is the chosen option. Next chapter (Chapter III) presents how this technique enables the formation of CNTs for gene delivery vectors by the covalent immobilization of a PEG-amine *via* the PFM group, which can be used as a linker to bind micro-RNA.

2.5. References

- 1 Bianco, A. *et al.* in *Medicinal Chemistry and Pharmacological Potential of Fullerenes and Carbon Nanotubes* Vol. 1 (eds Franco Cataldo & Tatiana Ros) 23-50 (Springer Netherlands, 2008).
- 2 Jeon, I.-Y., Chang, D. W., Kumar, N. A. & Baek, J.-B. *Functionalization of Carbon Nanotubes*. (2011).
- 3 Lu, F. *et al.* Advances in Bioapplications of Carbon Nanotubes. *Advanced Materials* **21**, 139-152 (2009).
- 4 Prato, M., Kostarelos, K. & Bianco, A. Functionalized Carbon Nanotubes in Drug Design and Discovery. *Accounts of Chemical Research* **41**, 60-68 (2008).
- 5 Wenrong, Y., Pall, T., Gooding, J. J., Simon, P. R. & Filip, B. Carbon nanotubes for biological and biomedical applications. *Nanotechnology* **18** (2007).
- 6 Dai, H. Carbon Nanotubes: Synthesis, Integration, and Properties. *Acc. Chem. Res.* **35**, 1035-1044 (2002).
- 7 Balasubramanian, K. & Burghard, M. Chemically functionalized carbon nanotubes. *Small (Weinheim an der Bergstrasse, Germany)* **1**, 180-192 (2005).
- 8 Tasis, D., Tagmatarchis, N., Bianco, A. & Prato, M. Chemistry of Carbon Nanotubes. *Chemical Reviews* **106**, 1105-1136 (2006).
- 9 Chu, P. K., Chen, J. Y., Wang, L. P. & Huang, N. Plasma-surface modification of biomaterials. *Materials Science and Engineering: R: Reports* **36**, 143-206 (2002).
- 10 Francesch, L., Garreta, E., Balcells, M., Edelman, E. R. & Borrós, S. Fabrication of Bioactive Surfaces by Plasma Polymerization Techniques Using a Novel Acrylate-Derived Monomer. *Plasma Processes and Polymers* **2**, 605-611 (2005).
- 11 Förch, R., Zhang, Z. & Knoll, W. Soft Plasma Treated Surfaces: Tailoring of Structure and Properties for Biomaterial Applications. *Plasma Processes and Polymers* **2**, 351-372 (2005).
- 12 Francesch, L., Borros, S., Knoll, W. & Förch, R. Surface Reactivity of Pulsed-Plasma Polymerized Pentafluorophenyl Methacrylate (PFM) toward Amines and Proteins in Solution. *Langmuir* **23**, 3927-3931 (2007).
- 13 Duque, L. *et al.* Reactions of Plasma-Polymerised Pentafluorophenyl Methacrylate with Simple Amines. *Plasma Processes and Polymers* **7**, 915-925 (2010).
- 14 Horna, D. *et al.* Efficient cell reprogramming using bioengineered surfaces. *Advanced healthcare materials* **1**, 177-182, doi:10.1002/adhm.201200017 (2012).
- 15 Francesch, L. *Surface modification of polymers by plasma polymerization techniques for tissue engineering* Ph.D Thesis thesis, Ph.D Thesis - Universitat Ramon Llull, (2008).
- 16 Gupta, B., Plummer, C., Bisson, I., Frey, P. & Hilborn, J. Plasma-induced graft polymerization of acrylic acid onto poly(ethylene terephthalate) films: characterization and human smooth muscle cell growth on grafted films. *Biomaterials* **23**, 863-871 (2002).
- 17 Bech, L. *et al.* Double Plasma Treatment-Induced Graft Polymerization of Carbohydrated Monomers on Poly(ethylene terephthalate) Fibers. *Langmuir* **23**, 10348-10352 (2007).
- 18 Chua, S.-J., Ke, L., Kumar, R. S. & Zhang, K. Stabilization of electrode migration in polymer electroluminescent devices. *Applied Physics Letters* **81**, 1119 (2002).
- 19 Kato, K., Uchida, E., Kang, E.-T., Uyama, Y. & Ikada, Y. Polymer surface with graft chains. *Progress in Polymer Science* **28**, 209-259 (2003).
- 20 Lee, S.-D., Hsiue, G.-H., Chang, P. C.-T. & Kao, C.-Y. Plasma-induced grafted polymerization of acrylic acid and subsequent grafting of collagen onto polymer film as biomaterials. *Biomaterials* **17**, 1599-1608 (1996).
- 21 Zhao, B. & Brittain, W. J. Polymer brushes: surface-immobilized macromolecules. *Progress in Polymer Science* **25**, 677-710 (2000).
- 22 Hollen, J. R. & Bell, A. T. *Techniques and Applications of Plasma Chemistry*. (Wiley, 1974).
- 23 Collaud Coen, M., Dietler, G., Kasas, S. & GrVðning, P. AFM measurements of the topography and the roughness of ECR plasma treated polypropylene. *Applied Surface Science* **103**, 27-34 (1996).

- 24 Csucs, G., Michel, R., Lussi, J. W., Textor, M. & Danuser, G. Microcontact printing of novel co-polymers in combination with proteins for cell-biological applications. *Biomaterials* **24**, 1713-1720 (2003).
- 25 O'Shaughnessy, W. S., Marí-Buyé, N., Borrós, S. & Gleason, K. K. Initiated Chemical Vapor Deposition of a Surface-Modifiable Copolymer for Covalent Attachment and Patterning of Nucleophilic Ligands. *Macromolecular Rapid Communications* **28**, 1877-1882 (2007).
- 26 Rozkiewicz, D. I. *et al.* Covalent Microcontact Printing of Proteins for Cell Patterning. *Chemistry - A European Journal* **12**, 6290-6297 (2006).
- 27 Feiler, A. A., Sahlholm, A., Sandberg, T. & Caldwell, K. D. Adsorption and viscoelastic properties of fractionated mucin (BSM) and bovine serum albumin (BSA) studied with quartz crystal microbalance (QCM-D). *Journal of Colloid and Interface Science* **315**, 475-481 (2007).
- 28 Hemmersam, A. G., Foss, M., Chevallier, J. & Besenbacher, F. Adsorption of fibrinogen on tantalum oxide, titanium oxide and gold studied by the QCM-D technique. *Colloids and Surfaces B: Biointerfaces* **43**, 208-215 (2005).
- 29 Yin, Y. *et al.* Acetylene plasma coated surfaces for covalent immobilization of proteins. *Thin Solid Films* **517**, 5343-5346 (2009).
- 30 Santos, S. F., Zanette, D., Fischer, H. & Itri, R. A systematic study of bovine serum albumin (BSA) and sodium dodecyl sulfate (SDS) interactions by surface tension and small angle X-ray scattering. *Journal of Colloid and Interface Science* **262**, 400-408 (2003).
- 31 Fajjes, M., Pérez, X., Pérez, O. & Planas, A. Glycosynthase Activity of *Bacillus licheniformis* 1,3-1,4- β -Glucanase Mutants: Specificity, Kinetics, and Mechanism†. *Biochemistry* **42**, 13304-13318 (2003).
- 32 Viladot, J.-L., de Ramon, E., Durany, O. & Planas, A. Probing the Mechanism of *Bacillus* 1,3-1,4- β -d-Glucan 4-Glucanohydrolases by Chemical Rescue of Inactive Mutants at Catalytically Essential Residues†. *Biochemistry* **37**, 11332-11342 (1998).
- 33 Viñas, J. L. *et al.* Inhibitory action of Wnt target gene osteopontin on mitochondrial cytochrome c release determines renal ischemic resistance. *American Journal of Physiology - Renal Physiology* **299**, F234-F242 (2010).
- 34 Vinuesa, E. *et al.* Macrophage involvement in the kidney repair phase after ischaemia/reperfusion injury. *The Journal of Pathology* **214**, 104-113 (2008).
- 35 Bai, Y. *et al.* Surface Modification for Enhancing Antibody Binding on Polymer-Based Microfluidic Device for Enzyme-Linked Immunosorbent Assay. *Langmuir* **22**, 9458-9467 (2006).
- 36 Calderon, J. G. & Timmons, R. B. Surface Molecular Tailoring via Pulsed Plasma-Generated Acryloyl Chloride Polymers: Synthesis and Reactivity. *Macromolecules* **31**, 3216-3224 (1998).
- 37 d'Agostino, R. Plasma Deposition, Treatment and Etching of Polymer Films. *Academic Press: Boston, MA* (1990).
- 38 Han, L. M., Timmons, R. B. & Lee, W. W. Pulsed plasma polymerization of an aromatic perfluorocarbon monomer: Formation of low dielectric constant, high thermal stability films. *Journal of Vacuum Science & Technology B: Microelectronics and Nanometer Structures* **18**, 799 (2000).
- 39 Panchalingam, V., Chen, X., Savage, C. R., Timmons, R. B. & Eberhart., R. C. Molecular Tailoring of Surfaces via Pulsed RF Plasma Depositions. *Journal of Applied Polymer Science: Applied Polymer Symposium* **54**, 123-141 (1994).
- 40 Yasuda, H. & Hsu, T. Some aspects of plasma polymerization investigated by pulsed R.F. discharge. *Journal of Polymer Science: Polymer Chemistry Edition* **15**, 81-97 (1977).
- 41 Marí-Buyé, N. *et al.* Functionalized, Swellable Hydrogel Layers as a Platform for Cell Studies. *Advanced Functional Materials* **19**, 1276-1286 (2009).
- 42 Gong, J. *et al.* Micro- and Nanopatterning of Inorganic and Polymeric Substrates by Indentation Lithography. *Nano Letters* **10**, 2702-2708 (2010).
- 43 Bracher, P. J., Gupta, M. & Whitesides, G. M. Patterned paper as a template for the delivery of reactants in the fabrication of planar materials. *Soft Matter* **6**, 4303-4309 (2010).
- 44 Cvelbar, U., Pejovnik, S., Mozetič, M. & Zalar, A. Increased surface roughness by oxygen plasma treatment of graphite/polymer composite. *Applied Surface Science* **210**, 255-261 (2003).

- 45 Ha, S. W., Hauert, R., Ernst, K. H. & Wintermantel, E. Surface analysis of chemically-etched and plasma-treated polyetheretherketone (PEEK) for biomedical applications. *Surface and Coatings Technology* **96**, 293-299 (1997).
- 46 Song, B., Meng, L. H. & Huang, Y. D. Influence of plasma treatment time on plasma induced vapor phase grafting modification of PBO fiber surface. *Applied Surface Science* **258**, 5505-5510 (2012).
- 47 Rechendorff, K., Hovgaard, M. B., Foss, M., Zhdanov, V. P. & Besenbacher, F. Enhancement of Protein Adsorption Induced by Surface Roughness. *Langmuir* **22**, 10885-10888 (2006).
- 48 Ma, Z., Mao, Z. & Gao, C. Surface modification and property analysis of biomedical polymers used for tissue engineering. *Colloids and Surfaces B: Biointerfaces* **60**, 137-157 (2007).
- 49 Duque, L. *et al.* Reactions of Plasma-Polymerised Pentafluorophenyl Methacrylate with Simple Amines. *Plasma Processes and Polymers* **7**, 915-925 (2010).
- 50 Roach, P., Farrar, D. & Perry, C. C. Interpretation of Protein Adsorption: Surface-Induced Conformational Changes. *Journal of the American Chemical Society* **127**, 8168-8173 (2005).
- 51 Krajewska, B. Application of chitin- and chitosan-based materials for enzyme immobilizations: a review. *Enzyme and Microbial Technology* **35**, 126-139 (2004).
- 52 McLean, R. S. & Sauer, B. B. Tapping-Mode AFM Studies Using Phase Detection for Resolution of Nanophases in Segmented Polyurethanes and Other Block Copolymers. *Macromolecules* **30**, 8314-8317 (1997).
- 53 Pattani, V., Li, C., Desai, T. & Vu, T. Microcontact printing of quantum dot bioconjugate arrays for localized capture and detection of biomolecules. *Biomedical Microdevices* **10**, 367-374 (2008).
- 54 Roach, P., Eglin, D., Rohde, K. & Perry, C. C. Modern biomaterials: a review - bulk properties and implications of surface modifications. *Journal of Materials Science: Materials in Medicine* **18**, 1263-1277 (2007).
- 55 Walczyk, D., Bombelli, F. B., Monopoli, M. P., Lynch, I. & Dawson, K. A. What the Cell "Sees" in Bionanoscience. *Journal of the American Chemical Society* **132**, 5761-5768 (2010).
- 56 Kah, J. C. Y., Chen, J., Zubieta, A. & Hamad-Schifferli, K. Exploiting the Protein Corona around Gold Nanorods for Loading and Triggered Release. *ACS Nano* **6**, 6730-6740 (2012).
- 57 Mirshafiee, V., Mahmoudi, M., Lou, K. Y., Cheng, J. J. & Kraft, M. L. Protein corona significantly reduces active targeting yield. *Chemical Communications* **49**, 2557-2559 (2013).
- 58 Monopoli, M. P. *et al.* Physical-Chemical Aspects of Protein Corona: Relevance to in Vitro and in Vivo Biological Impacts of Nanoparticles. *Journal of the American Chemical Society* **133**, 2525-2534 (2011).
- 59 Yin, Y. *et al.* Acetylene plasma polymerized surfaces for covalent immobilization of dense bioactive protein monolayers. *Surface and Coatings Technology* **203**, 1310-1316 (2009).
- 60 Q-Sense. <http://www.q-sense.com/qcm-d-technology>, (Desembre 2010).
- 61 Dolatshahi-Pirouz, A. *et al.* Bovine serum albumin adsorption on nano-rough platinum surfaces studied by QCM-D. *Colloids and Surfaces B: Biointerfaces* **66**, 53-59 (2008).
- 62 Peng, Z. G., Hidajat, K. & Uddin, M. S. Conformational change of adsorbed and desorbed bovine serum albumin on nano-sized magnetic particles. *Colloids and Surfaces B: Biointerfaces* **33**, 15-21 (2004).
- 63 Carter, D. C. & Ho, J. X. *Advances in Protein Chemistry*. Vol. 45 (1994).
- 64 Höök, F. *et al.* Variations in Coupled Water, Viscoelastic Properties, and Film Thickness of a Mefp-1 Protein Film during Adsorption and Cross-Linking; A Quartz Crystal Microbalance with Dissipation Monitoring, Ellipsometry, and Surface Plasmon Resonance Study. *Analytical Chemistry* **73**, 5796-5804 (2001).
- 65 Hlady, V. & Buijs, J. Protein adsorption on solid surfaces. *Current Opinion in Biotechnology* **7**, 72-77 (1996).
- 66 Koutsopoulos, S., van der Oost, J. & Norde, W. Structural features of a hyperthermostable endo-beta-1,3-glucanase in solution and adsorbed on "invisible" particles. *Biophysical Journal* **88**, 467-474 (2005).
- 67 Planas, A. Bacterial 1,3-1,4-[beta]-glucanases: structure, function and protein engineering. *Biochimica et Biophysica Acta (BBA) - Protein Structure and Molecular Enzymology* **1543**, 361-382 (2000).

- 68 Mateo, C., Palomo, J. M., Fernandez-Lorente, G., Guisan, J. M. & Fernandez-Lafuente, R. Improvement of enzyme activity, stability and selectivity via immobilization techniques. *Enzyme and Microbial Technology* **40**, 1451-1463 (2007).
- 69 Goddard, J. M. & Hotchkiss, J. H. Polymer surface modification for the attachment of bioactive compounds. *Progress in Polymer Science* **32**, 698-725 (2007).
- 70 Farley, D. C. *et al.* Factors that influence VSV-G pseudotyping and transduction efficiency of lentiviral vectors, *in vitro* and *in vivo* implications. *The Journal of Gene Medicine* **9**, 345-356 (2007).
- 71 Stevenson, M. *et al.* Incorporation of a laminin-derived peptide (SIKVAV) on polymer-modified adenovirus permits tumor-specific targeting via $\alpha 6$ -integrins. *Cancer Gene Therapy* **14**, 335-345 (2007).
- 72 Bainbridge, J. W. B. *et al.* Effect of Gene Therapy on Visual Function in Leber's Congenital Amaurosis. *New England Journal of Medicine* **358**, 2231-2239 (2008).
- 73 Cavazzana-Calvo, M. *et al.* Gene Therapy of Human Severe Combined Immunodeficiency (SCID)-X1 Disease. *Science* **288**, 669-672 (2000).
- 74 Bengali, Z., Rea, J. C., Gibly, R. F. & Shea, L. D. Efficacy of immobilized polyplexes and lipoplexes for substrate-mediated gene delivery. *Biotechnology and Bioengineering* **102**, 1679-1691 (2009).
- 75 Mei, L., Jin, X., Song, C., Wang, M. & Levy, R. J. Immobilization of gene vectors on polyurethane surfaces using a monoclonal antibody for localized gene delivery. *The Journal of Gene Medicine* **8**, 690-698 (2006).
- 76 Wang, C.-H. K., Jiang, S. & Pun, S. H. Localized Cell Uptake of His-Tagged Polyplexes Immobilized on NTA Self-Assembled Monolayers. *Langmuir* **26**, 15445-15452 (2010).
- 77 Dunn, C. A. *et al.* BMP gene delivery for alveolar bone engineering at dental implant defects. *Molecular Therapy* **11**, 294-299 (2005).
- 78 Fishbein, I. *et al.* Local Delivery of Gene Vectors From Bare-Metal Stents by Use of a Biodegradable Synthetic Complex Inhibits In-Stent Restenosis in Rat Carotid Arteries. *Circulation* **117**, 2096-2103 (2008).
- 79 Wang, C.-H. K. & Pun, S. H. Substrate-mediated nucleic acid delivery from self-assembled monolayers. *Trends in Biotechnology* **29**, 119-126 (2011).

Chapter III.

Modification of Carbon Nanotubes by PECVD for Gene Delivery Vectors

Originally published as:

A. Cifuentes-Rius, A. de Pablo, V. Ramos-Perez, S. Borrós, *Plasma Processes and Polymers*, **2013** (submitted)

V. Ramos-Perez, A. Cifuentes, N. Coronas, A. de Pablo, S. Borrós. In: K. Hamad-Schifferli, P. Bergese, *Nanomaterial Interfaces in Biology: Methods and Protocols*, **2013**. Boston: Springer. 302

3.1. Introduction

The previous chapter (Chapter II) has shown the complete study of both PECVD and plasma grafting techniques as interesting methodologies for preparing ultrathin films of PFM to obtain smart, bioactive surfaces. The development of microparticles with enzymatic activity and fabrication of cell reprogramming surfaces proved the versatility of the plasma grafting approach together with its applicability to gene delivery applications. On the other hand, the ppPFM thin film deposition by PECVD showed higher efficiency rates of immobilization. Large amounts of active sites are required for the attachment of the DNA or an intermediate linker capable to specifically load and release the desired genetic material. Therefore, the modification by PECVD appears to be more suitable for the functionalization of carbon nanotubes.

As it has been introduced in Chapter I and Chapter II, despite promising advantages, the use of carbon nanotubes (CNTs) for biomedical applications is limited due to their low biocompatibility.¹⁻³ Naïve carbon nanotubes present highly hydrophobic surfaces, which result in poor water solubility and dispersibility, making them unsuitable for biological applications. To improve the biocompatibility of carbon nanotubes, surface modification or functionalization is required to afford solubility in aqueous solutions.^{4,5} Modification of CNTs may be performed by covalent and non-covalent methods.^{1,6,7} Covalent functionalization exploits the chemical reactivity of CNTs to form bonds between the CNT surface and a hydrophilic moiety. Covalent bonding of modifying moieties having hydrophilic groups in their structure results in increased water solubility of modified CNTs. In contrast, non-covalent modification techniques are based on hydrophobic interactions between the CNT surface and the hydrophobic region of an amphiphilic moiety. CNT wrapping with multiple amphiphilic moieties having surfactant-like activity results in solubilization of CNTs in aqueous media.^{1,8-12} Both techniques provide efficient CNT modification strategies for biological applications, resulting in increased biocompatibility and reduced toxicity, as will be discussed in Chapter IV. In any case, it is clear that by adjusting the surface modification of CNTs it is possible to tailor their capability to bind genetic material and use their ability to cross the cellular membrane to transfect the genetic material to the cell.^{13,14}

However, covalent functionalization results more attractive due to its more controlled procedure, allowing the formation of surfaces with a higher degree of specificity and greater tunable properties.^{15,16} Among all the approaches to covalently modify CNTs surface described in other works, most of all involve multi step reactions and rather harsh conditions to achieve the desired

functional group, which may damage the sidewalls or tips of the CNTs, as commented in Chapter II.^{6,15} Plasma polymerization has been proved to be a relatively simple, fast and dry method for the modification of different surfaces without affecting the mechanical properties of the bulk material.¹⁷⁻¹⁹ It is basically used to control the surface chemistry of the desired material, originally developed to modify polymers surfaces, providing homogeneous reactive coatings with a high degree of specificity for the immobilization of molecules.²⁰⁻²² In the recent years, it has been also used for the chemical modification of more sophisticated materials such as hydroxyapatite powder, metal nanoparticles, carbon nanofibers and also nanotubes due to all the advantages that this technique offers.^{23,24} By this method, the carbon nanotube surface can be also tuned in order to improve wettability, dispersibility, stability and biocompatibility, altogether with the retention of its structural integrity.¹⁸

Plasma treatment can be used whether to previously activate the surface before the polymerization is carried out or to directly polymerize the desired monomer present in the reactor chamber by effect of the RF glow-discharge. In the last decade, plenty of plasma polymerization on CNTs studies have been carried out. These are mainly focused on applications involving electronic sensors, where this technique is used to increase the interaction and improve the final properties of composite materials by coating them with different types of polymers.^{25,26} However, few investigations have been done where the final application of the treated CNTs is in a biological system.^{18,27,28}

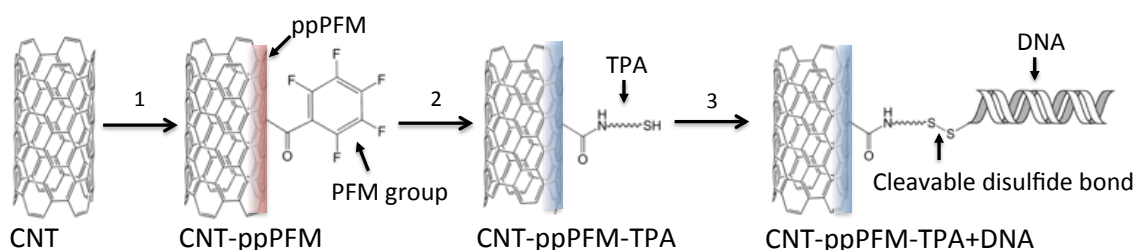
From this reduced group, there are still some drawbacks that need to be addressed. In some studies performed by Vohrer *et al.*, the hydrophilization of CNT sheets (called bucky papers) by plasma treatment with different non-polymerizable monomer gases including their possible post-reactions.²⁸ They achieved a gentle oxidation of the CNTs when treating them with N₂ gas in a symmetrical reactor consisting of two plane parallel electrodes followed by an oxidation post-treatment with an oxygen flow. Their treated CNTs showed a high increase in solubility reducing the 150° in water contact angle of the unmodified bucky papers to 10° for the oxidized ones. With this treatment, they ensured no alteration of their morphology. Nonetheless, their X-ray photoelectron spectroscopy (XPS) results revealed a constant decrease in the oxidation degree of the CNTs over time, eventually losing the functionality achieved. This phenomenon may have a negative effect regarding the application where these nanoparticles have to be used. On the other hand, Chen *et al.* used the polymerization of two types of monomers, acetaldehyde and ethylenediamine, in order to permanently immobilize different types of polysaccharides and thus provide highly hydrated coatings to the CNT surface.¹⁸ Firstly, they successfully proved to modify their as-synthesized aligned CNT film on both an amorphous carbon layer or directly grown on a silicon wafer with acetaldehyde and ethylenediamine by a RF glow discharge plasma treatment and in a home-built plasma reactor.

After plasma activation of the individual CNT surface, they were able to immobilize Amino-Dextran and Periodate-Oxidized Dextran chains through a Schiff-base formation, followed by reductive stabilization of the Schiff-base linkage with sodium cyanoborohydride. Although this approach allowed the formation of highly hydrophilic and soluble CNTs without significant changes in the nanotube's structure integrity, it still involved complicated and cost effective multi-step reactions before the desired properties of the CNTs were achieved. Regardless, this study showed how plasma polymerization results in a promising technique to homogeneously modify the CNT surface. This statement was confirmed in a work of Ávila-Orta *et al.*, where thin PPEG (plasma polyethylenglycol) layers (1-3 nm thick) were deposited on CNTs.²⁷ They used sensitive techniques such as high-resolution transmission electron microscopy (HRTEM) and Fourier-transform infrared spectroscopy (FTIR) to study their polymer films. Moreover, they proved that this plasma coating provided the needed hydrophilicity in order to disperse the modified nanotubes in water, methanol and ethylene glycol, maintaining the dispersion stable with time. Even if these PPEG-modified CNTs might be an effective solution to disperse CNTs for all kind of applications, to use them in cell biology and especially for cell transfection a specific functionalization on the CNT surface may be required. Therefore, the deposition of a polymer coating that can provide chemical reactive sites for the specific anchoring of active molecules may become highly promising.^{21,22} This type of functionalization can be achieved by the ppPFM polymerization by PECVD, as demonstrated in Chapter II.

Additionally, the versatility of the PECVD polymerization allows the deposition of a wide variety of monomers, which provide different chemical surface properties.²⁹ Therefore the polymerization of allylamine (AA) by this technique is also studied in this chapter. This monomer is especially interesting given its ability to polymerize forming a polymer layer (pAA) with exposed primary amines on the surface. Such amino groups are protonated when subjected to aqueous buffer, especially at pH around 5.5, giving rise to a positively charged surface.³⁰⁻³² These types of modified surfaces are presented as successful devices to condensate nucleic acids in high ratios through the ionic interaction between the negatively charged phosphate backbone of the DNA and the protonated amines from the surface. Concurrently, Abou Rich *et al.* proved the successfully pAA coating by plasma on CNT surfaces but the effectiveness of these modified particles to condensate DNA and thus be used as gene delivery vectors is still unknown.²⁶

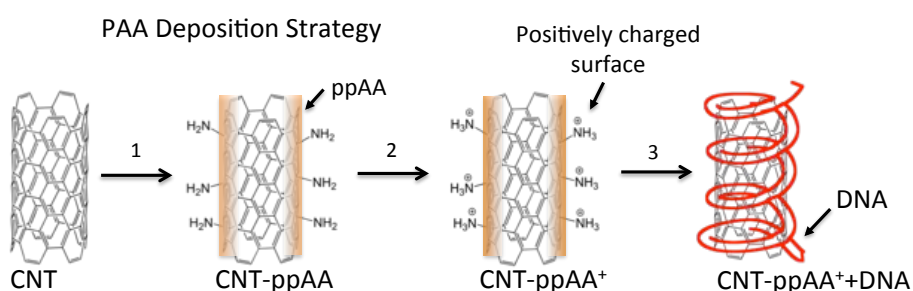
In this work we aim to prove how the functionalization of carbon nanotubes can be achieved by PECVD, leading to a highly reactive surface able to form efficient complexes with genetic material. To do so, two strategies are presented. First, we test the immobilization of the nucleic acid *via* a

covalent bond through a polyethylene glycol (PEG) linker. This approach consists in the covalent anchoring of a thiol-PEG-amine (TPA) through the PFM moieties of the ppPFM coating (Scheme 3.1). The TPA chemical linker is thought not only to carry the genetic material of interest *via* a disulfide bond but also may improve the dispersibility of the functionalized CNTs, since PEG based molecules are established macromolecules with high dispersing properties in water based media.³³ Moreover, the thiol group at the end of the molecule allows the specific reaction with a thiol-terminated DNA, which will promote cleavage-release upon entering the reductive cell environment.³⁴



Scheme 3.1. Formation of CNT-based gene delivery vector *via* ppPFM polymerization. The strategy of the reaction follows: (1) deposition of the ppPFM, (2) anchoring of TPA through its amine group and (3) immobilization of DNA *via* a disulfide bond.

Secondly, it is known DNA can be adsorbed around the CNT surface, wrapping its structure.³⁵⁻³⁹ This adsorption can be enhanced by the electrostatic interaction between the negative phosphate groups present in the DNA structure and the positively charged surface of the CNTs. Hence, in this part of the thesis, we explore this wrapping capacity of the DNA on the modified-CNTs with PECVD-polymerized AA (ppAA). Plasma conditions are firstly optimized to achieve the successful ppAA deposition on the CNT surface (CNT-ppAA) in order to yield a positively charged surface able to interact with the DNA of interest (Scheme 3.2). Moreover, good dispersion rates are expected due to the electrostatic repulsion created between particles.⁴⁰



Scheme 3.2. Obtaining the ppAA-modified CNT-mediated transfection vector. The procedure follows: (1) ppAA disposition, (2) subsequent amine groups protonation at pH 5 and (3) final DNA condensation.

3.2. Experimental Section

3.2.1. Employed Carbon Nanotubes (CNTs)

Multi-walled Carbon Nanotubes (MWNTs) used in this work were purchased from Sigma-Aldrich and were obtained by a Chemical Vapor Deposition (CVD) method. These had a length of 5-9 μm and a diameter of 110-170 nm. This type of CNT was denominated as rigid CNT (rCNT), as it will be explained in Chapter IV.

3.2.2. Surface Modification of CNTs by PECVD

Plasma Reactor and Polymerization

For the plasma modification of carbon nanotubes with both ppPFM and ppAA, the same general protocol was followed. First, the desired quantity of rCNT powder was placed on a 35 mm PS plate (BD, Franklin Lakes, NJ, USA; PSp), maximizing the surface of the rCNT exposed. Then, the capsule was placed inside the plasma reactor chamber underneath the copper coil (Scheme 2.4). The reactor was closed and the vacuum pump was slowly opened until the base pressure reached 0.02-0.03 mbar. A round flask containing the desired monomer (PFM or AA) was connected to one of the entrance connections and was protected from light. At the same time, the cold trap was activated adding a mixture of dry ice and acetone ($-78\text{ }^{\circ}\text{C}$). The monomer of interest was introduced into the chamber opening the needle valve, which connected the flask with the reactor. The entrance of gas was allowed for 15 min to ensure that there was no air inside the balloon and only monomer vapor entered the reactor avoiding any further contamination of the resulting film. Pink colored plasma around the copper coil was generated after the RF generator was connected at an input power (W_i) of 15 W and with a duty cycle (DC) of 10/20. The polymerization process varied in function of the monomer used and after that time, the plasma was turned off. The entrance of gas was kept for another 15 min to assure a complete reaction of the vapor with both the remaining active sites generated on the rCNTs surface and the already formed polymer. In order to achieve a homogeneous modification along the entire rCNT surface, this procedure was carried out 3 times, gently mixing the rCNTs on the PSp in between. Silicon wafers were used as a control on each batch of the rCNTs polymerization for further use in the characterization of the modification.

PFM Deposition Conditions

PFM polymerization on rCNTs surface was performed as previously described and the conditions used are summarized in Table 3.1. The flask containing the PFM monomer (Apollo Scientific) was heated at 45 °C in order to facilitate the generation of the vapor and subsequent entrance to the reaction chamber. The type of modified substrate (rCNTs in a powder form) required that the procedure had to be repeated 3 times. Therefore, different durations (t_{PECVD}) of a single polymerization step were analyzed in order to guarantee a proper ppPFM reactive film.

Table 3.1. Plasma conditions used for the ppPFM deposition on CNTs.

Sample ID	DC (W/W)	W_i (W)	W_{eq} (W)	t_{PECVD} (min)	t_{total} (min)
rCNT-ppPFM-1	10/20	15	7.5	1	3
rCNT-ppPFM-3	10/20	15	7.5	3	9
rCNT-ppPFM-5	10/20	15	7.5	5	15
rCNT-ppPFM-10	10/20	15	7.5	10	30

ppAA Coating Specifications

To obtain amines as a chemical functionality on the rCNT surface, the monomer allylamine (Sigma, 98% purity; AA) was used. AA vapor was entered to the reactor chamber without heating and the polymerization time for each batch was set at 5 min (Table 3.2).

Table 3.2. PECVD conditions applied for the ppAA deposition on CNTs.

Sample ID	DC (W/W)	W_i (W)	W_{eq} (W)	t_{PECVD} (min)	t_{total} (min)
rCNT-ppAA	10/20	15	7.5	5	15

3.2.3. Characterization of the Modified CNTs

Water Contact Angle (WCA)

All treated rCNTs (ppPFM and ppAA) were modified together with a silicon wafer used as a control of the polymerization process, which was immediately analyzed after plasma treatment. The consequently polymerized wafer at same conditions as the rCNTs was analyzed by WCA (DSA100

Krüss) and therefore the quality, nature and homogeneity of the coating were determined. The same procedure was done for a bare silicon wafer used as a reference.

High Resolution Transmission Electron Microscopy (HRTEM)

Both ppPFM-modified and unmodified carbon nanotubes were characterized by HRTEM (JEOL LTD. 200 KV) equipped with an energy dispersive X-Ray spectroscopy detector (Oxford LINCA, EDS) and the analysis was performed at the *Servei de Micròscopia de la Universitat Autònoma de Barcelona*. It was able to produce high-resolution images by applying an electron beam on the studied substrates and give quantitative information about the chemical composition of the analyzed sample. The obtained data allowed the evaluation of size (length and diameter), morphology and surface chemistry of the rCNTs before and after PFM polymerization. Samples were dissolved in ethanol in order to ensure rapid evaporation of the solvent when a drop of CNT solution was deposited on the holy carbon cooper grid (Gilder Grids). The concentration used for all samples was around 10 µg/mL.

X-Ray Photoelectron Spectroscopy (XPS)

ppPFM-polymerized rCNT samples were analyzed by XPS (PHI-ESCA-5500) at the *Servei Científicotècnic de la Universitat de Barcelona* (SCT) in order to obtain detailed information about the chemistry of the polymer layer. Deconvolution of the carbon signal was carried out to identify the main chemical bonds present in the formed polymer structure. Naïve rCNTs were also characterized by this technique as a control and results for both samples were plotted together.

Fourier Transform Infrared Spectroscopy (FTIR)

Retention of the ppAA functionality during plasma polymerization was carried out by FTIR (Nicolet iS10) from the *Grup d'Enginyeria Molecular* (GEM) at IQS. Silicon wafers polymerized together with the rCNTs were analyzed by this technique, giving the spectrum corresponding to the polymer thin film obtained on the surface. Such characterization allowed the determination of the chemical structure of the deposited layer. A baseline was obtained from the analysis of a bare silicon wafer.

Dynamic Light Scattering (DLS) and Zeta Potential Analysis

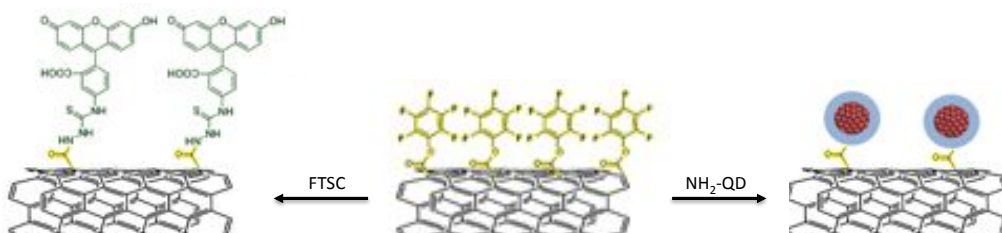
Size and zeta potential measures were carried out with a Zetasizer Nano ZS (Malvern Instruments). rCNTs, rCNT-ppPFM and rCNT-ppAA solutions of approximately 10 µg/mL were prepared in Milli-Q

water and 25 mM sodium acetate buffer (Merk Millipore; NaOAc) at pH 5 for the latter. Samples were dispersed in an ultrasonic bath for 15 min prior to the analysis.

3.2.4. Reactivity of the ppPFM-coated rCNTs

Fluorescent Decoration

The immobilization of FTSC as used in Chapter II (Scheme 2.6) and Quantum Dots (Qdot® 655 ITK™ Amino (PEG), Life Technologies; QDs) was tested (Scheme 3.3). FTSC and QDs were dissolved in water at concentration of 0.5 mM and 16 nM, respectively, and were subsequently mixed with the ppPFM-coated rCNTs (approximately 2 mg of CNTs per batch were used). Samples were first dispersed in an ultrasonic bath for 15 min and left in gentle agitation for another 15 min. After the reaction was complete, both fluorescent rCNTs (F-rCNT) were centrifuged at 16200 rcf for 5 min and redissolved in Milli-Q water. This washing procedure was carried out twice to ensure the total removal of unbound fluorescent dye. Final concentration of the complexes was around 1 mg/mL. During the whole process, samples were protected from light. Final F-rCNTs were stored protected from light until further use. To verify that the functionalization had been successful, F-rCNTs were diluted 100 times in Milli-Q water and were analyzed by fluorescence microscopy (AxioVs40 Zeiss Imaging Solutions). Additionally, HRTEM was employed to image the QDs-functionalized rCNTs.



Scheme 3.3. Fluorescently-labeled rCNTs (F-rCNTs). Fluorescent complexes obtained by the covalent immobilization of FTSC or QDs *via* the PFM reaction.

Anchoring of a Thiol-PEG-Amine (TPA)

For the chemical linker immobilization on the rCNT-ppPFM surface, a 3 mg/mL solution of TPA (PEG Creative Works, 1 kDa) in Milli-Q water was prepared. Immediately, a constant flow of was bubbled into the solution avoiding the oxidation of the free thiol group. Subsequently, ppPFM-modified rCNTs were added to the solution obtaining a final concentration of 1 mg/mL. Samples were

sonicated for 10 min and were left at room temperature and gentle agitation for 15 minutes more. Again, the now TPA-functionalized rCNTs were washed 3 times by centrifugation (16200 rcf, 5 min), dissolving in Milli-Q water each time. rCNT-ppPFM-TPA were finally dried under vacuum overnight and characterized by XPS.

3.2.5. Cell Viability of the Decorated-rCNTs

To study the cellular uptake and cell viability of the decorated particles, macrophages RAW 264.7 (ATCC) were employed and the study was performed at the tissue culture (TC) facilities of the IiB. In a 6-well plate, 40,000 cells per well were plated and grown overnight at 37 °C and 5% CO₂ in supplemented medium. The medium was formed by DMEM/F-12 high glucose 4.500 mg/L (GLUTAMAX™), 1% penicillin streptomycin (Invitrogen; P/S) and 10% of fetal bovine serum (Gibco®; FBS). After 24 h, F-CNTs were dissolved in sterile PBS 1x (Dulbecco's, PAA Laboratories) at a final concentration of 1 mg/mL. The solution was dispersed in an ultrasonic bath for 15 min followed by 3 sonication cycles of 15 pulses with an ultrasonic probe (Sonics Vibra-Cell) at 130 W and 20 kHz. The resulting dispersed solution was dissolved in supplemented medium in order to achieve a final F-rCNT concentration of 50 µg/mL and, after washing the cells with PBS 1x, the new medium containing the decorated particles was added. After 12 h of incubation at 37 °C and 5% CO₂, cells were washed with PBS 1x, fresh media was added and were analyzed in the fluorescent microscope (Leica UK Ltd, Milton Keynes, UK).

3.2.6. Dispersibility Studies of the ppPFM-modified rCNTs

The dispersibility of 1 mg/mL of rCNT-ppPFM in different solvents varying polarity were evaluated and plotted following the Hansen parameters (Table 3.3).⁴¹

Table 3.3. Solvents used for the dispersibility studies.(ordered by growing dielectric constant)

Solvent	Type	ε
Toluene	Non-polar aprotic	2.38
Diethyl ether	Non-polar aprotic	4.34
Ethyl acetate	Non-polar aprotic	6.02
Dichloromethane	Non-polar aprotic	8.09
Ethanol	Protic	24.30
Acetonitrile	Polar aprotic	36.02
Water	Protic	78.05

Furthermore, the aggregation in solution of the rCNTs modified with ppPFM compared to the non-modified in ethanol (Sigma) was studied in the microscope. Solutions of 10 $\mu\text{g}/\text{mL}$ were prepared, dispersed in an ultrasonic bath for 15 min and deposited in glass slide. The aggregates size and morphology formed after covering the sample with a coverslip were determined.

3.2.7. Cell Transfection Studies of the DNA Vectors

Formation and Characterization of the Complex

rCNT-ppAA systems were complexed with a reporter gen (3300 base pair) encoding the production of green fluorescent protein (GFP), which can be easily determined by the fluorescent microscope. The plasmid (pGFP) was expressed, isolated and purified using the PureLink[®] HiPure Plasmid Miniprep Kit (Life Technologies) according to the manufacturer's instructions. After the polymerization of ppAA on the rCNT surface, the freshly modified rCNTs were dissolved in 25 mM acetated buffer ensuring pH 5 that would lead to the protonation of the amines. Different ratios (w/w) of ppAA-modified rCNTs and pGFP (from 1:1 to 200:1) at a fixed quantity of plasmid were prepared and incubated for 1 h at 37 °C. The complexation ratio was analyzed by agarose gel electrophoresis. Agarose (Sigma) was dissolved at 0.8% in TAE (Tris-acetate-EDTA) buffer 1x and 6 μL of ethidium bromide. TAE buffer was prepared from mixing 2.42 g of Trizma[®] base, 0.57 mL of acetic acid, 0.185 g of EDTA (ethylenediaminetetraacetic acid) and 500 mL of Milli-Q water. All TAE reagents were purchased from Sigma-Aldrich. The gel was loaded with the different complexes and was run at 65 V for 1 h. After that time, the resulting gel was imaged.

Cell Transfection with the rCNT-ppAA+pGFP Vectors

Macrophages RAW 264.7 were prepared as described before (3.2.5). After 24 h, pGFP was condensed on the rCNT-ppAA at the ratio of study, and incubated for 1 h at 37 °C. The resulting complexes were diluted in complete medium achieving a final concentration of rCNTs around 50 $\mu\text{g}/\text{mL}$, which was added to the wells. After the incubation of the complexes with the macrophages for 12 h, cells were washed with PBS 1x and fresh media was added. Cells were left at 37 °C and 5% CO_2 for 48 h more, when they were analyzed in a fluorescent microscope (Leica UK Ltd, Milton Keynes, UK).

3.3. Results and Discussion

3.3.1. PECVD Modification of rCNTs with ppPFM

Optimization of the Plasma Polymerization Time

The initial part of this chapter aims to achieve a homogeneous and reactive ppPFM thin film on the rCNT surface by PECVD. As previously described and confirmed before (Chapter II), PFM can be polymerized on a substrate by plasma techniques. The reactivity of the resulting ppPFM-modified surface is enhanced with the higher retention of the PFM functionality.^{21,42} Hence, the greater amounts of PFM moieties exposed to the surface lead to an increase of the hydrophobic behavior of the obtained surface. As a result, WCA is able to track the ppPFM deposited film.

Although the polymerization of the rCNTs was carried out 3 times in order to guarantee a homogeneous modification along the rCNT surface, it was expected that some areas would be more exposed to the effect of the polymerization than others. Therefore, the duration of each polymerization batch becomes a crucial parameter to be adjusted in order to obtain a final thin film with the desired properties. For this reason, the resulting layer of 3-times polymerized silicon wafers varying the pulsed plasma duration for each polymerization was analyzed (Figure 3.1).

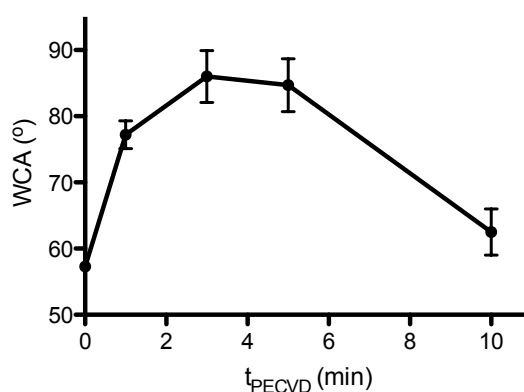


Figure 3.1. WCA of the resulting ppPFM film depending on the polymerization time (t_{PECVD}). The polymerization was carried out 3 times on a silicon wafer as done for the rCNTs and the total time (t_{total}) was considered as the aggregate of these 3 polymerization as shown in Table 3.1.

Results in Figure 3.1 show the hydrophobicity of the resulting ppPFM coatings when each polymerization step was done for 1 to 10 min (t_{PECVD}) and was repeated 3 times. It can be seen that

after 1 min of polymerization (3 min in total) was not enough to achieve the desired PFM group retention. The measured $77.2^\circ \pm 2.1^\circ$ were still far from the $80-90^\circ$ expected for the highly reactive ppPFM thin films studied before (Chapter II). However, when each polymerization procedure lasted between 3 or 5 minutes, the hydrophobicity was increased, reaching the desired values for this kind of coatings ($86.0^\circ \pm 3.9^\circ$ and $84.7^\circ \pm 4.0^\circ$, respectively). Moreover, it was proved that despite being exposed to a total time of polymerization (t_{total}) of between 9 and 15 min, the quality of the reactive layer was maintained. Nevertheless, for larger polymerization times, the chances of side reactions, etching effects and polymer film degradation are increased, which would lead to the formation of poorly reactive coatings. This was confirmed with the decrease of the WCA ($63.5^\circ \pm 3.5^\circ$) when the polymerization was carried out for 10 min (30 min total time).

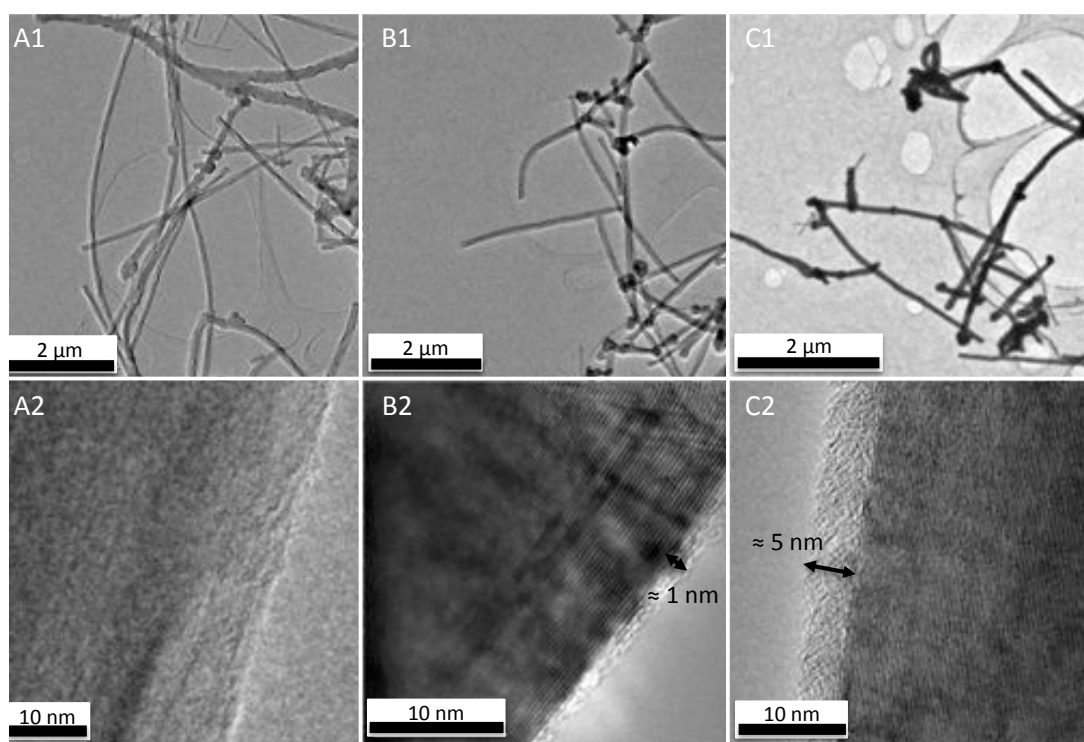


Figure 3.2. HRTEM images of the rCNT-ppPFM systems. Pictures corresponding to (A) naïve rCNTs and the polymerized for (B) 3 min and (C) 5 min. (1) First row of images prove that the structural properties of the modified CNTs (B1 and C1) remains unaltered as the bare rCNTs (A1). (2) Second row of images show a magnification of an individual rCNT, where the ppPFM thin film is confirmed in the rCNTs polymerized for (B2) 3 min and (C2) 5 min if compared to (A2) the bare rCNTs.

Apparently, ppPFM films obtained after polymerization times from 3 to 5 min (rCNT-ppPFM-3 and rCNT-ppPFM-5, respectively) seemed to have a similar behavior and thus both periods of time were used for the modification of rCNTs. The resulting complexes were characterized by HRTEM and

summarized in Figure 3.2. These images suggest that the bulk properties regarding shape of the rCNTs remain unaltered after plasma modification for 3 and 5 min. Any remarkable damage is observed neither on the rCNT surface nor on the tips. Therefore, sufficiently mild conditions are applied when pulsed plasma polymerization is carried out in order to preserve the rCNT morphology. The same size consistency is observed in terms of diameters and lengths of the different types of rCNTs measured from the TEM images (Figure 3.3). However, all samples exhibit a certain degree of polydispersity, given the fact that the rCNT synthesis process by chemical vapor deposition (CVD) does not allow an accurate control of the final obtained size and the number of carbon layers formed.⁴³⁻⁴⁵

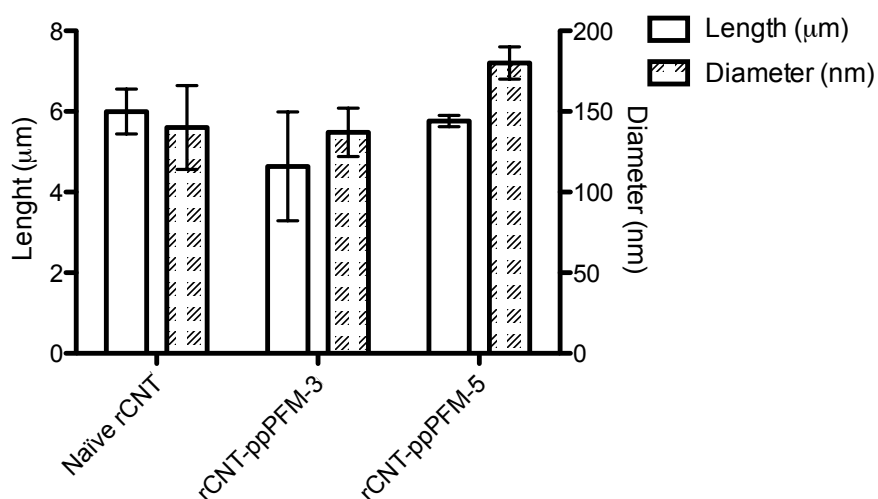


Figure 3.3. Length and diameter of the rCNT-ppPFM complexes. The error bar (standard deviation) is obtained by measuring 5 to 10 different nanotubes from different TEM images.

If an individual rCNT of each type is zoomed in (Figure 3.2A2, B2 and C2), two different regions can be observed. On one hand, the rCNT surface, which offers a higher contrast due to the larger number of stacked carbon films and allow the distinction of different atomic layers (2.5 \AA) that forms it. On the other hand, right in the interface of the rCNT surface, a less contrasted zone with an amorphous structure is noticed, corresponding to the ppPFM thin film. The formed ppPFM is observed along the rCNT, homogeneously covering the surface exposed to plasma. Moreover, different thickness was measured for the samples modified for 3 min and the ones polymerized for 5 min. Thickness for the 3 min treated samples was typically around 1 nm whereas for polymerizations carried out for 5 min, thickness varied from 4 to 6 nm. Therefore, the formation of the ppPFM on the rCNTs is sustained and it is evidenced that the polymerization time had a direct effect on the deposited thickness layer.

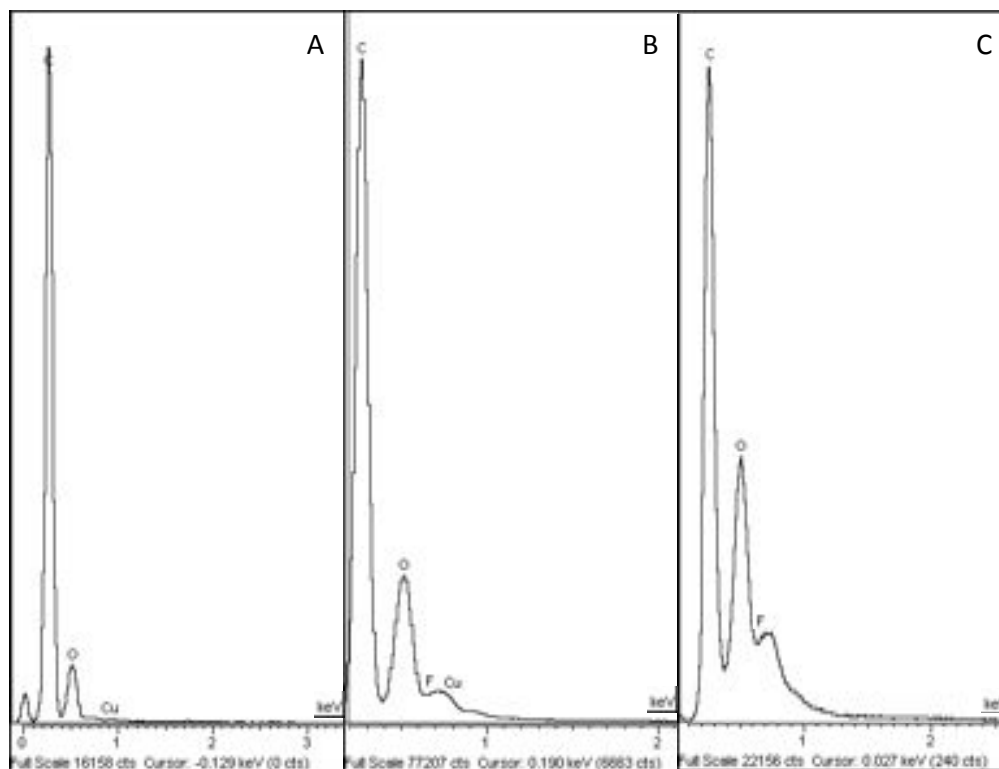


Figure 3.4. X-Ray microanalysis of the HRTEM-imaged rCNT-ppPFM. Results of (A) naïve rCNTs and rCNTs polymerized for (B) 3 min and (C) 5 min. Signal was measured as intensity (cps) vs. energy (eV).

An X-Ray microanalysis of the studied samples was performed allowing the calculation of the relative atomic percentage present (Figure 3.4 and Table 3.4, respectively). These results demonstrated that at higher plasma exposition times, the relative amount of oxygen increased, probably due to small quantities of oxygen present in the reactor during the PFM polymerization. This remaining oxygen can react with the rCNTs forming a heterogeneous mix of chemical functionalities on the surface, such as hydroxyl, peroxide or carboxylic groups.^{19,28}

Table 3.4. Atomic percentages of the TEM-analyzed samples.

Sample ID	%C	%O	%Cu	%F
Naïve rCNT	93.03	4.62	2.35	-
rCNT-ppPFM-3	88.35	10.91	0.94	*
rCNT-ppPFM-5	63.61	15.68	-	0.71

* Value below the quantification limit

In the sample treated for 3 min (rCNT-ppPFM-3), a weak signal of fluorine (characteristic signal of the PFM) was detected, in spite of being overlapped by the copper signal corresponding to the grid

where the sample was placed. The fluorine content was not enough to be determined by this technique because the quantification limit of the detector is 0.1% and the large presence of carbon complicated its quantification. However, when the polymerization was carried out for 5 min (rCNT-ppPFM-5), a 0.71% of fluorine was detected meaning that a higher covering of the surface was achieved, in accordance with the thickness observed on the HRTEM images.

This study corroborates the formation of a stable and homogeneous ppPFM thin film with a high density of reactive groups when rCNTs are polymerized for 5 min (15 min in total). As a result, these conditions were set for the further analysis carried out.

Thereby, the chemistry of the ppPFM thin film deposited on the rCNT surface for the polymerization time of 5 min was deeply analyzed by XPS (Figure 3.5). The wide scan spectra obtained for both the naïve and the rCNT-ppPFM are shown in Figure 3.5A. Results revealed the presence of carbon and oxygen for both samples, and fluorine and nitrogen were found only on the modified with ppPFM (Figure 3.5B). When considering the atomic percentages calculated and the O/C ratio (Table 3.5), nearly 4 times more of oxygen intensity was detected, together with the appearance of nitrogen. The reasons have already been commented, indicating the presence of air in the reaction chamber, which give rise to the oxygenated functionalities.^{19,28} A reaction between the film and the oxygen and water molecules desorbed from the walls of the plasma vessel, during and after the polymerization, may have also contributed to the composition of the coating.^{46,47}

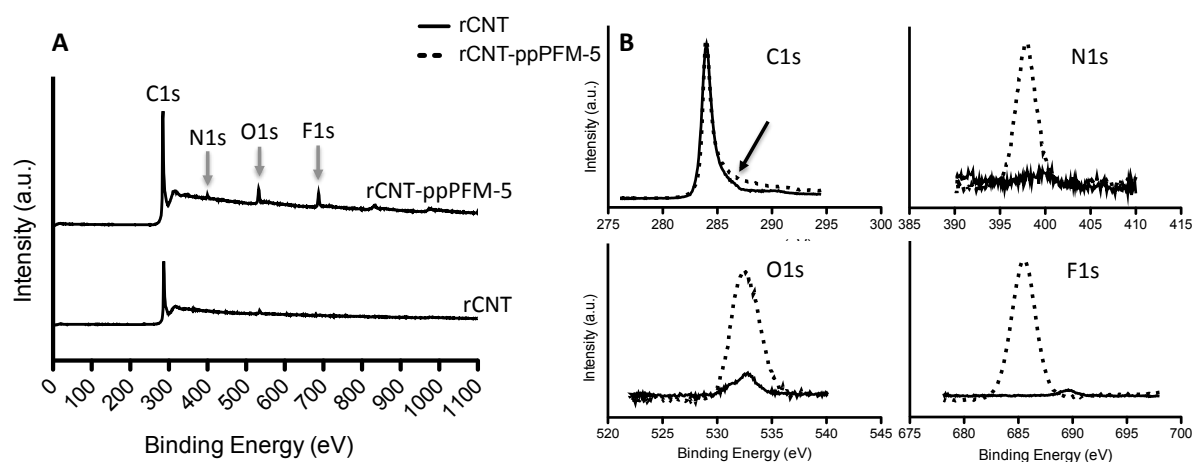


Figure 3.5. XPS of the ppPFM-modified rCNTs. (A) XPS wide spectra of the bare rCNTs and the rCNT-ppPFM and (B) comparison of the modified sample with the control on each atomic signal detected (carbon, oxygen, nitrogen and fluorine). The arrow on C1s plot shows the profile difference between samples, marking the modest shoulder appeared on the ppPFM-modified rCNTs.

Table 3.5. Atomic percentage of rCNTs and rCNT-ppPFM and the normalized oxygen ratio for both samples.

Data obtained from the XPS analysis.

Sample ID	Atomic Percentage				Ratio
	%C	%O	%N	%F	O/C
rCNT	98.5	1.7	-	-	0.02
rCNT-ppPFM-5	86.8	6.3	0.7	6.0	0.07

The presence of fluorine on the ppPFM-modified sample (6%) confirmed the deposition of the fluorinated polymer. Additionally, if the carbon signal was looked in detail (Figure 3.5B), a main peak with the maximum intensity was observed at 284 eV for both samples. However, a little shoulder between 285 and 290 eV was noticed on the modified sample that was not present on the bare rCNTs. This principal peak at 284 eV, which was the only one observed on the unmodified rCNTs, corresponds to the C-H/C-C and is typically present in rCNT structures.⁴⁸ To determine the nature of the other carbon bonds existing in the ppPFM-modified samples, the C1s core level signals were fitted on different functionalities containing oxygen and fluorine (Figure 3.6). Nitrogen functionalities were not considered, since nitrogen was found only in limited amounts at the surface coating (0.7%). The spectrum was fit with other four signals apart from the C-C/C-H that was set at 284 eV. The α -ester carbon ($\underline{\text{C}}\text{-COO}$) and the carboxylate (COO) were detected at 285.7 eV and 289.4 eV, respectively. The fluorinated carbon (C-F) was found at 288.2 eV. The signals of the ether carbon (C-O) and the α -carbon fluorinated carbon ($\underline{\text{C}}\text{-CF}$) functionalities have been reported to be usually too near from each other that can become difficult to distinguish.⁴⁹ Therefore they were both assigned at the 287.8 eV peak. All these signals are responsible of the shoulder present on the general C1s signal.

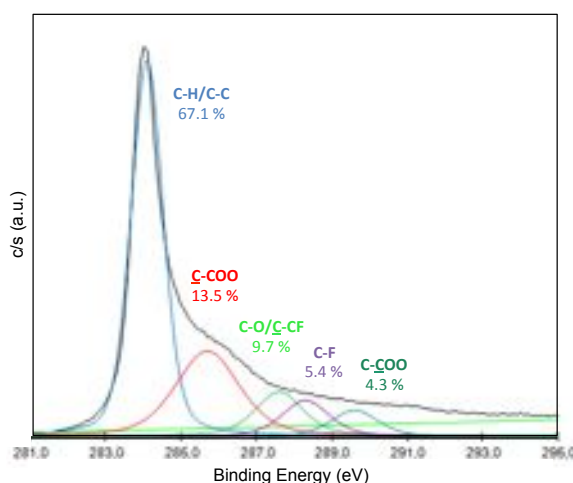


Figure 3.6. Deconvolution of the XPS spectrum for the ppPFM-modified rCNTs.

Although the high presence of the hydrocarbon signal corresponding to the rCNT structure considerably masked the other functionalities, these results show a positive retention of the fluorinated ring and the ester group.

rCNT-ppPFM Characterization and Reactivity Evaluation

As previously reported in Chapter II, the conjugation of a fluorescent molecule has been validated as an easy way to confirm the fluorinated ester retention and evaluate the reactivity of the obtained thin film. For that purpose, the selected fluorescent dye has to contain an amine group on its structure, which enables the covalent reaction with the deposited PFM layer.^{21,42} Moreover, the functionalization of the modified rCNTs with fluorescent dyes, allows the tracking of these nanomaterials *in vitro* and *in vivo* imaging applications.^{50,51} In general, CNTs have intrinsic fluorescence in the near infrared (NIR).^{52,53} However, only individual CNTs are able to emit NIR fluorescence and thus obtaining this kind of decorated vectors can improve their detection sensibility.⁵⁴⁻⁵⁶

In this study, FTSC and QDs were used to affirm the reactivity and homogeneity of the ppPFM coating on the rCNT surface. The latter, is composed a CdSe core with a ZnS shell and was immobilized on the ppPFM surface through the PEG-amine coating on its surface, a molecule proved to react with PFM groups before (Chapter II). ppPFM-modified rCNTs for a t_{PECVD} of 5 min were incubated with solutions of both fluorescent dyes together with a sample control of bare rCNTs. Samples were all observed in the fluorescent microscope after several washing steps with Milli-Q water under sonication (Figure 3.7).

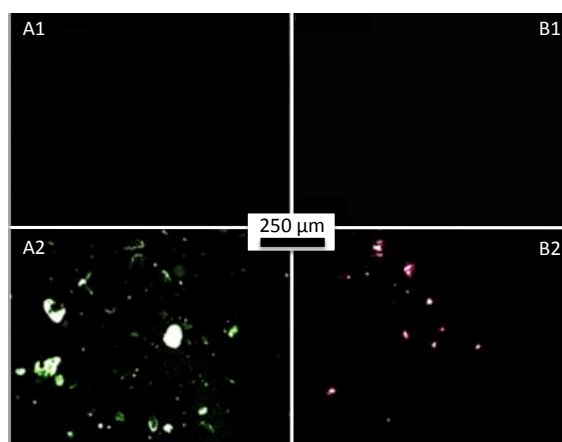


Figure 3.7. Fluorescent microscopy images of the functionalized F-rCNTs. ppPFM-modified samples reacted with (A) FTSC and (B) QDs. Both the (1) control and the (2) rCNT-ppPFM-5 were analyzed.

Large aggregates of FTSC-functionalized rCNTs (Figure 3.7A2) showed fluorescent signal whereas no fluorescence was detected from the control (Figure 3.7A1), confirming that the covalent attachment of the fluorescent molecule with the CNT surface was successful. Similar behavior was observed for the rCNTs functionalized with QDs except that less aggregation took place. This is probably due to the fact that the amino-PEG coating of the QD favors the dispersion of the rCNTs forming aggregates of between 10 to 40 μm . On the other hand, FTSC is a hydrophobic molecule that causes higher rCNT aggregation (10 and 100 μm). The low dispersibility observed of the F-rCNTs, even using QDs, together with a quenching effect may have caused a decrease in the fluorescent signal observed.⁵⁷⁻⁵⁹

One key advantage in the usage of QDs for the functionalization of rCNTs is that they present enough contrast to be observed by HRTEM due to their inorganic nature. Thus, the QD-functionalized rCNTs were analyzed by this technique (Figure 3.8). HRTEM images reveal a high density of nanoparticles homogeneously decorating the rCNT surface. It is also possible to distinguish the bonding through the amorphous layer corresponding to the ppPFM coating observed before (Figure 3.2) and here again (Figure 3.8). The diameter of these nanocrystals is 5-8 nm, the same size of the QDs used, confirming the covalent attachment of QDs on the CNT surface.

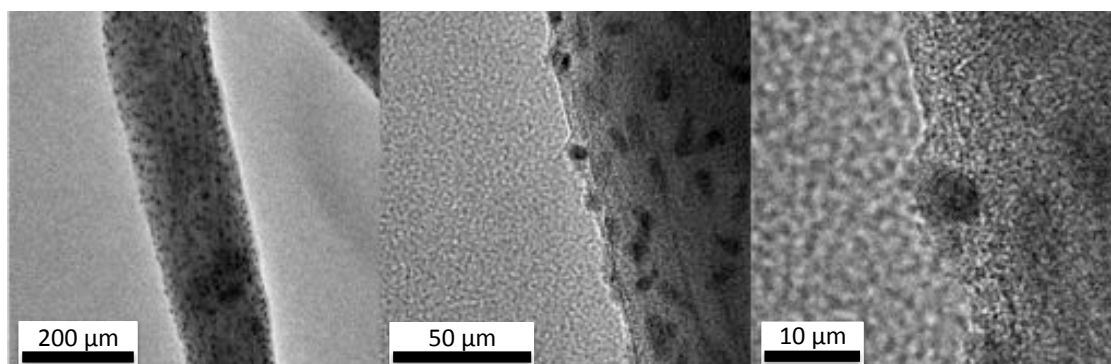


Figure 3.8. HRTEM images of the rCNTs functionalized with QDs.

The X-Ray microanalysis carried out on the TEM-studied samples also corroborated this immobilization because the elements forming the QDs (Cd, Se, Zn, S) were only found on the functionalized rCNTs (Figure 3.9). Therefore, the previous statement saying that both the low dispersibility and the quenching effect might have caused a decrease in the fluorescence observed by the microscope is ratified given the large number of QD that are actually seen attached on the rCNT surface.

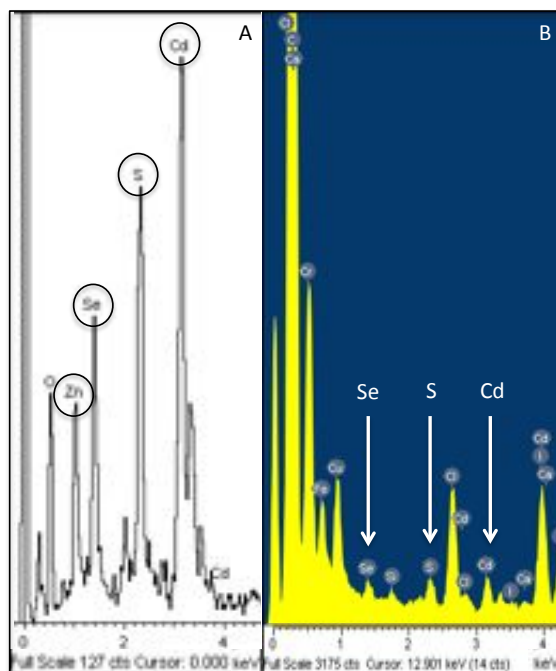


Figure 3.9. X-Ray microanalysis of the (A) Quantum Dots and the (B) QD-functionalized rCNTs.

As a result to this study, the reactivity and homogeneity of the ppPFM-modified CNTs is proved and the formed complexes formed with fluorescent dyes exhibit fluorescence and a high degree of functionalization. This type of functionalization opens the possibility to track the *in vivo* biodistribution of F-rCNTs, as it will be seen in Chapter IV, and their interaction with cells *in vitro*.

Cellular Uptake and Viability of the F-rCNTs

Although remarkable fluorescence intensity is lost due to a quenching effect, the tracking of the fluorescent rCNTs (F-CNT) is still possible as demonstrated before. To evaluate the capacity of the decorated rCNTs to cross the cell membrane together with the cell viability of this type of vectors, macrophages cells were incubated with different F-CNT. Cherukuri *et al.* already reported that macrophages cells are able to ingest nanotubes 1 μm long in significant quantities by phagocytosis.⁶⁰ In this case, cells were incubated for 12 h with F-rCNTs with both FTSC and QDs at 100 $\mu\text{g}/\text{mL}$ and 50 $\mu\text{g}/\text{mL}$, respectively (Figure 3.10).

Figure 3.10A confirmed that macrophages did not show intrinsic fluorescence. Similarly, the macrophages incubated with FTSC-functionalized rCNTs showed no fluorescence, probably due to the formation of larger aggregates in the cell medium because of the hydrophobic behavior of the FTSC (Figure 3.10B). The presence of proteins and other species in the medium are known to adsorb

on the hydrophobic surface of the nanotubes favoring its aggregation, as it will be discussed in Chapter IV. How proteins tend to bind strongly on hydrophobic surfaces was also proved in Chapter II. Additionally, the high concentration of F-rCNTs used may induce an increase of the aggregation effect causing a substantial decrease of fluorescence emission. Such aggregation tendency may difficult the internalization of the rCNTs into the cell, as studied in Chapter IV. However, Figure 3.10C show that small rCNT particles were observed inside the macrophages cells without altering its cellular morphology, suggesting a positive uptake and viability. Since the high concentration of rCNTs eventually enhanced cell death, it was reduced with the QD-decorated rCNTs and after several washes, fluorescence was observed apparently inside the cell (Figure 3.10C). In spite of the formation of aggregates, which avoided the proper study of the characteristic nanoneedle effect when interacting with the cells, the cellular uptake of the QD-functionalized rCNTs can be tracked.

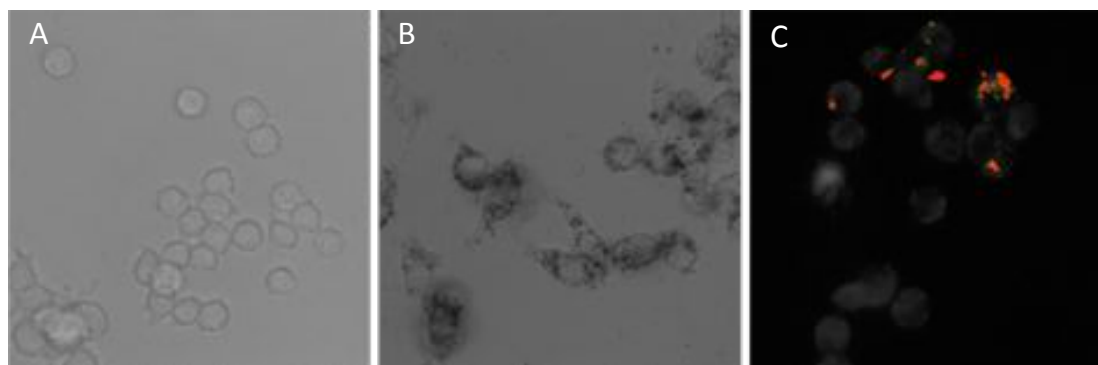


Figure 3.10. *In vitro* fluorescence tracking of the F-rCNTs. Images of the macrophages (A) control and incubated with (B) FTSC-functionalized rCNTs (100 µg/mL) and (C) QD-anchored rCNTs (50 µg/mL).

Fluorescence was only observed in cells incubated with QD-decorated rCNTs.

Study of the rCNT-ppPFM Dispersibility

At this point, surface modification of rCNTs with the deposition of a homogeneous ppPFM thin film by PECVD conserving the rCNT morphology has been demonstrated. However, a study of the dispersibility that these treated rCNTs may offer has to be also studied given the remarkable aggregation rate previously observed.

In general, the dispersion of CNT involves a great challenge owing to the combination of mainly two factors.^{2,7,43,61} In the first place, given their tubular structure with a high aspect ratio and flexibility, CNTs are prone to bundle forming small groups difficult to be mechanically dissociated. On the other hand, due to their surface curvature, the sp^2 bond types that link the carbon atoms are in a state of

tension, increasing the surface energy. Therefore, when interacting one each other through Van der Waals forces, the structure is stabilized. The poor dispersibility becomes an important handicap for the processing of CNTs in the majority of applications, especially in aqueous media, diminishing its biocompatibility.

Firstly, both bare rCNTs and rCNT-ppPFM-5 were dispersed in ethanol and observed in the microscope (Figure 3.11). Large aggregates of around 250 μm were observed for the unmodified CNTs, whereas the dispersion degree was substantially improved with the deposition of the ppPFM film on the rCNT surface. The later formed particles from 4 up to 15 μm (Figure 3.11B). In Figure 3.11A, a clear tendency of the CNT to form aggregates forming large filaments was observed, probably enhanced by the fast evaporation of the solvent.

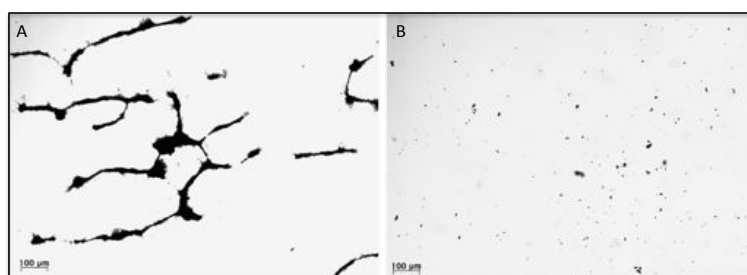


Figure 3.11. Dispersion of the ppPFM-modified rCNTs in ethanol. Images of (A) bare rCNT and (B) rCNT-ppPFM.

Concurrently, the dispersibility of the modified rCNT-ppPFM-5 was evaluated in water and also in organic solvents of different polarities as indicated in Table 3.3 (Figure 3.12).



Figure 3.12. Dispersibility of rCNT-ppPFM in different solvents. Images of (A) right after sonication and (B) after settling at room temperature for 1 h.

Initially, right after sonication of the samples, a dark and uniformly dispersed phase was formed, except when the dispersant agent was water or ethanol (polar solvents). In these cases, a larger concentration of agglomerates was observed. After several minutes, the formation of two phases occurred when part of the rCNT-ppPFM-5 settled on the bottom of the vial. This behavior was emphasized after 1 h and the different solubilization capacities of each solvent used were inferred from the chromaticity of the supernatant. As it was expected due to the hydrophobic nature of the ppPFM coatings on the rCNT surface, all non-polar solvents were able to achieve more stabilized dispersions than the polar ones (water and ethanol). Using acetonitrile, which is a polar aprotic solvent, a low dispersibility was also observed. On the other hand, the non-polar aprotic solvents such as ethyl acetate, toluene and especially dichloromethane, exhibited a better dispersibility due to their capacity to stabilize the hydrophobic nature of the rCNTs. It is noteworthy that the diethyl ether was not able to solubilize the rCNT-ppPFM-5 despite belonging to the group of non-polar aprotic solvents as well. This observation highlights that other dispersibility parameters besides the polarity of the solvent used play a crucial role in the CNT solubilization process, as it was described in the study developed by H. T Ham et al.⁴¹

In Ham's work, the dispersibility of SWNT in different organic solvents and surfactants agents was studied, correlating the dispersion rate in the solvent with the Hansen solubility parameters (Equation 3.1). In said equation, δ_t is the total solubility parameter, the dispersive component (δ_d) describes the non-polar type of interactions, the polar component (δ_p) gives information about the dipole-dipole interactions, and the (δ_h) parameter, defines the hydrogen-bond attractions. After the evaluation of the disperse phase chromaticity of the described samples, the Hansen parameters for the studied solvents were searched (Table 3.3) and consequently plotted (Figure 3.13).

$$\delta_t^2 = \delta_d^2 + \delta_p^2 + \delta_h^2$$

Equation 3.1

Figure 3.13A shows two clear areas in the arrangement of the studied solvents. On one hand, the non-polar solvents converged concentrated in a well-defined zone with δ_h values below 10 MPa^½ and δ_p inferior to 8 MPa^½. On the other hand, the polar solvents (water, ethanol and acetonitrile) owned δ_p values superior to 8 MPa^½ and variable δ_h values, which was directly related to the ability of the solvent to form hydrogen bonds. Given the observations commented above, all solvents with high δ_p values were not able to stabilize the ppPFM-modified CNT in suspension, independently if they were protic or non-protic. However, the diethyl ether, despite being a non-polar solvent, was

not able to stabilize the modified nanotubes in suspension. This is when the dispersive component needs to be evaluated. In such case, diethyl ether exhibited the lowest δ_d value ($14.5 \text{ MPa}^{1/2}$) inferior to both polar and non-polar solvents (Figure 3.13B). Moreover, for high δ_d values, where solvents such as toluene and dichloromethane were found, the dispersion capacity of the rCNT-ppPFM increased, which was consistent with what was experimentally observed. This plot demonstrates the importance of the dispersive parameter in terms of the actual solubilization of the modified rCNTs. This component has a predominant effect in comparison to the polar parameter or the capacity of the solvent to form hydrogen bonds. However, the overall effect of all parameters needs to be taken into account. Figure 3.13C proved that the solvents that facilitate dispersion (toluene and dichloromethane) were located in the region defined between δ_d values superiors to $17.5 \text{ MPa}^{1/2}$ and values of δ_p and δ_h below $6.5 \text{ MPa}^{1/2}$. Therefore, solvents that present these characteristics are identified as the ones that facilitate the dispersion of the ppPFM-modified rCNTs.

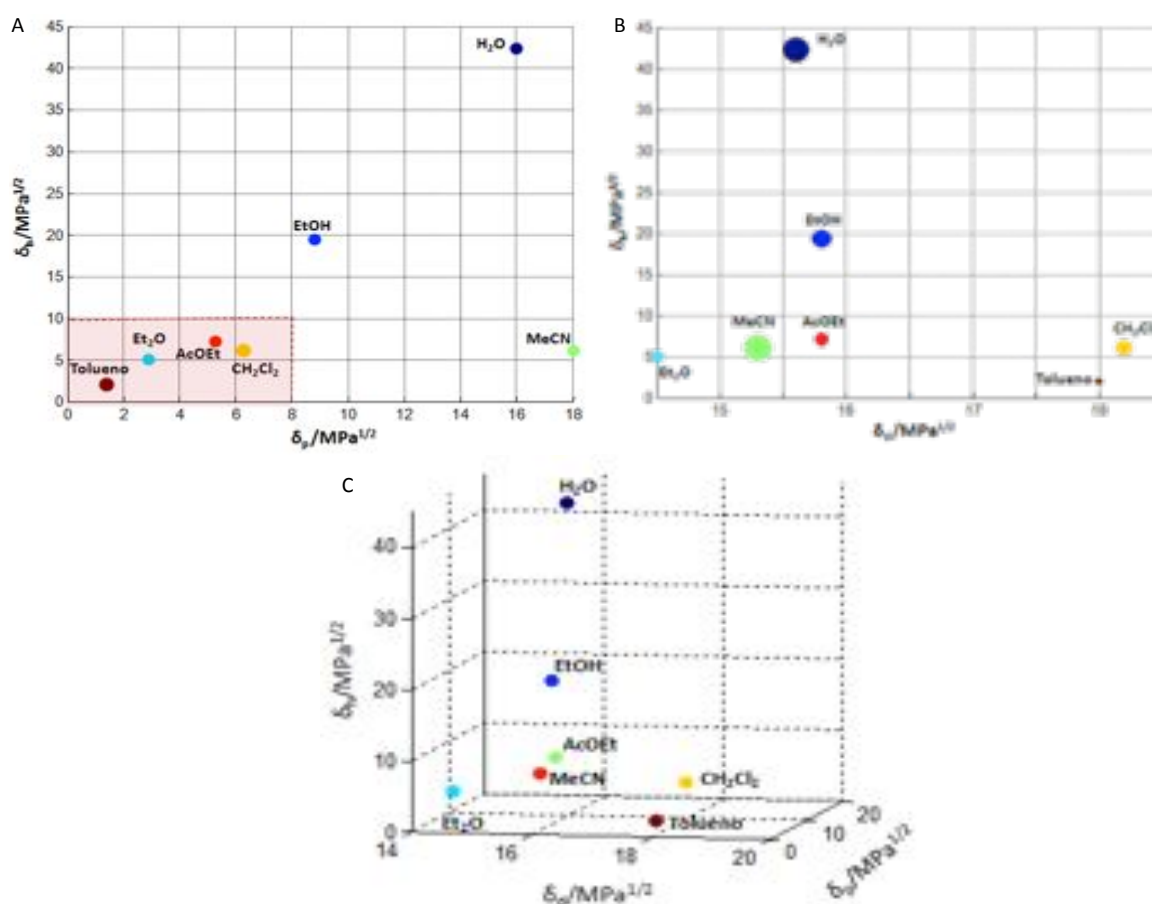


Figure 3.13. Graphic representation of the Hansen parameters. It shows the correlation between (A) δ_h and δ_p , (B) δ_h and δ_d , and (C) the dependence observed for the 3 parameters. For both first plots, (A) and (B), the dot size is proportional to the parameter value.

As a result, this study becomes a helpful tool for choosing the proper solvent in order to gain the desired solubilization for the handling and manipulation of rCNTs. Nevertheless, in biomedical and cell biology applications, the dispersion of the functionalized rCNTs has to be successful in aqueous media therefore other strategies must be studied.

Covalent Binding of the TPA linker on the ppPFM-modified rCNTs

Given the low dispersibility rate of the ppPFM-treated rCNTs in aqueous media together with the specificity of the reactive deposited polymer towards primary amines, the attachment of a chemical linker on the CNT surface in charge of improving its solubilization is examined. As previously demonstrated in Chapter II, ppPFM coatings are able to successfully react with the PEG-amine, a molecule characterized for its hydrophilic nature and its capacity to be solubilized in water.^{62,63} Therefore, the linkage of this type of molecule on the rCNT-ppPFM vectors may improve the solubility and dispersibility of the final complex. Moreover, if the used PEG-amine has a thiol group on the other end, allows the conjugation with the oligonucleotide of interest (also with a thiol group on the 5' end) through a disulfide bond. The reductive environment of the cellular cytoplasm leads to the cleavage of the formed disulfide bond, releasing the genetic material into the cell.³⁴

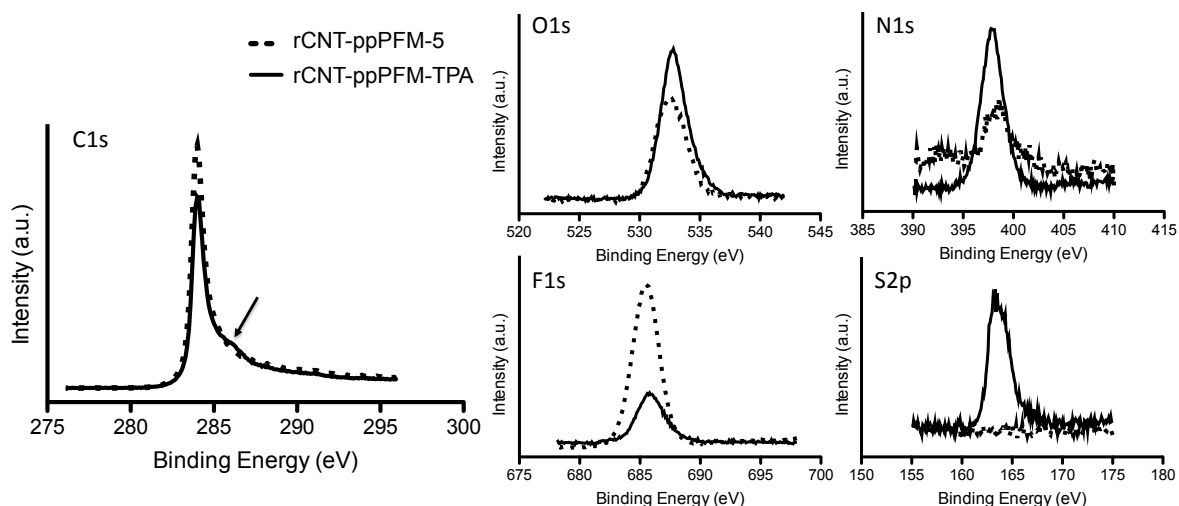


Figure 3.14. XPS analysis of the TPA-functionalized rCNTs. Comparison of each atomic signal detected (carbon, oxygen, fluorine and sulfur) for both the ppPFM-modified and the TPA-functionalized rCNTs. The arrow on C1s plot remarks the slight shoulder noticed for the rCNT-ppPFM-TPA.

Thereby, ppPFM-modified rCNTs were incubated with TPA under Ar atmosphere in order to minimize its oxidation. The functionalized samples were analyzed by XPS together with the initial

rCNT-ppPFM, which was used as a control. The main peaks obtained are summarized in Figure 3.14 and Table 3.6.

The general spectrum basically suggested two main changes between samples; the decrease of fluorine content and the appearance of the signal corresponding to sulfur on the TPA-functionalized rCNTs. Both phenomena mean that the successful anchoring of the chemical linker took place. Furthermore, the increase (around 20%) of oxygen and nitrogen (more than 50%) present could also be due to the PEG chain immobilization.

Table 3.6. Atomic percentage both the ppPFM-modified rCNTs and the subsequently functionalized with TPA obtained from the XPS data, together with their corresponding oxygen, nitrogen and fluorine ratios.

Sample ID	Atomic Percentage					Ratio		
	%C	%O	%N	%F	%S	O/C	N/C	F/C
rCNT-ppPFM	86.8	6.3	0.7	6.0	-	0.07	0.01	0.07
rCNT-ppPFM-TPA	87.2	7.9	2.0	2.4	0.5	0.09	0.02	0.03

Although the fluorine signal decreased nearly a 60% compared to the rCNT-ppPFM substrates due to the TPA anchoring on the surface, some traces of fluorine were still present in these samples, evincing that the reaction of the TPA with the PFM group was incomplete. The complete reaction of the PFM until no signal is observed is hardly achievable due to the unexposed PFM groups that remain in the inner part of the thin film, as confirmed in previous studies.⁴²

Table 3.7. Summary of the percentage contributions of the different functionalities identified for both samples: the ppPFM-modified and the subsequent functionalization with TPA.

Chemical Functionalities	Binding Energy (eV)	Contribution %C1s	
		rCNT-ppPFM	rCNT-ppPFM-TPA
C-H/C-C	284.0	67.1	49.1
C-COO/C-N	285.7	13.5	25.2
C=O/C-CF	287.8	9.7	10.4
C-F/N-C=O	288.2	5.4	8.6
C-COO	289.6	4.3	6.7

When analyzing the obtained carbon signal, both samples showed nearly the same profile except for a moderate increase of the shoulder previously noticed and marked with an arrow in Figure 3.14. Table 3.7 shows the binding energies obtained for the two analyzed substrates, which not only differ in contribution but also in the nature of the functionalities that could be attributed. Again, the

hydrocarbon signal was set at 284 eV and different functionalities involving oxygen, fluorine and nitrogen were fit. At 285.7 eV the α -ester carbon ($\underline{\text{C}}\text{-COO}$) was again detected with a significant increase of contribution on the rCNT-ppPFM-TPA sample, explaining the slight increase of the shoulder at this energy. This increase may be owing to the formation of nitrogen functionalities not considered before. Such functionalities appear as consequence of the reaction between the amine of the TPA and the PFM group. The signal of $\underline{\text{C}}\text{-COO}$ and C-N were close enough to be indistinguishable. A similar phenomenon occurs at 287.8 eV and 288.2 eV, whose contributions experienced a slight increase for the TPA-functionalized samples due to the additional presence of nitrogenated functionalities. The former was assigned to the ether carbon (C-O) and the α -carbon fluorinated carbon ($\underline{\text{C}}\text{-CF}$) as before. However, for the rCNTs containing TPA, could also be attributed to the α -carbon nitrogenated carbon ($\underline{\text{C}}\text{-CN}$) of the PEG chain. The latter, at 288.2 eV, corresponded to the already justified fluorinated carbon (C-F) and for the rCNT-ppPFM-TPA, the amide carbon (N-C=O) could be also considered. Nonetheless, it was impossible to differentiate which functionality predominated on the TPA-functionalized CNTs. Therefore, it should be assumed that part of the fluorinated functionalities was present also in these samples, as commented before.

As said, the presence of sulfur on the TPA-functionalized rCNTs also suggests the presence of the linker. To distinguish whether the S present is in its reactive form (R-SH) or has already reacted with another S forming a disulfide bridge (R-S-S-R), the obtained signal is studied in detail (Figure 3.15). According to literature, the binding energies for thiol functionalities are comprised between 163.2 eV and 163.9 eV, whereas a disulfide bond can be found around 163.2-164.2 eV.⁶⁴ The lack of resolution due to the low intensity recorded did not allow to make an unequivocally distinction but an approximate analysis of the overall peak was carried out. Basically, two main peaks were obtained, one at 163.2 eV and the other one at 164.2 eV. These results affirmed that 60% of the sulfur present was in its reduced form (R-SH).

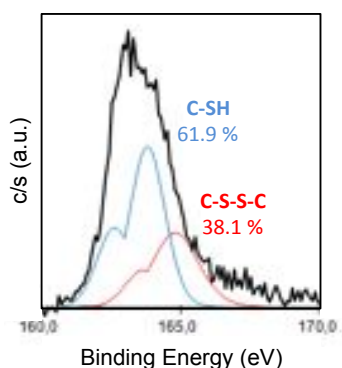


Figure 3.15. Analysis of the S2p peak of the rCNT-ppPFM-TPA. Data obtained from the XPS spectrum.

As a result, ppPFM-coated rCNTs can successfully immobilize TPA, which can be used as a chemical linker to bind small oligonucleotides like siRNA or miRNA. The possibility to anchor these acid nucleic through a disulfide bond has a significant potential for the efficient release and subsequent gene silencing.

3.3.2. DNA Condensation to the rCNT via Ionic Interaction

The previous section (3.3.1) has proved that the ppPFM coating is an interesting tool to achieve functionalized rCNTs. It allows the anchoring of fluorescent dyes and chemical linkers like TPA. Such type of functionalization is especially useful when short oligonucleotides like siRNA or miRNA are immobilized. However, the formation of these complexes involves a multi step and a rather complicated procedure. Therefore, another strategy that may facilitate the conjugation of all type of genetic material to the rCNT surface is the polymerization of allylamine (AA) also by PECVD. This technique ensures a total and homogeneous coating of PECVD-polymerized AA (ppAA) along the rCNT surface as previously demonstrated for the deposition of ppPFM layers. Moreover, rCNTs modified with ppAA by this technique could easily be dispersed in aqueous media, specifically in acetate buffer at pH 5 due to the protonation of the amine groups.³⁰⁻³² These positive charges all over the surface would make the ppAA-modified CNTs less prone to aggregation owing to the increase of the electrostatic repulsion between particles.⁴⁰ Additionally, the amine protonation would allow the complexation with the DNA, due to its negatively charged phosphate backbone.³⁰⁻³² Thus, the amount of DNA able to interact with the CNT might be increased compared to the covalent binding provided by the ppPFM coating affording a potential transfection agent.

ppAA Thin Film Characterization

WCA and IR spectroscopy confirmed the formation of the ppAA thin layer ensuring the proper PECVD polymerization of this monomer in the already studied reactor. Silicon wafers were modified together with the rCNTs allowing the characterization of the deposited polymer.

The formation of a ppAA film and the retention of the amine functional group on the surface were confirmed by IR spectroscopy. The absorption spectrum of the control (bare silicon wafer) was subtracted from the obtained spectrum of the ppAA-coated substrate (Figure 3.16). Peaks around 3339 cm^{-1} , 1650 cm^{-1} and 750 cm^{-1} were found, corresponding to different tension and flexion modes typically associated with amine groups.⁶⁵ Typically, at approximately 3335 cm^{-1} , primary

amines show two tension bands belonging to N-H bonds, whereas secondary amines just evidence one. On the spectrum obtained in this work only one wide band at 3339 cm^{-1} was noticed masking the other one, which appeared as a shoulder (marked with the arrow). These results suggest that plasma polymerization technique leads to a ppAA film with a more limited retention of primary amines compared to other methods.⁶⁶ This is probably because most of the primary amines firstly formed, tend to react and form secondary amines. This phenomenon has been previously described in literature and agrees with the ppAA polymerization mechanism by PECVD explained elsewhere.⁶⁶ The vibrations of the band deformation at 1650 cm^{-1} were superposed with another range of bands between 1500 and 1300 cm^{-1} corresponding to different vibration and tension modes from the C-H bonds of the polymer chain.

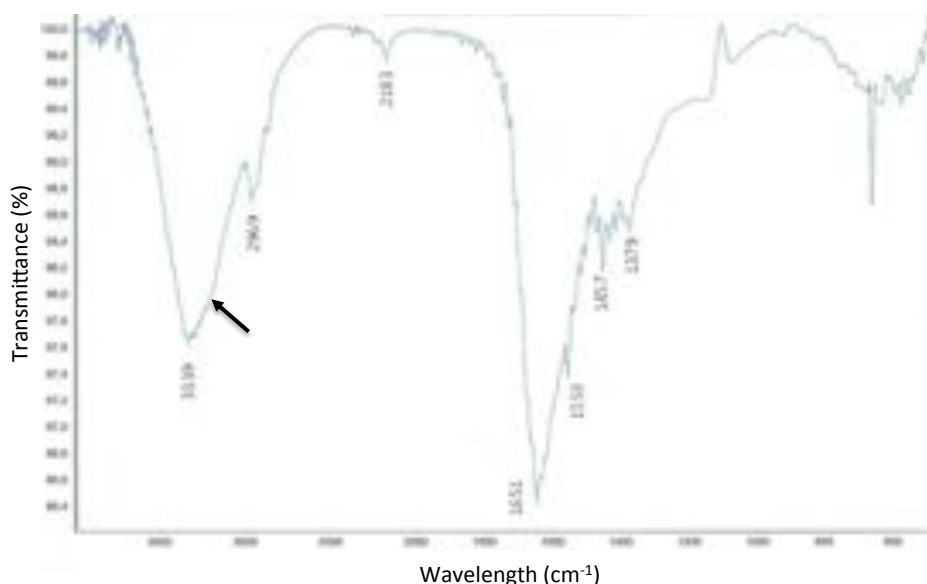


Figure 3.16. IR spectrum of the ppAA coating achieved by PECVD on a silicon wafer surface.

Nevertheless, WCA results exhibited the increase in wettability coating with the ppAA layer, decreasing the contact angle from the typical $57.3^\circ \pm 0.2^\circ$ of the unmodified surface to $35.0^\circ \pm 2.1^\circ$ (Figure 3.17).

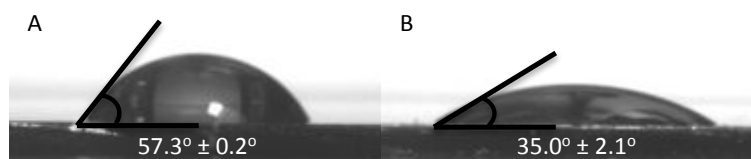


Figure 3.17. WCA of (A) the non-modified silicon wafer and (B) coated with ppAA.

Therefore, a clear hydrophilic behavior was achieved due to the ppAA coating, which would be crucial for the rCNT dispersion. Additionally, it also suggested that the primary amines present were enough to achieve a positively charged surface. This last statement was confirmed by measuring the size and charge of the resulting dispersion of rCNT-ppAA at pH 5 (Figure 3.18). Although the size measured by DLS is only valid for spherical nanoparticles, the measurement of the functionalized rCNTs could give qualitative information about the dispersion degree of the sample if the concentration is maintained constant.^{67,68} Size measurements in Figure 3.18A showed that the size distribution was kept similarly to the naïve rCNTs after the modification with ppPFM due to its hydrophobic nature. On the other hand, the ppAA-coated rCNTs decreased the final particle size confirming a better dispersion of the protonated rCNT-ppAA. Zeta potential analysis demonstrated the positively charged surface obtained after the ppAA polymerization when compared to the naturally negatively charged rCNTs. The negatively charged surface of the rCNTs was increased after the modification with ppPFM. The positive charges on the rCNT-ppAA surface would be responsible of the final interaction with the DNA of interest.

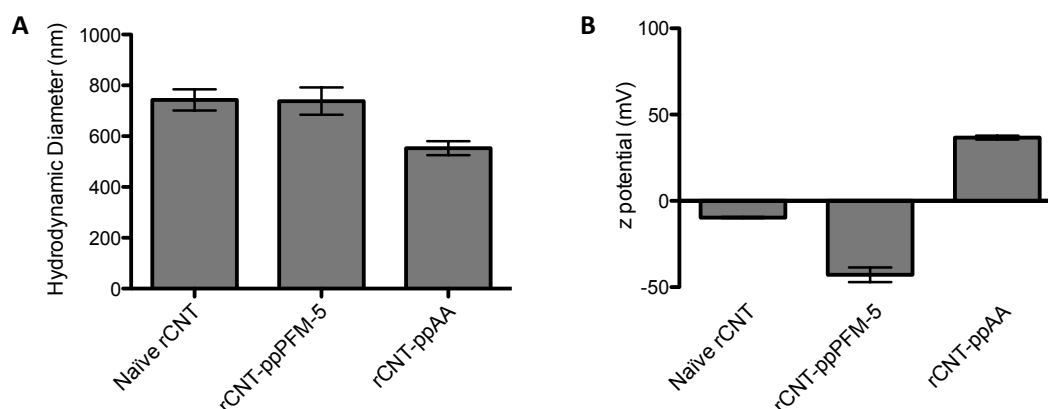


Figure 3.18. Size and charge of the rCNTs-ppPFM and rCNT-ppAA complexes. (A) D_H and (B) zeta potential of the naïve rCNT, ppPFM-modified rCNTs and the coated with ppAA.

Formation of the rCNT-ppAA Complex with DNA

After the demonstration of the ppAA deposition on the rCNT surface, its versatility as a transfection vector was carried out. For this study a plasmid encoding the generation of green fluorescent proteins (pGFP) was used and the complex was formed due to the electrostatic interaction of the DNA with the positively charged rCNT-ppAA. Previous studies demonstrated that the condensation of DNA on the nanotubes surface occurs by means of a wrapping mechanism of the genetic material around the CNT, and this process may vary depending on the CNT diameter.^{8,39} Owing to this

wrapping effect, the dispersion degree could be maintained, remaining as individual CNTs and thus the diffusion of the complex through the cell membrane following the nanoneedle mechanism would be favored.

Before the formation of the plasmid vector, the load capacity of DNA presented by the rCNTs-ppAA needs to be determined. The aim is to determine the amount of genetic material that can be charged per unit mass of carbon nanotubes. To evaluate the capacity of the ppAA-modified CNTs to condensate DNA, a gel retardation assay was performed at varying the complexation ratios. The ratios studied ranged from 1:1 to 200:1 (Figure 3.19).

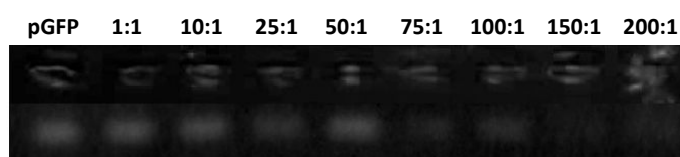


Figure 3.19. Agarose gel electrophoresis of the CNT-ppAA:pGFP (w/w) ratios.

The migration of the different species on an agarose gel depends on the relation charge/mass of the sample. Due to their large size, rCNTs were not able to run through the gel, whereas the plasmid was able to migrate towards the positive electrode connected to the gel due to its intrinsic negative charge. A control (pGFP alone) showed the position in the gel where the plasmid had to be found, and this signal was detected until the 150:1 ratio. This meant that per each mass unit of pGFP, at least 150 of rCNT-ppAA were needed to successfully condensate all the plasmid added, avoiding the presence of free pGFP in the solution.

Evaluation of the Cell Transfection Efficiency of the pGFP Vectors

Once the formation of the complex was confirmed, cell studies were also carried out. Testing the pGFP vectors allows the confirmation of the cellular uptake and DNA release of the rCNT-ppAA+pGFP complexes. Hence, macrophages were incubated with these pGFP transfection vectors and the GFP expression was evaluated by fluorescent microscope (Figure 3.20). After 48 h of incubation, control macrophages showed no fluorescence (Figure 3.20A and B), while nearly 80% of the cell population was found green when incubated with the rCNT-ppAA+pGFP vectors (Figure 3.20C, D and E). Such results confirm that the formed pGFP vectors were successfully internalized into the macrophages and the condensed plasmid was effectively released and expressed producing GFP. Figure 3.20D show small aggregates on practically every transfected cell, indicating an

acceptable dispersion of the rCNTs in the presence of serum proteins of the cell culture. Nevertheless, other areas were filled of large particle agglomerates that may cause cell alteration, mutagenesis and eventually cell death.

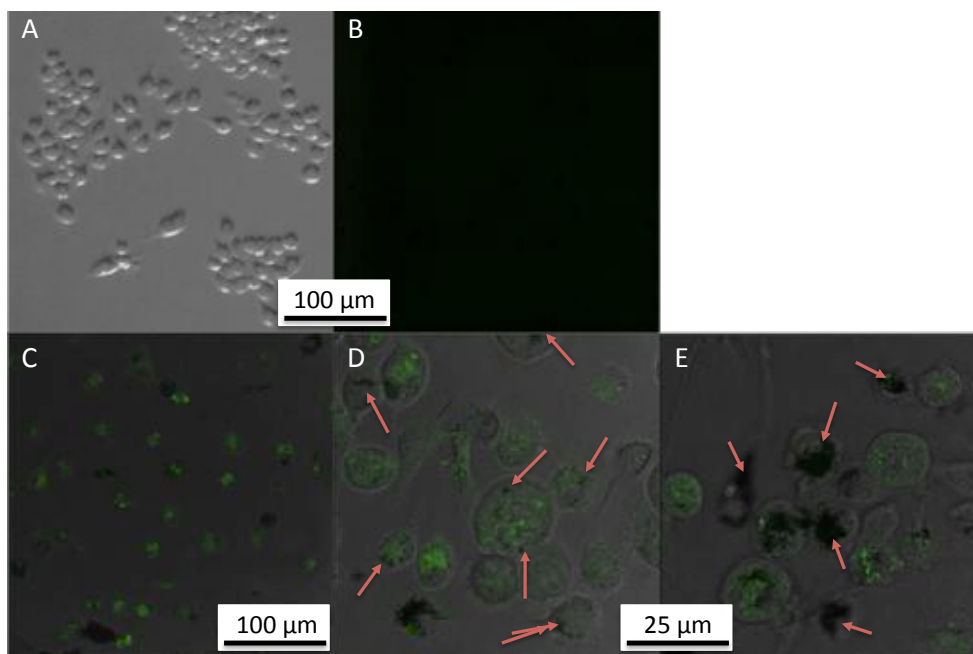


Figure 3.20. Cell transfection of the rCNT-ppAA+pGFP complexes. (A) Microscope image of macrophages control culture confirming (B) no intrinsic fluorescence when untreated. (C) General view of the macrophages exhibiting green fluorescence after rCNT-ppAA+pGFP incubation (almost 80% of transfection). More detailed images of the transfected macrophages showing the presence of (D) modest and (E) large aggregates of rCNT.

Regardless, ppAA-coated rCNTs allow the complexation of a plasmid reporter pGFP capable to confirm the complex internalization and transfection. The GFP expression observed demonstrates that these vectors are able to uptake into macrophages releasing the nucleic acid condensed on their surfaces. As a result, the functionalization of CNTs by this technique becomes an interesting tool to produce effective gene delivery vectors. However, it is essential to gain a deeper understanding of the dispersibility, the cytotoxicity and general behavior in biological fluids of this type of complexes. This sort of questions will be treated in the next chapter (Chapter IV).

3.4. Concluding Remarks

This part of the thesis presents the modification of rCNTs by PECVD using two different monomers, PFM and AA. It has been demonstrated that both type of monomers can be polymerized on the rCNT surface in a home-built plasma reactor, allowing the formation of gene delivery vectors from the naïve rCNTs, which are incompatible with the biological milieu. Once polymerized, they provide different properties to the rCNT surface and thus the resulting complex would behave differently.

On one hand, the polymerization of PFM on rCNTs has been successfully achieved maintaining the conditions optimized for the PECVD technique in the previous chapter ($P_i = 15$ W, $DC = 10/20$, $t = 5$ min/batch). However, the procedure needs to be carried out 3 times (total time of PECVD applied is 15 min), gently shaking the sample in between batches, due to the powder nature of the CNT. TEM images show that under these conditions the morphology of the CNT remains unaltered but also that the ppPFM layer obtained is homogeneously distributed along the CNT surface with a thickness between 4 and 6 nm. EDS and XPS analysis confirm the chemical composition of the polymer coating and the resulting highly reactive surface is demonstrated by the immobilization of fluorescent dyes such as FTSC and QDs. These fluorescently-labeled rCNTs are presented as interesting candidates for bioimaging agents when incubated with macrophages. Finally, a chemical linker has been successfully anchored *via* the PFM group leaving a thiol group exposed, which offers the possibility to of bind the DNA of interest through a disulfide bridge.

Further on, the optimization of the PECVD technique for rCNT modification opened a wide range of possibilities in order to achieve any functionalization of interest on the rCNT wall. The polymerization of AA by PECVD results in the ppAA coating, which offers a high density of amines exposed on the rCNT surface. Having protonated amine groups (pH 5) on the rCNT wall can potentially be used as a vector for genetic material due to the interaction with the negative charges of the oligonucleotide backbone. This approach allows the study of the wrapping effect of the DNA on the rCNT surface against the direct covalent immobilization towards a disulfide bridge. In this regard, the former results in a more facile and faster way to obtain gene vectors made of rCNTs compared to the laborious steps that the covalent binding involves.

WCA, IR Spectroscopy and zeta potential studies confirm the proper polymerization of ppAA on the rCNT walls and its positive residues at pH 5. The formed rCNT-ppAA are able to complex pGFP in a ratio of 150:1 (CNT:pGFP in mass) and the transfection efficiency in macrophages is around the 80%. However, large aggregates of rCNTs are observed in the cell culture, which might decrease the cell

viability and increase the cytotoxicity of the system. Although dispersion studies of both systems (rCNT-ppPFM and rCNT-ppAA) are also carried out in this chapter, a deeper insight on how the final physicochemical properties of the CNTs after modification affects the cytotoxicity, cellular uptake and transfection of these gene vectors is required.

3.5. References

- 1 Bianco, A. *et al.* in *Medicinal Chemistry and Pharmacological Potential of Fullerenes and Carbon Nanotubes* Vol. 1 (eds Franco Cataldo & Tatiana Ros) 23-50 (Springer Netherlands, 2008).
- 2 Jeon, I.-Y., Chang, D. W., Kumar, N. A. & Baek, J.-B. *Functionalization of Carbon Nanotubes*. (2011).
- 3 Lin, Y. *et al.* Advances toward bioapplications of carbon nanotubes. *J. Mater. Chem.* **14**, 527-541 (2004).
- 4 Chen, J., Chen, Q. & Ma, Q. Influence of surface functionalization *via* chemical oxidation on the properties of carbon nanotubes. *Journal of colloid and interface science* **370**, 32-38 (2012).
- 5 Chen, R. J., Zhang, Y., Wang, D. & Dai, H. Noncovalent Sidewall Functionalization of Single-Walled Carbon Nanotubes for Protein Immobilization. *Journal of the American Chemical Society* **123**, 3838-3839 (2001).
- 6 Balasubramanian, K. & Burghard, M. Chemically functionalized carbon nanotubes. *Small (Weinheim an der Bergstrasse, Germany)* **1**, 180-192 (2005).
- 7 Hirsch, A. Functionalization of Single-Walled Carbon Nanotubes. *Angewandte Chemie International Edition* **41**, 1853-1859 (2002).
- 8 Liu, Y., Chipot, C., Shao, X. & Cai, W. Solubilizing carbon nanotubes through noncovalent functionalization. Insight from the reversible wrapping of alginic acid around a single-walled carbon nanotube. *The journal of physical chemistry. B* **114**, 5783-5789 (2010).
- 9 Ntim, S. A., Sae-Khow, O., Witzmann, F. A. & Mitra, S. Effects of polymer wrapping and covalent functionalization on the stability of MWCNT in aqueous dispersions. *Journal of Colloid and Interface Science* **355**, 383-388 (2011).
- 10 Petrov, P., Stassin, F., Pagnouille, C. & Jerome*, R. Noncovalent functionalization of multi-walled carbon nanotubes by pyrene containing polymers. *Chemical Communications*, 2904-2905 (2003).
- 11 Sun, Y.-P., Fu, K., Lin, Y. & Huang, W. Functionalized carbon nanotubes: properties and applications. *Accounts of chemical research* **35**, 1096-1104 (2002).
- 12 Vaisman, L., Wagner, H. D. & Marom, G. The role of surfactants in dispersion of carbon nanotubes. *Advances in Colloid and Interface Science* **128-130**, 37-46 (2006).
- 13 Dovbeshko, G. I., Repnytska, O. P., Obratsova, E. D., Shtogun, Y. V. & Andreev, E. O. Study of DNA interaction with carbon nanotubes. *Semicond Phys Quantum Electron Optoelectron* **6**, 105-108 (2003).
- 14 Guo, Z., Sadler, P. J. & Tsang, S. C. Immobilization and Visualization of DNA and Proteins on Carbon Nanotubes. *Advanced Materials* **10**, 701-703 (1998).
- 15 Bahr, J. L. & Tour, J. M. Covalent chemistry of single-wall carbon nanotubes. *Journal of Materials Chemistry* **12**, 1952-1958 (2002).
- 16 Dyke, C. A. & Tour, J. M. Covalent Functionalization of Single-Walled Carbon Nanotubes for Materials Applications. *The Journal of Physical Chemistry A* **108**, 11151-11159 (2004).
- 17 Chen, C., Ogino, A., Wang, X. & Nagatsu, M. Plasma treatment of multiwall carbon nanotubes for dispersion improvement in water. *Applied Physics Letters* **96**, 131504 (2010).
- 18 Chen, Q., Dai, L., Gao, M., Huang, S. & Mau, A. Plasma Activation of Carbon Nanotubes for Chemical Modification. *The Journal of Physical Chemistry B* **105**, 618-622 (2001).
- 19 Yasuda, H. *Plasma polymerization*. (Academic Press, 1985).
- 20 Duque, L., Menges, B., Borros, S. & Förch, R. Immobilization of biomolecules to plasma polymerized pentafluorophenyl methacrylate. *Biomacromolecules* **11**, 2818-2823 (2010).
- 21 Francesch, L., Borros, S., Knoll, W. & Förch, R. Surface Reactivity of Pulsed-Plasma Polymerized Pentafluorophenyl Methacrylate (PFM) toward Amines and Proteins in Solution. *Langmuir* **23**, 3927-3931 (2007).
- 22 Francesch, L., Garreta, E., Balcells, M., Edelman, E. R. & Borrós, S. Fabrication of Bioactive Surfaces by Plasma Polymerization Techniques Using a Novel Acrylate-Derived Monomer. *Plasma Processes and Polymers* **2**, 605-611 (2005).

- 23 Khare, B. N. *et al.* Functionalization of Carbon Nanotubes by Ammonia Glow-Discharge: Experiments and Modeling. *The Journal of Physical Chemistry B* **108**, 8166-8172 (2004).
- 24 Garreta, E., Tricás, N., Quintana, L., Semino, C. E. & Borrós, S. Plasma Polymerization on Hydroxyapatite Powders to Increase Water Dispersability for Biomedical Applications. *Plasma Processes and Polymers* **3**, 553-561 (2006).
- 25 Tseng, C. H., Wang, C. C. & Chen, C. Y. Modification of multi-walled carbon nanotubes by plasma treatment and further use as templates for growth of CdS nanocrystals. *Nanotechnology* **17**, 5602-5612 (2006).
- 26 Abou Rich, S. *et al.* Polymer coatings to functionalize carbon nanotubes. *Physica E: Low-dimensional Systems and Nanostructures* **In Press, Corrected Proof** (2012).
- 27 Ávila-Orta, C. A. *et al.* Surface modification of carbon nanotubes with ethylene glycol plasma. *Carbon* **47**, 1916-1921 (2009).
- 28 Vohrer, U., Zschoerper, N. P., Koehne, Y., Langowski, S. & Oehr, C. Plasma Modification of Carbon Nanotubes and Bucky Papers. *Plasma Processes and Polymers* **4**, S871-S877 (2007).
- 29 Förch, R., Zhang, Z. & Knoll, W. Soft Plasma Treated Surfaces: Tailoring of Structure and Properties for Biomaterial Applications. *Plasma Processes and Polymers* **2**, 351-372 (2005).
- 30 Chen, Q., Förch, R. & Knoll, W. Characterization of Pulsed Plasma Polymerization Allylamine as an Adhesion Layer for DNA Adsorption/Hybridization. *Chemistry of Materials* **16**, 614-620 (2004).
- 31 Zhang, Z., Knoll, W., Foerch, R., Holcomb, R. & Roitman, D. DNA Hybridization on Plasma-Polymerized Allylamine. *Macromolecules* **38**, 1271-1276 (2005).
- 32 Hook, A. L., Thissen, H., Quinton, J. & Voelcker, N. H. Comparison of the binding mode of plasmid DNA to allylamine plasma polymer and poly(ethylene glycol) surfaces. *Surface Science* **602**, 1883-1891 (2008).
- 33 Zhang, M., Desai, T. & Ferrari, M. Proteins and cells on PEG immobilized silicon surfaces. *Biomaterials* **19**, 953-960 (1998).
- 34 Liu, Z., Winters, M., Holodniy, M. & Dai, H. siRNA Delivery into Human T-Cells and Primary Cells with Carbon-Nanotube Transporters. *Angewandte Chemie International Edition* **46**, 2023-2027 (2007).
- 35 Enyashin, A. N., Gemming, S. & Seifert, G. DNA-wrapped carbon nanotubes. *Nanotechnology* **18** (2007).
- 36 Heller, D. A. *et al.* Optical Detection of DNA Conformational Polymorphism on Single-Walled Carbon Nanotubes. *Science* **311**, 508-511 (2006).
- 37 Kam, N. W. S., Liu, Z. & Dai, H. Carbon Nanotubes as Intracellular Transporters for Proteins and DNA: An Investigation of the Uptake Mechanism and Pathway. *Angewandte Chemie* **118**, 591-595 (2006).
- 38 Zheng, M. *et al.* Structure-Based Carbon Nanotube Sorting by Sequence-Dependent DNA Assembly. *Science* **302**, 1545-1548 (2003).
- 39 Johnson, R. R., Johnson, A. T. C. & Klein, M. L. Probing the Structure of DNA-Carbon Nanotube Hybrids with Molecular Dynamics. *Nano Letters* **8**, 69-75 (2008).
- 40 Raffa, V., Ciofani, G., Vittorio, O., Riggio, C. & Cuschieri, A. Physicochemical properties affecting cellular uptake of carbon nanotubes. *Nanomedicine* **5**, 89-97 (2010).
- 41 Ham, H. T., Choi, Y. S. & Chung, I. J. An explanation of dispersion states of single-walled carbon nanotubes in solvents and aqueous surfactant solutions using solubility parameters. *Journal of Colloid and Interface Science* **286**, 216-223 (2005).
- 42 Duque, L. *et al.* Reactions of Plasma-Polymerised Pentafluorophenyl Methacrylate with Simple Amines. *Plasma Processes and Polymers* **7**, 915-925 (2010).
- 43 Hilding, J., Grulke, E. A., George Zhang, Z. & Lockwood, F. Dispersion of Carbon Nanotubes in Liquids. *Journal of Dispersion Science and Technology* **24**, 1-41 (2003).
- 44 Tagmatarchis, N., Zattoni, A., Reschiglian, P. & Prato, M. Separation and purification of functionalised water-soluble multi-walled carbon nanotubes by flow field-flow fractionation. *Carbon* **43**, 1984-1989 (2005).
- 45 Verissimo, C., Gobbi, A. L. & Moshkalev, S. A. Synthesis of carbon nanotubes directly over TEM grids aiming the study of nucleation and growth mechanisms. *Applied Surface Science* **254**, 3890-3895 (2008).

- 46 Calderon, J. G. & Timmons, R. B. Surface Molecular Tailoring via Pulsed Plasma-Generated Acryloyl Chloride Polymers: Synthesis and Reactivity. *Macromolecules* **31**, 3216-3224 (1998).
- 47 Panchalingam, V. *et al.* Molecular surface tailoring of biomaterials via pulsed RF plasma discharges. *Journal of Biomaterials Science, Polymer Edition* **5**, 131-145 (1994).
- 48 Shulga, Y. M. *et al.* XPS study of fluorinated carbon multi-walled nanotubes. *Journal of Electron Spectroscopy and Related Phenomena* **160**, 22-28 (2007).
- 49 Francesch, L. *Surface modification of polymers by plasma polymerization techniques for tissue engineering* Ph.D Thesis thesis, Ph.D Thesis - Universitat Ramon Llull, (2008).
- 50 Hong, H., Gao, T. & Cai, W. Molecular imaging with single-walled carbon nanotubes. *Nano Today* **4**, 252-261 (2009).
- 51 Jiang, S., Gnanasammandhan, M. K. & Zhang, Y. Optical imaging-guided cancer therapy with fluorescent nanoparticles. *Journal of The Royal Society Interface* **7**, 3-18 (2010).
- 52 Lacerda, L., Raffa, S., Prato, M., Bianco, A. & Kostarelos, K. Cell-penetrating CNTs for delivery of therapeutics. *Nano Today* **2**, 38-43 (2007).
- 53 Liu, Z., Tabakman, S., Welsher, K. & Dai, H. Carbon nanotubes in biology and medicine: In vitro and *in vivo* detection, imaging and drug delivery. *Nano Research* **2**, 85-120 (2009).
- 54 Bottini, M. *et al.* Full-Length Single-Walled Carbon Nanotubes Decorated with Streptavidin-Conjugated Quantum Dots as Multivalent Intracellular Fluorescent Nanoprobes. *Biomacromolecules* **7**, 2259-2263 (2006).
- 55 Shi, D. *et al.* Quantum-Dot-Activated Luminescent Carbon Nanotubes via a Nano Scale Surface Functionalization for *in vivo* Imaging. *Advanced Materials* **19**, 4033-4037 (2007).
- 56 Yang, S.-T., Luo, J., Zhou, Q. & Wang, H. Pharmacokinetics, Metabolism and Toxicity of Carbon Nanotubes for Biomedical Purposes. *Theranostics* **2**, 271-282 (2012).
- 57 Barone, P. W., Baik, S., Heller, D. A. & Strano, M. S. Near-infrared optical sensors based on single-walled carbon nanotubes. *Nature Materials* **4**, 86-92 (2005).
- 58 Biju, V., Itoh, T., Baba, Y. & Ishikawa, M. Quenching of Photoluminescence in Conjugates of Quantum Dots and Single-Walled Carbon Nanotube. *The Journal of Physical Chemistry B* **110**, 26068-26074 (2006).
- 59 Didenko, V. V. & Baskin, D. S. Horseradish peroxidase-driven fluorescent labeling of nanotubes with quantum dots. *BioTechniques* **40**, 295-296, 298, 300-302 (2006).
- 60 Cherukuri, P., Bachilo, S. M., Litovsky, S. H. & Weisman, R. B. Near-Infrared Fluorescence Microscopy of Single-Walled Carbon Nanotubes in Phagocytic Cells. *Journal of the American Chemical Society* **126**, 15638-15639 (2004).
- 61 Dai, H. Carbon Nanotubes: Synthesis, Integration, and Properties. *Acc. Chem. Res.* **35**, 1035-1044 (2002).
- 62 Michel, R., Pasche, S., Textor, M. & Castner, D. G. Influence of PEG Architecture on Protein Adsorption and Conformation. *Langmuir* **21**, 12327-12332 (2005).
- 63 Yang, S.-T. *et al.* Covalently PEGylated Carbon Nanotubes with Stealth Character *In Vivo*. *Small* **4**, 940-944 (2008).
- 64 Lindberg, B. J. *et al.* Molecular Spectroscopy by Means of ESCA II. Sulfur compounds. Correlation of electron binding energy with structure. *Physica Scripta* **1** (1970).
- 65 Stuart, B. H. *Infrared Spectroscopy: Fundamentals and Applications*. (John Wiley & Sons, 2004).
- 66 Choukourou, A. *et al.* Mechanistic Studies of Plasma Polymerization of Allylamine. *The Journal of Physical Chemistry B* **109**, 23086-23095 (2005).
- 67 Pecora, R. Dynamic Light Scattering Measurement of Nanometer Particles in Liquids. *Journal of Nanoparticle Research* **2**, 123-131 (2000).
- 68 Shannahan, J. H. *et al.* Comparison of Nanotube-Protein Corona Composition in Cell Culture Media. *Small* **9**, 2171-2181 (2013).

Chapter IV.

Effect of the Physicochemical Properties of CNTs in Biological Applications

Originally published as:

V. Ramos-Perez, A. Cifuentes, N. Coronas, A. de Pablo, S. Borrós. In: K. Hamad-Schifferli, P. Bergese, *Nanomaterial Interfaces in Biology: Methods and Protocols*, **2013**. Boston: Springer. 302

A. Cifuentes-Rius, I. Font, N. Coronas, N. Boase, K. Thurecht, V. Ramos-Perez, S. Borrós. *Advanced Healthcare Materials*, **2013** (*in preparation*)

4.1. Introduction

In the previous chapter, the covalent functionalization of rCNTs by PECVD has been successfully achieved and studied in detail. However, it has been demonstrated how some parameters such as the dispersive properties of the resulting modified CNTs solution, the concentration used, and the formation of supramolecular complexes when in contact with the biological medium are of vital importance.¹⁻³ All these factors may have a direct impact on their cellular uptake and cytotoxicity due to the formation of large aggregates that may eventually cause cell death. Thereby, a deeper understanding of these crucial parameters is required in order to maximize the cellular internalization process without major toxicity issues.

In the recent years, different investigations about cellular uptake of CNTs and their cytotoxic effects have been carried out, resulting in a collection of conflicting published data.¹⁻⁶ Some research studies confirm low or insignificant cellular responses when SWNTs or MWNTs are exposed to several cell types, while others report toxic effects after the use of these delivery vectors.^{3,7,8} Nevertheless, among the majority of these studies, it is highlighted that there are several crucial parameters playing an important role in the internalization process and cytotoxicity. Not surprisingly, these parameters are closely related to both the mechanical traits of the used CNTs and its subsequent chemical modification, and together are known as physicochemical properties. The latter, as discussed in the previous chapter (Chapter III), have a direct influence on the biocompatibility and the degree of dispersion achieved in solution. The result would entail having individual CNTs well dispersed in the aqueous media or the formation of nanotube clusters and/or bundles, which are highly undesirable for biological applications. Suitable CNT dispersions may facilitate the diffusion of the particle through the plasma membrane following the nanoneedle effect whereas CNTs aggregation is more likely to decrease the viability of this delivery vector.⁹⁻¹¹ As said, mechanical characteristics of the CNTs have also a remarkable effect in their cellular uptake and can influence the dispersibility of the resulting complex as well. In other words, the nanotube length and rigidity are likely to play a key role on the penetration capability and may considerably vary the toxicity of the system.^{4,12,13}

In this regard, different procedures in the fabrication of CNTs are available, producing nanotubes in different lengths and diameters.¹⁴⁻¹⁶ For the case of MWNTs, the type of CNT studied in this thesis, the diameter mainly depends on the number of graphene layers forming the nanotubular structure, which directly affects the rigidity of the resulting nanotube. Both parameters, length and rigidity, are closely related to toxicity issues that the CNTs may cause.^{2,4,13} Kostarelos suggested that short or

tangled MWNTs could be successfully engulfed by macrophages and thus cleared *via* the lymphatic system, whereas long and rigid MWNT were not completely phagocytized causing mutagenesis and eventually cancer. However, the use of flexible CNTs that are prone to tangle may facilitate the formation of aggregates avoiding its threshold to the cell *via* nanopenetration and therefore forcing the endocytosis uptake.¹ Hence, the production of CNTs able to accomplish all the required mechanical and physical properties in order to be easily internalized by passive diffusion across the cellular membrane with a reduced level of toxicity is still far to be determined.

Additionally, some limitations in the fabrication of the CNTs may cause intrinsic differences between them complicating the homogeneity in size and shape within the same type of nanotube.^{2,3,17} Other differences such as subtle variations in local and overall charge, the remains of catalyst residues used during fabrication (typically Fe, Co and Ni) or several structural defects are prone to occur and may represent an issue in terms of toxicity.^{3,18} These impurities and flaws present in the inner structure of individual CNTs are hardly removed after production and subsequent purification.

To solve some of the problems explained above, the shortening of CNTs *via* oxidation methods has been presented as an interesting tool to control the length and presence of defects and metal impurities.^{14,15,19} Other approaches have been developed in the last decade, such as the mechanical cutting *via* sonication of the CNTs in contact with abrasive particles or through its exposure to a highly energetic electron beam.²⁰⁻²² Nevertheless, all these procedures require the application of rather harsh conditions to the nanotubes, damaging their sidewalls, increasing the amount of structural defects and ultimately altering their morphology. Thus, chemical oxidation of the CNTs takes advantage of the already existing defects in their structure, besides the new ones created during the process, in order to cut the nanotube in a more controlled way.^{14,15,19,23} The shortening process of the CNTs may also initiate from other highly energetic points of the nanotube morphology such as the end caps. Different oxidizing solutions have been employed for this purpose, typically acid based, and its oxidizing strength would depend on the CNTs used given their different mechanical properties.^{24,25}

On the other hand, since biomedical applications require stably dispersed nanotubes for the reasons previously commented, much attention is focused on the preparation of water-soluble carbon nanotubes. Typically, synthesis of carbon nanotubes yield tubes in the form of bundles.¹⁶ For such applications, individual nanotubes are more attractive than bundles, therefore the general idea is to separate the tubes in aqueous solutions by the addition of stabilizing or dispersant materials that prevents re-bundling and favors a stable dispersed state. In Chapter III we demonstrated that rCNTs could be covalently modified by PECVD techniques with ppPFM and ppAA, making them able to

condensate DNA, and how these vectors may become promising gene carriers for delivery applications. However, non-covalent functionalization of carbon nanotubes can also improve their chemical compatibility with the biological medium, enhancing their water solubility and improving their biocompatibility.^{11,26-28} These non-covalent treatments are achieved by coating the nanotube surface with amphiphilic molecules and are of a great interest as well, since the π system of the graphene sheets is not disturbed and the optical and electrical properties of CNTs are preserved. A wide variety of non-covalent surface treatments using surfactants, polymers or even biomolecules have been explored to obtain individually dispersed nanotubes in aqueous solutions.

Surfactants are amphiphilic compounds that have both polar and non-polar groups in the same molecule. In general, two clearly defined features can be identified in the surfactant structure, the hydrophilic region of the molecule or the polar head group and the hydrophobic region or the tail group that usually consists of one or few hydrocarbon chains. Such features are responsible for adsorption at the interface of immiscible phases. Surfactants adsorb onto hydrophobic surfaces due to strong hydrophobic attractions between the solid surface and the surfactant's hydrophobic tail, while exposing their polar head to the hydrophilic medium. This mechanism has been used extensively to stabilize supramolecular structures, such as stable colloidal dispersions.²⁹ Typically, dispersion of carbon nanotubes in aqueous solutions is achieved by adsorption of surfactant molecules on the nanotube surface *via* hydrophobic interactions, resulting in nanotube unbundling by steric and/or electrostatic repulsions. This process is favored with the help of ultrasonication, which is likely to help the surfactant molecules to intercalate between bundled nanotubes. A mechanism of nanotube dispersion from bundles has been proposed, where formation of gaps or spaces at the bundle ends under sonication promotes surfactant adsorption followed by propagation along the bundle length in a way that resembles an exfoliation or an unzipping mechanism.³⁰ Complete surfactant coating results in separation of individual nanotubes, which remain stable in aqueous media. The resulting nanotube-surfactant complex shall prevent rebundling and maintain nanotubes soluble in aqueous media. A wide variety of surfactants have been explored, resulting in different degrees of dispersion and stability. Different surfactant parameters, such as their nature, concentration and type of interaction (e.g. ionic vs. non-ionic) have been described to play a crucial role in the dispersibility of CNTs.³¹ The influence of the charge of the surfactant head-group has been investigated in various surfactant-CNT systems, revealing no clear preference between cationic or anionic head groups for nanotube dispersion.³²

The use of surfactant-coated carbon nanotubes has become a widely used procedure for aqueous applications; however, surfactants are known to mediate cell-toxicity, membrane de-stabilization

and/or protein unfolding. Therefore, engineering synthetic amphiphilic polymers able to fulfill same dispersion procedure as surfactants may increase biocompatibility. It has been reported that a variety of polymers are able to disperse carbon nanotubes bundles and render individually stabilized carbon nanotubes in aqueous media by polymer wrapping. In general, the interactions of the polymer chains and the surface of the nanotubes have been described as robust and uniform, and independent of the presence of excess amounts of polymer.^{26,33-36} Wrapping of carbon nanotubes with water-soluble polymers is a thermodynamically favorable process that limits hydrophobic exposure of nanotubes to aqueous medium. In addition, polymer wrapping enhances steric stabilization, resulting in prevention of nanotube aggregation. Based on experimental observations and computational studies, it has been suggested that solubilization of nanotubes occur in a multi-helical wrapping manner, where high surface and near monolayer coverage of tightly associated polymer around individual nanotubes is achieved.³⁶

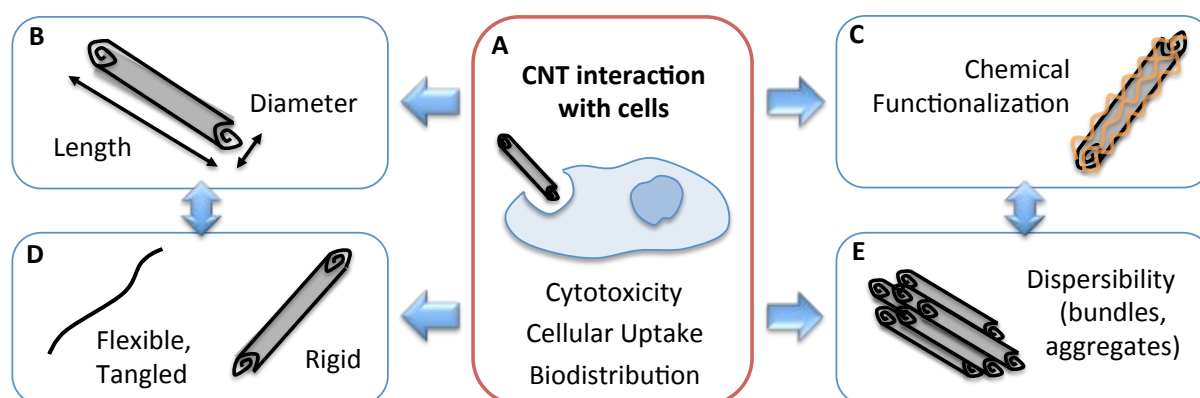
Although synthetic molecules and polymers have been shown to become chemically conjugated to or adsorbed on the surfaces of carbon nanotubes, it is quite challenging to obtain uniform, functional and biocompatible coatings for biological applications. Therefore, coating of nanostructures with biomolecules has been classically explored as an efficient strategy to overcome possible incompatibilities with the biological milieu. Biomolecules *per se*, such as proteins, lipids, polysaccharides and nucleic acids, are able to disperse carbon nanotubes to a certain extent without the need of covalent bonding.³⁷⁻⁴² In this case, dispersion is achieved by van der Waals interaction between the graphitic wall of the carbon nanotubes and the hydrophobic domains of such biomolecules.

Especially, nanomaterials conjugation with proteins is gaining prominence in the nanotechnology and bioengineering fields, forming what is known as protein corona, as it will be deeply analyzed in Chapter V.^{5,28,43,44} Proteins have been shown to adsorb strongly on the surface of carbon nanotubes, resulting in stable water-dispersed protein-CNT complexes. Several proteins, including bovine serum albumin, and enzymes, such as glucose oxidase have been successfully found to adsorb on the surface of carbon nanotubes.^{37,38} However, it is largely accepted that a fraction of proteins fail to retain their native structure upon adsorption on the nanotube surface, leading to partial loss of their biological activity.

It is generally accepted that all these physicochemical parameters of the CNTs have also a high impact in their behavior *in vivo*.⁴⁵⁻⁵² Therefore, biodistribution of these systems may vary when changing anyone of their properties like size (length and diameter), dispersibility (final geometry of

complexes formed in the biological medium), or chemical functionalization (surface charge and immobilized compounds).

As a result, this chapter seeks to solve some of these questions and achieve this suitable type of CNT not only by studying different types of nanotubes with differences in their physicochemical properties but also by optimizing the subsequent shortening of the used CNTs (s-CNTs) with different oxidizing agents. It has to be taken into account, that this oxidizing treatment may also improve the solubilization in water of these s-CNTs due to the creation of carboxylic acid chemical groups on the surface. Thus, the biocompatibility of these vectors are increased, alongside with the reduction of metal impurities and structural defects.²⁵ Hence, this chapter seeks to investigate the resulting dispersibility and cytotoxicity of the used nanotubes and their shortened versions, and how these parameters can be tuned by covalent and non-covalent functionalization (Scheme 4.1).

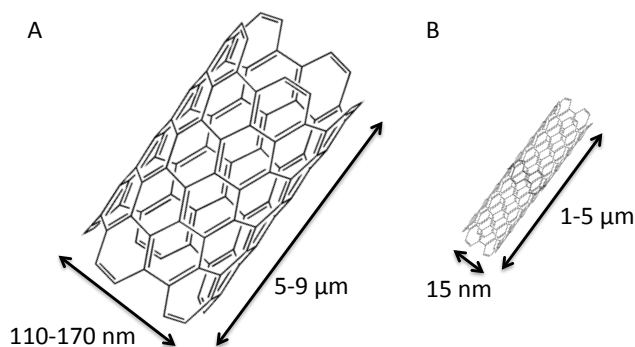


Scheme 4.1. Effect of the physicochemical properties of CNTs in their interaction with cells. Factors influencing the (A) cell internalization, viability and biodistribution of the CNTs: (B) size, (C) chemical functionalization, (D) stiffness and (E) dispersibility.

4.2. Experimental Section

4.2.1. CNT types Studied

Two types of MWNT were used in this part of this thesis (Scheme 4.2).



Scheme 4.2. Carbon nanotubes employed in this work; (A) rigid CNT (rCNT) and (B) flexible CNT (fCNT).

The same used in the previous chapter (chapter III), known as rigid CNTs (rCNTs) due to its high thickness (110-170 nm diameter) were studied in this part. These were purchased from Sigma-Aldrich, were obtained by CVD and were 5-9 μm long. Thinner MWNT were used as a comparison, known as flexible CNTs (fCNTs). They were also produced by CVD to strict length and diameter specifications (1 – 5 μm length, 15 nm diameter) and purified to > 95%.

4.2.2. Shortening Process

Cutting of CNTs by KMnO_4 Oxidation Treatment

rCNTs were heated to 590 °C for 3 h in a porcelain flask in order to oxidize and remove the amorphous carbon. Approximately, 25 mg of heat-treated carbon nanotubes were dispersed in 30 mL of 0.2 M solution of potassium permanganate (BioUltra with greater purity to 99.0%, Fluka; KMnO_4). Few drops of sodium hydroxide (Panreac; NaOH) 0.2 M were added until the pH of the dispersion was 10. The mixture was placed in an ultrasonic bath for 20 min and then refluxed for 40 min at 100 °C. The mixture was agitated for 20 h after adding 0.7 g of sodium sulfite (purity 99%, Panreac; Na_2SO_3) and 7 mL of concentrated sulfuric acid (Panreac; H_2SO_4). Milli-Q water was added to the mixture until the volume reached approximately 100 mL in order to stop the reaction, when it

was centrifuged (Hettich EBA 21) for 20 min at 1000 rcf. Part of the supernatant was removed and the pellet and the rest of aqueous phase were filtered through a polytetrafluoroethylene membrane (Millipore, FGLP 00 of 047) of 0.22 μm of pore size. During filtration, several washes were carried out; first, with a solution of 0.4 g/L NaOH, second with Milli-Q water, and finally with concentrated HCl to remove the manganese oxide (MnO_2) formed due to the reduction of the potassium permanganate. The washing procedure was continued until there was no typical brown color of manganese oxide remains on the filter. After filtration, the membrane with the filtered nanotubes (s-rCNTs) was vacuum dried for 2-3 days.

Basically, the same procedure was carried out for the fCNTs, except from the previous heating treatment. Adding the Milli-Q water to stop the reaction, 50 mL of HCl was added to dissolve the MnO_2 produced during the oxidation process. Once the solution was transparent, it was filtered through a 0.22 μm porous membrane. Finally, shortened fCNTs (s-fCNTs) were washed with Milli-Q water and lyophilized.

Oxidation of rCNTs using Piranha Solution

Only rCNTs were employed for this procedure. After the heating treatment, 1 mL of piranha per mg of rCNTs present was added. The piranha solution was prepared freshly by mixing H_2SO_4 and H_2O_2 in a ratio of 4:1 (v/v). The mixture with the rCNTs was agitated for 1 h (p1-rCNT) or 6 h (p6-rCNT). After this time, 1 L of Milli-Q water per each 100 mL of solution was added to reduce the oxidizing characteristics of the piranha. The dispersion was centrifuged for 30 min at 1000 rcf and part of the supernatant was removed. The remaining pellet and supernatant were again filtered through a polytetrafluoroethylene membrane of 0.22 μm of pore size. During filtration, the shortened rCNTs (p1-rCNT and p6-rCNT) were washed with Milli-Q water until pH 7 and finally with ethanol (Panreac). The membrane with the nanotubes was vacuum dried for 2-3 days.

Characterization of the shortened CNT (s-CNT)

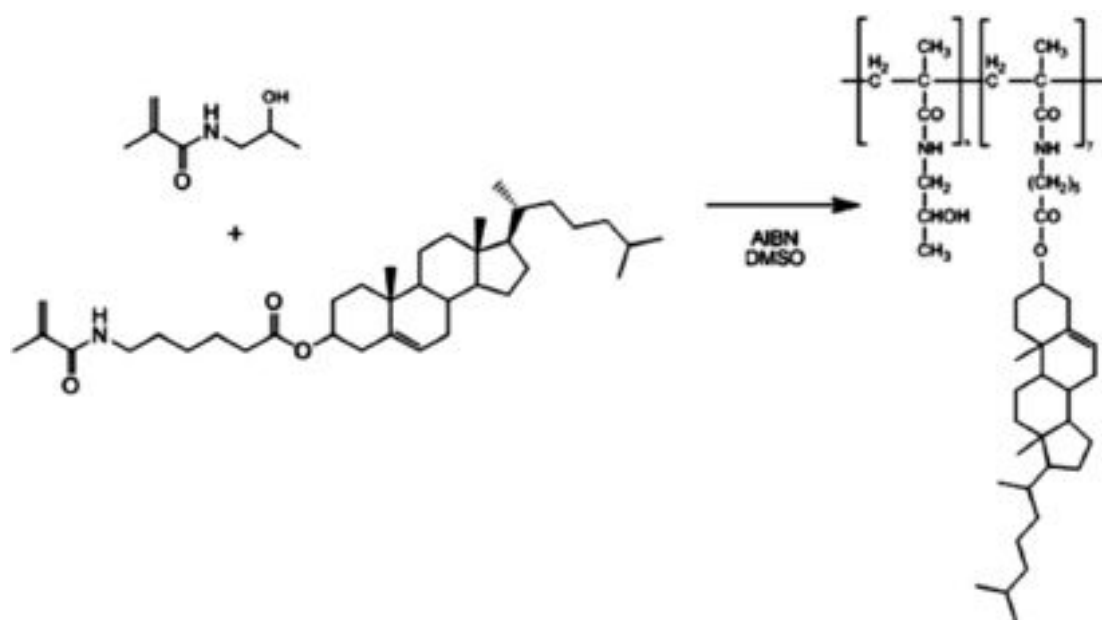
All types of CNTs (rCNTs and fCNTs) and their shortened versions were analyzed by HRTEM (JEOL LTD. 200 KV) equipped with an energy dispersive X-ray Spectroscopy (EDS) detector (Oxford LINCA). The HRTEM analysis was performed at the *Servei de Microscòpia de la Universitat Autònoma de Barcelona*. Similarly as in Chapter III, the chemical composition of the sample was also determined.

From the HRTEM images, 10-20 CNTs were measured and the average length was calculated.

4.2.3. Dispersibility Studies

Functionalization of CNTs

All types of CNTs (rCNTs, s-rCNTs, fCNTs and s-fCNTs) were non-covalently functionalized with cetyltrimethylammonium bromide (Sigma-Aldrich; CTAB), an amphiphilic polymer Poly[N(2-hydroxypropyl)methacrylamide (pHPMA) and proteins present in the human serum (Sigma-Aldrich; HS). The amphiphilic polymer pHPMA, with a content of 5% cholesterol, was synthesized in our laboratory (Materials Engineering Group (GEMAT), Institut Químic de Sarrià (IQS)) as shown in Scheme 4.3.



Scheme 4.3. Amphiphilic polymer (pHPMA) synthesis. Scheme of the pHPMA synthesized in the GEMAT group (IQS) able to disperse carbon nanotubes in water. The polymer was obtained by free radical polymerization of a monomer N-(2-hydroxypropyl) methacrylamide (HPMA) with a methacroylated derivative of cholesterol (Ma-ACAP-chol) synthesized in the lab. The total concentration of monomers was fixed at 12.5% (w/w), and the concentration of initiator azobisisobutyronitrile (AIBN) in 2.0% (w/w), which after the polymerization and purification resulted in a pHPMA copolymer having a molecular weight average of 25,000 g/mol.

All CNTs were weighted and dissolved in a solution of each dispersing agent as shown in Table 4.1, in order to achieve a final concentration of 1 mg/mL in solution. CTAB was dissolved in Milli-Q water. pHPMA was firstly dissolved in dimethyl sulfoxide (Sigma-Aldrich; DMSO) and subsequently diluted in Milli-Q water to achieve a maximum of 2% of DMSO (v/v). HS solution was prepared filtering the as-received HS and diluting it in phosphate buffer (Sigma-Aldrich; PhB) 5 mM and pH 7.4.

Table 4.1. Concentrations used to disperse the CNT by non-covalent functionalization.

Dispersing Agent	Concentration
CTAB	5 mM
pHPMA	4 mg/mL
HS	10%

Moreover, CNTs were also modified with ppAA by PECVD following the protocol described in Chapter III. After placing the CNTs into the reactor chamber, the AA monomer was fed into reactor (Scheme 2.4) and the polymerization parameters were set at W_i of 15 W, 10/20 of DC . The polymerization was carried out for 5 min and repeated 3 times, shaking the CNT powder in between. After modification, CNTs were dissolved in acetate buffer (25 mM and pH 5; NaOAc) obtaining the same final concentration of 1 mg/mL in solution.

All samples were dispersed in an ultrasonic bath for 2 h. After this time, 50 μ L of each sample was stored for further quantification and characterization. The rest was employed to track the stability over time of the systems in solution.

Characterization of the Functionalized-CNTs

Solutions around 10 μ g/mL of each system (rCNTs, s-rCNTs, fCNTs and s-fCNTs), including non-functionalized CNTs, were prepared in Milli-Q water, except for the HS-coated and ppAA-modified CNTs that were dissolved in PhB 5 mM (pH 7.4) and NaOAc 25 mM (pH 5), respectively. Zeta potential and DLS measurements were carried out using a Zetasizer Nano ZS (Malvern Instruments) followed by the dispersion of the samples for 15 min in an ultrasonic bath.

Analysis of the Dispersibility and Time Stability in Aqueous Media

Firstly, a set of dispersions (from 2.5 μ g/ml to 40 μ g/ml) was prepared by diluting the original dispersions (1 mg/ml) with Milli-Q water for the CNT-CTAB and CNT-pHPMA complexes, PhB 5 mM for the CNT-HS ones and NaOAc 25 mM for the ppAA-modified CNTs. These dispersions were dispersed for 30 min before placing them to a 96-well plate (flat bottom; Nunc) and the absorption at 500 nm was measured using a microplate reader (Infinite M200, Tecan Group Ltd.). The absorbance acquired at this wavelength was used to determine the concentration of the CNTs in solution by the previous preparation of a calibration curve with a set of dispersions at a known concentration.

After sonication, samples were left at room temperature (RT) and 100 μL of the suspension (without stirring) were subtracted from each vial after 30 min, 1 h, 2 h, 16 h and 24 h. The subtracted volume was immediately analyzed in the microplate reader measuring the absorbance at 500 nm.

Pictures of the vials were taken right after sonication and also after being left 1 h and 24 h at RT.

4.2.4. Evaluation of the Cell Viability of the Complexes

Cytotoxicity was measured in 3T3 cells (ATCC) using the MTS assay (CellTiter 96[®] AQ_{ueous} One Solution Cell Proliferation Assay) from Promega. Before that, images of the wells were taken with the microscope (Olympus IX51). All analysis were developed at the tissue culture facilities of the Australian Institute for Bioengineering and Nanotechnology (AIBN) at University of Queensland (UQ).

Study of the Effect of Size, Incubation Time and CNT Concentration

Cells were plated into 4 different 96-well plate at a concentration of 10000 cells/well (150 μL /well) in supplemented medium formed by DMEM/F-12 high glucose 4.500 mg/L (GLUTAMAX[™]), 1% P/S (Invitrogen) and 10% of FBS (Gibco[®]). After allowing 24 h for the cell attachment at 37 °C and 5% CO₂, CNTs (rCNTs, s-rCNTs, fCNTs and s-fCNTs) were diluted appropriately in fresh media in order to have a final concentration of 4, 10 and 30 $\mu\text{g}/\text{mL}$. 150 μL of each solution was added to the plates in triplicates. Cells were washed with sterile PBS 1x and new media was added after 3 hours for one plate, 24 h for another and 48 h for the third. The forth plate was left in continuous exposure to the CNTs until the cytotoxicity assay was carried out (after 72 h). Cell viability for the 3 plates was determined by the addition of MTS (diluted at 20% in fresh DMEM as specified by the supplier) after 72 h. Before adding the MTS reagent, cells were washed with 100 μL of sterile PBS 1x and the absorbance was measured at 490 nm in order to determine the background absorbance of the CNTs for further calculations. Once with the MTS reagent, cells were left 40 min at 37 °C and 5% CO₂ and the absorbance at 490 was measured again. The absorbance of a positive control with only 3T3 cells (considered 100% of viability for further quantification) and a negative one with the MTS reagent alone (both in triplicates) was also determined.

Analysis of the Influence of the CNT Chemical Functionalization on the Cytotoxicity

Solutions of all kinds of CNTs (rCNTs, s-rCNTs, fCNTs and s-fCNTs) differently coated (CTAB, pHPMA, HS and ppAA) were prepared to a final concentration of 100 $\mu\text{g}/\text{mL}$ as previously commented in

section 4.2.3 (Table 4.1). Complexes were washed twice by centrifugation at 10000 rcf for 30 min and the first supernatant was stored to be analyzed as well.

Cells were plated and grown as above described. After 24, they were incubated with 4 µg/mL of each type of CNT with the different coatings in fresh supplemented DMEM. Same dilutions were done for the supernatant stored from the particles washes, corresponding to the excess of dispersing agent unbound from the CNT surface. Absorbance at 490 nm was measured following 48 h of continuous exposure of the CNTs. The determination of a background absorbance value of the CNTs into the cells in PBS and the measurement of positive and negative controls were also carried out.

4.2.5. Study of the *In Vivo* Biodistribution of CNTs in Mice

Preparation of Fluorescently-Labeled CNT Complexes

An infrared (IR) dye (IRDye® 750 Infrared Dye NHS Ester) purchased from Li-Cor was covalently immobilized on the ppAA-modified CNT surface. All types of ppAA-coated CNTs (rCNTs, s-rCNTs, fCNTs and s-fCNTs) were dissolved in PhB 10 mM at pH 9 in order to obtain around 600 µL of sample volume (500 µg/mL). Then, 50 µL of the 1 mg/mL dye solution in DMSO anhydrous (Sigma-Aldrich) was added and the mixture was left overnight at RT and protected from light. After this time, the fluorescently-labeled CNTs were washed twice. The washing procedure involved the centrifugation of the particles at 13500 rcf and dissolving with PBS 1x at pH 7.

The concentration of fluorescently-labeled CNT solution was determined in the microplate reader as explained before. Moreover, the quantity of covalently attached dye was quantified measuring the absorbance at 756 (maximum absorbance) and knowing that its extinction coefficient in PBS is $260000 \text{ M}^{-1}\cdot\text{cm}^{-1}$. A baseline of ppAA-coated CNTs at same concentration was also measured.

Biodistribution Study in Mice

All animal experiments were performed in compliance with the local ethics committee of the Australian Institut for Bioengineering and Nanotechnology (AIBN) and the Centre for Advanced Imaging (CAI) at the University of Queensland (UQ).

In this study, 150 µL of the fluorescently-labeled CNTs (F-CNTs) were intravenously injected by the tail vein to each C57BL/6J mouse at concentration ranging from 150 to 300 µg/mL. Each type of CNT

(rCNT, s-rCNT, fCNT and s-fCNT) was injected 3 different mice. The biodistribution of the fluorescent CNTs were monitored *in vivo* over a period of 1 h, 8 h and 24 h after injection using fluorescence imaging (Carestream Molecular Imaging *In vivo* MX Pro, Bruker). All mice were sacrificed 24 h post-injection and their main tissue organs (liver, stomach and intestines, lung, kidneys, spleen and heart) were immediately dissected and fluorescently imaged *ex vivo*. All data was processed using the ImageJ software.

4.2.6. Evaluation of the pGFP Complexes

Formation of the ppAA-coated CNT Complexes with pGFP

Complexes of pGFP with of all types of ppAA-modified CNTs were formed and characterized by gel agarose electrophoresis as detailed in Chapter III. Basically, complexes of CNT-ppAA were prepared and incubated with the same pGFP (ratios from 1:1 to 200:1 (w/w)). Complexes were loaded to the gel wells and it was run for 1 h at 65 V.

Cell Transfection Analysis of the pGFP Vectors

Cell transfection was carried on 3T3 cells, which were plated as explained in section 4.2.4 and were also performed at AIBN facilities (UQ). CNT-ppAA+pGFP solutions (4, 10 and 30 $\mu\text{g}/\text{mL}$) were prepared in fresh DMEM and added to the cells (triplicates). Cells were washed after 24 h. After 48 h, the transfection was confirmed by a fluorescent microscope (Olympus IX51) and flow cytometer (AccuriTM C6, BD Biosciences). A positive control was used (GeneJuice[®] Transfection Reagent, Merk Millipore; GJ) and prepared by mixing 2.7 μL of GJ with 300 μL of DMEM. After 5 min at RT, 60 μL of pGFP (18 $\mu\text{g}/\text{mL}$) was added and left for 15 min at RT. The resulting mixture was diluted 6 times in order to ensure that 50 ng/well (100 μL) of pGFP were incubated with the cells (triplicates). Moreover, cell viability was also determined by the MTS assay previously explained (section 4.3.3).

The same procedure was carried out with cos-7 cells (ATCC). However, only rCNTs and s-rCNTs modified with ppAA were tested in a concentration of 4 $\mu\text{g}/\text{mL}$. The GFP production was confirmed by fluorescence microscopy (Leica UK Ltd, Milton Keynes, UK).

4.3. Results and Discussion

4.3.1. Shortening of CNTs

The importance of the physical properties of the CNTs employed as gene or drug delivery vectors has been previously discussed. Becker and co-workers, Raffa *et al.* and Kostarellos, among others, have already reported the importance of the final length of these nanomaterials in terms of cellular uptake and biocompatibility.^{3,4,9,53} However, there are several conflicting results due to the lack of consistency resulting from differences in the experimental protocols used. Moreover, different types of CNTs with different kinds of functionalization are being tested, which makes the comparison of the results even more difficult. Therefore, the need of controlling all these parameters in order to understand the resulting behavior of the functionalized complexes has attracted most of the attention in the recent years. As a result, this first part of the chapter aims to develop a CNT shortening method to obtain short CNTs (s-CNTs) with a reduced length but maintaining the mechanical properties such as rigidity/flexibility from the originally purchased CNTs.

In the recent years, some oxidation treatments have become efficient means of creating short CNTs.^{14,15,23,25} The shortening of CNTs by chemical oxidation starts with the oxidative attack of already existing active sites, such as sidewall defects known as Stone-Wales defects (rings made up of 5 to 7 carbon) and the less energetically stable end caps of each individual CNT. As a continuation to this oxidation process, the consumption of the graphene sidewall around the vacancy defect or nanotube end induces the actual shortening of the nanotube. Some studies suggest that the use of strong oxidative acids leads to the generation of more defects on the CNT structure that helps to obtain shorter CNTs.^{15,25} However, the employment of these aggressive reagents may dramatically affect their structural integrity. Therefore, of special interest is to develop a shortening procedure that exposes the CNTs to rather mild conditions in order to reduce the negative impact on their chemical and physical intrinsic properties. In this context, it is especially interesting to evaluate and control the effect of the cutting methodology on the CNT morphology.

Optimization of the Shortening Process on rCNTs

The cutting approach followed in this study was based on a combination of the previous work done by Aitchison *et al.* (2007) and Ziegler and colleagues (2005).^{14,15} In the first one, CNTs were treated with a KMnO_4 solution whereas the second used a piranha oxidation treatment. Given the mild

oxidation conditions that the former approach entailed, CNTs were incubated with the KMnO_4 solution (0.2 M) for 20 h (s-CNTs). On the other hand, the piranha solution (4:1 v/v H_2SO_4 : H_2O_2) involved a more aggressive oxidation that caused the reduction of the treatment time (1 h and 6 h for the p1-CNTs and p6-CNTs, respectively). The same type of CNTs (rCNTs) used in the previous chapter (Chapter III) was employed for these treatments and the resulting shorter rCNTs (s-rCNTs) were characterized by HRTEM and compared to naïve rCNTs (Figure 4.1).

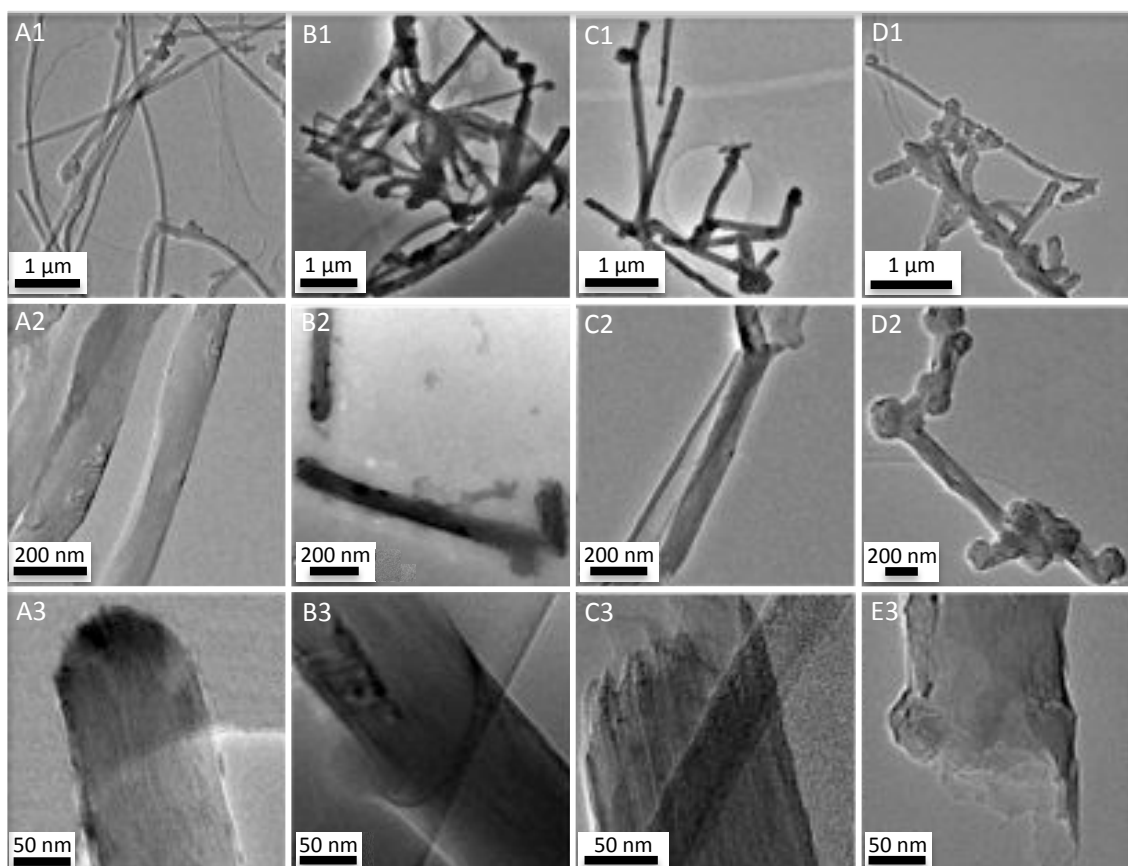


Figure 4.1. Shortening procedure evaluation of rCNTs by HRTEM. Images of the (A) as purchased rCNTs, (B) treated with KMnO_4 solution 0.2 M for 20 h (s-rCNTs), and after the incubation with the piranha solution (4:1 v/v H_2SO_4 : H_2O_2) for (C) 1 h (p1-rCNTs) and (D) 6 h (p6-rCNTs).

HRTEM images in Figure 4.1 show that the 3 treatments carried out in this work led to shorter CNTs. From these images (and others not shown), the resulting length of the CNTs after each treatment was determined. Therefore, between 10 and 20 individual CNTs are measured, confirming a significant length reduction after oxidation (Figure 4.2). The obtained results suggest that all treatments reduced the rCNT length by half; even it was decreased around 60% when the piranha solution was used. A high polydispersity was also observed on all types of CNTs, probably due to the

combination of two factors. The first one, as already commented in Chapter III, is basically as a result of the lack of control during the rCNT synthesis, leading to the production of differently-sized nanotubes. Secondly, the fact that the same cutting procedure cannot be guaranteed for all rCNTs present in the solution aggravates the different shortening degree observed. As stated before, it is known that the rCNT oxidation is initiated on the most energetic points along their surface, which are usually centered on the tips and on their structural defects (Stone Wales).^{14,15,17,19,23,54,55} Since neither of these two parameters can be controlled in the CNT production, the effect of the oxidizing agent is hardly foreseeable.

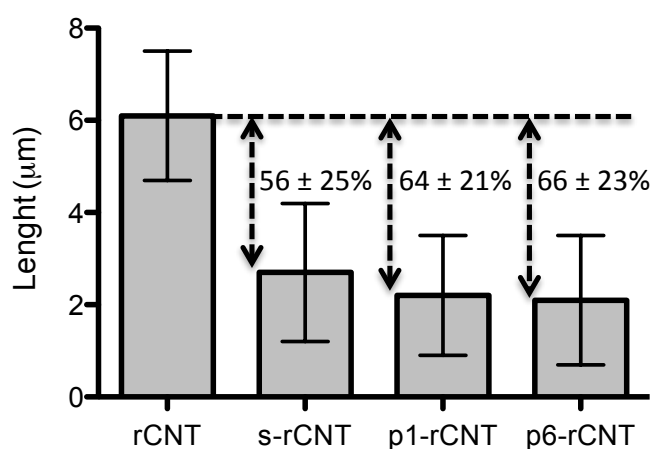


Figure 4.2. Average length (μm) of all shortened rCNTs. Results compared to the naive rCNTs.

Shorter CNTs were successfully obtained and the morphology of the oxidized rCNT was studied in detail. By carefully looking at the TEM images on the first row of Figure 4.1 (Figure 4.1-1), samples treated with piranha solution for 6 h (p6-rCNTs, Figure 4.1D1) presented a large amount of protuberances along the CNT surface. These irregularities were not observed on the other samples, both oxidized and untreated (Figure 4.1A1, B1 and C1). This observation was confirmed on closer examination (second row of Figure 4.1, Figure 4.1-2). Specifically, this phenomenon was not observed for the treated rCNTs with the same oxidizing agent but for a shorter time of incubation (p1-rCNTs, Figure 4.1C2). Therefore, the deformation of the CNT surface might be directly related to the long duration of the treatment with an excessively aggressive oxidizing solution such as piranha. In this hostile environment, the carbon of the rCNTs and the piranha solution react causing an excess of carbon dioxide (CO_2) gas production. This gas bubbles becomes trapped on the rCNT structure, forming the irregularities observed.¹⁴ Hence, the shortening procedure in these conditions was dismissed due to the high alteration that this treatment caused to the rCNT structure.

Concurrently, when looking at the rCNTs in more detail (third row of Figure 4.1, Figure 4.1-3), it could be seen that whatever cutting approach was applied to the rCNTs, the oxidation caused the opening of their end tips. Given their curvature and due to the likely presence of rings formed by 5 atoms of carbon, they are energetically less stable and thus easily react with any oxidizing agent present.^{14,19,54,56,57} However, the resulting rCNT ends after the piranha treatment (Figure 4.1C3 and D3) exhibited a more degraded and less homogeneous cut when compared to the s-rCNTs obtained by KMnO_4 (Figure 4.1B3). In this last case, (s-rCNTs) the morphology of the treated tips was minimally altered and the structural integrity seemed to be maintained, looking similar to the naïve rCNT caps (Figure 4.1A3). Additionally, Figure 4.1B2 confirmed that the KMnO_4 solution, despite being a less aggressive treatment comparing to the piranha oxidation (even for 1 h, shown in Figure 4.1C3), was not only able to cut the rCNTs from the ends but also from specific points of the sidewall.

Besides the morphologic change suffered after cutting, the chemical modification of the treated rCNTs was determined by EDS and compared to the naïve rCNTs (Figure 4.3).

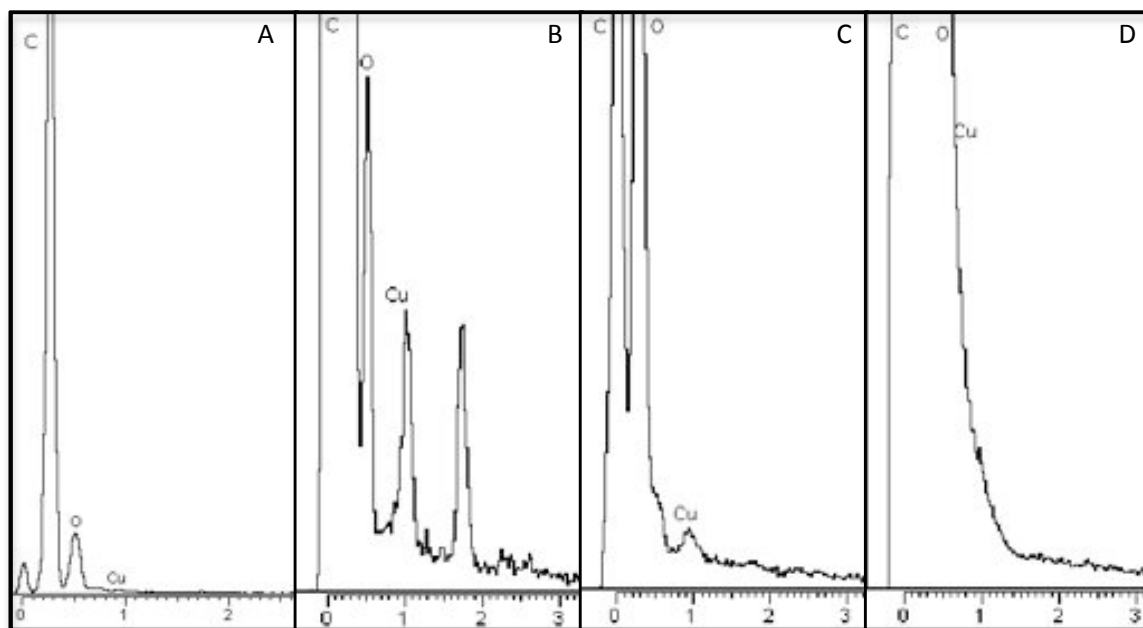


Figure 4.3. EDS of the shortened rCNTs. Results of the HRTEM-analyzed samples; (A) naïve rCNTs, and oxidized rCNTs by (B) KMnO_4 reagent and by piranha solution for (C) 1 h and (D) 6 h.

The relative atomic percentage was also calculated (Table 4.2). This elemental chemical analysis evidenced an increase of oxygen content on the treated samples. The variation observed was moderate for the s-rCNTs and p1-rCNTs, whereas it was more significant for the p6-rCNTs. In other

words, the oxidation degree of the treated rCNTs is likely to be in accordance with the aggressiveness of the shortening method applied.

Table 4.2. Relative atomic percentages of the elements found in the TEM-imaged samples.

Sample ID	%C	%O	%Cu
rCNT	92.95	4.61	2.31
s-rCNT	93.54	4.85	1.70
p1-rCNT	87.97	4.92	7.11
p6-rCNT	69.35	22.58	8.07

HRTEM characterization allowed the analysis of the effect of each oxidizing treatment regarding the final rCNTs structure, morphology and chemistry. As a result, the rCNTs shortened by the KMnO_4 solution (s-rCNTs) showed a higher retention of the initial physical properties and the structural integrity of the naïve rCNTs. Given the fact that it is a less aggressive oxidation reagent and that the treatment requires a longer period of time, it leads to a major control of the cutting process.

Shortening of Thin and Flexible CNTs (fCNTs)

The unquestionable importance of the physical properties of the CNTs employed as a delivery vector in terms of cell uptake has already been discussed.^{1,2,4,5} As it has been stated, it is of special interest the influence that the diameter and thus the rigidity of the CNTs has in the internalization process.¹³ Hence, a thinner type of CNT was studied in this work (around 15 nm), which results in a more flexible type of CNT. These flexible CNTs (fCNTs) are 1 to 5 μm long. A cutting protocol to achieve shorter fCNTs with the same physical properties was adapted from the one optimized for the rCNTs.

Since the fCNTs are thinner than rCNTs, their robustness may be lower and thus the aggressiveness of the environment that they are able to handle is probably modest.¹⁵ In this context, significant sidewall damage and surface etching is likely to occur to the nanotubes with smaller diameter. Hence, the shortening method employing the KMnO_4 solution was applied to the fCNTs and the resulting short fCNTs (s-fCNTs) were also tracked by HRTEM (Figure 4.4). It is noticed that fCNTs showed less contrast compared to the rCNTs due to the lower amount of graphene layers that make them up, which is actually the cause of their lower diameter and, accordingly, their flexible behavior. Additionally, it should also be remarked how the fCNTs were more prone to bend than the rCNTs.

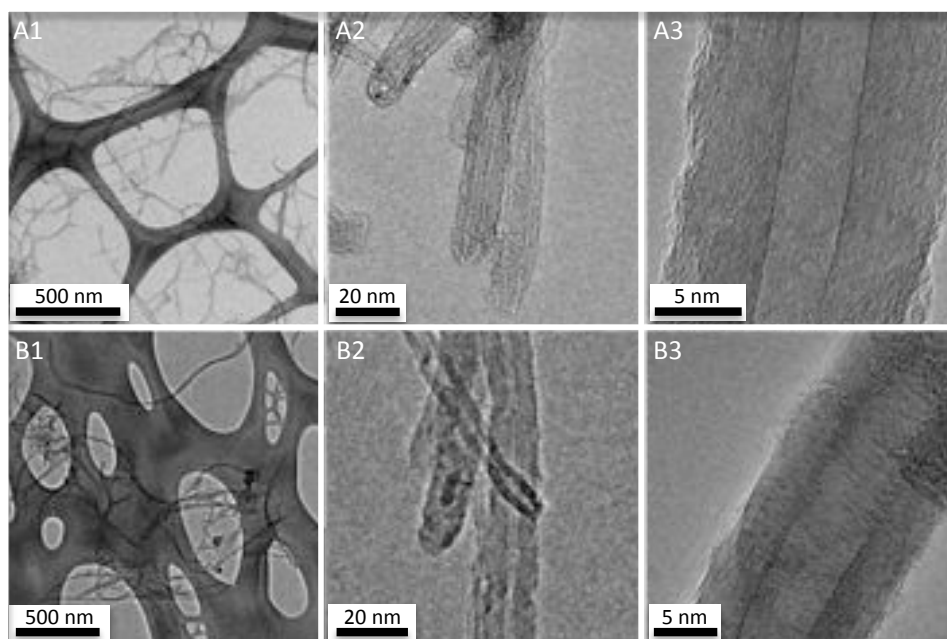


Figure 4.4. HRTEM images of the (A) naïve fCNTs and (B) the s-fCNTs, their shortened version.

Figure 4.4 exhibits that fCNTs were successfully cut resulting in shorter fCNTs (s-fCNTs), without altering the structural integrity of the naïve fCNTs. Measuring the length of 10-20 individual s-fCNTs, a reduction of approximately 60% was achieved (Figure 4.5). Therefore, fCNTs decreased from around 3 μm to nearly 1 μm (s-fCNTs) on average. Again, large error bars were obtained due to the high polydispersity as a consequence of the variation of sizes found in the original fCNTs combined with the different cutting degrees that this approach entails. Therefore, the length of the s-fCNTs varied from 200 nm to 4 μm , whereas the untreated fCNTs measured between 1 and 5 μm .

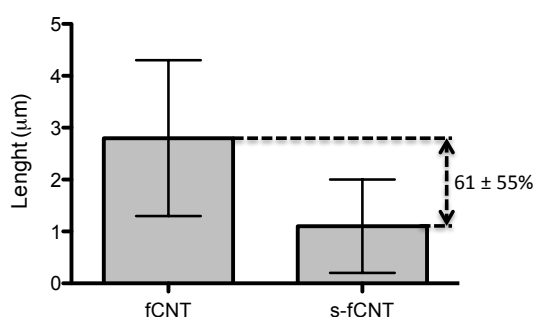


Figure 4.5. Mean of the lengths of the naïve fCNTs and s-fCNTs. Values measured using the HRTEM images.

As done for the rCNTs, EDS analysis allowed the determination of the chemical composition of the treated and bare fCNTs. Results are shown in Figure 4.6 and relative atomic percentages of the elements found in the samples are summarized on Table 4.3.

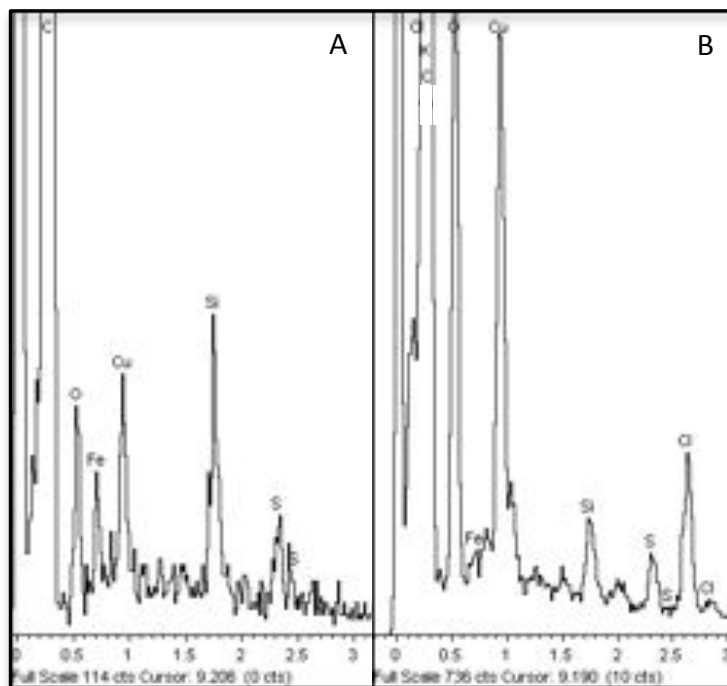


Figure 4.6. EDS of the flexible CNTs before and after shortening. Analysis of (A) naive fCNTs and (B) cut s-fCNTs imaged by HRTEM.

By focusing on the elements present on the naïve fCNTs (Table 4.3), some differences from the rCNTs could be appreciated. Specifically, some elements not detected on the rCNTs were indeed found on the flexible tubes (Si, S, Fe). These types of impurity are typically residues from the production and purification procedures of the fCNTs. When fCNTs were treated with KMnO_4 not only the nanotube length was decreased but also the presence of impurities was minimized. Interestingly, different researchers confirm that these impurities, especially catalyst metal contaminants introduced during their synthesis and purification, are one of the key factors that induce toxicity.^{2,3,18,58}

Table 4.3. Relative atomic percentages of the fCNTs and s-fCNTs analyzed by HRTEM

Sample ID	%C	%O	%Si	%S	%Fe	%Cu	%Cl	%K
fCNT	97.72	0.67	0.29	0.09	0.37	0.87	-	-
s-fCNT	95.77	2.31	0.08	0.07	0.03	1.57	0.17	0.05

Hence, results on Table 4.3 demonstrate that obtaining short nanotubes by an oxidizing treatment with KMnO_4 leads to the reduction and almost total elimination of all the residues found on the original fCNTs.

4.3.2. Dispersibility of the Different CNTs

As it has been introduced in Chapter I, while CNT length and metal impurities present on the purchased powder may have a remarkable effect on toxicity issues, the degree of dispersion is also a crucial parameter to be taken into account.¹⁻³ Moreover, this factor could also make a difference in the interaction of the CNTs with cells in terms of cellular internalization, since the agglomerated state has a direct impact on the final shape and surface area of the CNTs.^{9,10} Therefore, special attention needs to be paid in their proper solubilization of CNTs if individual and highly dispersed tubes are desired.

It has already been commented that pristine CNTs lack appropriate functional groups to enable covalent binding of biocompatible groups in order to make CNTs compatible with the biological milieu. Therefore, the surface of the CNTs requires modification by different chemical synthetic methods, by covalent or non-covalent functionalization, to generate appropriate functional groups, enabling covalent attachment or physical adsorption of suitable solubilizing, bioactive, or biocompatible moieties.

In this work, dispersion studies were carried out before and after the functionalization of the different types of CNTs (rigid and flexible) and their shortened versions. On the one hand, dispersibility of ppAA-modified CNTs by PECVD was studied, given the effectiveness of the rCNT-ppAA to bind pGFP as demonstrated in the previous chapter (Chapter III). On the other, different dispersion methodologies following the non-covalent functionalization principle were carried out. To do so, a cationic surfactant, the cetyltrimethylammonium bromide (CTAB), a synthetic polymer designed by our group (GEMAT), the Poly[N(2-hydroxypropyl)methacrylamide (pHPMA), and proteins present in the human serum (HS) were employed.

Characterization of the Functionalized CNTs

The two types of CNTs with different physical properties (rCNTs and fCNTs) and their shortened versions (s-rCNTs and s-fCNTs) were functionalized with a variety of coatings. Zeta potential measurements of the resulting CNTs confirmed its proper functionalization (Figure 4.7).

Naïve CNTs in water showed negative charge, specially the shortened ones due to the oxidation process suffered, which caused the formation of hydroxyl, carbonyl and especially carboxyl groups on the sidewalls and, predominantly, on the tips of CNTs.^{24,59} The CTAB-stabilized CNTs presented positive zeta potential, as a result of individual nanotubes being covered by surfactant molecules. A

positively charged surface was also measured for the ppAA-modified particles, evidencing the protonation of the amines at pH 5, as demonstrated in Chapter III. The dominance of the negative species on the HS led to a negatively charged CNT surface coated with the serum proteins. Neutral charge was obtained for the rCNTs and s-rCNTs coated with pHPMA, confirming the adhesion of this non-charged polymer on the nanotube surface. However, the synthetic polymer was not able to wrap the flexible CNTs. Such phenomenon is possibly caused by the large and rigid cholesterol groups of the pHPMA, which are not able to access the tangled CNT surface due to steric hindrance.

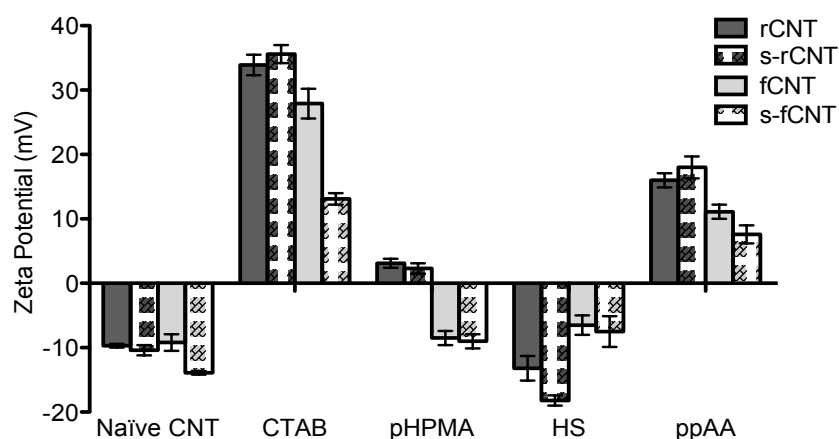


Figure 4.7. Zeta potential of the CNTs with different functionalities. Results of the two types of CNTs (rigid and flexible) and their shortened versions after being functionalized with CTAB, pHPMA, HS and ppAA.

DLS measurements of the coated-CNTs compared to the naïve ones allowed a qualitative determination of the dispersion degree (Figure 4.8), as commented in Chapter III.²⁸

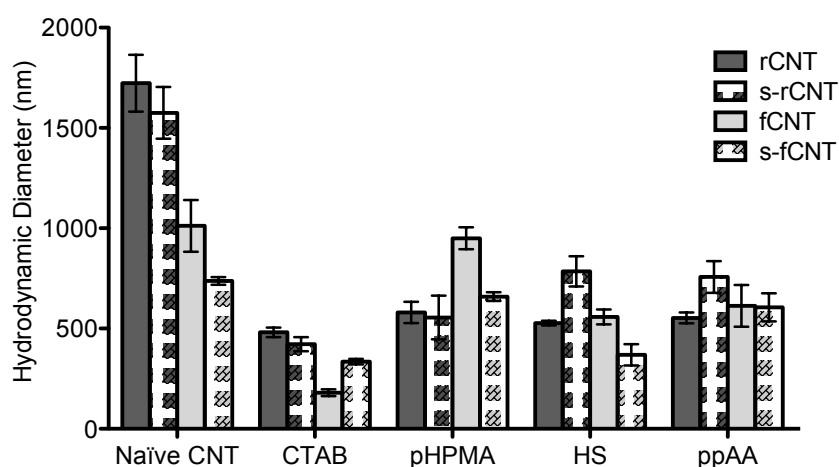


Figure 4.8. Hydrodynamic diameter of the CNTs with different functionalities. D_H measured by DLS of CNTs (rCNTs, s-rCNTs, fCNTs and s-fCNTs) after being functionalized by CTAB, pHPMA, HS and ppAA.

If the concentration of CNTs in the samples is maintained constant, the presence of large particles in solution suggests a lack of dispersion of the CNTs due to the unsuccessful debundling of the CNT aggregates. In other words, at same concentration, the smaller the particle size found in the corresponding dispersant agent, the better dispersion degree is achieved. By looking at the obtained results, CTAB-coated CNTs showed a higher dispersion degree for all cases. Nevertheless, in general terms, all type of functionalization led to a higher dispersibility of the CNTs, in exception of the pHPMA coating on the fCNTs and s-fCNTs. Flexible CNTs were not dispersed with pHPMA, as the zeta potential measurements suggested, since the resulting dispersion had the same size as the naïve particles in water.

Stability of the Dispersion over Time

Not only the achievement of suitable dispersion rates of the CNTs using different functionalities, but also the stabilization of the individual CNTs in solution over time is an important parameter to be studied. Solutions of functionalized CNTs (1 mg/mL) were prepared and after sonication in an ultrasonic bath for 2 h, the behavior of the dispersions was analyzed in detail (Figure 4.9 and (Figure 4.10).

Figure 4.9 shows modest differences between the thick rCNTs and its cut version, whereas remarkable changes are noticed on the flexible ones. Moreover, s-fCNTs showed a better stability than s-rCNTs. The shortening treatment may have caused a higher oxidation degree on the thinner nanotubes due to their lower resistance compared to the thicker ones, favoring its stabilization in water. In general terms, both rigid CNTs exhibited a better dispersion degree than the observed for the fCNTs, at least during the first hour after sonication. These observations were confirmed when the concentration of the functionalized CNTs that remained in solution was measured by UV-Vis spectroscopy, after leaving the dispersion settling down for 30 min, 1 h, 2 h, 16 h and 24 h at room temperature (Figure 4.10). In general, rCNTs and their shortened version (s-rCNTs) showed similar stability over time, whereas the fCNTs dispersibility significantly differed from the s-fCNTs. The former was more prone to settle than their shortened version, which exhibited higher stability in solution.

CTAB-coated CNTs were able to remain in solution for longer times than other surface modifications for both rCNTs and s-rCNTs (Figure 4.10, blue line; A and B, respectively). Lower stability of the other coatings (pHPMA, HS and ppAA; red, green and purple lines, respectively) was observed for the s-rCNTs compared to the rCNTs.

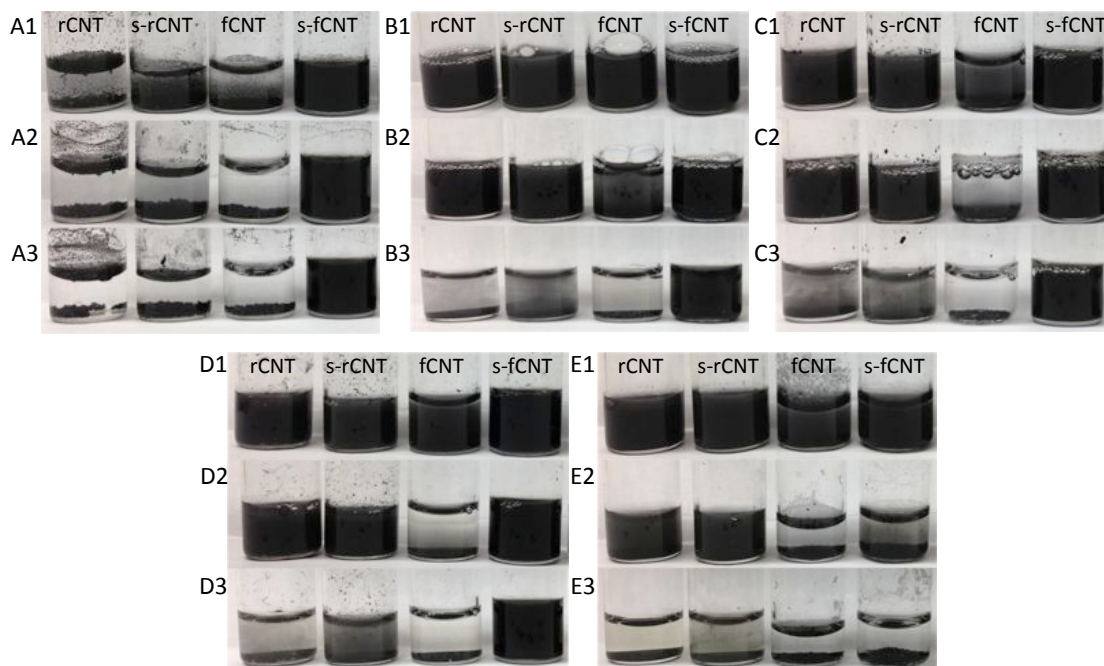


Figure 4.9. Dispersibility of CNTs with different functionalities. Vials corresponding to (A) naïve CNTs in Milli-Q water and functionalized with (B) CTAB, (C) pHPMA, (D) HS and (E) ppAA. (1) After sonication, (2) after 1 h at room temperature and (3) after 24 h. All CNTs were analyzed (rCNTs, s-rCNTs, fCNTs and s-fCNTs).

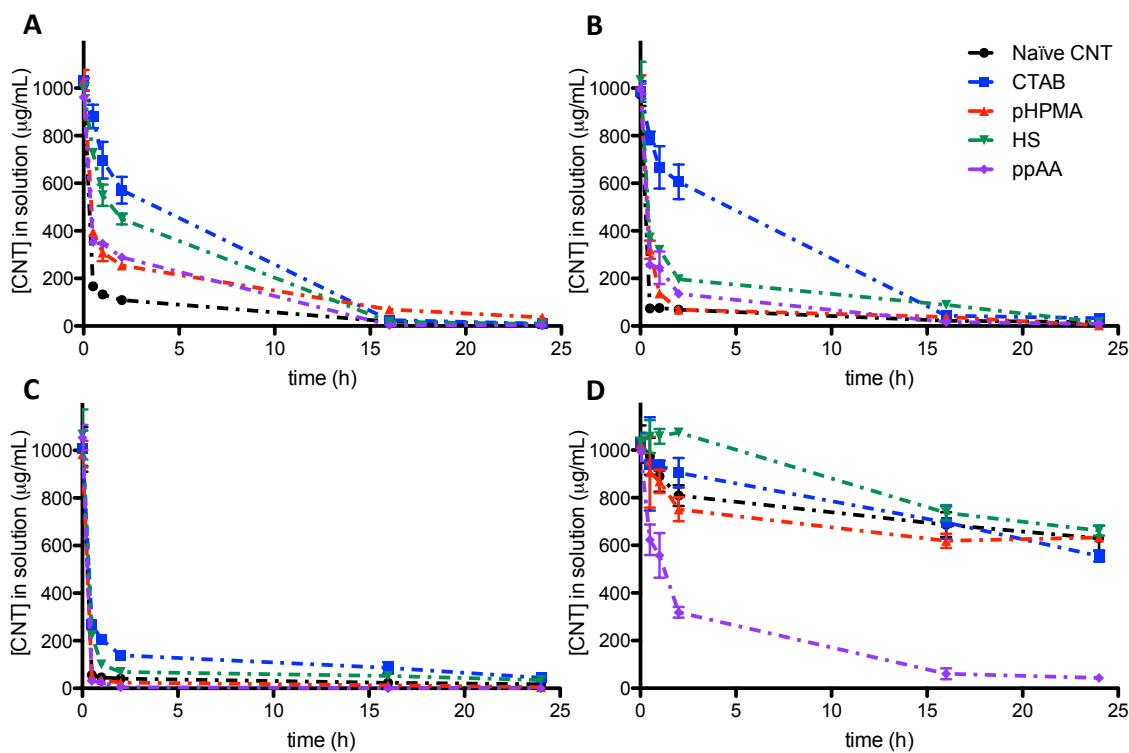


Figure 4.10. Concentration of functionalized-CNTs remaining in solution over time. Data obtained for (A) rCNTs, (B) s-rCNTs, (C) fCNTs and (D) s-fCNTs.

Firstly, although this loss of hydrophobicity does not affect the absorption of the CTAB, it may have been enough to decrease the pHPMA wrapping due to its larger hydrophobic group. Secondly, as it has been extensively discussed in Chapter II, fewer amounts of proteins from the HS are favored to attach on activated and moderately hydrophilic surfaces, whereas higher adsorption can be achieved on hydrophobic surfaces.^{60,61} Thus, s-rCNTs are prone to immobilize lower amount of proteins, showing a modest stability in solution when compared to rCNTs. However, the immobilization is enough to disperse the s-rCNTs in PhB. It is known that, although oxidized CNTs are soluble in aqueous solutions *per se*, they may aggregate in the presence of salts and other components found in biological fluids, and thus may not be used directly for most biological applications.⁶² As a result, any remaining oxidized groups on the ppAA-coated s-rCNTs may cause the decrease of the final dispersibility observed in presence of acetate buffer at pH 5.

On the other hand, significant differences were observed between the untreated flexible CNTs and their shortened version (Figure 4.10C and Figure 4.10D, respectively). fCNTs were barely dispersed with any of the stabilizing agents after 1 h of sonication, whereas well-stabled dispersions were obtained with the functionalized s-fCNTs. The tangled behavior of this thin and flexible type of CNTs in water probably complicates the proper functionalization in solution. By contrast, the improved dispersion that this kind of CNTs exhibited after the oxidation treatment allowed a superior functionalization and thus facilitated a longer stabilization. The high hydrophilicity of the s-fCNT surface due to the presence of a greater amount of active groups after cutting was already demonstrated by zeta potential (Figure 4.7). These results were confirmed by looking at the well-dispersed solution obtained in water (Figure 4.9A), which resulted in a highly stable dispersion over time (Figure 4.10C, black line). The hydrophilicity obtained for these s-fCNTs was significantly higher than the observed for the s-rCNTs (Figure 4.10B, black line). As a result, the excess of active sites may cause the immobilization of greater amounts of proteins and thus increases the dispersibility and stability of the complex in PhB (Figure 4.10C, green line). On the contrary, the ppAA-coating was not enough to stabilize the oxidized s-fCNTs in acetate buffer and aggregates were formed faster than without the deposited thin film in water (Figure 4.10C, black line). Moreover, because the ppAA deposition by PECVD consists in a dry process, the improved dispersibility of the oxidized s-fCNTs in water lack of importance and thus a similar behavior as the fCNTs was observed. Note that s-fCNTs supposedly coated with pHPMA presented the same stability as the non-functionalized s-fCNTs in water, confirming that the synthetic polymer was not able to successfully wrap the nanotube surface (Figure 4.10C; black line and red line, respectively).

Figure 4.11 presents the percentage of individual CNT remaining in solution after 1 h of sonication, where the observations discussed above can be confirmed. This study corroborates that various types of coatings could facilitate CNT dispersion and also demonstrates how the physicochemical properties of each type of CNT are equally important in the achievement of well-dispersed solutions. The behavior of these systems in solution would also have a direct impact in the cytotoxicity observed when used in biological applications.

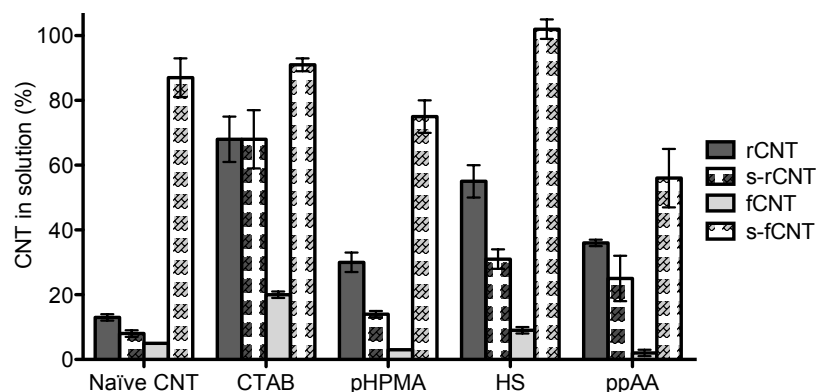


Figure 4.11. Percentage of CNTs dispersed in solution after 1 h of sonication. Data obtained for rCNTs, s-rCNTs, fCNTs and s-fCNTs, non-modified and functionalized with CTAB, pHPMA, HS and ppAA.

4.3.3. Effect of the CNT Structure and Surface Modification on Cellular Viability

As already commented, a lot of confusing and contradictory reports have been published in the recent years regarding toxicity issues when employing CNTs *in vivo* or *in vitro*. Among these inconsistencies, some are derived from the protocol followed such as the concentration of CNTs used and the incubation times explored. Others are caused by the physicochemical properties of the CNTs already discussed, which include length, defects and impurities present and dispersion degree. Consequently, these factors that may have a direct effect on the resulting cytotoxicity of the CNTs were assessed.

Assessment of the Effect of the Size, Incubation Time and CNT Concentration

Both types of CNTs (rCNTs and fCNTs) and their shortened versions (s-rCNTs and s-fCNTs), were dispersed in DMEM containing FBS, which is known to disperse CNTs similarly as HS did in the previous section.²⁸ Subsequently, 10 µg/mL CNT solutions were incubated into 3T3 cells for 3 h, 24 h,

48 h and 72 h, and cell viability after 72 h was measured by the MTS reagent protocol (Figure 4.12). Untreated rCNTs exhibited the same cell viability profile as their shortened version (s-rCNTs). As seen in the previous section, although they differ in length, both have similar physicochemical properties and dispersibility behavior, and as a result, similar cytotoxicity.

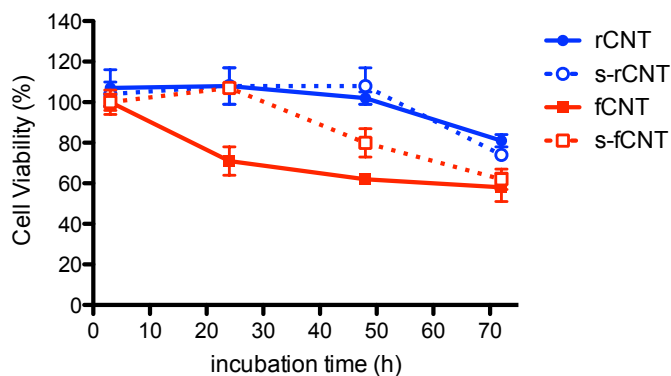


Figure 4.12. Cell viability of CNTs (rCNTs, s-rCNTs, fCNTs and s-fCNTs) in function of the incubation time.

Microscope images in Figure 4.13 suggest that the rigidity of the thicker CNTs allowed a better dispersion within the cell medium than the flexible CNTs and thus a higher amount of individual rCNTs and s-rCNTs could be found. It has been observed that fCNTs are more prone to tangle and form larger aggregates, which may induce an increase of cytotoxicity (Figure 4.13C and D). This decrease in cell viability was especially detected at higher incubation times. s-fCNTs showed a superior cell viability for larger incubation periods than the fCNTs, probably due to the fact that less impurities were present on the oxidized nanotubes, as previously demonstrated.

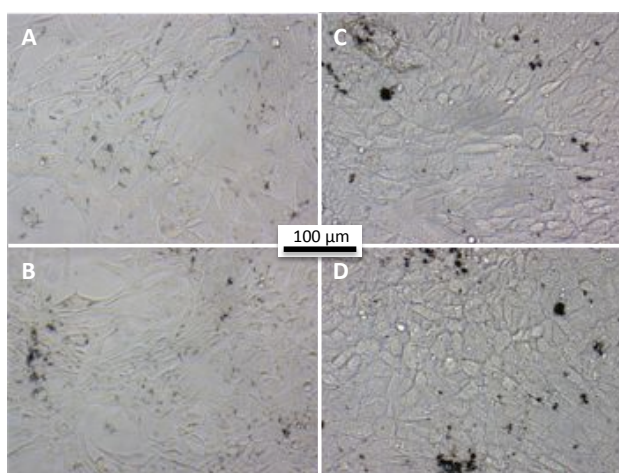


Figure 4.13. Microscope image (20x) of 3T3 cells incubated with CNTs. Images taken after 24 h incubation of 10 μg/mL (A) rCNTs, (B) s-rCNTs, (C) fCNTs and (D) s-fCNTs.

A similar tendency was observed when studying the effect of the concentration of CNTs used (Figure 4.14). Cell viability remained practically unaltered for both rigid CNTs. Only at high concentration of rCNTs (30 $\mu\text{g}/\text{mL}$) incubated for 24 h (Figure 4.14B) the viability decreased in approximately 10%, whereas cells treated with s-rCNTs showed full viability. Such phenomenon may be probably explained due to slight differences in dispersibility at high CNT concentrations. This hypothesis is reinforced by the fact that s-fCNTs exhibited superior cell viability than fCNTs at low concentrations (4 $\mu\text{g}/\text{mL}$ and 10 $\mu\text{g}/\text{mL}$), as it was expected.

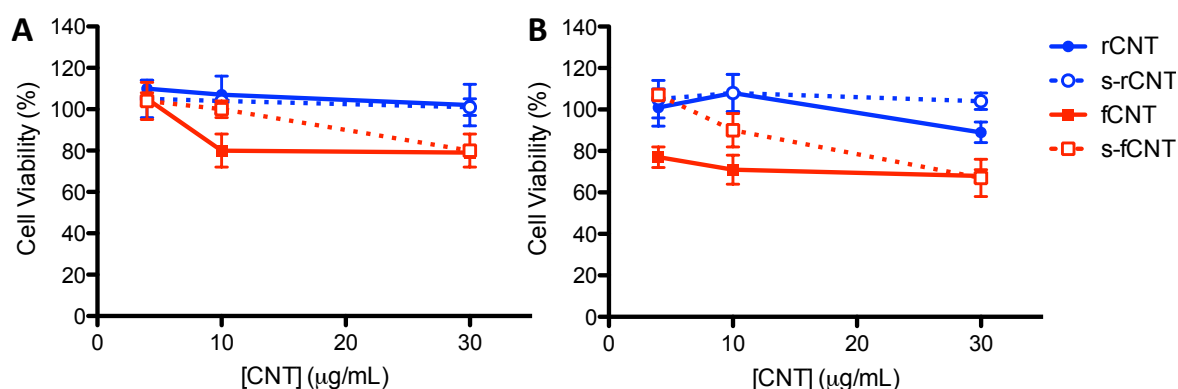


Figure 4.14. Cell viability of the CNTs at different concentration. Values measured after incubation in 3T3 cells at (A) 3 h or (B) 24 h.

Analysis of the Influence of the CNT Chemical Functionalization

The chemical nature of the coating on the CNT surface is of vital importance to circumvent dispersibility issues, as demonstrated before, and therefore would also have a direct effect on the cytotoxicity of these vectors. To investigate its influence, 4 $\mu\text{g}/\text{mL}$ of differently functionalized CNTs were incubated in 3T3 cells for 48 h and the cell viability was measured after this time (Figure 4.15). It is known that non-covalent functionalization approaches consist in a dynamic interaction of the stabilizing agent and the CNT surface, which involves a constant exchange of the surface ligand with the surrounding media.^{31,36,37} To discern the actual cytotoxicity of the non-covalent functionalization agent (CTAB, pHPMA and HS) from the final coated-CNTs, the first supernatant extracted from the washings of the CNTs was also analyzed.

Figure 4.15 exhibits the high cell viability achieved for all types of HS-coated CNTs (CNT-HS), probably due to the low toxicity also observed for the HS supernatant.

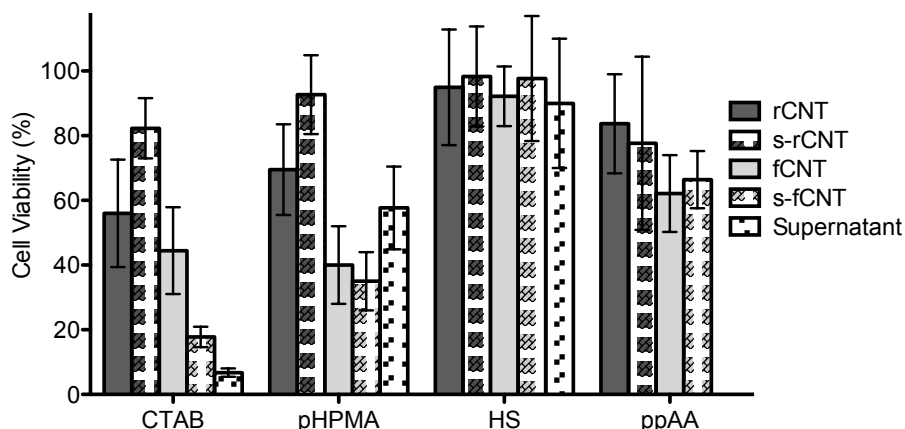


Figure 4.15. Cytotoxicity of CNTs with different functionalities. Data obtained after 48 h of incubation of rCNTs, s-rCNTs, fCNTs and s-fCNTs coated with CTAB, pHPMA, HS and ppAA (4 $\mu\text{g}/\text{mL}$).

Images in Figure 4.16 show the formation of aggregates, especially for the s-fCNT-HS (Figure 4.16E). This result is inconsistent with the inferred from the dispersibility assay described in section 0 (Figure 4.10, purple lines), where these complexes showed an acceptable stability in solution over time. However, the presence of other components in the cell culture medium may have affected the dispersive properties previously observed.²⁸ It is known that particles interact with proteins when introduced into a biological media making up the protein corona, which exhibits a high payload capacity, as will be deeply analyzed in Chapter V.⁴³ In this regard, the low cytotoxicity observed when protein coronas are formed around CNTs give rise to a potential modification approach for the formation of gene vectors.⁶³

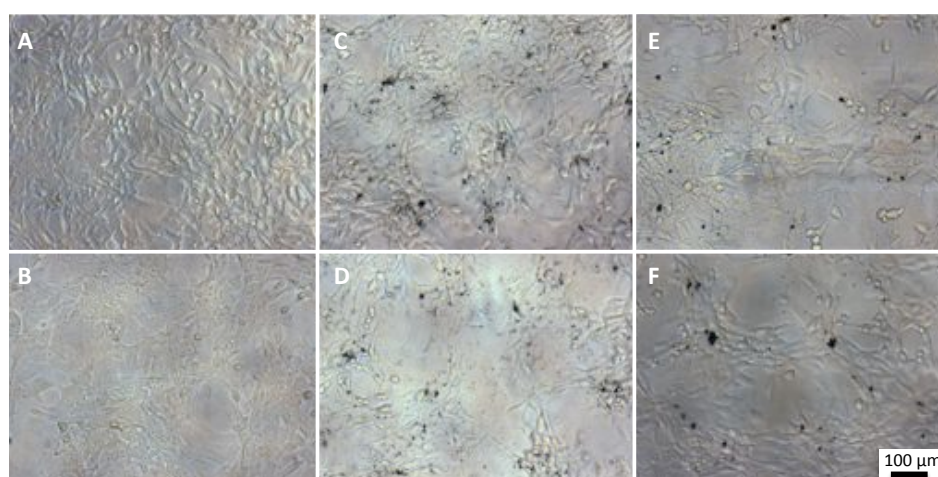


Figure 4.16. Microscope images of CNT-HS in cells. 3T3 cells incubated for 48 h in supplemented DMEM (A) free of CNTs, (B) with the supernatant (containing free HS) of the washed CNTs, and incubated with 4 $\mu\text{g}/\text{mL}$ of (C) rCNT-HS, (D) s-rCNT-HS, (E) fCNT-HS and (F) s-fCNT-HS.

On the contrary, when CTAB was used, cell viability was reduced to 80% for the s-rCNTs, to nearly 50% for the rCNTs and fCNTs, and to 20% for the s-fCNTs (Figure 4.15). These results are consistent with previous observations made by others.⁶⁴⁻⁶⁶ The cytotoxicity of s-fCNT-CTAB complexes was almost as high as the observed for the CTAB extracted from the supernatant. This could be due to the fact that the CTAB adsorbed on the s-fCNTs is weakly bound on the nanotube surface due its high hydrophilicity and thus is prone to be easily detached from the surface when introduced into the biological medium. As a result, the unbound CTAB molecules cause the sharp decrease of the cell viability observed, as occurs for the supernatant containing also free CTAB.⁶⁷ Figure 4.17 shows the decrease in the number of healthy cells into the CTAB containing wells, especially for the two cases discussed before, s-fCNT-CTAB and the CTAB supernatant (Figure 4.17B and F, respectively). The aggregates observed for the rCNT-CTAB and fCNT-CTAB images (Figure 4.17C and E, respectively) are likely to be the cause of the decrease in the cell viability. The positively charged surface of these complexes facilitates the binding of the negative species like proteins present in the serum media, causing the formation of the clusters observed. On the other hand, s-rCNT-CTAB exhibited a better degree of dispersion. Such observation could be due to the slight hydrophilicity caused by the oxidation process, which prevented the surface from the binding of large amounts of CTAB ligands. (Figure 4.10B, blue lines).

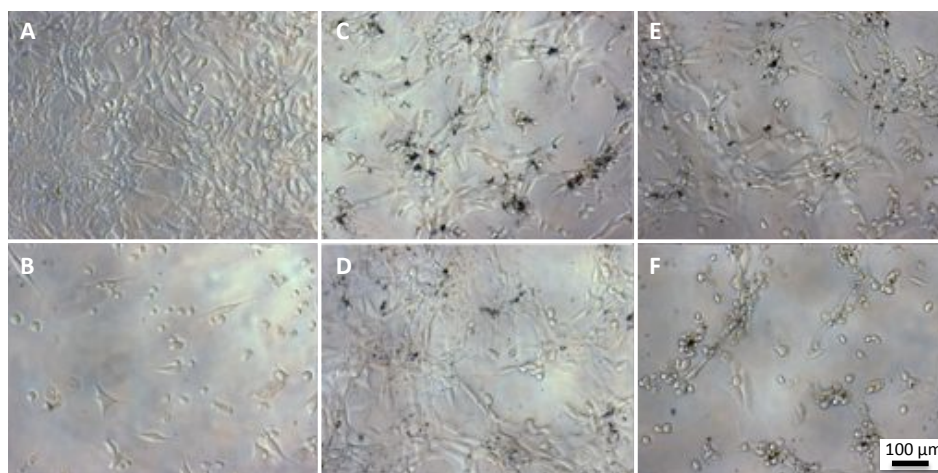


Figure 4.17. Microscope images of CNT-CTAB in cells. 3T3 cells incubated for 48 h in supplemented DMEM (A) free of CNTs, (B) with the supernatant (containing free CTAB) of the washed CNTs, and incubated with 4 $\mu\text{g}/\text{mL}$ of (C) rCNT-CTAB, (D) s-rCNT-CTAB, (E) fCNT-CTAB and (F) s-fCNT-CTAB.

The certain degree of cytotoxicity observed for the rCNT-CTAB and s-rCNT-CTAB complexes could be amended with the coating of the CNTs surface with a synthetic polymer such as pHPMA (Figure 4.15). The cell viability of the supernatant (around 60%) revealed that this polymer was not as toxic

as CTAB. Therefore, the resulting coated-CNTs showed lower cytotoxicity. This was not the case for the fCNTs and s-fCNTs because pHPMA was not able to coat this type of thin CNTs, as proved before. Consequently, large aggregates were formed in the cell culture medium whereas the polymer-coated rigid nanotubes (rCNT-pHPMA and s-rCNT-pHPMA) showed a better dispersion rate (Figure 4.18).

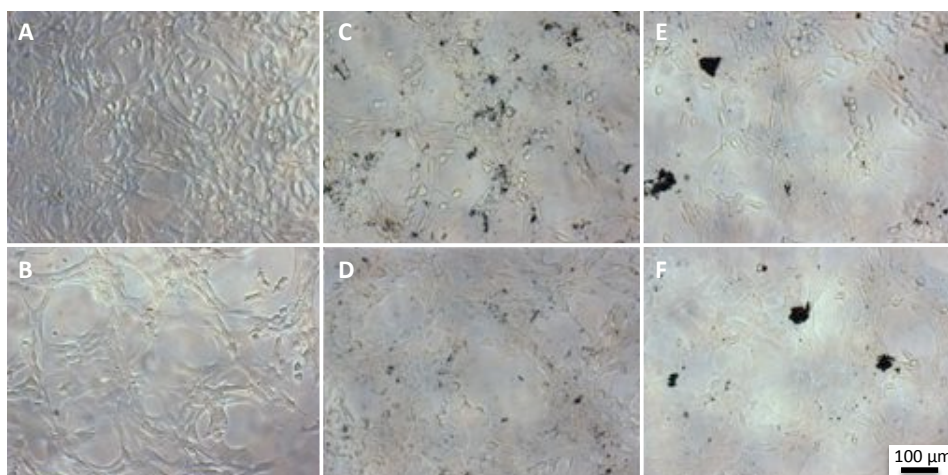


Figure 4.18. Microscope images of CNT-pHPMA in cells. 3T3 cells incubated for 48 h in supplemented DMEM (A) free of CNTs, (B) with the supernatant (containing free pHPMA) of the washed CNTs, and incubated with 4 $\mu\text{g}/\text{mL}$ of (C) rCNT-pHPMA, (D) s-rCNT-pHPMA, (E) fCNT-pHPMA and (F) s-fCNT-pHPMA.

So far, the cell viability of the resulting coated-CNTs with different non-covalent functionalities has been studied. As it is demonstrated in Chapter III, the covalently-modified CNTs with ppAA can potentially bind DNA due to its positively charged amines groups and this is why these type of systems are of special interest. The cell viability of these vectors was kept around the 60-80% after 48 h of incubation (Figure 4.15) showing a suitable dispersion degree in the cell medium (Figure 4.19). Noteworthy, both rigid and flexible CNTs and their shortened versions behaved similarly in the cell culture medium. The reduction of cell viability might be caused due to the moderate positive charge that ppAA-coated CNTs present on the surface, as the zeta potential data revealed (Figure 4.7). Similar results were obtained in Li *et al.* work, where strong cationic functionalizations were found to induce toxicity, whereas weak amine cationic coatings exhibited higher cell viability.⁶⁸ Moderate positively charged surfaces might still promote aggregation due to the interactions with the proteins from the cell culture but without causing a dramatic effect in terms of cytotoxicity. On the other hand, these CNT-ppAA vectors have proved to successfully bind DNA and thus altering the final surface charge (Chapter III). In any case, these positively charged ppAA-modified CNTs (without DNA) present a low cytotoxicity and suitable stability in the cell medium, resulting in a promising

system to load DNA. Given the encouraging results observed *in vitro*, how these vectors behave also *in vivo* might be of great interest for the study of targeted delivery of DNA.

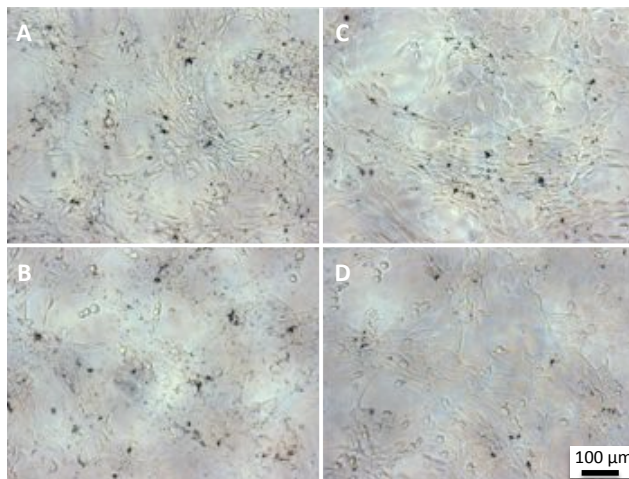


Figure 4.19. Microscope images of CNT-ppAA in cells. 3T3 cells incubated for 48 h with 4 $\mu\text{g}/\text{mL}$ of (A) rCNT-ppAA, (B) s-rCNT-ppAA, (C) fCNT-ppAA and (D) s-fCNT-ppAA.

4.3.4. Study of the *In Vivo* Biodistribution of the CNTs in Mice

In general, nanoparticles are known to be cleared rapidly from the circulation by the reticuloendothelial system (RES).^{69,70} However, as it has been already introduced in Chapter I, tailoring the geometrical shape and surface characteristics of nanocarriers may influence the pharmacokinetic profile and the biodistribution of the resulting delivery system.^{69,71,72} Likewise, differences in the blood circulation, clearance, organ biodistribution and accumulation of CNTs regarding size (length and diameter) and chemical functionalization have been also reported.^{45,48-52,73,74}

Elucidating the *in vivo* pharmacokinetic, biodistribution and toxicological profiles of the CNTs studied in this work is of vital importance in the understanding on how these systems behave inside the body. Rigid and flexible CNTs and their shortened versions were evaluated following intravenous administration to mice in order to determine the organ targeting dependence with regard to their physicochemical properties. This kind of study would enable the selection of the most promising candidate to maximize the nanocarrier uptake when a particular organ is the target for a therapeutic delivery.

In vivo fluorescence imaging provides a qualitative/semi-quantitative measurement of the nanocarrier behavior upon intravenous administration and is the chosen technique to carry out this preliminary study. In Chapter III, the ability of the CNTs to be fluorescently labeled has been demonstrated. In this context, given the potential in binding and delivering nucleic acids of the ppAA-modified complexes, together with the suitable stability in the biological medium and low cytotoxicity observed before, these functionalized CNTs were chosen for the *in vivo* fluorescent tracking. The amino groups present on their surfaces allowed the covalent anchoring of an infrared (IR) dye and enabled the labeling of the ppAA-modified CNTs (fluorescent CNTs, F-CNTs). The used dye contained an amine-reactive chemical group (NHS ester), which formed a covalent bond with the primary amines present in the CNT surface.

Once all types of CNTs were labeled, 150 μ L of a well-dispersed solution in PBS 1x (around 150-300 μ g/mL) were administered intravenously to the mice. The injected mice were imaged after 1, 8 and 24 hours of injection (Figure 4.20). After 1 day of injection, mice were sacrificed and the main organs (liver, stomach and intestines, lungs, kidneys, spleen and heart) were immediately collected and imaged. Neither mortality nor any toxic side effects were observed with any of the mice injected with F-CNTs during the 24-hours period of the study. Figure 4.20 shows the positive uptake of the F-CNTs in all cases (rCNTs, s-rCNTs, fCNTs and s-fCNTs); which were apparently distributed throughout most of the organs within 24 h. Others have also reported this behavior, proving that CNTs may easily pass through a number of compartments to reach targets around the whole mouse body.^{45,52} However, to determine the exact organs and the relative uptake that took place, each organ has to be imaged *ex vivo* (Figure 4.21).

The accumulation of CNTs especially in the liver, lungs and spleen, suggested that the rapid uptake took place *via* the mononuclear phagocytes in the RES (Figure 4.21). Such an uptake mechanism involving the RES is known to be a general phenomenon on the fate of nanoparticles *in vivo*, including the nanotubes.^{46,49,52,71} These results are not surprising due to the capacity of the macrophages to engulf foreign materials such as viruses, bacteria and dust particles, and also CNTs as seen in the Chapter III. Some studies confirm that CNT levels in RES organs rapidly decrease with time being almost totally excreted from the body.^{48,74} Nevertheless, others suggest that the accumulation of CNTs in these organs is not easily excreted, which may eventually induce potential damage and toxicity.^{46,52,75,76} In this regard, some of these investigations have indicated that the injected CNTs may be excreted following two possible pathways depending on their size.^{46,76}

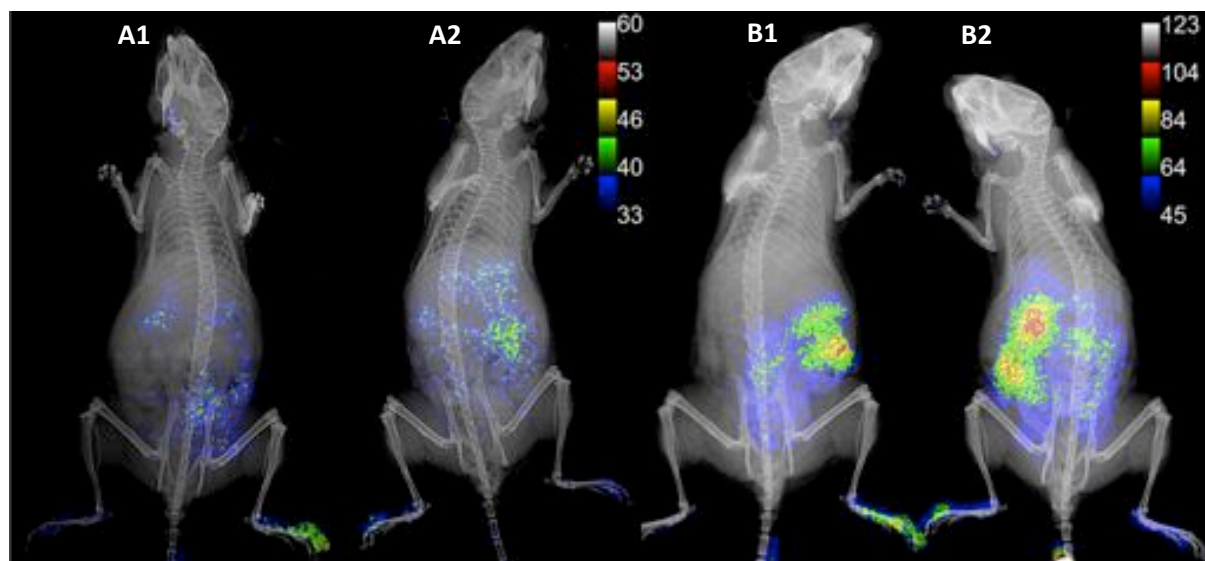


Figure 4.20. Comparison of *in vivo* biodistribution of the F-CNTs injected in mice. Fluorescence images acquired 24 h after the injection of (A1) rCNTs, (A2) s-rCNTs, (B1) fCNTs and (B2) s-fCNTs. The calibration bar on the left correspond to the A images and for mice B the one in the right applies. Prior to injection, ppAA-modified CNTs were fluorescently labeled with a IR dye through the amine group on the CNT surface.

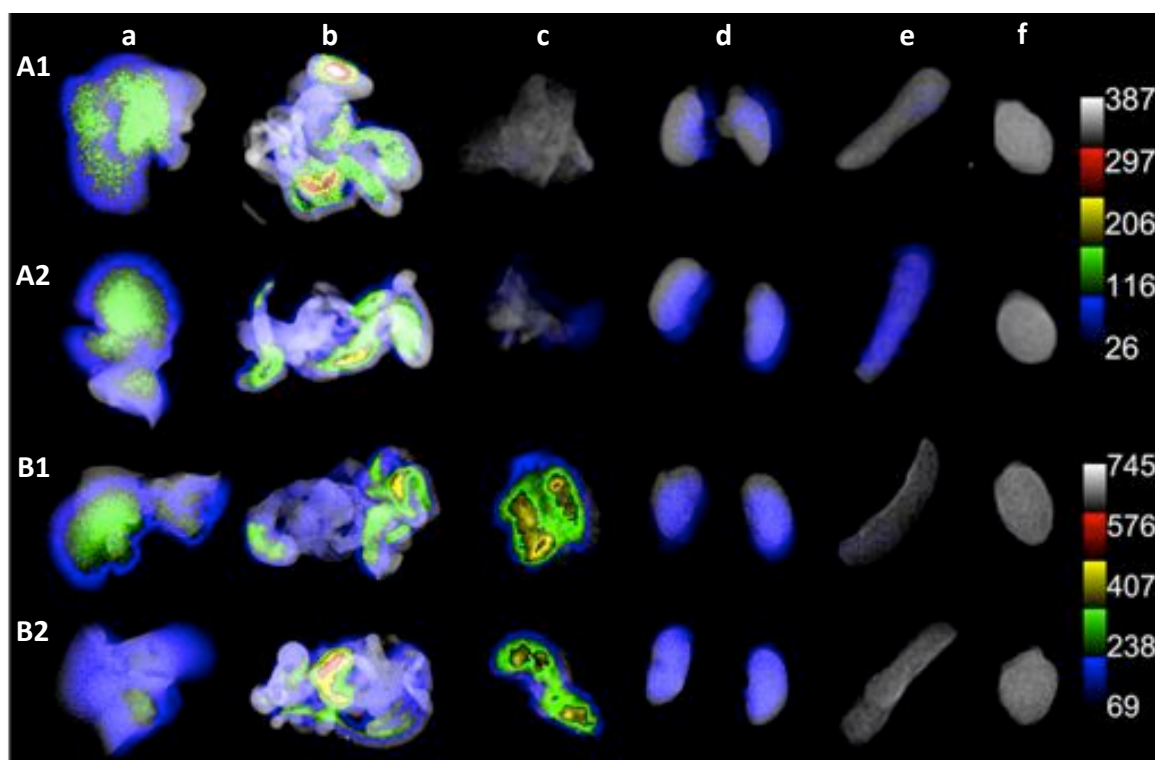


Figure 4.21. *Ex vivo* organ biodistribution of the F-CNTs after 24 h of injection. Fluorescent images corresponding to of the fluorescently-labeled (A1) rCNTs, (A2) srCNTs, (B1) fCNTs and (B2) sfCNTs of the liver, stomach and intestine, lungs, kidneys spleen and heart (from left to right). The calibration bar on the top belongs to the A images and for organs of the B samples the one in the bottom applies.

First, large nanotubes are likely to be accumulated in the liver and then excreted through the biliary pathway, ending up in feces. This phenomenon may cause the high F-CNT retention exhibited particularly in the stomach and intestines. Such results suggest that CNTs employed in this study might be excreted by the gastrointestinal tract after being accumulated in the liver, as was also observed by Zhan and colleagues.⁵¹ On the other hand, it has been pointed out that single CNTs can be cleared through the kidney and thus *via* the urinary pathway. Therefore, the certain degree of accumulation in the kidneys of all types of F-CNTs used in this work confirms the presence of short tubes able to permeate through the glomerular pores. Therefore, the polydispersity of the CNT samples confirmed at the beginning of the chapter was also observed *in vivo*.

On the contrary, Lacerda and co-workers stated that the length of the CNTs is not a critical parameter in the renal clearance process, being its diameter what is really important.⁶ Nanotubes of 20-30 in diameter were proved to be small and dispersed enough to pass through the glomerular filtration barrier. To corroborate this behavior, the biodistribution of the flexible (thin, 15 nm) and rigid (thick, 150-170 nm) CNTs used in this work should be compared. Although only radiolabeling allows precise quantification of the CNTs accumulated and cleared in the body, *in vivo* fluorescence imaging can provide a semi-quantification of the particle uptake. It has to be considered that neither the amount of dye attached on the different types of CNTs nor the concentration of the CNTs administered to the mice was kept constant between samples. Therefore, the final quantity of dye injected covalently bound to each kind of F-CNTs (rCNTs, s-rCNTs, fCNTs and s-fCNTs) was measured by UV-Vis spectroscopy, which was used to normalize the fluorescence intensities found in the organs. Since three mice were used for all F-CNTs studied in this work, the semi-quantitative biodistribution data obtained could be plotted (Figure 4.22).

These results exhibits that the rigid CNTs and their shortened version (rCNTs an s-rCNTs) were prone to have higher accumulation in the stomach and intestines. After 24 h, their larger size is likely to favor the clearance *via* de biliary pathway, when compared to the flexible tubes. However, flexible CNTs (fCNTs and s-fCNTs) had a superior uptake in the lungs. Others reported similar results, specifically when SWNT or thin MWNT were employed.^{77,78} Yang *et al.* suggested that the high accumulation in the pulmonary vessels is typically caused by the less dispersed nanotubes.⁷⁸ Such phenomenon is consistent with the dispersibility studies from the section 0, where it was demonstrated that flexible CNTs tend to easily form larger aggregates. Additionally, Yang and colleagues confirm that the accumulation of CNTs in the lungs rapidly decreases over time following two possible clearance pathways. One is the excretion through the alveolar macrophages in form of mucus, which allows the secretion of the CNTs *via* the mucociliary transport. The other consists in

the transfer of these CNTs to the spleen through the lymph nodes. The latter, could explain the higher retention of the rigid CNTs (rCNTs and s-rCNTs) found in the spleen when compared to the observed for the flexible nanotubes (fCNTs and s-fCNTs). These results suggest that the rigid and thicker CNTs are more rapidly cleared, probably due to the better dispersive behavior in the biological milieu. Noteworthy, the accumulation observed in the RES organs (liver and kidneys) was similar for all types of CNTs used. The positive uptake in both organ tissues confirmed the presence of large CNTs, mainly retained in the liver, and short tubes, which are excreted through the renal system for all samples.

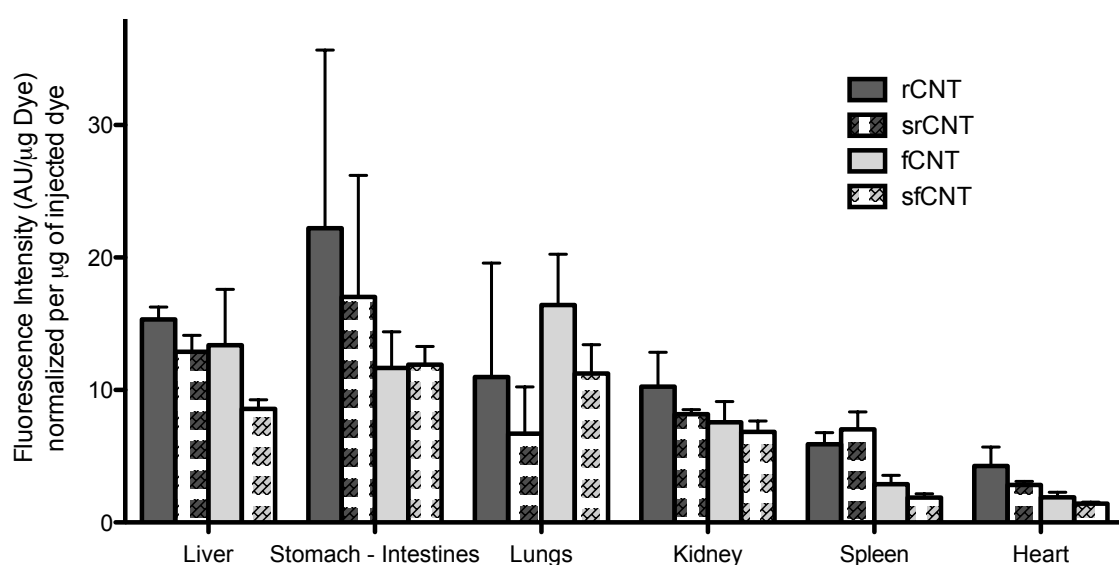


Figure 4.22. Semi-quantitative analysis of the organ biodistribution. Accumulation of rCNTs, s-rCNTs, fCNT and s-fCNTs fluorescently labeled *via* the ppAA modification in mice measured 24 h post-injection. Data is presented as the mean \pm SD ($n = 3$).

These preliminary results successfully prove that the chemical binding between an IR dye and the ppAA deposited by PECVD on the nanotube surface leads to the production fluorescently-labeled CNTs, which are highly feasible for bioimaging studies. This work shows semi-quantitative information about the distinct *in vivo* biodistribution profile of the different types of CNTs assessed in this chapter. Further investigations should allow the total quantification of CNT accumulation in the organ tissues by *in vivo* radiotracing of radiolabeled systems. Moreover, a deeper research in the clearance half-life and blood circulation should be considered in order to identify the pharmacological profile of the *in vivo* administrated CNTs. These studies will provide a better understanding of the uptake mechanism and organ biodistribution of these systems, which is essential for targeted gene delivery.

4.3.5. Assessment of the ppAA-Coated CNT Systems for GFP Gene Delivery

In Chapter III, we proved the use of rCNT-ppAA vectors to load pGFP and successfully transfect macrophages. Similarly, the assessment of DNA binding capacity of their shortened version (s-rCNTs) and both flexible nanotubes (fCNTs and s-fCNTs) coated with ppAA was tested. As a result, the transfection efficiency of the resulting DNA vectors could be evaluated. This approach would confirm if these vectors are able to get internalized into the cell of interest, release the carrying gene and evidence its transfection capacity by the production of GFP. Additionally, the cytotoxicity of these complexes was also evaluated.

Transfection Vector Formation and Characterization by Gel Retardation Assay

Once the CNTs were successfully modified with polyallylamine by PECVD (ppAA) the complex with the genetic material was formed through ionic interaction between the negatively charged phosphate groups on the DNA backbone, and the positively charged amines on the surface of the modified CNTs at pH 5. However, before the formation of the final plasmid vector, the loading capacity of DNA presented by the CNTs was evaluated. The aim is to determine the amount of genetic material that can be complexed *per* unit mass of carbon nanotubes. Therefore, agarose gel electrophoresis was used to probe the CNTs complexation ratio when the same amount of DNA was exposed to increasing amounts of CNTs, as carried out in the Chapter II for the rCNTs. When the DNA does not migrate towards the positive electrode indicates that it is complexed with the CNTs, as they are unable to pass through the pores of the gel due to the large size of the complex.

A 150:1 ratio was obtained for rCNT-PAA per pGFP (Chapter III, Figure 3.19), which was reduced to 25:1 when s-rCNT-PAA were used (Figure 4.23A). These results show that a lower quantity of CNTs was required to load the same amount of pGFP when the shortened version of rigid CNTs was employed. Specifically, 150 μg of rCNTs were needed to bind 1 μg of pGFP, whereas the same quantity of DNA was loaded to 25 μg of s-rCNTs. Because s-rCNTs were mainly shorter than the untreated rCNTs, the former showed a higher specific area per unit mass, which allowed a greater loading efficiency. In addition, Figure 4.23 shows the resulting agarose gel retardation assay after testing the complex formation between pGFP and both flexible CNTs (fCNT-ppAA and s-fCNT-ppAA, Figure 4.23B and C, respectively). fCNT-ppAA exhibited the same complexation efficiency as s-rCNT-ppAA (25:1), probably due to the same effect of size explained before. The lower diameter and length of the fCNTs enabled a higher pGFP loading capacity, which was increased with the length reduction of the s-fCNTs (10:1 ratio).

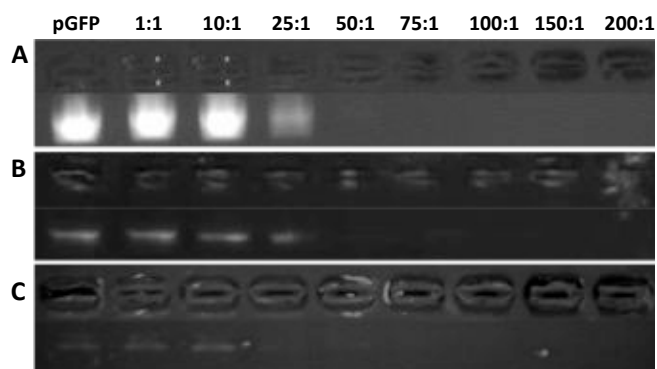


Figure 4.23. Agarose gel electrophoresis of different CNT-ppAA+pGFP (w/w) ratios. The images correspond to the obtained gel of (A) s-rCNT-ppAA, (B) fCNT-ppAA and (C) s-fCNT-ppAA. The first row signal belongs to the pGFP alone, which is used as a marker.

Cellular Uptake, Toxicity and GFP Transfection Efficiency of the Complexes

The pGFP delivery vectors with each type of CNT were prepared following the appropriate ratio of complexation and were incubated at 37 °C for 1 h. The final complexes were diluted in DMEM and were incubated with 3T3 cells at different final concentrations (4, 10 and 30 µg/mL). Therefore, the final amount of pGFP per well was different for all samples, ranging from 4 to 450 µg/well (Table 4.4). The complexes were left in the cell culture for 24 h and after 48 h, the cell viability and transfection efficiency were assessed.

Table 4.4. Conditions of the CNT-ppAA+pGFP complexes.

Sample ID	[CNT] (µg/mL)	Complex Formation Ratio (w/w)	[pGFP] (µg/mL)	pGFP (ng/well)
rCNT-ppAA	4	150:1	0.03	4
	10		0.07	10
	30		0.20	30
s-rCNT-ppAA	4	25:1	0.20	24
	10		0.40	60
	30		1.20	180
fCNT-ppAA	4	25:1	0.20	24
	10		0.40	60
	30		1.20	180
s-fCNT-ppAA	4	10:1	0.40	60
	10		1.00	150
	30		3.00	450

Firstly, the cytotoxic assay carried out with the MTS reagent showed the decrease of cell viability with the increase of CNT concentration, consistently to what was observed before in the section 4.3.3 (Figure 4.24). Moreover, rCNTs and their shortened version (s-rCNTs) showed major cell viability at 4 and 10 $\mu\text{g}/\text{mL}$ (around 100%) than the flexible nanotubes, which was around 80%. Both observations might be caused by the aggregation tendency of the CNTs at higher concentrations, alongside the fact that flexible, tangled nanotubes are more prone to form large aggregates than the rigid ones. This tangled behavior may also affect the transfection capabilities of these systems. Their strong aggregation tendency may complicate the threshold of the vector to the cell without dramatic effects, together with the release of the loaded DNA.

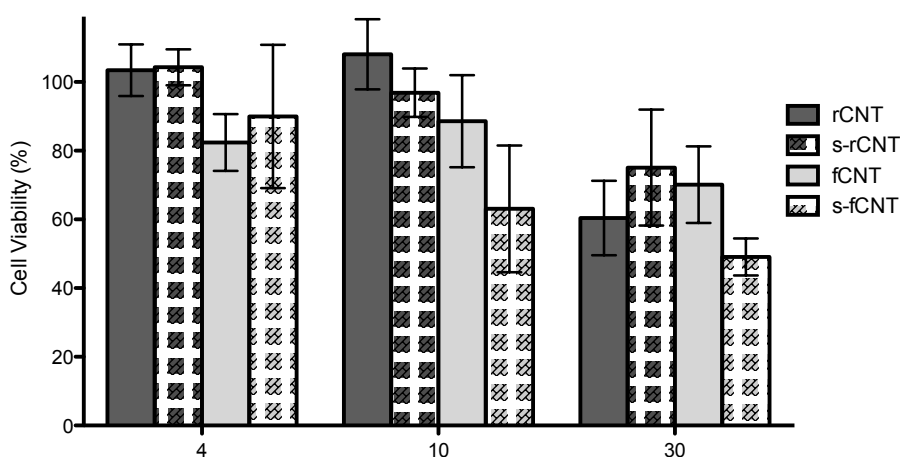


Figure 4.24. Cell viability of the pGFP complexes varying the CNT concentration. Data obtained after 48 h incubation in 3T3 cells.

The better dispersibility exhibited when low concentrations of CNTs were employed is probably why cells incubated with 4 $\mu\text{g}/\text{mL}$ CNTs were the ones that showed GFP transfection (Figure 4.25). Indeed, only the rigid-type of CNTs (rCNTs and s-rCNTs), which were proved to remain well dispersed in the biological medium, were able to transfect the 3T3 cells and subsequently produce GFP (Figure 4.25A and B), as suggested before. Therefore, it is confirmed that the aggregation of the flexible CNTs is likely to avoid the proper transfection, probably because the formation of these supramolecular complexes complicates successful internalization and release of the pGFP, and decreases the cell viability.

Although some aggregates were yet observed, especially in the s-rCNT samples (Figure 4.25B), the highly dispersed rigid CNT-ppAA+pGFP complexes were able to transfect and release the GFP plasmid. A positive control ensuring a release of 50 ng of GFP per well, confirmed that the amount of

DNA employed was not enough to obtain high transfection efficiencies (Figure 4.25C). Flow cytometry studies confirmed that less than 10% of the 3T3 cells were successfully transfected. These results are sustained when other fibroblast-like cells were transfected (*cos-7*), showing that the low efficiency observed was not dependent to the cell type employed.⁷⁹ However, slight transfection efficiency was again observed, probably due to the low amounts of plasmid loaded on the CNTs. As a result, a strategy in order to achieve higher loading capacities should be considered.

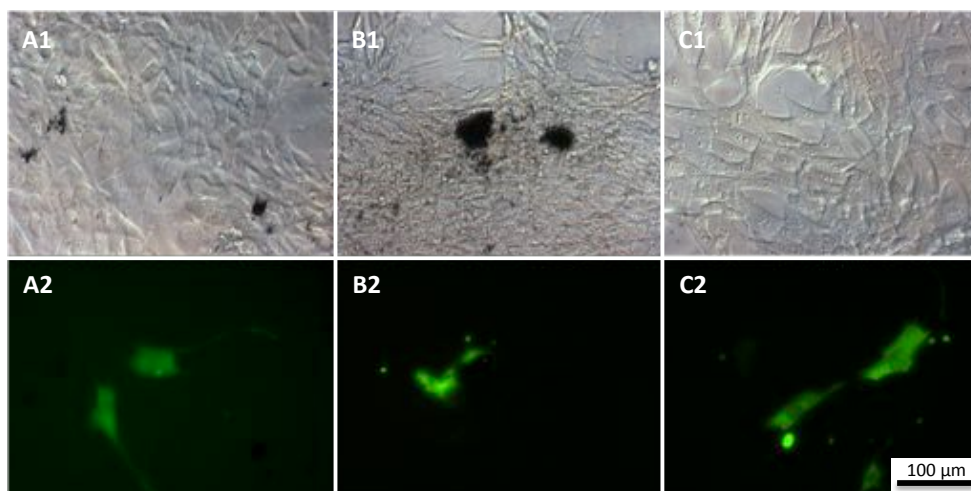


Figure 4.25. Transfection of 3T3 cells with CNT-ppAA+pGFP complexes. Microscope images of the 3T3 cells incubated with 4 $\mu\text{g}/\text{mL}$ of (A) rCNTs, (B) s-rCNTs, and a positive control (50 ng/well of pGFP). Each condition is shown in its (1) bright field and (2) fluorescence microscopy.

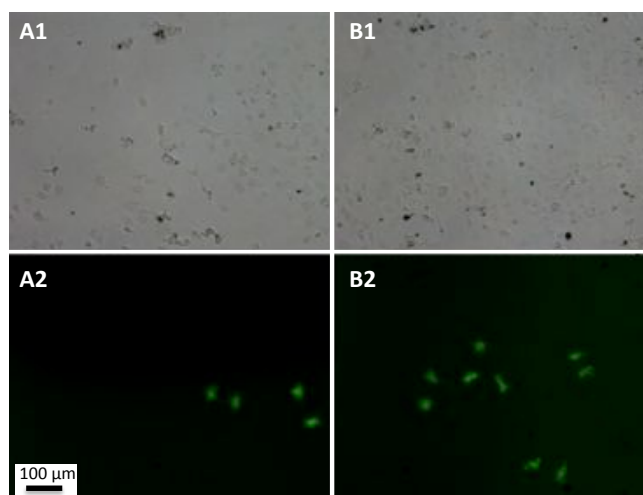


Figure 4.26. Transfection of *Cos-7* cells with CNT-ppAA+pGFP complexes. Microscope images of the *Cos-7* cells incubated with 4 $\mu\text{g}/\text{mL}$ of (A) rCNTs and (B) s-rCNTs. Each condition is shown in its (1) bright field and (2) fluorescence microscopy.

4.4. Concluding Remarks

This chapter demonstrates that thick and thinner CNTs can be shortened through mild oxidation treatments without affecting their morphology and leading to a more hydrophilic surface. These differences in length, rigidity, and especially in the hydrophobicity that characterizes the CNT surface, have a direct impact on the dispersibility, toxicity and interaction with the functionalizing agent.

Noteworthy, the effect of length between the naïve tubes and their shortened versions has a limited significance in terms of stability in solution and cytotoxicity. Such observations are probably due to the polydispersity observed within the same sample, which complicates the real distinction between the short and the long tubes present in the solution.

In general terms, rigid nanotubes (rCNTs and s-rCNTs) show a suitable degree of dispersion, higher cell viability and the ability to be functionalized with all types of coatings (CTAB, pHPMA, HS and ppAA). On the other hand, fCNTs are more prone to tangle in solution, which causes the formation of larger aggregates. Therefore, their stability decreases regardless of their surface functionalization, increasing the cytotoxicity. Although the dispersibility issues are solved when fCNTs are shortened, the high hydrophilization of the s-fCNTs surface together with their tangled behavior, induces the aggregation when are introduced into the cell culture medium due to the binding of serum proteins and thus, the formation of large supramolecular complexes.

The cell viability is maintained over time when ppAA-modified and especially HS conjugates are used. On the contrary, CTAB-coatings exhibit high cytotoxicity, which can be amended with the pHPMA wrapping on the CNT surface as a dispersing agent instead of using the surfactant. However, this type of amphiphilic polymer is not able to coat the thin and flexible tubes, probably due to the rigidity of its cholesterol group.

This work has also proved that the physicochemical properties of the CNTs also influence their behavior inside the body. *In vivo* fluorescence imaging of the fluorescently-labeled CNTs has allowed a semi-quantitative measurement of the organ biodistribution of these systems in mice, showing that they can be distributed throughout most of the organs within 24 h. The main difference observed between the flexible and rigid CNTs uptake is in the lungs. Basically, flexible tubes are largely accumulated in the lungs due to their higher aggregation tendency as a consequence of their thinner structure.

This different behavior between flexible and rigid nanotubes also affects the internalization of the resulting gene vector into the cell and thus its transfection efficiency. Despite that ppAA-coated flexible nanotubes have been proved to bind higher amounts of pGFP than rigid tubes by agarose gel electrophoresis, their tangled behavior complicates the threshold of the complex into the cell and the successful release of the loaded DNA.

Additionally, it has been confirmed that cytotoxicity increases when high concentrations of CNTs are employed. As a result, low amounts of CNTs have to be used, if high cell viability is required and thus, rather modest quantities of pGFP have to be added to the cells. Hence, a further improvement of the nanocarrier architecture *via* the introduction of functional groups that may enhance the loading capacity of DNA and improve the steric protection without increasing the cytotoxicity of the system has to be investigated. In this regard, HS coating has shown high cell viability and seems undeniable that the protein-particle interaction into a biological fluid cannot be avoided. The absorption of these proteins and other small biomolecules to the nanoparticle surface forms the protein corona, which has been recently proved to have high capacity for a payload improving drug and gene carrying properties. Thus, since the protein corona traits are still not well known, the understanding on how we can manipulate and optimize their properties for the increase of the nucleic acid binding on the CNTs for a particular biological application is needed.

4.5. References

- 1 Raffa, V., *et al.* Physicochemical properties affecting cellular uptake of carbon nanotubes. *Nanomedicine* **5**, 89-97 (2010).
- 2 Liu, Y., Zhao, Y., Sun, B. & Chen, C. Understanding the Toxicity of Carbon Nanotubes. *Accounts of Chemical Research* **46**, 702-713 (2013).
- 3 Firme Iii, C. P. & Bandaru, P. R. Toxicity issues in the application of carbon nanotubes to biological systems. *Nanomedicine: Nanotechnology, Biology and Medicine* **6**, 245-256, (2010).
- 4 Kostarelos, K. The long and short of carbon nanotube toxicity. *Nature Biotechnology* **26**, 774-776, (2008).
- 5 Lanone, S., Andujar, P., Keramanizadeh, A. & Boczkowski, J. Determinants of carbon nanotube toxicity. *Advanced Drug Delivery Reviews*, (2013).
- 6 Lacerda, L., Bianco, A., Prato, M. & Kostarelos, K. Carbon nanotubes as nanomedicines: From toxicology to pharmacology. *Advanced Drug Delivery Reviews* **58**, 1460-1470 (2006).
- 7 Zhao, Y., Xing, G. & Chai, Z. Nanotoxicology: Are carbon nanotubes safe? *Nature Nanotechnology* **3**, 191-192, (2008).
- 8 Donaldson, K. & Poland, C. A. Nanotoxicology: New insights into nanotubes. *Nature Nanotechnology* **4**, 708-710, (2009).
- 9 Raffa, V. *et al.* Can the properties of carbon nanotubes influence their internalization by living cells? *Carbon* **46**, 1600-1610, (2008).
- 10 Lacerda, L., Raffa, S., Prato, M., Bianco, A. & Kostarelos, K. Cell-penetrating CNTs for delivery of therapeutics. *Nano Today* **2**, 38-43 (2007).
- 11 Liu, Y., Chipot, C., Shao, X. & Cai, W. Solubilizing carbon nanotubes through noncovalent functionalization. Insight from the reversible wrapping of alginic acid around a single-walled carbon nanotube. *The journal of physical chemistry. B* **114**, 5783-5789 (2010).
- 12 Becker, M. L. *et al.* Length-Dependent Uptake of DNA-Wrapped Single-Walled Carbon Nanotubes. *Advanced Materials* **19**, 939-945, (2007).
- 13 Nagai, H. *et al.* Diameter and rigidity of multiwalled carbon nanotubes are critical factors in mesothelial injury and carcinogenesis. *Proceedings of the National Academy of Sciences* **108**, E1330-E1338, (2011).
- 14 Aitchison, T. J., Ginic-Markovic, M., Matisons, J. G., Simon, G. P. & Fredericks, P. M. Purification, Cutting, and Sidewall Functionalization of Multiwalled Carbon Nanotubes Using Potassium Permanganate Solutions. *The Journal of Physical Chemistry C* **111**, 2440-2446, (2007).
- 15 Ziegler, K. J. *et al.* Controlled Oxidative Cutting of Single-Walled Carbon Nanotubes. *Journal of the American Chemical Society* **127**, 1541-1547, (2005).
- 16 Dai, H. Carbon Nanotubes: Synthesis, Integration, and Properties. *Acc. Chem. Res.* **35**, 1035-1044 (2002).
- 17 Charlier, J. C. Defects in carbon nanotubes. *Accounts of chemical research* **35**, 1063-1069 (2002).
- 18 Pumera, M. & Miyahara, Y. What amount of metallic impurities in carbon nanotubes is small enough not to dominate their redox properties? *Nanoscale* **1**, 260-265, (2009).
- 19 Niyogi, S. *et al.* Chemistry of Single-Walled Carbon Nanotubes. *Accounts of Chemical Research* **35**, 1105-1113, (2002).
- 20 Li, J. & Banhart, F. The Engineering of Hot Carbon Nanotubes with a Focused Electron Beam. *Nano Letters* **4**, 1143-1146, (2004).
- 21 Liu, P., Arai, F. & Fukuda, T. Cutting of carbon nanotubes assisted with oxygen gas inside a scanning electron microscope. *Applied Physics Letters* **89**, (2006).
- 22 Stepanek, I. *et al.* Nano-mechanical cutting and opening of single wall carbon nanotubes. *Chemical Physics Letters* **331**, 125-131, (2000).
- 23 Bettinger, H. F. The reactivity of defects at the sidewalls of single-walled carbon nanotubes: the Stone-Wales defect. *The journal of physical chemistry. B* **109**, 6922-6924, (2005).
- 24 Chen, J., Chen, Q. & Ma, Q. Influence of surface functionalization *via* chemical oxidation on the properties of carbon nanotubes. *Journal of colloid and interface science* **370**, 32-38 (2012).

- 25 Datsyuk, V. *et al.* Chemical oxidation of multiwalled carbon nanotubes. *Carbon* **46**, 833-840, (2008).
- 26 Didenko, V. V., Moore, V. C., Baskin, D. S. & Smalley, R. E. Visualization of Individual Single-Walled Carbon Nanotubes by Fluorescent Polymer Wrapping. *Nano Letters* **5**, 1563-1567, (2005).
- 27 Mukhopadhyay, K. *et al.* Gold Nanoparticles Assembled on Amine-Functionalized Na,Y Zeolite: A Biocompatible Surface for Enzyme Immobilization. *Langmuir* **19**, 3858-3863 (2003).
- 28 Shannahan, J. H. *et al.* Comparison of Nanotube-Protein Corona Composition in Cell Culture Media. *Small* **9**, 2171-2181 (2013).
- 29 Seelenmeyer, S. & Ballauff, M. Analysis of Surfactants Adsorbed onto the Surface of Latex Particles by Small-Angle X-ray Scattering. *Langmuir* **16**, 4094-4099, (2000).
- 30 Strano, M. S. *et al.* Electronic Structure Control of Single-Walled Carbon Nanotube Functionalization. *Science* **301**, 1519-1522, (2003).
- 31 Vaisman, L., Wagner, H. D. & Marom, G. The role of surfactants in dispersion of carbon nanotubes. *Advances in Colloid and Interface Science* **128-130**, 37-46 (2006).
- 32 Moore, V. C. *et al.* Individually Suspended Single-Walled Carbon Nanotubes in Various Surfactants. *Nano Letters* **3**, 1379-1382, (2003).
- 33 Ntim, S. A., Sae-Khow, O., Witzmann, F. A. & Mitra, S. Effects of polymer wrapping and covalent functionalization on the stability of MWCNT in aqueous dispersions. *Journal of Colloid and Interface Science* **355**, 383-388 (2011).
- 34 Kumar, N. A., Bund, A., Cho, B. G., Lim, K. T. & Jeong, Y. T. Novel amino-acid-based polymer/multi-walled carbon nanotube bio-nanocomposites: highly water dispersible carbon nanotubes decorated with gold nanoparticles. *Nanotechnology* **20**, (2009).
- 35 Kang, Y. K. *et al.* Helical Wrapping of Single-Walled Carbon Nanotubes by Water Soluble Poly(p-phenyleneethynylene). *Nano Letters* **9**, 1414-1418, (2009).
- 36 O'Connell, M. J. *et al.* Reversible water-solubilization of single-walled carbon nanotubes by polymer wrapping. *Chemical Physics Letters* **342**, 265-271 (2001).
- 37 Valenti, L. E., Fiorito, P. A., García, C. D. & Giacomelli, C. E. The adsorption-desorption process of bovine serum albumin on carbon nanotubes. *Journal of Colloid and Interface Science* **307**, 349-356 (2007).
- 38 Azamian, B. R., Davis, J. J., Coleman, K. S., Bagshaw, C. B. & Green, M. L. H. Bioelectrochemical Single-Walled Carbon Nanotubes. *Journal of the American Chemical Society* **124**, 12664-12665, (2002).
- 39 Wu, Y. *et al.* Coating single-walled carbon nanotubes with phospholipids. *The journal of physical chemistry. B* **110**, 2475-2478, (2006).
- 40 Qiao, R. & Ke, P. C. Lipid-Carbon Nanotube Self-Assembly in Aqueous Solution. *Journal of the American Chemical Society* **128**, 13656-13657, (2006).
- 41 Zheng, J. *et al.* Adsorption of nucleic acid bases and amino acids on single-walled carbon and boron nitride nanotubes: a first-principles study. *Journal of nanoscience and nanotechnology* **9**, 6376-6380 (2009).
- 42 Gao, H. & Kong, Y. Simulation of DNA-Nanotube Interactions. *Annual Review of Materials Research* **34**, 123-150, (2004).
- 43 Kah, J. C. Y., Chen, J., Zubieta, A. & Hamad-Schifferli, K. Exploiting the Protein Corona around Gold Nanorods for Loading and Triggered Release. *ACS Nano* **6**, 6730-6740 (2012).
- 44 de Puig, H., Cifuentes Rius, A., Flemister, D., Baxamusa, S. H. & Hamad-Schifferli, K. Selective Light-Triggered Release of DNA from Gold Nanorods Switches Blood Clotting On and Off. *PLoS ONE* **8**, (2013).
- 45 Guo, J., Zhang, X., Li, Q. & Li, W. Biodistribution of functionalized multiwall carbon nanotubes in mice. *Nuclear medicine and biology* **34**, 579-583, (2007).
- 46 Moon, H. K., Lee, S. H. & Choi, H. C. In Vivo Near-Infrared Mediated Tumor Destruction by Photothermal Effect of Carbon Nanotubes. *ACS Nano* **3**, 3707-3713 (2009).
- 47 Singh, R. *et al.* Binding and Condensation of Plasmid DNA onto Functionalized Carbon Nanotubes: Toward the Construction of Nanotube-Based Gene Delivery Vectors. *Journal of the American Chemical Society* **127**, 4388-4396 (2005).
- 48 Wang, H. *et al.* Biodistribution of Carbon Single-Wall Carbon Nanotubes in Mice. *Journal of Nanoscience and Nanotechnology* **4**, 1019-1024, (2004).

- 49 Yang, S.-t. *et al.* Biodistribution of Pristine Single-Walled Carbon Nanotubes In Vivo. *The Journal of Physical Chemistry C* **111**, 17761-17764, (2007).
- 50 Yang, S.-T., Luo, J., Zhou, Q. & Wang, H. Pharmacokinetics, Metabolism and Toxicity of Carbon Nanotubes for Biomedical Purposes. *Theranostics* **2**, 271-282 (2012).
- 51 Zhan, L. *et al.* Biodistribution of co-exposure to multi-walled carbon nanotubes and graphene oxide nanoplatelets radiotracers. *Journal of Nanoparticle Research* **13**, 2939-2947, (2011).
- 52 Kang, B. *et al.* Biodistribution and accumulation of intravenously administered carbon nanotubes in mice probed by Raman spectroscopy and fluorescent labeling. *Carbon* **47**, 1189-1192, (2009).
- 53 Lam, C.-W., James, J. T., McCluskey, R., Arepalli, S. & Hunter, R. L. A review of carbon nanotube toxicity and assessment of potential occupational and environmental health risks. *Critical reviews in toxicology* **36**, 189-217 (2006).
- 54 Balasubramanian, K. & Burghard, M. Chemically functionalized carbon nanotubes. *Small (Weinheim an der Bergstrasse, Germany)* **1**, 180-192 (2005).
- 55 Collins, P. G. *Defects and disorder in carbon nanotubes*. (Oxford University Press: Oxford, 2010).
- 56 Ménard-Moyon, C., Kostarelos, K., Prato, M. & Bianco, A. Functionalized Carbon Nanotubes for Probing and Modulating Molecular Functions. *Chemistry & Biology* **17**, 107-115, (2010).
- 57 Sun, Y.-P., Fu, K., Lin, Y. & Huang, W. Functionalized carbon nanotubes: properties and applications. *Accounts of chemical research* **35**, 1096-1104 (2002).
- 58 Pulskamp, K., Diabaté, S. & Krug, H. F. Carbon nanotubes show no sign of acute toxicity but induce intracellular reactive oxygen species in dependence on contaminants. *Toxicology Letters* **168**, 58-74, (2007).
- 59 Liu, J. *et al.* Fullerene Pipes. *Science* **280**, 1253-1256, (1998).
- 60 Cifuentes, A. & Borrós, S. Comparison of Two Different Plasma Surface-Modification Techniques for the Covalent Immobilization of Protein Monolayers. *Langmuir* **29**, 6645-6651, (2013).
- 61 Hlady, V. & Buijs, J. Protein adsorption on solid surfaces. *Current Opinion in Biotechnology* **7**, 72-77 (1996).
- 62 Heister, E. *et al.* Higher Dispersion Efficacy of Functionalized Carbon Nanotubes in Chemical and Biological Environments. *ACS Nano* **4**, 2615-2626, (2010).
- 63 Ge, C. *et al.* Binding of blood proteins to carbon nanotubes reduces cytotoxicity. *Proceedings of the National Academy of Sciences* **108**, 16968-16973 (2011).
- 64 Alkilany, A. M. *et al.* Cellular Uptake and Cytotoxicity of Gold Nanorods: Molecular Origin of Cytotoxicity and Surface Effects. *Small* **5**, 701-708, (2009).
- 65 Wang, S. *et al.* Challenge in understanding size and shape dependent toxicity of gold nanomaterials in human skin keratinocytes. *Chemical Physics Letters* **463**, 145-149, (2008).
- 66 Zhang, Y., Xu, D., Li, W., Yu, J. & Chen, Y. Effect of Size, Shape, and Surface Modification on Cytotoxicity of Gold Nanoparticles to Human HEp-2 and Canine MDCK Cells. *Journal of Nanomaterials* **2012**, (2012).
- 67 Lewinski, N. *et al.* Cytotoxicity of Nanoparticles. *Small* **4**, 26-49, (2008).
- 68 Li, R. *et al.* Surface charge and cellular processing of covalently functionalized multiwall carbon nanotubes determine pulmonary toxicity. *ACS nano* **7**, 2352-2368 (2013).
- 69 Li, S.-D. & Huang, L. Pharmacokinetics and biodistribution of nanoparticles. *Molecular pharmaceutics* **5**, 496-504, (2008).
- 70 Longmire, M., Choyke, P. L. & Kobayashi, H. Clearance properties of nano-sized particles and molecules as imaging agents: considerations and caveats. *Nanomedicine (London, England)* **3**, 703-717, (2008).
- 71 Almeida, J. P. M., Chen, A. L., Foster, A. & DRezek, R. In Vivo Biodistribution of Nanoparticles. *Future Medicine* **6**, 815-831 (2011).
- 72 Moghimi, S. M., Hunter, A. C. & Andresen, T. L. Factors Controlling Nanoparticle Pharmacokinetics: An Integrated Analysis and Perspective. *Annual Review of Pharmacology and Toxicology* **52**, 481-503, (2012).
- 73 Lacerda, L. *et al.* Carbon-Nanotube Shape and Individualization Critical for Renal Excretion. *Small* **4**, 1130-1132, (2008).

- 74 Singh, R. *et al.* Tissue biodistribution and blood clearance rates of intravenously administered carbon nanotube radiotracers. *Proceedings of the National Academy of Sciences of the United States of America* **103**, 3357-3362 (2006).
- 75 Grubek-Jaworska, H. *et al.* Preliminary results on the pathogenic effects of intratracheal exposure to one-dimensional nanocarbons. *Carbon* **44**, 1057-1063, (2006).
- 76 Liu, Z. *et al.* In vivo biodistribution and highly efficient tumour targeting of carbon nanotubes in mice. *Nature Nanotechnology* **2**, 47-52, (2007).
- 77 Wei, Q. *et al.* Biodistribution of co-exposure to multi-walled carbon nanotubes and nanodiamonds in mice. *Nanoscale Research Letters* **7**, (2012).
- 78 Yang, S.-T. *et al.* Covalently PEGylated Carbon Nanotubes with Stealth Character In Vivo. *Small* **4**, 940-944 (2008).
- 79 Kostarelos, K. *et al.* Cellular uptake of functionalized carbon nanotubes is independent of functional group and cell type. *Nature Nanotechnology* **2**, 108-113, (2007).

Chapter V.

Increasing Loading Capacity: Protein Coronas

Originally published as:

A. Cifuentes-Rius, H. de Puig, J. Kah, S. Borros, K. Hamad-Schifferli. *ACS Nano*, **2013** (article ASAP, DOI: 10.1021/nn404166q)

H. de Puig, A. Cifuentes Rius, D. Flemister, S. H. Baxamusa and K. Hamad-Schifferli. *PLoS ONE*, **2013**, 8 (7), e68511

5.1. Introduction

Chapter III and Chapter IV have demonstrated that chemical functionalization (covalent or non-covalent) of CNTs have a direct effect on their dispersibility, biocompatibility and capacity for gene loading and cell transfection. Although important advances in the understanding of the optimal CNT-mediated gene vector features have been done in this previous work, there are some significant drawbacks that urge to be solved. On the bright side, GFP expression has indeed been successfully achieved with the internalization of pGFP complexed on ppAA-modified CNTs. However, the use of insufficient concentration of plasmid is forced, causing low transfection efficiencies. It all comes down to the cytotoxicity observed due to the particle aggregation experienced when high concentrations of CNTs are used. Moreover, the dispersibility of the nanoparticles (NPs) can unpredictably change as soon as they become into contact with the serum proteins of the cell medium. Therefore, a modification system that not only allows a higher loading of DNA per CNT but also preserves the physicochemical properties when introduced into a biological milieu is extremely desirable.

When NPs are introduced into biological fluids and systems, the proteins and small molecules that are present adsorb onto the NP surface, forming a protein corona.^{1,2} The protein corona is multilayered and held together by numerous non-covalent bonds. Because corona properties are so complex, it is difficult not only to characterize it but also to predict its behavior. Furthermore, the corona physically masks the surface of the NP, and can conceal the function of antibodies, ligands, or aptamers directly attached to the NP.³⁻⁵ Despite continued efforts to render NP surfaces non-fouling, growing evidence shows that corona formation cannot be avoided.⁶

However, important advances in understanding the protein corona have been made. While the NPs have varied among studies, the key finding is that certain classes of proteins bind strongly to the NPs making up the “hard corona,” while others interact more weakly with the NP, forming the “soft corona”.⁷⁻⁹ Once formed, the corona is not static, where its proteins are continuously exchanging with free species in the surroundings. These species change as the NP moves through different physiological environments, causing the protein corona to evolve.¹⁰⁻¹³ These advances in understanding the protein corona properties have brought us closer towards developing basic “design rules” that would enable us to manipulate their properties and optimize them for a particular biological application.

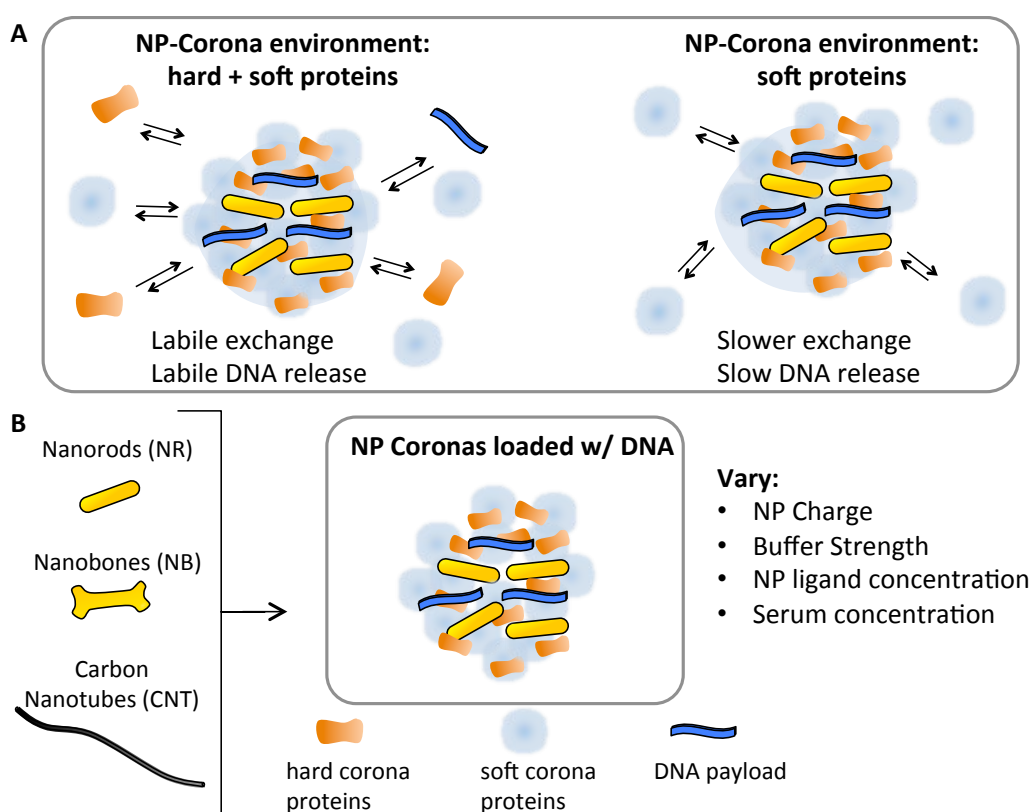
Protein coronas have promising properties that can be exploited.¹⁴ The corona is large and multilayered, and can be used to improve carrier properties for drug delivery by holding high amounts of therapeutic payloads. Recently, Kah and colleagues demonstrated that protein coronas on gold nanorods (NRs) can be loaded with DNA and doxorubicin at capacities 5-10× higher than what is achievable by covalent chemistry.¹⁵ Furthermore, because the protein corona is formed from endogenous proteins, unwanted immune responses against the therapeutic carrier could be minimized or prevented altogether.¹⁶ Moreover, the presence of proteins on the NP surface could also facilitate transmembrane internalization due to the higher amount of exposed ligands on the corona, which could assist recognition by cell membrane receptors.¹⁷ Thus, NR-coronas result in unique carriers with enhanced physical and biological properties, and have great promise for improving drug delivery.

Besides CNTs, gold nanorods are also an interesting choice for *in vivo* and *in vitro* applications due to their low toxicity in biological environments.¹⁸⁻²⁰ Several methods utilizing seed-mediated growth in the presence of a structure-directing surfactant have been developed to synthesize gold nanorods with tunable size and aspect ratios (AR).^{17,21} Indeed, it has been found that by tuning their size their optical properties can be also tuned, which makes gold NRs particularly attractive. They can be synthesized to absorb light in the infrared (IR) region, where biological tissue does not absorb, and thus enabling their use for photothermal therapy.²² By using such technique, it is possible to selectively kill targeted cells or enable externally controlled drug and gene delivery. In order to do so, the absorption peak of the gold NRs has to be inside the “tissue window”, between 600 and 1300 nm, where the penetration of light is maximal. This ensures that the gold nanorods with surface plasmon resonance (SPR) inside the tissue window will absorb light preferentially. Ultrafast photothermal heating of the NRs at their SPR induces the melting of the particles, causing the dissociation of their chemical functionality on the surface from the gold nanorods.^{15,23} Moreover, previous work from Hamad-Schifferli group showed that is possible to selectively release different single-stranded DNA (ssDNA) sequences from NRs with different ARs.¹⁸ This kind of approach is especially interesting when two types of nucleic acids have to be selectively released in the same medium, such as switching blood clotting on and off by the introduction of an inhibitor (aptamers) and a specific antidote with spatial and temporal control.

In this regard, depending on the delivery application, different modes of payload release may be desirable. Some applications require release at a constant rate to optimize the therapeutic index. In other cases, it is necessary to halt payload release until activation by an external trigger, such as a change in biological or chemical environment, as explained before.²⁴ Therefore, guidelines for

constructing a protein corona that exhibits a particular release behavior would add further value to its potential as a therapeutic carrier. All the advanced characteristics that gold nanorods offer, alongside to their surface properties, allowing the functionalization also with protein coronas, makes them a promising candidate to elucidate this protein corona behavior. NRs have unique optical properties due to their lack of symmetry that, at the same time, determines their SPR wavelength, which depends on the NR aspect ratio. As a result, NRs with defined AR can be easily tracked by UV-Vis spectroscopy and thus facilitate the characterization of the formed protein coronas.

This chapter is built upon these common observations about protein coronas to manipulate and optimize their properties for therapeutic delivery. It is expected that when NPs with protein coronas are in an environment with an abundance of hard corona proteins, exchange will occur between those in the environment and on the NP (Scheme 5.1A).¹³



Scheme 5.1. Graphical representation of the corona design approach. (A) Schematic of the corona exchange concept. NRs with human serum coronas loaded with DNA (NR-HS-DNA) in the presence of hard (orange) and soft (blue) corona proteins experience more labile release and higher release, while in the presence of soft corona proteins experience slower and lower release of DNA. (B) Formation of HS-DNA conjugates around NRs, NBs, and CNTs. The loading and passive release of a DNA payload is monitored for different NP charges, corona compositions, buffer strengths, and serum concentrations.

If the corona on the NP contains a payload, this exchange would induce payload release. However, if only soft corona proteins are present in the environment, the amount of exchange will be limited, resulting in less payload release. Therefore, one can use these two different protein classes to manipulate the exchange and consequently the release profile.

This exchange strategy is employed on NPs of interest to biological applications (NRs, gold nanobones, NBs and carbon nanotubes, CNTs) with coronas formed from human serum (HS) (Scheme 5.1B). NRs and NBs are gold nanorods of different aspect ratios with SPR of 800 nm and 1100 nm, respectively, which will be used to probe selective payload release. NR, NB, and CNT-coronas were loaded with a DNA oligonucleotide payload and their release profiles were monitored. The effect of varying buffer strength, passivating ligand concentration, and HS amount on the passive release of DNA were also examined, and the robustness of the NR-coronas in changing buffer conditions and blood plasma were explored. It is shown how corona properties to either minimize leakage for triggered release applications, or to control the rate of constant passive release can be strategically tuned.

5.2. Experimental Section

All the experiences carried out in this chapter unless otherwise noted were performed at the Hamad-Schifferli Lab, in the Mechanical and Biological Engineering Department at Massachusetts Institute of Technology (MIT).

5.2.1. Nanoparticle Preparation

Gold Nanorod (NR) Synthesis

Gold NRs and NBs were synthesized by standard seed and non-seed mediated methods from the literature.²⁵ For the synthesis of gold nanorods (NRs), a single surfactant non-seed-mediated growth method in 20 mL batches was used. 240 μ L of 50 mM gold chloride trihydrate (HAuCl_4) were added to 16.67 mL of 0.2 M cetyltrimethylammonium bromide (CTAB) mixed with 300 μ L of 100 mM Sodium Chloride (NaCl), and the solution turned orange; 240 μ L of 10 mM silver nitrate (AgNO_3) were added to the solution, followed by gentle mixing; 200 μ L of 100 mM Ascorbic Acid (AA) were added, followed by inversion until the solution turned colorless. 128 μ L of 0.3125 mM sodium borohydride (NaBH_4) were added. The solution sat on the bench undisturbed overnight at room temperature, during which time it turned reddish brown, indicating the presence of NRs. TEM analysis showed that the NRs had dimensions of $35 \pm 5 \text{ nm} \times 10 \pm 1 \text{ nm}$.

Gold Nanobone (NB) Synthesis

Gold nanobones were synthesized by a binary-surfactant seed mediated growth method. First, gold seeds were prepared by mixing 7.5 mL of 0.2 M CTAB with 2.5 mL of 1 mM HAuCl_4 and 0.6 mL of ice-cold 0.01 M NaBH_4 . After, the growth solution was prepared by adding 25 mL of 1 mM HAuCl_4 and 1 mL of 4 mM AgNO_3 into a mixture of 10 mL of 0.2 M CTAB and 15 mL of 0.3 M benzyldimethylhexadecylammonium chloride (BDAC), and the solution turned orange. 0.3 mL of 0.1 M ascorbic acid was added to the solution, followed by gentle mixing until the solution turned colorless. Finally, 0.05 mL of the seed solution was added to the growth solution. The solution was kept undisturbed overnight and turned reddish-purple, forming long gold nanocapsules. The day after the synthesis, 1 mL of 0.1 M ascorbic acid were added to every 50 mL of long nanocapsules solution, turning them into nanobones. TEM imaging showed that the NBs have dimensions 85×11

nm. All the reagents were purchased from Sigma-Aldrich, except for NaCl, which was from Mallinckrodt.

After the synthesis, NRs and NBs were washed to remove the excess reagents (30 min at 13500 rcf) resuspended in MilliQ water and stored until usage. NPs were centrifuged twice in the desired concentration of CTAB (from 0.5 to 10 mM, but typically 5 mM) before proceeding to the corona formation.

Carbon Nanotube (CNT) Solubilization

Carbon nanotubes (CNTs) used in this work were the same as the ones used in Chapter IV, including the shortened versions produced in the same chapter. ppPFM-modified CNTs were also employed (Chapter II) and were subsequently functionalized with HS as described in Chapter III. The formation of the coronas on rCNTs and ppPFM-modified nanotubes and its characterization was performed at IQS, following the same protocol and using the same equipment model o

Highly well-dispersed CNT-CTAB were obtained after dissolving the CNT in 5 mM CTAB (2 mg/mL), followed by sonication (2 h) and centrifugation (16200 rcf, 1 h) to isolate the highly dispersed carbon nanotubes from the bundles. A set of dispersions (from 2.5 µg/mL to 40 µg/mL) was prepared by diluting the original dispersion (2 mg/mL; CNT-CTAB) with 5 mM CTAB. These dispersions were sonicated for 30 min before UV-Vis analysis. The absorption at 500 nm was used to determine the concentration of the final well-dispersed CNTs. Knowing that the purchased CNTs were 5 µm length, 15 nm diameter and 2.1 g/mL density average, the concentration obtained was converted to nM. CNT-CTAB conjugates were washed with MilliQ water by using centrifuge filters (Amicon Ultra-0.5 mL, Merck Millipore).

5.2.2. Corona Formation

Human serum (HS) and human serum albumin (HSA) were purchased from Sigma-Aldrich. The DNA used had a sequence of 5'-CAG CGT GCG CCATCC TTC CC-TMR-3' (BCL2, MW = 6998.8, Integrated DNA Technologies, Inc.).

The corona formation was carried out *via* sequential and combined method. Both needed a previous centrifugation (13500 rcf for 30 min) of 1 mL of washed nanoparticles (NRs, NBs and CNTs). The obtained pellet was resuspended with the corona cocktail.

Sequential Method

In the sequential method, the pellet was first resuspended with 500 μ l of HS or HSA (5% (v/v) unless otherwise indicated) in 1-20 mM phosphate buffer (PhB, pH 7.4), incubated at 37 °C for 6 h, centrifuged at 4500 rcf for 20 min and resuspended with 500 μ L of 1 μ M DNA in PhB.

Combined Assembly

For the combined assembly, the corona cocktail was previously prepared together (protein and DNA) with same final concentrations as described before (500 μ L of 1 μ M DNA and 5% HS in PhB) which was used to resuspend the pellet. All nanoparticles were incubated overnight at 37 °C to enable DNA loading and, after incubation, were washed twice with 500 μ L PhB.

Blocking of the NP-Coronas

In the blocking process, the last wash during the corona formation was carried out with 500 μ l of HS or HSA solution (0.06, 0.15 and 0.3% (v/v)) in 5 mM PhB.

Formation of Coronas for Selective Triggered Release

To study how to selectively trigger payload release, coronas of human serum (HS) were formed around NRs and NBs using the previously described combined loading approach. NR-Coronas were loaded with a thrombin binding aptamer (TBA) whereas NB-coronas with its complementary DNA, which was used as an antidote (anti) because it can reverse TBA's effect by-base pairing with it. Single-stranded DNA was purchased from Integrated DNA Technologies and fluorescently labeled for quantification with tetramethylrhodamine (TMR) and fluorescein (FAM), respectively. The sequences used were 5' GGTTGGTGTGGTTGG-TMR 3' (TBA) and 5' AACCAACACAACCAA-FAM 3' (anti).

5.2.3. Nanoparticle and Corona Characterization

Both naked NPs and the corona conjugates were analyzed by UV-Vis spectrophotometry. For NRs and CNTs the scan carried out was from 400 to 900 nm (Cary 100 UV-Vis spectrophotometer, Agilent Technologies) while for the NBs it was from 400 to 1100 nm (Cary 500i UV-Vis-NIR spectrophotometer, Agilent Technologies). NR and NB concentrations of all samples could be

determined from the obtained UV-Vis spectra and known extinction coefficients. CNT concentration was calculated from the calibration curve, as explained previously.

Alteration of the nanoparticles' morphology when the corona was formed was characterized by TEM. Changes in size and charge were also determined by using dynamic light scattering (DLS, DynaPro Titan, Wyatt Technology Corporation) and zeta potential (Malvern Zetasizer Nano ZS90).

DNA Loading by Fluorescence

Each sample was thermally treated in order to quantify the DNA initially loaded on the formed NP-coronas. In order to do that, 30 μ L aliquots of the NP-coronas were heated at 90 °C for 30 min, and centrifuged at 13500 rcf. The concentration of DNA in the supernatants was quantified by fluorescence spectroscopy of the TMR tag ($\lambda_{\text{ex}} = 557$ nm and $\lambda_{\text{em}} = 581$ nm) attached on the 5' end of the DNA. The same process but without heating was carried out for other 30- μ L aliquots of each sample as a control.

Similarly, the DNA loading of the formed coronas around both naïve rCNTs and ppPFM-coated rCNTs and fCNTs were measured by using a Spex Fluoromax-4 spectrofluorometer (Horiba Jobin-Yvon, Edison, NJ) at the *Grup d'Enginyeria Molecular* (GEM) at IQS.

Passive DNA Release Profiles

Passively released DNA was measured by quantifying the DNA in the supernatant after a certain period of time. Samples were left at room temperature for 15 days and every time point an aliquot (30 μ L) was extracted. The aliquots were centrifuged at 13500 rcf for 12 min and the supernatant was diluted in PhB for fluorescence spectroscopy analysis. The leaking percentage was obtained by dividing the passively released concentration of DNA by the loading measured after the thermal treatment (90 °C during 30 min) on day 1.

Passive DNA Release in Blood Plasma

The NR-HS-DNA was prepared with 5% (v/v) HS and 1 μ M DNA as detailed previously. Following the formation of the DNA loaded corona, the NR-HS-DNA were washed twice by centrifugation at 4500 rcf for 20 min in 5 mM PhB prior to blocking by 0.3% HSA in 5 mM PhB. The blocking was performed under 1 h incubation at 37 °C before centrifuging the NR-HS-DNA at 5,000 rcf for 20 min and resuspending them in 1 mL of human blood plasma. The blood plasma was obtained from whole

human blood (Research blood components) by centrifugation at 4500 rcf for 20 min. The NR-HS-DNA were kept in blood plasma at 37 °C over a period of 15 days, during which 100 µL were aliquoted at fixed time points to quantify for the amount of DNA released.

Selective Release from NR/NB Mixture

Laser irradiations were performed using pulsed femtosecond (fs) light. For the 800 nm irradiation, the 532 nm output of a Q-switched Nd:YLF laser (Empower, Spectra-Physics) was used to pump a Ti:Sapphire regenerative amplifier (Spitfire, Spectra-Physics), which amplifies the 82 MHz output of a Ti:Sapphire oscillator, producing 50-475 µJ light centered at 800 nm, with a duration of 100 fs, a repetition rate of 1 kHz, and a spot size of 6 mm. The 1100 nm irradiation was achieved with a two-stage BBO/KNbO₃ optical parametric amplifier, pumped with a 800 nm pulse (Coherent Legend USX: <25 fs, 1 kHz), producing ~13.6 µJ pulses, with a duration of ~45 fs, centered at 1100 nm. The beam was focused to a spot size of ~100-120 µm. In a typical experiment, 100 µl of the NR/NB mixture were irradiated in a 3x3 mm quartz cuvette for 20 min. After irradiation, samples were spun at 14000 rcf for 15 min, and the supernatants were collected to quantify the DNA released and for blood clotting tests. NP melting was confirmed by observing a decrease in their absorbance spectra.

5.3. Results and Discussion

5.3.1. Optimizing the Protein Corona

Employing Different Corona Formation Strategies and Proteins

The composition of the protein corona around nanoparticles of polymers, silica, gold, carbon and other materials has been characterized by mass spectrometry and other techniques.^{1,6} It has been found that opsonins and apolipoproteins bind strongly to the NP to constitute the “hard corona” and are difficult to be removed.¹³ Surprisingly, the corona surrounding NPs does not have a high abundance of albumin, despite making up nearly half of human serum. Instead, some studies have pointed out that human serum albumin (HSA) binds weakly to the NPs, making up the soft corona.²⁶⁻²⁸ Corona composition varies with particle type, size, and surface chemistry, but in general, these two classes of corona proteins are generally observed.²⁹

To determine how these factors may affect the use of protein coronas to hold a payload for gene delivery applications, coronas around CTAB coated gold NRs (40 x 10 nm) were prepared using human serum albumin (HSA), human serum (HS) and equine serum (ES). HS and ES contain a mix of hard and soft corona proteins, whereas pure human serum albumin (HSA), which is the major component of HS (which has a HSA concentration of ~6 mg/mL), is known as a soft corona protein.^{2,13} Figure 5.1 shows that the particles behaved differently depending on the type of protein added and the preparation method.



Figure 5.1. Vials of the NR-coronas. Coronas prepared with ES, HS and HSA (from left to right).

Additionally, different procedures in order to form the protein corona with the highest loading capacity were tested, based on a previously published approach.¹⁵ In that sense, protein coronas were formed following the combined approach (CoNR) or the sequential assembly (SeNR). The former consists in the addition of the protein and DNA already mixed, whereas in the latter the

protein corona is firstly formed and the DNA is added afterwards. The corona payload was a 20 base DNA oligo tagged with the fluorophore TAMRA (5' CAG CGT GCG CCA TCC TTC CC –TMR 3').

For each of the corona formation strategies and proteins used (ES, HS and HSA), the absorbance of the particles (Figure 5.2) and the DNA loading per NR was measured (Figure 5.3 and Figure 5.4).

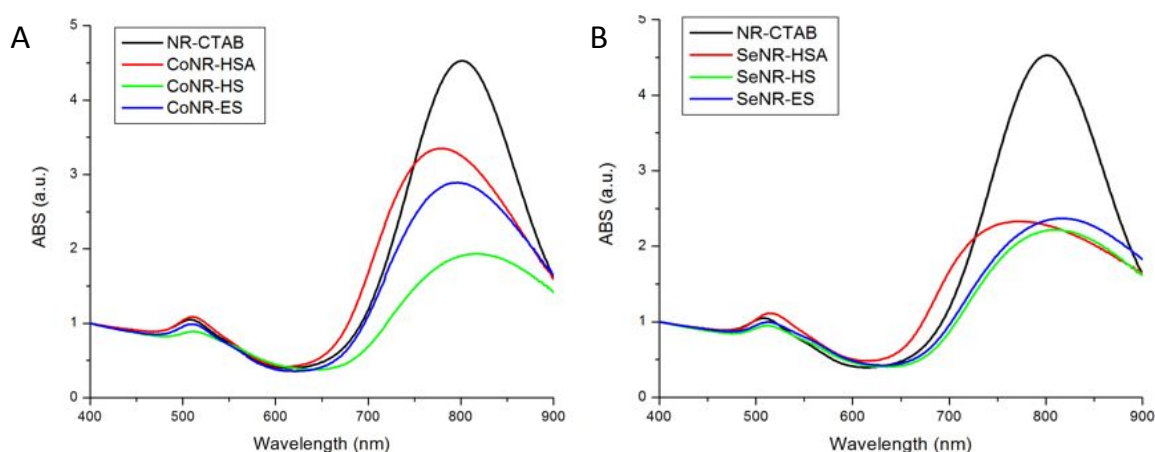


Figure 5.2. Absorbance spectra of the NR-corona using different type of proteins. Coronas prepared following (A) the combined method and the (B) sequential one. Longitudinal surface plasmon resonance (LSPR) of the NRs is still visible, with a minor red shift and slight broadening over the NR-CTAB.

In the combined approach, the CTAB coated NRs (Figure 5.2A, black) were not aggregated, but after the addition of proteins and DNA, the longitudinal surface plasmon resonance (LSPR) red shifts and broadening indicated that the NRs were in proximity to one another in the corona. This proximity caused the aggregation of the particles, which was seen as a decrease in the absorbance ratio A_{800}/A_{400} . Initially, the NR-CTAB had an absorbance ratio of 4.4 ± 0.2 and a LSPR peaked at 796 ± 6 nm. Among the three systems tried, HSA was the protein that caused the lowest aggregation on the particles, showing an absorbance ratio of 3.1 ± 0.3 and $LSPR_{max}$ at 783 ± 5 nm (Figure 5.2A, red), while HS was responsible for the highest aggregation with an absorbance ratio of 1.8 ± 0.3 and $LSPR_{max}$ at 808 ± 10 nm (Figure 5.2A, green). As for equine serum, the absorbance ratio was 2.5 ± 0.8 , and $LSPR_{max}$ at 796 ± 10 nm (Figure 5.2A, blue). Even though the NR-coronas contained multiple NRs, the absorption spectrum indicated that the NRs were sufficiently separated not to have their LSPRs strongly interact. On the other hand, by sequential loading (Figure 5.2B), all the NR-coronas (HSA, HSA and ES) had similar absorbance ratios (2.4 ± 0.2 , 2.2 ± 0.1 and 2.4 ± 0.1 , respectively) and LSPR peak, which was at 778 ± 6 nm for the NR-HSA, 805 ± 6 nm for the NR-HS and 805 ± 18 nm for the NR-ES.

The loading on the NPs was then measured for all cases by supernatant loss. To do so, particles were centrifuged and the amount of DNA present in the supernatant, therefore not attached in the corona, was quantified in order to calculate an approximate loading on the particles. DNA concentration was measured by fluorescence spectroscopy of the fluorophore tag bound to the DNA (Figure 5.3). Measuring DNA loadings by supernatant loss showed similar results for all kinds of coronas but overestimated the loading on the NRs, as DNA could be potentially released during the subsequent washes of the NPs.

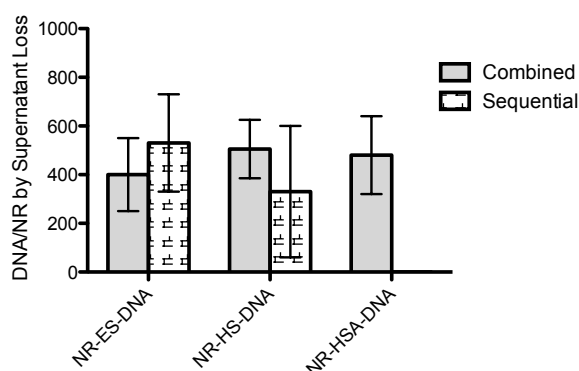


Figure 5.3. Loading from coronas measured by supernatant loss.

In order to confirm these results, the conjugated NRs were heated at 90 °C for half hour and the fluorescence of the fluorescently tagged DNA that could be released by heat displacement was measured (Figure 5.4).

While high temperature was able to disassemble the corona to release both HS and DNA, it was noted that heating did not displace the entire payload in the corona, as was found previously.¹⁵ Also, the amount of serum and payload released by heat displacement changes with time and underestimates the DNA loading. A more accurate quantification would require combining several techniques including chemically dissolving the NPs or displacing the proteins in the corona by detergents. However, thermal displacement was found to give consistent readings if the conditions were kept constant; hence all measurements were done consistently for comparison. Therefore, heat displacement was used as the reference value to calculate the total coverage of the NR-coronas. While HSA, HS and ES could form a corona around NPs, their ability to carry DNA payload was found very different. Notoriously, error bars obtained were large compared to covalent attachment strategies due to the complex nature of corona formation, as it involves non-covalent interactions between multiple species and it can undergo a constant dynamic exchange with its surrounding media.

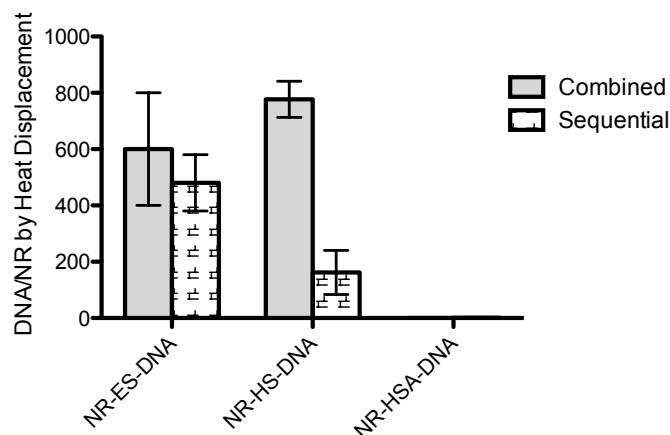


Figure 5.4. Loading of NR-coronas measured by heat displacement.

Figure 5.4 shows that both ES and HS yield high loading of payload on the NPs due to the fact that they are comprised of mixtures of proteins, some of which are strong binders to the NPs. In contrast, NR-HSA coronas had negligible DNA loading for both assembly approaches. Although a corona was formed from HSA, as evidenced by the increase in D_H (Figure 5.5A), it was not as effective as HS or ES at loading DNA. This is most likely due to the fact that HSA is a soft corona protein, which forms a larger and more loosely bound corona, and does not interact strongly with DNA. Based on these results, it appears that components in the serum other than HSA are responsible for holding the NRs, corona, and DNA payload together.

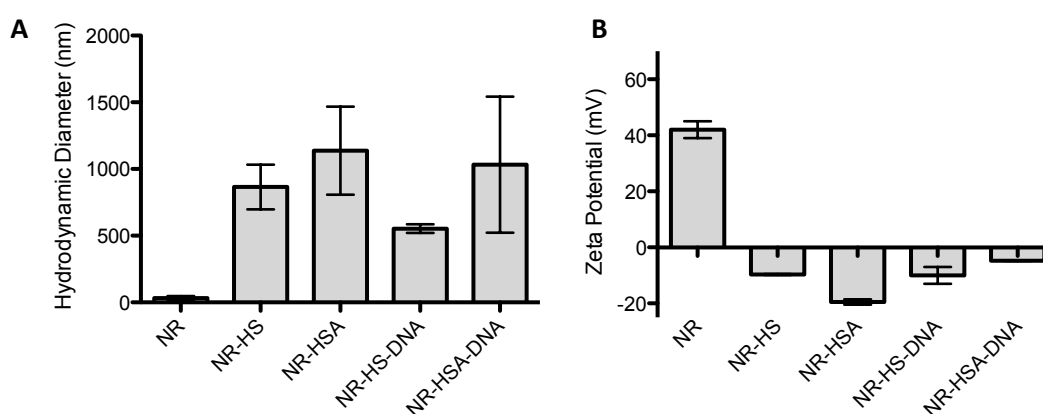


Figure 5.5. Size and charge of the NR-coronas. (A) Hydrodynamic diameter of coronas formed with HS, ES and HSA measured by DLS and (B) their corresponding zeta potential. Coronas were formed by the combined approach.

Besides, DLS measurement (Figure 5.5A) revealed that when coronas were formed from either HS or HSA, larger species appeared. NRs had an average $D_H = 32 \pm 15$ nm which increased to $D_H = 865 \pm$

167 nm with HS corona formation or $D_H = 1138 \pm 330$ nm with HSA corona formation. These size increases suggested that both HS and HSA formed large coronas around a cluster of multiple NPs, and that HSA apparently formed a larger corona than HS. This could be due to the fact that HSA is a soft corona protein, which has a weaker interaction with the NPs. The size increase was not as large for coronas formed with DNA payloads, which could be due to differences in the corona composition or binding strength in the presence of the negatively charged DNA. Even though the NR-coronas contained multiple NRs, the absorption spectrum indicated that the NRs were sufficiently separated not to have their SPRs strongly interact. Zeta potential measurements of all three positively charged NPs showed that as the NP-coronas were formed, they adopt a similar negative charge (Figure 1f) due to the negative species that dominate HS composition (Figure 5.5B).

As a result of this study, protein corona around NRs were formed using the combined method and HS, given the higher DNA loadings obtained and demonstrated in this work. NR-coronas formed in such conditions exhibit good colloidal stability in solution after corona formation (Figure 5.6A).³⁰

TEM images show large, diffuse agglomerates containing many NRs, confirming that there are not one but many NPs in a corona (Figure 5.6B). Such observation may have a direct impact on the loading capacities of the final NR-corona.

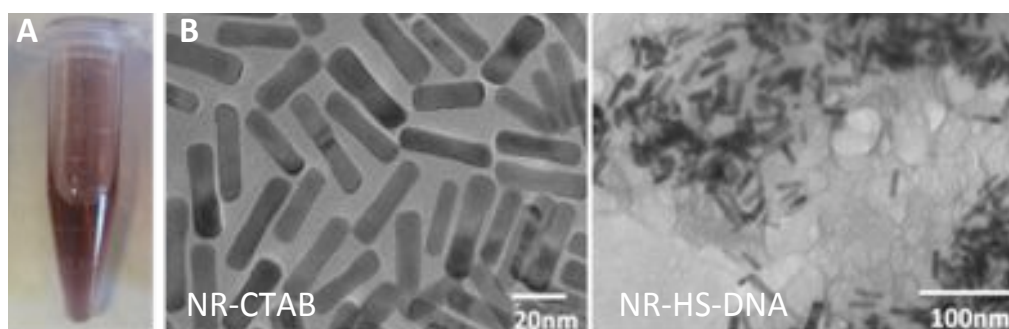


Figure 5.6. Characterization of the NR-coronas. (A) Image of the vial after corona formation confirming that NR-HS-DNA are stable in solution and (B) TEM images of NRs and NR-HS-DNA evidencing that the corona is formed with many NPs.

Tuning DNA Loading by Varying Corona Formation Conditions

To determine optimal parameters for highest DNA loading on NRs, the conditions for corona formation were varied. Such conditions were tuning the phosphate buffer (PhB) concentration, HS percentage and CTAB concentration (Figure 5.7). DNA loading (number of DNA/NR) was measured on the first day of the experiment by heating the sample at 90 °C for 30 min and quantifying the

TAMRA-conjugated DNA released in the supernatant.¹⁵ We observed that the DNA loading measured at day 1 is often lower than the amount of DNA passively released after 10 days, which shows that protein corona properties are complicated, and that it is difficult to displace the entire amount of DNA from the coronas when they are initially formed.

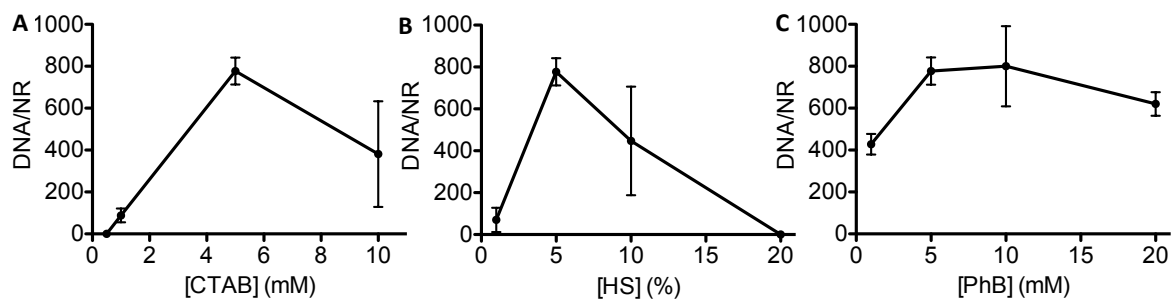


Figure 5.7. Effect of environmental and assembly conditions on loading of DNA from NR-HS-DNA, varying (A) CTAB, (B) HS and (C) phosphate buffer (PhB) concentration during corona assembly and their effect on DNA loading per NR.

Firstly, how the concentration of CTAB affected DNA loading in the corona (Figure 5.7A) was examined. DNA loading was negligible at $[CTAB] < 1$ mM, but increased slightly to 88 ± 33 DNA/NR for $[CTAB] = 1$ mM. DNA loading peaked at 777 ± 64 DNA/NR at $[CTAB] = 5$ mM, before decreasing to 380 ± 252 DNA/NR at $[CTAB] = 10$ mM. Because CTAB binds weakly to the NPs, it is in dynamic flux with the environment, where it switches between bound and unbound states. Due to its charge, CTAB can interact with both the DNA and the negatively charged corona proteins. Excess CTAB can form stable micelles that could interact with the free HS proteins and DNA, thus competing with corona formation and DNA loading on the NP surface. This excess of CTAB will not only have a negative effect on the loading capacities of the formed protein coronas, but may also increase the cytotoxicity of these DNA vehicles when used in biological systems, as seen in the previous chapter (Chapter IV) and reported before.¹⁷ On the other hand, if the CTAB concentration is below its critical micelle concentration, cmc ($cmc_{CTAB} = 1.2$ mM^{31,32}), the NPs are not fully passivated,^{15,33,34} so fewer HS proteins are able to interact with the NPs and form a corona and load DNA. Therefore, CTAB is intimately involved in corona formation and its concentration affects DNA loading on the NPs.

Secondly, the effect of varying HS concentration from 1-20 % during corona formation and DNA loading (Figure 5.7B) was also examined. DNA Loading was low for 1% HS (70 ± 58 DNA/NR) and peaked at 777 ± 64 DNA/NR for 5% HS. At higher HS concentrations, the loading decreased (477 ± 259 DNA/NR for 10% HS coronas), becoming negligible at 20% HS. This shows that the concentration

of HS used to form the corona also affects the amount of DNA loaded. When large amounts of HS are present, the HS proteins may compete with the DNA for the positively charged surface of the NPs, thus reducing the loading of DNA within the corona. Moreover, the excess of HS may lead to the formation of larger aggregates, as suggested by the red shifts and peak broadening of the LSPR, which in turn reduces their stability in solution (Figure 5.8A). The resulting absorption spectra suggested that coronas formed at higher HS concentrations were more prone to form larger aggregates, except at 20% of HS, in which case the possible increase of the electrostatic interaction between the negatively charged particles led to a decrease of the clustering effect of the corona.

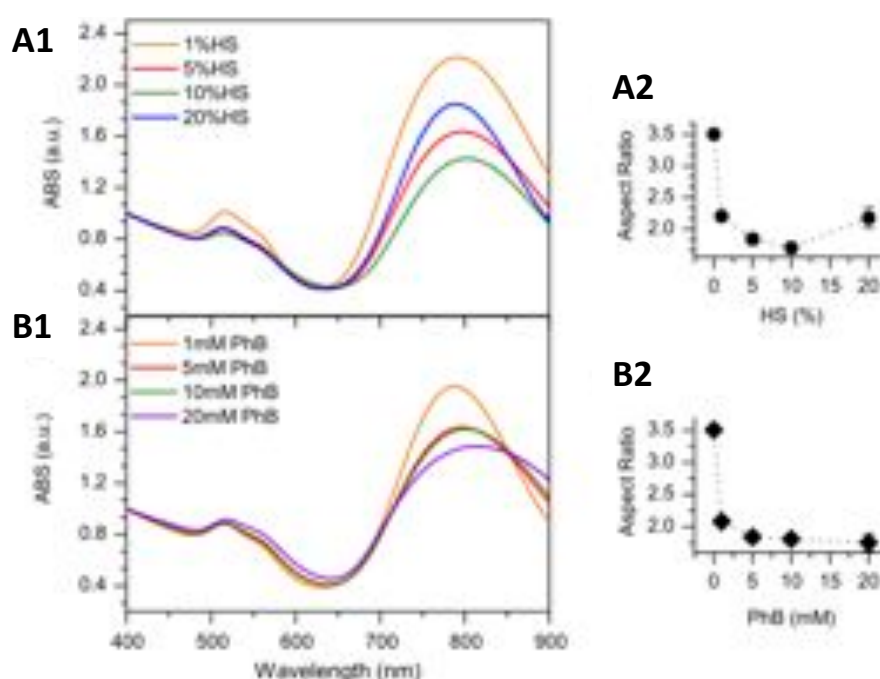


Figure 5.8. Absorption spectra of NRs after the formation of the protein corona. Measurements carried out in different (A) HS concentrations and (B) buffer strengths, showing that both parameters affect the nature of the NR. Moreover, the aspect ratio (inset) for both cases decreased compared to the NR-CTAB.

Lastly, the phosphate buffer (PhB) concentration was varied during corona formation and DNA loading (Figure 5.7C). The DNA loading profile varied with PhB, showing that PhB influences the protein corona integrity and thus its ability to hold payload, which is most likely due to the charge screening modulating the electrostatic interactions between the DNA, corona proteins, and CTAB. Of all the three parameters, PhB had the weakest effect on corona loading. However, it had a similar effect on the absorption spectra (Figure 5.8B) as the observed for the HS, where the increase of PhB induced a broadening of the 800 nm peak and a decrease of the aspect ratio when compared to the native CTAB-coated NRs (without corona) in Milli-Q water.

5.3.2. Assessment of the Evolution of Protein Corona

Kinetics of the Protein Corona Formation

The effect of the corona formation around the NRs on the absorption spectrum with time is also analyzed (Figure 5.9).

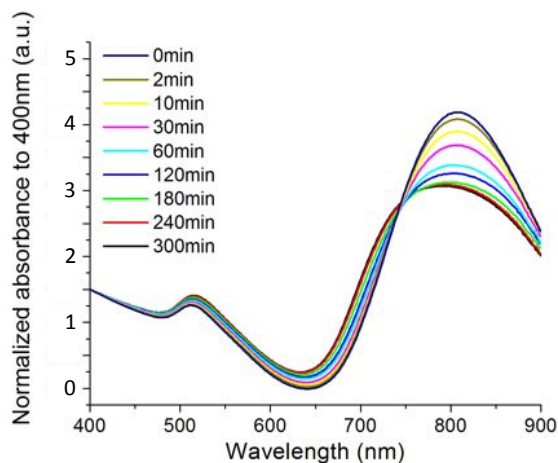


Figure 5.9. Time-evolution of the absorption spectra of the NR-coronas. Data collected as the protein corona was being formed.

By monitoring the kinetics of formation of protein coronas a decrease in their AR was observed, indicating that particles were interacting and coming within proximity of one another. The appearance of an isosbestic point $\sim 740\text{nm}$ during the corona formation could also be seen, which suggests that throughout the reaction there is equilibrium between the particles in and out of the corona.

Effect of the Corona Formation Parameters on the Passive Release

Changing [CTAB], HS%, and [PhB] also affected the passive release of DNA as shown in Figure 5.10. Results are plotted as released DNA per NP and the leaking percentage considering 100% the loading measured after thermal treatment ($90\text{ }^{\circ}\text{C}$, 30 min) on day 1.

NR-HS-DNA showed low DNA release during the first 4 days for the three concentrations of CTAB that showed non-negligible DNA loading (1, 5, and 10 mM) (Figure 5.10A). Release increased thereafter, with a large release at day 7, particularly in the presence of 5 and 10 mM CTAB. This initial 3 – 4 day lag was observed previously for NRs coated with coronas of equine serum.¹⁵ Previous

studies have found that the composition of the corona changes during an initial period, before the corona hardens (after ~48 h).¹⁰ This initial lag is beneficial for triggered release experiments, where the corona can be used to hold the payload within the first three days without significant passive release. The amount of DNA passively released increased with [CTAB] (Figure 5.10B).

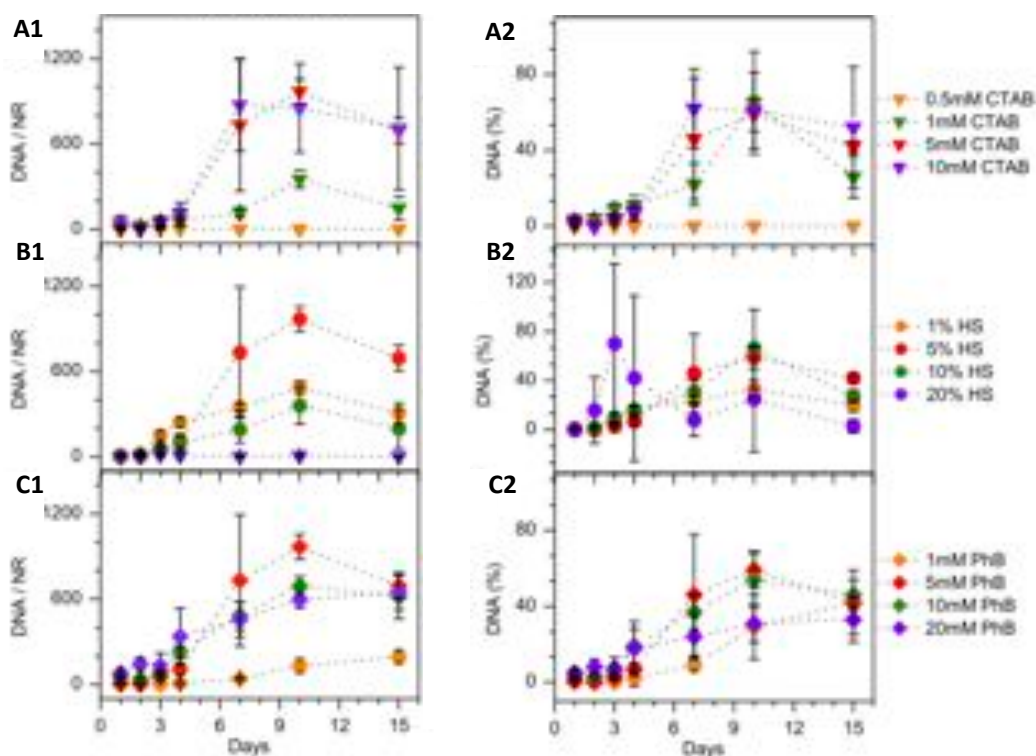


Figure 5.10. DNA passive release profiles of NR-coronas. Effect of varying (A) CTAB (B) HS, and (C) PhB concentration on DNA leakage. Data expressed in (1) DNA released per NR and (2) percentage of DNA released.

Varying HS% and [PhB] also affected passive release, and the amount released correlated with the amount of DNA initially loaded (Figure 5.10B). The initial 3-4 day lag was shortened to 2 days for high PhB concentrations (20 mM) and low HS concentrations (1%), indicating that the ability of the protein corona to hold on to the DNA payloads at earlier time points is also dependent on the protein and ionic environment.

Evolution of Protein Corona Affects Passive Release

The coronas around NPs are known to change in different environments. The effect of making NR-HS-DNA coronas at one ionic strength, and then introducing them to a solution with a different ionic strength was explored (Figure 5.11).

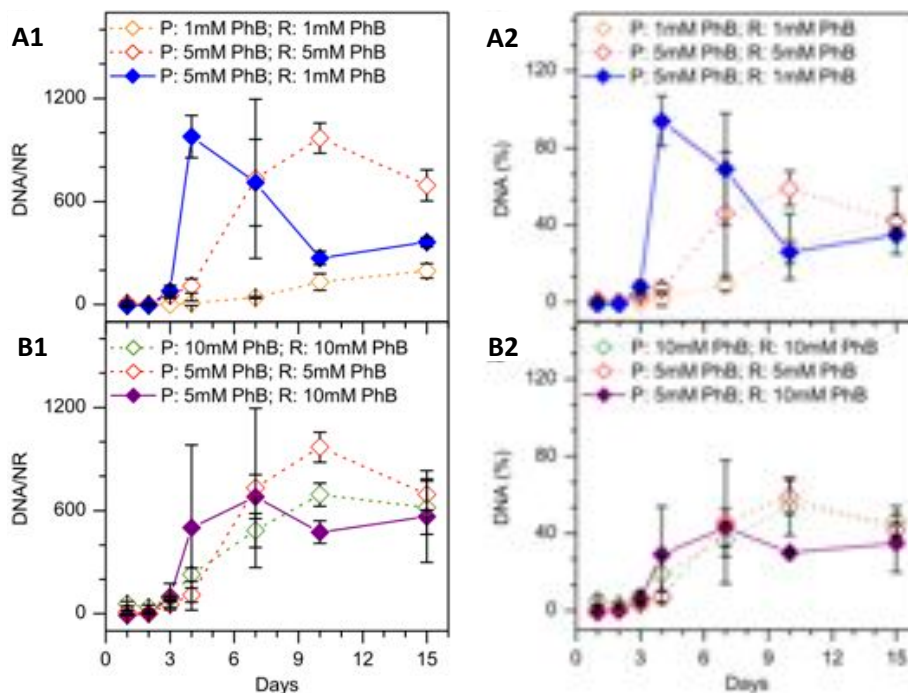


Figure 5.11. Passive release of NR-coronas in different buffer concentrations. Effect of forming NR-HS-DNA in one PhB concentration, and measuring the passive release in a different PhB concentration. (A) NR-HS-DNA were prepared (P) in [PhB] = 5 mM using 5% HS, and then passive release (R) measured in 5 mM (red diamonds) and 1 mM (blue diamonds). NR-HS-DNA prepared in [PhB] = 1 mM and a passive release profile measured in 1mM (orange diamonds). (B) NR-HS-DNA prepared in 5 mM PhB and released in 10 mM PhB (purple diamonds) and 5 mM PhB (red diamonds). NR-HS-DNA formed in 10 mM PhB and released in 10 mM PhB (green diamonds) for comparison. Passive release expressed as (1) DNA released per NR and (2) leakage percentage.

NR-HS-DNA were formed in [PhB] = 5 mM and then release profiles were measured in [PhB] = 1 mM, 5 mM, and 10 mM. We observed that the coronas formed at 5 mM PhB and then introduced to 1 mM PhB (Figure 5.11A, blue diamonds) have a passive release profile that is different from the coronas formed and released at 5 mM PhB (Figure 5.11A, red diamonds) and those formed and released at 1 mM PhB (Figure 5.11A, orange diamonds). Similarly, the NR-HS-DNA formed at 5 mM PhB and released at 10 mM PhB (Figure 5.11B, purple diamonds) also show a different release profile between that formed and released at 10 mM PhB (Figure 5.11B, green diamonds) and that formed and released at 5 mM PhB (Figure 5.11B, red diamonds). Both release profiles in 1 mM and 10 mM PhB show the same initial 3 day lag as that of coronas made and released in 5 mM, indicating that when the coronas are formed in one PhB concentration and then used for release in another, the release profile retains some of its original release properties, resulting in an intermediate

behavior. Thus, the corona has some resilience that can be maintained in different buffer solutions for several days.

Exploiting Corona Exchange for Manipulating Payload Release

Despite its poor loading capacity, HSA can potentially function as a blocking agent for NR-HS-DNA, where it could be used to form an additional corona layer around already formed coronas to block passive DNA release on already-formed coronas. Because HSA is a soft corona protein, it has limited exchange with the hard corona proteins in HS, and consequently results in slower release of DNA from the corona (Scheme 5.1B). This property can be exploited to hold the payload in the corona for an extended period of time prior to their triggered release. In contrast, HS contains hard corona proteins that can exchange with those in the NR-HS-DNA to promote payload release. Therefore, a rational selection of protein environment could provide us with a handle for manipulating the payload release profile.

Extending the idea that HS and HSA have different capacities to form payload-carrying coronas, the ability of the protein environment to manipulate the passive release of DNA from NR-HS-DNA was tested. Passive release of DNA from NR-HS-DNA whose corona was exchanged with HS or HSA was compared. Corona exchange was achieved by placing NR-HS-DNA in a solution of HS or HSA, and release was quantified by measuring the DNA in the supernatant as a function of time. Release was compared to NR-HS-DNA that were not exchanged with HS or HSA (“no block”).

The release profile changed depending on the protein environment (Figure 5.12).

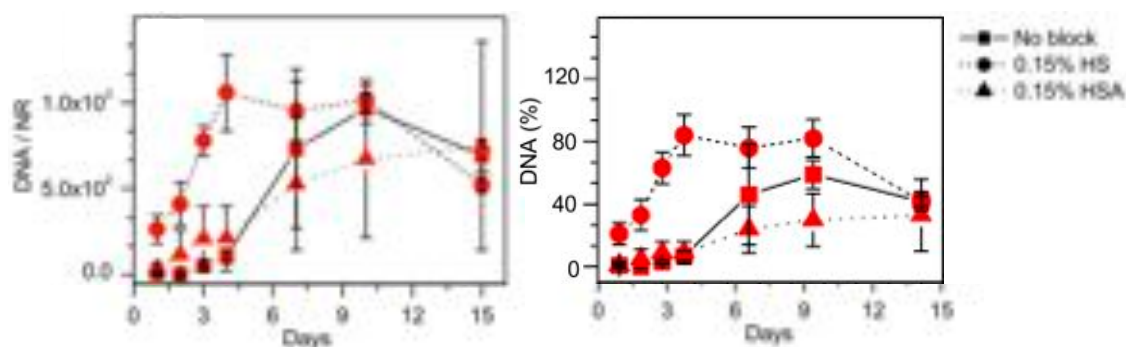


Figure 5.12. Passive release DNA profiles of coronas in an exchange environment of 0.15% HS (circles), 0.15% HSA (triangles), or no protein (squares) on NRs. Passive release expressed as DNA released per NR (left) and leakage percentage (right).

If the NR-coronas were placed in 0.15% soft corona proteins (HSA), less DNA was released (Figure 5.12, red triangles) compared to the control without corona exchange (Figure 5.12, red squares). HSA was thus able to reduce the passive release of DNA from the NR-HS-DNA, most likely by minimizing the protein exchange in the corona. However, when corona exchange was performed in 0.15% HS, a burst of payload release occurred during the first 4 days (Figure 5.12, red circles). In fact, ~20 % (264 ± 83 DNA/NR) of payload was already passively released at day 1, whereas the same amount of release is not reached until day 7 for the HSA exchange. This is most likely due to significant protein exchange occurring between the free HS proteins and those in the corona, supporting our postulation that other components in HS other than HSA are perturbing the corona to release more payload. The responsible protein components are most likely the hard corona proteins in the HS that are able to exchange with the existing corona proteins on the NRs because of similar binding affinity. Therefore, an appropriate selection of blocking proteins can provide a means to control payload release rate.

Additionally, the effect of varying the HS and HSA concentration in blocking to tune passive release was examined (Figure 5.13).

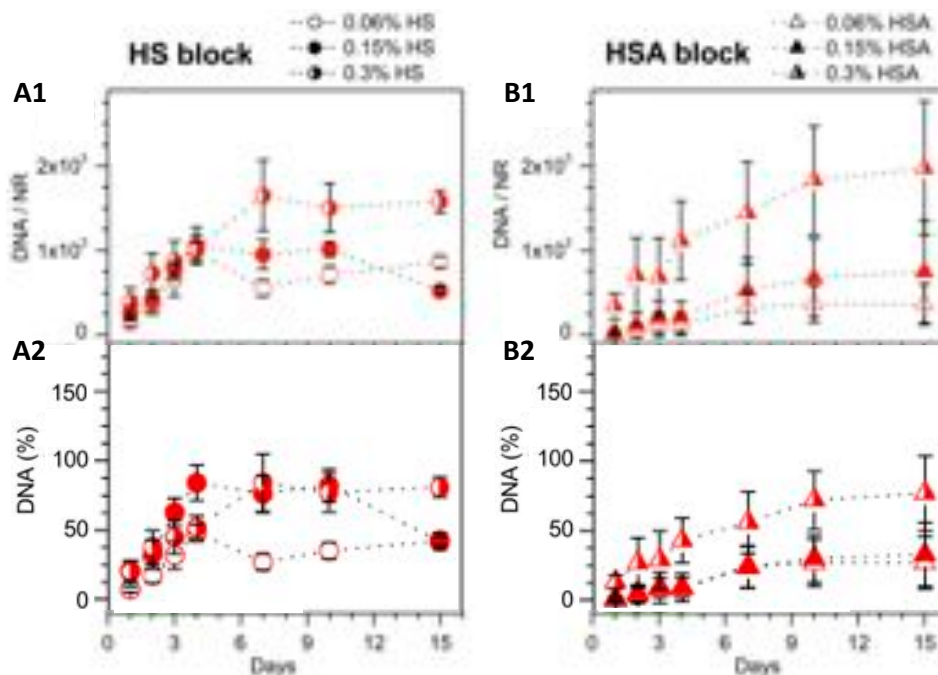


Figure 5.13. Leakage of NR-coronas at different exchange environments. Passive release of DNA from coronas on NR by varying the amount of (A) HS and (B) HSA exchange (0.06%, 0.15%, and 0.3% HS and HSA). Passive release expressed as (1) DNA released per NR and (2) leakage percentage.

Increasing the HS% used for corona exchange increased the DNA released from the NRs (Figure 5.13A). A similar trend was observed for increasing the HSA% although the release amounts were lower, confirming that HSA is better at blocking the coronas than HS (Figure 5.13B). Evidently, a higher protein concentration in the NR-HS-DNA environment facilitates a greater degree of exchange, thus inducing a larger amount of DNA released.

Leakage in Blood Plasma

Since the application of these engineered nanoparticles is associated to the interaction with a biologic fluid containing both hard and soft corona proteins, the corona composition and behavior might be affected. Therefore, passive release of DNA from NR-HS-DNA in human blood plasma, which contains both hard and soft corona proteins, was also investigated. Profiles of passively released DNA from 1.5 nM of NR-HS-DNA with and without blocking with 0.3% HSA were measured (Figure 5.14).

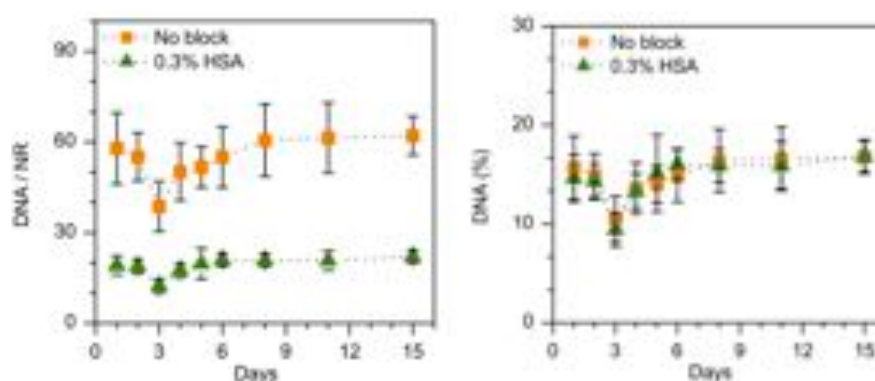


Figure 5.14. Leakage of DNA in blood plasma. Values from NR-HS-DNA with no blocking (orange squares) and NR-HS-DNA in blood plasma blocked by 0.3% HSA (green triangles). Passive release expressed as DNA released per NR (left) and leakage percentage (right).

In the absence of blocking, 369 ± 89 DNA strands were loaded per NR, out of which 58 DNA/NR (15.7% of loaded DNA) was released at Day 1 after preparation (Figure 5.14, orange squares). The amount of released DNA remained relatively constant until Day 15, and no initial lag was observed. This shows that as soon as the NR-HS-DNA are placed into plasma, a small amount of DNA is released, probably due to the exchange with hard corona proteins in the plasma. Released DNA decreased slightly at 3 days, perhaps due to the corona reorganization, where DNA loads back onto the NR-HS-DNA as the blood plasma proteins contributed to the existing corona. The DNA release profile was similar for NR-HS-DNA blocked by 0.3% HSA. In this case, 130 ± 37 DNA were loaded per

NR, of which 19 DNA/NR was released at Day 1 (Figure 5.14, green triangles). Although the amount of DNA released was much lower, the percentage of loaded DNA that was released on Day 1 (14.6% of loaded DNA) is only slightly lower compared to that without blocking. This shows that blocking can decrease the concentration of passively released DNA.

In practice, effective blocking by HSA may be difficult to achieve since the blood plasma contains a large number of hard and soft corona proteins that can easily exchange with the corona on the NRs, including the HSA used for blocking. This is evident from the similar dip at Day 3 for this experiment, suggesting that corona reorganization could also be taking place with the 0.3% HSA present. However, in both cases, we observed no further increase in the DNA leakage beyond Day 8. This shows that the protein corona can be used to hold the loaded DNA stably for more than a week in blood.

5.3.3. Using Gold Nanrods for Selective Triggered Release Applications

Gold nanorods (NRs) have gained considerable interest for therapeutic applications because they can be selectively excited at wavelengths where tissue is transparent to release multiple species that can impact complex processes, so they have many advantages for triggering payload release.^{18,35-38} As it has been introduced at the beginning of this chapter, the unique optical properties of gold NRs rely on their lack of symmetry. Their aspect ratio (length divided by width) can be tuned by synthesis conditions and it determines the wavelength of the SPR. Therefore, gold nanorods with different aspect ratios will have different SPRs. Such features will allow the selective melting of a mixture NRs of different AR by applying the ultrafast thermal heating at their specific SPR.¹⁸

Proving Selective Laser Irradiation of Differently Sized NRs

Cetyltrimethylammonium bromide (CTAB)-coated gold particles that absorbed at two distinct wavelengths were synthesized.^{25,39,40} On the one hand, the same rod-shaped nanorods previously analyzed with an AR = 3.7 and $D_H = 45$ nm had a LSPR at 763 nm. On the other hand, bone-shaped “nanobones” (NBs) with AR = 4.8 and $D_H = 55$ nm had a LSPR at 1065 nm. Firstly, melting of the NRs and NBs by external laser excitation at their maximum LSPR was confirmed separately (Figure 5.15A and B, respectively). Secondly, because NRs and NBs exhibited distinct absorption features, selective excitation by fs-pulsed lasers of a NR/NB mixture was tested. 800 nm irradiation of a NR/NB mixture resulted in melting of the NRs only, seen by a decrease of the LSPR at 800 nm (Figure 5.16A). Melting

induces the NRs to change shape to spheres, which shifts and decreases their LSPR.⁴¹ The LSPR at 1100 nm did not change, indicating that NBs were not melted because 800 nm coincides with a minimum in their absorption (Figure 5.15B, black line). Likewise, NRs do not absorb at 1100 nm (Figure 5.15A, black line), so 1100 nm irradiation resulted in a decrease of the NB LSPR but did not affect the NR LSPR, indicating selective melting of the NBs (Figure 5.16B).¹⁸

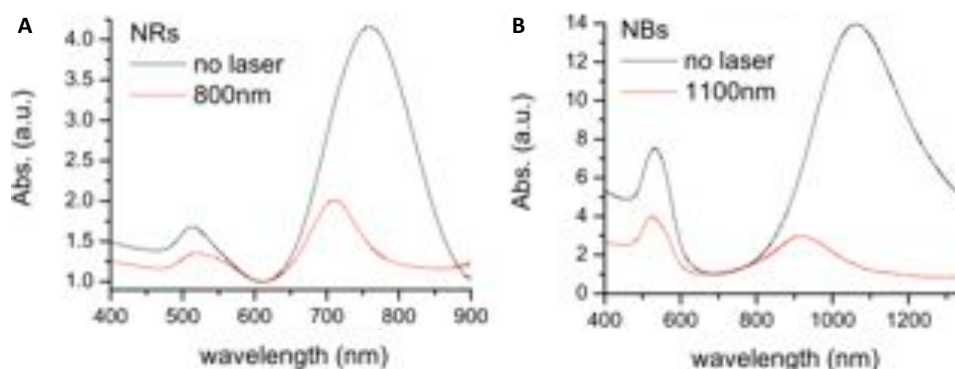


Figure 5.15. Melting the NR-CTAB and NB-CTAB. The melting of the (A) NR-CTAB and (B) the NB-CTAB (b) was separately tested. It could be observed that the NR-CTAB melted after 800 nm irradiation, and that the NB-CTAB could melt after irradiation at 1100 nm, as evidenced by the decrease in their respective LSPR peaks.

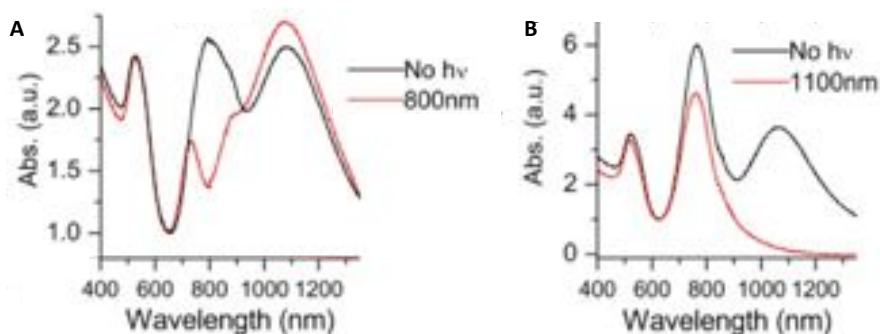


Figure 5.16. Selective melting of a NR/NB-CTAB mixture. Absorption spectra of (A) mixture of NR-CTAB + NB-CTAB before (black) and after (red) 800 nm irradiation; and (B) NR-CTAB + NB-CTAB before (black) and after (red) 1100 nm irradiation.

Evaluation of the Protein Corona on Gold Nanobones

The same procedure to form coronas in the conditions optimized for the NRs (5 mM CTAB, 5% HS and 5 mM PhB) was followed for the preparation on NBs (85 x 11 nm). The DNA employed in this study was also the same as before (20 base DNA oligo tagged with a fluorophore TAMRA). The resulting conjugates were characterized together with the NB-CTAB particles (Figure 5.17).

Similar behavior as the one previously described for the NR-coronas was detected for the NB-coronas. NB-HS-DNA showed that the longitudinal surface plasmon resonance (LSPR) of the NBs was still visible, with a minor red shift and slight broadening over the CTAB coated NRs (Figure 5.17A, solid vs. dashed lines). LSPR red shifts and broadening indicated that the NBs were in proximity to one another in the corona, which was confirmed by TEM (Figure 5.17E). Therefore, the cluster formation observed for the NR-coronas was equally revealed for the NBs by TEM imaging. DLS also support this suggestion, as a D_H increase was also detected, indicating that a cluster of multiple NBs formed the corona (Figure 5.17C). The corona formation also affected the NB charge, since the HS and DNA absorption changed the positively charged NB-CTAB to negative, confirming its proper formation (Figure 5.17D).

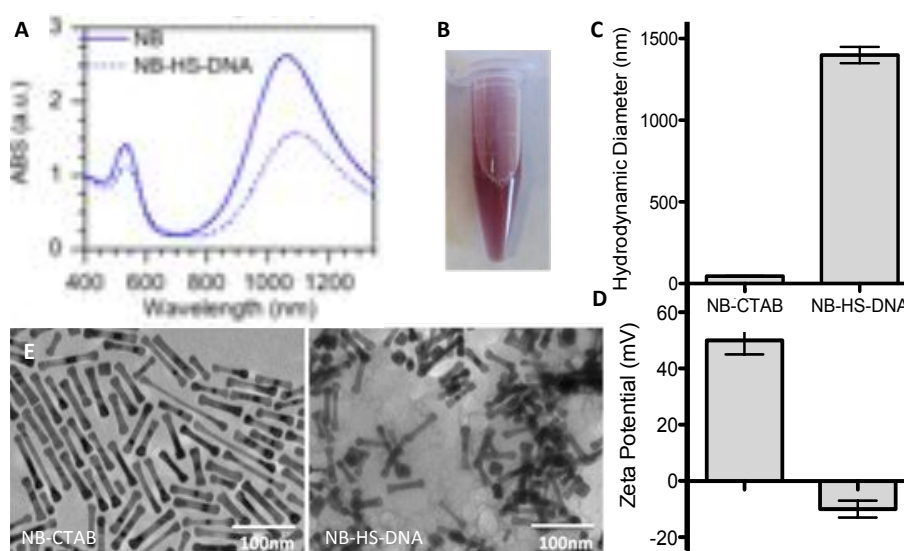


Figure 5.17. Characterization of NB-coronas. (A) Absorption spectra of NBs before (solid line) and after (dashed line) the formation of the protein coronas. (B) Image of the vial after corona formation show that nanoparticles were stable in solution. (C) Average hydrodynamic diameter, D_H , measured by DLS and (D) Zeta potential of NBs and NB-HS-DNA. (E) TEM images of NB-CTAB and NB-HS-DNA.

Corona formation around NBs also allowed an excellent stability in buffer (Figure 5.18B). Furthermore, NB-HS-DNA had 710 ± 130 DNA/NB and a surface loading density of 0.2 DNA/nm², which is lower compared to the values obtained for the NR (777 ± 64 DNA/NR, 1 DNA/nm²). These results show that coronas can be formed and loaded with DNA on different NPs, although their loading densities may differ.

Additionally, the same corona exchange phenomenon studied for the NR-coronas was also analyzed for the recently developed NB-coronas. The initial 3 – 4 day lag observed for the NR-HS-DNA was

also needed for the NB-coronas to be able to carry out triggered release experiments by an external energy source. Therefore, passive release of DNA from NB-HS-DNA whose corona was exchanged with HS or HSA, both in different concentrations, was also monitored (Figure 5.18).

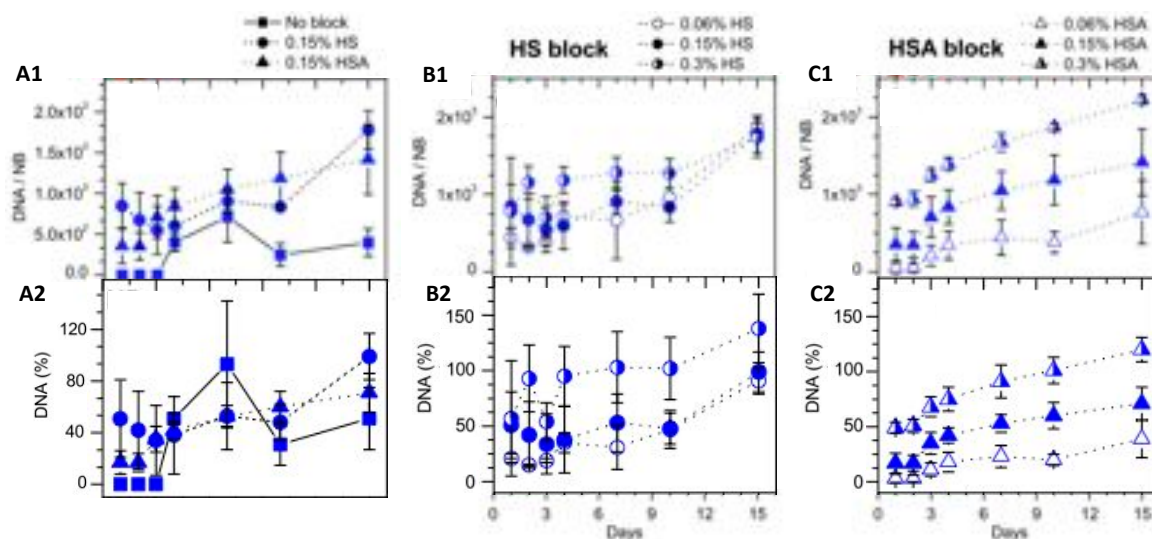


Figure 5.18. Passive release DNA profiles of NB-coronas. DNA leakage in an exchange environment of (A) 0.15% HS (circles), 0.15% HSA (triangles), or no protein (squares) on NR, (B) different concentrations of HS, and (C) varying the amount of HSA. Passive release expressed as (1) DNA released per NR and (2) leakage percentage.

NB-HS-DNA without corona exchange passively released DNA with a profile similar to the NRs, starting with negligible release in the first 3 days and then increasing with time (Figure 5.18A, squares). However, corona exchange with 0.15% HSA seemed to increase the amount of DNA passively released at the beginning (354 ± 218 DNA/NB or $17 \pm 9\%$ of initially loaded DNA at Day 1) (Figure 5.18A, triangles). This amount is even higher (848 ± 279 DNA/NB or $51 \pm 30\%$ of loaded DNA) in the presence of 0.15% HS (Figure 5.18A, circles). Apparently, coronas formed on larger NBs are more prone to leakage, and HSA seems less effective in blocking passive release compared to NRs (Figure 5.12). As was previously reported, NP size can also influence corona formation.^{2,21,42} While blocking was not observed with 0.15% HSA compared to the control in NBs, differential passive release between HS and HSA as with NRs was still demonstrated.

Similar behavior to the one observed for the NRs (Figure 5.13), could also be seen for the NB-coronas when changing the HS (Figure 5.18B) and HSA (Figure 5.18C) concentration in blocking. In both cases, an increase of released DNA was evidenced. However, it was again confirmed that HSA at low concentrations acts as a better blocking agent than HS, since the amount of DNA released quantified was slightly lower.

Characterization of the Protein Corona for Selective Payload Release

Coronas of human serum (HS) were formed around the particles following the same strategy optimized at the beginning of the chapter and reported elsewhere.¹⁵ However, this time, NR-coronas were loaded with a DNA with a different sequence (5' GGTTGGTGTGGTTGG-TMR 3') from the previously used, known as thrombin binding aptamer (TBA) and typically used for blood clotting applications given its capability to inhibit thrombin and consequently coagulation (NR-HS-TBA).^{43,44} The complimentary sequence fluorescently labeled with a different fluorescent tag (5' CCAACCACCAACC-FAM 3') was used to form the NB-coronas, and it acts as an antidote because it can reverse TBA's effect by base-pairing with it (NB-HS-antidote). Therefore, selective excitation of these two different NRs to release TBA and its antidote becomes an interesting tool to enable the pair to act as an on/off switch for coagulation.

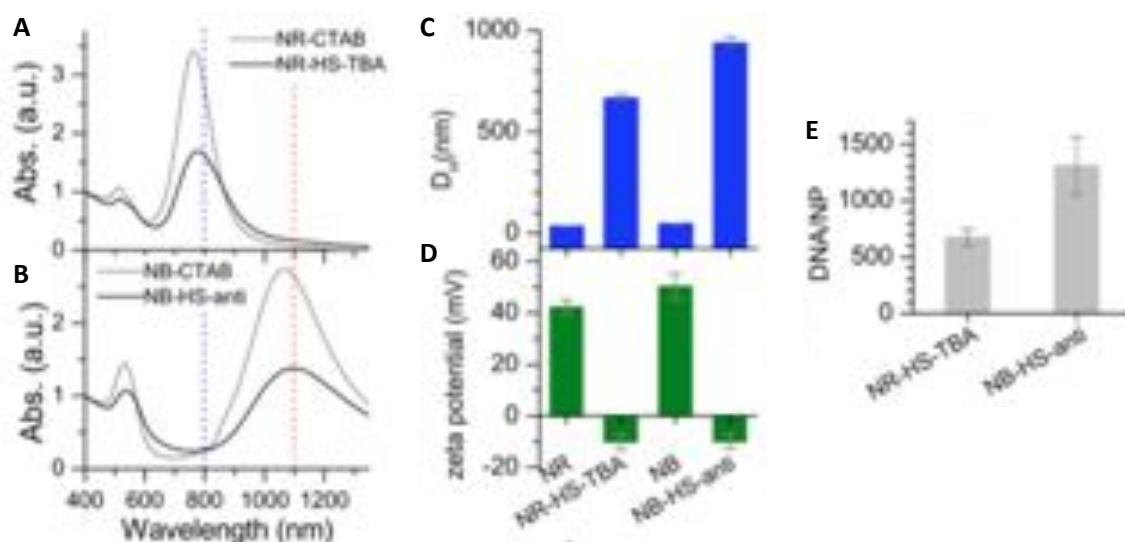


Figure 5.19. NRs and NBs synthesized and loaded for triggered release. Absorption spectra of (A) NRs, NR-HSA-TBA coronas (LSPR max = 777 nm), (B) NB, NB-HSA-antidote (LSPR max = 1093 nm). (C) D_H (DLS) of NRs, NR-HS-TBA, NBs, NB-HS-antidote, indicating that a corona contains multiple not a single NR or NB, but multiple ones. (D) Zeta potential of NRs, NR-HS-TBA = -9.8 mV, NBs, NB-HS-antidote = -10.1 mV (E) Quantified DNA payloads of NR-HS-TBA and NB-HS-antidote.

The NR-HS-TBA had $D_H = 662 \text{ nm} \pm 25$, and NB-HS-antidote $D_H = 938 \pm 50 \text{ nm}$, indicating that a corona contains multiple particles (Figure 5.19C). However, NR and NB LSPRs were not significantly shifted, so excitation at 800 and 1100 nm was still feasible (Figure 5.19A and B, respectively). Zeta potentials for NR-HS-TBA and NB-HS-anti were negative because HS is negative (Figure 5.19D).¹⁰ DNA loading was $674 \pm 74 \text{ TBA/NR}$ and $1307 \pm 255 \text{ antidote/NB}$ (Figure 5.19E).

Selective Triggered Release from the NR/NB-Coronas

Laser irradiation of NR and NB-corona could trigger DNA release. NB-HS-anti were irradiated at 1100 nm and their LSPR decreased, confirming NB melting (Figure 5.20A). Released antidote quantified by fluorescence was $[anti] = 430 \pm 17$ anti released per NB Figure 5.20, inset). NR-HS-TBA were irradiated at 800 nm and their LSPR decreased, confirming melting, and released $[TBA] = 223 \pm 8$ DNA released per NR (Figure 5.20B, inset). These experiments show that laser irradiation can release TBA from coronas on NRs and antidote from NB-coronas.

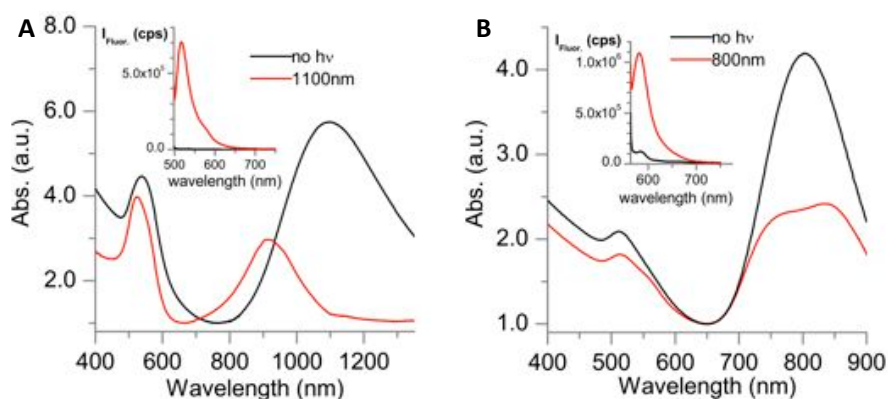


Figure 5.20. Selective release of NR/NB-corona mixture. (A) Absorption spectrum of NB-HS-TBA before (black) and after (red) 1100 nm irradiation. (B) Absorption spectrum of NR-HS-TBA before (black) and after (red) 800 nm irradiation. Inset: fluorescence spectrum of released TBA before (black) and after (red) 800 nm irradiation.

At this point, the selective release of TBA from NRs and antidote NBs coronas was evaluated (Figure 5.21A).

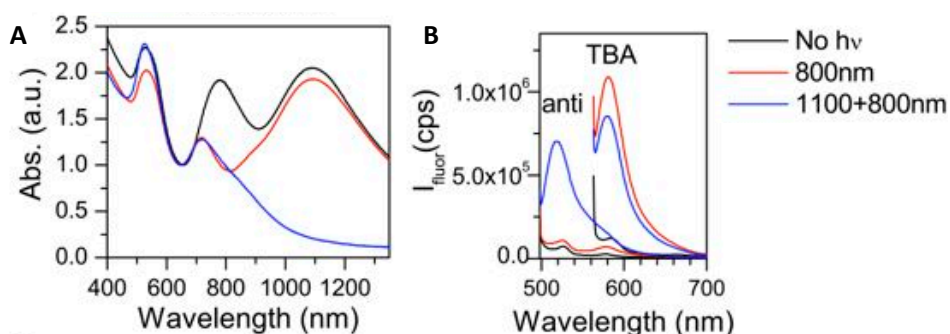


Figure 5.21. Selective melting of NRs and NBs. NR-HS-TBA and NB-HS-antidote were mixed at a ratio so that the TBA:antidote was 1:1. a) NR-HS-TBA + NB-HS-anti mixture before (black) and after 800 nm irradiation (red), after 800 nm and then 1100 nm irradiation (blue) b) fluorescence of released supernatant before (black) and after 800 nm irradiation (red), and after 800 nm + 1100 nm irradiation (blue).

Quantifying release showed that 800 nm irradiation released 252 TBA/NR, but only 1.3 nM antidote (around 4 released anti/NB). Next, the NR-HS-TBA + NR-HS-antidote mixture was irradiated at 1100 nm. The 1100 nm LSPR decreased, confirming NB melting (Figure 5.21A, blue). FAM fluorescence increased, indicating that 692 antidote/NB was released (Figure 5.21B, blue), while 63 nM TBA was released (nearly 20 TBA/NR).

This work demonstrates that external laser excitation can selectively release different type of DNA (in that case, a thrombin inhibitor and its antidote) from the protein corona, allowing the NR/NB pair to act, for instance, as an on/off switch for blood clotting. Furthermore, the use of protein coronas for loading and release of payloads from NRs opens up new possibilities for selective release applications.

5.3.4. Protein Corona Formation on CNTs

CNT-Coronas Characterization

Protein coronas on CNTs were also tested. Coronas were made from human serum (HS) *via* combined method and using the conditions optimized for the NR and found to have the highest loadings (5 mM CTAB, 5 mM PhB and 5% HS). Given the well-dispersed behavior observed for the CTAB-coated CNTs in the previous chapter (Chapter IV), highly-dispersed CNTs (HD-CNTs) were first obtained by eliminating the bundles and large aggregates not dispersed after 2 h sonication with CTAB 5 mM. After several washes to ensure the minimum presence free CTAB in solution, the corona formation was carried out using a 5% of HS in 5 mM PhB. All four types of CNTs (rCNTs, s-rCNTs, fCNTs, s-fCNTs) were studied, and as previously done, the resulting protein coronas were characterized in detail.

Figure 5.22 show that the corona was formed around all types of CTAB-coated CNTs. For the rigid and thick CNTs (rCNTs) in both forms, shortened and untreated, individual nanotubes could be found, whereas for the fCNTs and s-fCNTs the corona caused the clustering of several nanotubes as seen for the NRs and NBs. Specially, the corona formed on the flexible CNTs after cutting (s-fCNTs) seemed to form a tighter and more dense corona (Figure 5.22D2). Such observation is probably due to the fact that the remaining active sites generated after the oxidation treatment during the shortening process are still able to interact with the proteins present in the HS. DLS of the CNT-coronas, compared to the HD-CNTs, supported this observation, since high hydrodynamic diameters were measured for the both coronas formed with flexible CNTs (fCNTs and s-fCNTs), whereas the

absorption of the HS on the CNT surface caused a more moderate increase o size for the rCNTs and s-rCNTs (Figure 5.23A). Zeta potential data confirmed that HS components were adsorbed to the positively charged CTAB-coated CNTs, causing the negative charge observed for the CNT-coronas, and previously observed for the NR and NBs (Figure 5.23B).

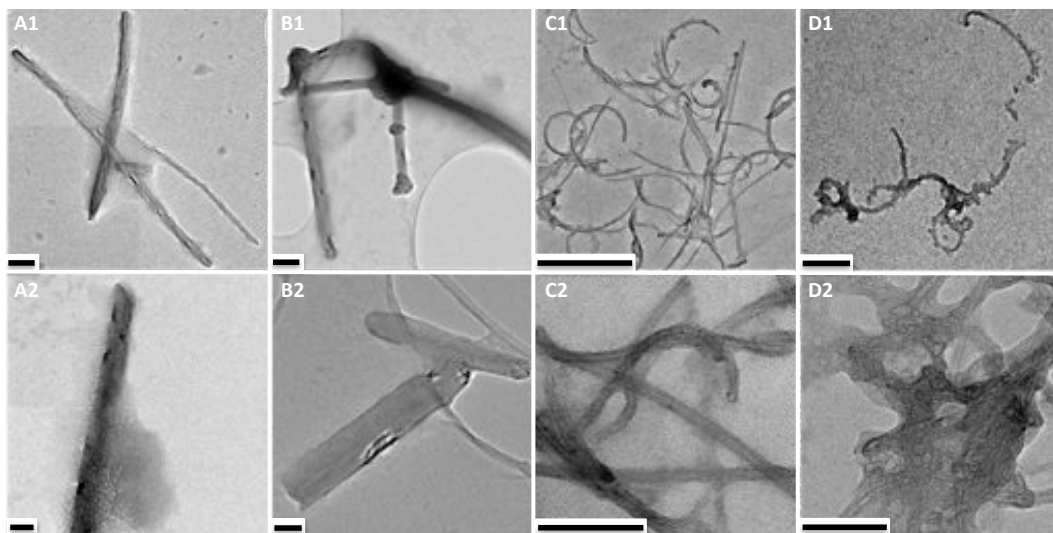


Figure 5.22. HRTEM images of the CNT-coronas. Coronas formed using (A) thick and rigid CNTs (rCNTs), (B) their shortened version s-rCNTs, or (C) thin and flexible CNTs (fCNTs), and (B) after being cut (s-fCNTs). Scale bars correspond to (1) 300 nm and (2) 100 nm.

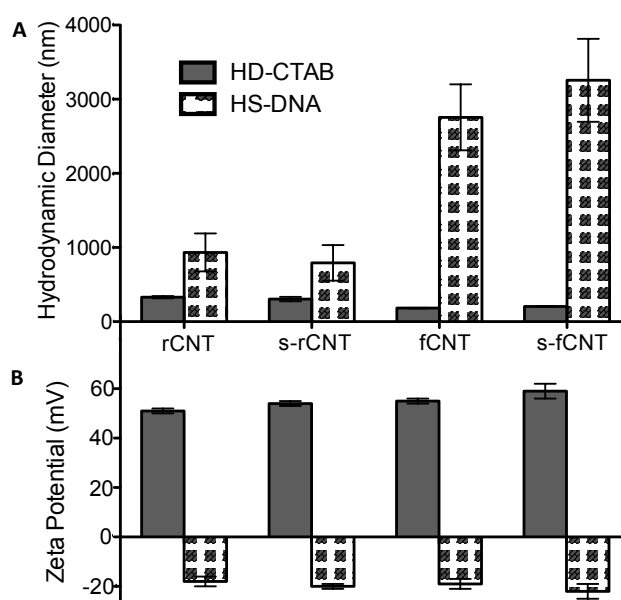


Figure 5.23. Size and charge of the CNT-coronas. (A) D_H and (B) zeta potential of HD-CNTs and CNT-coronas made with HS and DNA.

Evaluation of the Loading Capacities of the Different CNT-Coronas

After the formation of the protein corona on CNTs was successfully confirmed, the capacity of each type of CNT to load DNA was explored. To do so, the fluorescently labeled DNA initially loaded was released by heat displacement, as used before, and was quantified by fluorescence (Figure 5.24). Higher quantities of DNA/CNT were able to be loaded for all 4 types of CNTs compared to the NR and NB, as expected after their bigger size. However, only the flexible CNTs showed a satisfactory loading density (between 3 and 10 DNA/cm²) whereas only around 0.1 DNA/cm² was obtained for the rigid CNTs. These phenomenon might be due to the fact that what actually allows the loading on the corona is the formation of clusters, as demonstrated for the NRs. Therefore, as deduced from the TEM images, only the flexible CNTs, both untreated and shortened, were able to tangle and form large aggregates which would be responsible to hold the payload (Figure 5.22 C and D). Rigid nanotubes, on the other hand, remained individually isolated, with a higher dispersion degree but lower amount of loaded DNA (Figure 5.22 A and B).

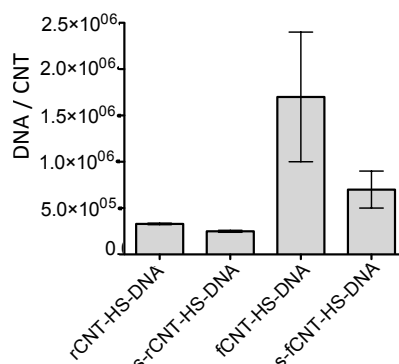


Figure 5.24. Loading capacities of the CNT-coronas.

Surprisingly, between the fCNTs and their shortened version (s-fCNTs) significant differences in their loading capacities were observed. The former exhibited a higher loading capacity, in contrast to what would be expected as larger and denser s-fCNT-coronas were observed on the TEM images and the DLS measures (Figure 5.22 and Figure 5.23A, respectively). The still exposed active sites after the oxidation treatment of the shorter flexible CNTs (s-fCNTs) might have caused the formation of a tighter and thicker corona due to the covalent union of some proteins present in the HS, such as the HSA, as it was similarly discussed in Chapter II. However, as it has been demonstrated in this chapter, HSA is not the responsible for the corona loading and therefore, the covalent union of this protein on the CNT surface might have avoided its proper formation. In accordance with this assumption, rCNTs and fCNTs were modified with PFM following the protocol previously developed

in Chapter III, and after polymerization, the corona was formed. The resulting complexes were characterized by DLS and zeta-potential, and their loading capacities were measured (Figure 5.25). In Chapter II, the ability of the PFM group to bind the BSA protein was proved, and its immobilization capacity and the conformation of the anchored protein were deeply analyzed. Similarly, it would be expected that the HSA present in the HS of the corona would be immobilized on the ppPFM-modified surface of the CNTs, as it was suggested for the increase of size (Figure 5.25A). Both types of CNTs (fCNTs and rCNTs) exhibited low loading capacities, specially compared to the obtained with the CTAB-coated fCNTs (Figure 5.24). As a result, the covalent union of the HSA during the corona formation does not improve the loading capacity of the complexes. Therefore, the ability of the corona to hold higher amounts of payload is due, not only to the formation of clusters and the other species apart from the HSA present in the HS, but also due to the ionic interaction of these negative species with the positively charged CTAB-coated surface.

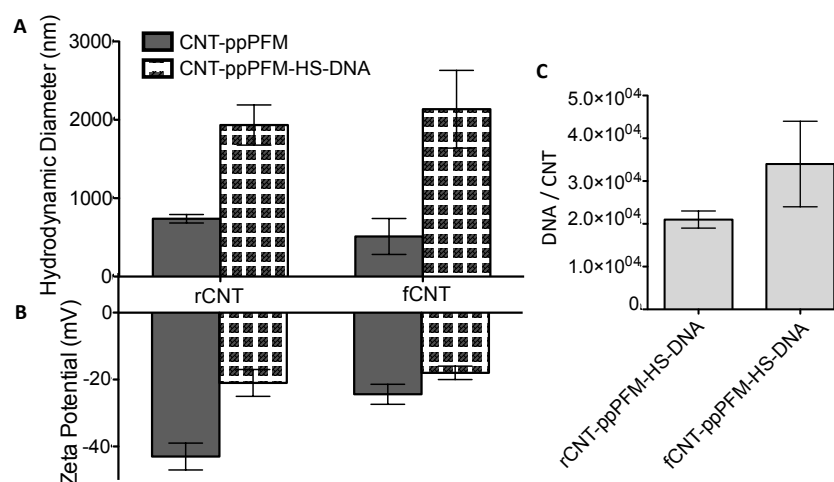


Figure 5.25. Size, charge and DNA loadings of the coronas formed with CNT-ppPFM. (A) DLS and (B) zeta potential of the ppPFM-modified rCNTs and fCNTs, before and after the corona formation. (C) Loading capacities of the resulting coronas employing ppPFM-coated rCNTs and fCNTs.

Examining the Passive Release and Exchange of the CNT-Coronas

As carried out for the coronas formed on NR and NB, the passive release of the CNT-coronas and its exchange with the surrounding media was also studied (Figure 5.26). This study was performed for the fCNT-coronas, which showed the maximum loading and therefore a more significant evolution could be monitored. As expected, fCNT-HS-DNA also exhibited the same initial 3-day lag in the passive release of DNA for all 3 cases (control, corona exchange with HSA and corona exchange with HS), after which the release increased significantly (Figure 5.26A). After 3 days, the released

concentration of DNA was lowest with HSA-blocking (Figure 5.26A, triangles), reaching only $45 \pm 28\%$ of the loading at day 15, and highest after corona exchange with HS (Figure 5.26A, circles), similar to the observations for NRs and NBs. These results confirmed that apart from size, the amount of CTAB passivation plays a dominant role in influencing corona formation, loading and release. Since the concentration of CTAB passivating each of the NPs differs due to surface chemistry and available surface area, this could be responsible for the differences in loading, blocking and exchange dynamics, and consequently passive release behavior.

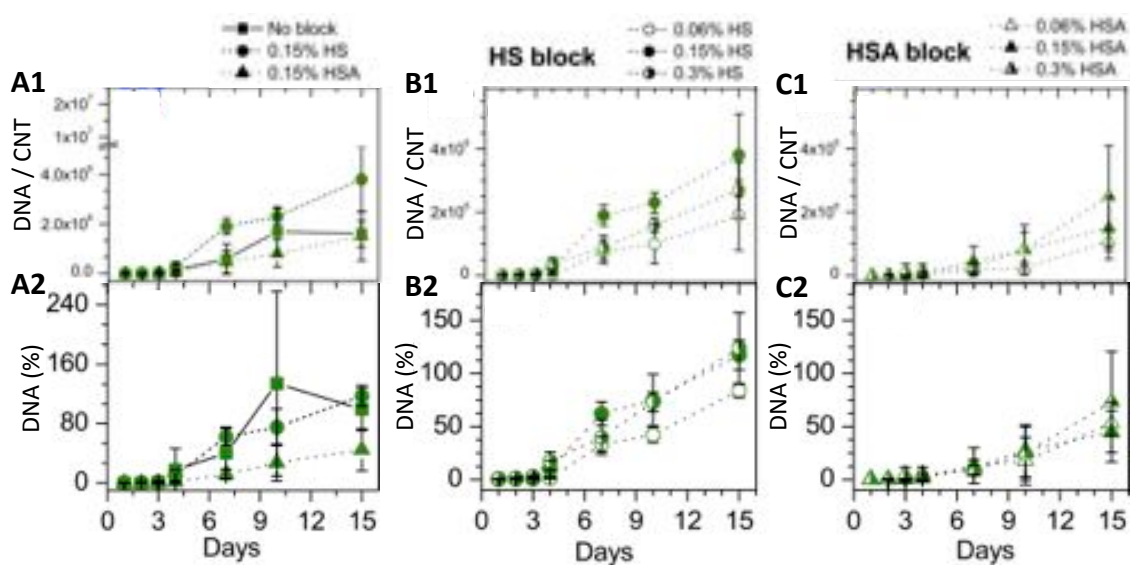


Figure 5.26. DNA release from the fCNT-HS-DNA with different exchange conditions. (A) Comparison of the passive release of DNA from the f-CNT-coronas in an exchange environment of 0.15% HS (circles), 0.15% HSA (triangles), or no protein (squares) on b) NBs and c) CNTs. Passive release profiles of the fCNT-HS-DNA when varying the amount of (E) HS and (C) HSA in the media. Passive release expressed as (1) DNA released per NR and (2) leakage percentage.

As observed for the NRs and NBs, the increase of HSA% in the media (Figure 5.26B) did not have a significant effect on the passive release profile of the fCNT-coronas, whereas the higher concentrations of HS led to a faster DNA leakage from the corona. This results supports the previous results, confirming that the HSA is not able to exchange with the existing corona in contrast to the HS, which induces an increase of the passive DNA release.

This study demonstrates that the formation of the protein corona around different types of nanoparticles (gold NRs, NBs and CNTs) can be successfully achieved. Moreover, this strategy allows possibility to tune their passive release, generating a promising tool for gene delivery applications.

5.4. Concluding Remarks

The results of this work show that protein coronas can be used for enhanced loading on gold nanoparticles for both triggered release applications and passive release. When the former is needed, the leaking has to be minimized until there is an external signal. It has been demonstrated that protein coronas exhibit high payload capacity while still enabling triggered release *via* laser excitation of NRs. As a result, selective DNA release can be achieved by using coronas on NRs of different aspect ratios. Thus, this kind of nanoparticles can act as handles for controlling biological processes.

On the other hand, this chapter demonstrates that it is possible to tune the passive release profile of protein coronas by varying the corona composition and NP surface properties. By exploiting the fact that hard and soft corona proteins have different exchange rates, strategic exposure to hard or soft corona proteins can tune the rate of release of a DNA payload from NPs. Hard corona proteins exchange more and result in higher release, while soft corona proteins cause a lower degree of exchange and can be used to decrease passive release. By adsorbing HSA onto already-formed NP-HS-DNA coronas, DNA release rate can be slowed. This strategy can be employed on different types of NPs including CNTs and, although their loading densities differed, is easily extended to other NPs with similar ligands. These results can aid the manipulation of corona properties to optimize them for biological applications.

This chapter gives rise to a new strategy in order to improve the modest loading capacities of the CNTs, observed in the previous chapter. In general, protein corona has emerged as another determinant issue to be considered in the *in vitro* and *in vivo* biological application of nanoparticles. Further research is required to fill the gaps in our knowledge of the cellular internalization mechanism of these systems, alongside with their behavior *in vivo* and toxic effects. Full understanding of these issues will enable the rational design of CNT-based nanopharmaceuticals in the near future.

In that scenario, this whole thesis has sought to demonstrate that well-functionalized CNTs by both non-covalent and covalent methodologies are promising candidates for gene delivery applications, given their geometrical traits with a high aspect ratio, which enables penetration into the cell. One of the major issues affecting nanotube biomedical applications is the existing variability in their physical properties (shape, length and diameter) and the type of chemical modification, having a direct effect on the degree of CNT dispersion, the entry mechanisms that govern their cellular

internalization and their safety threshold value. Despite the fact that the diversity of CNTs materials themselves complicates to evaluate or predict their interactions with cells or tissues, in this work we intended to understand these critical features that seem to determine the CNT toxicity, their cell internalization and cargo release, and *in vivo* biodistribution. Carefully optimizing their physicochemical parameters to minimize their aggregation is highly favorable. In our opinion, the more important issue is to be able to produce CNTs with consistent properties, basically in length, in order to gain a higher control of the behavior of these systems in the biological milieu. We believe that this concern will be resolved when shorter CNTs are achieved maintaining a certain degree of rigidity that will favor its penetration into the cell *via* the nanoneedle effect. Having such type of physical characteristics with the appropriate surface chemistry that will allow the anchoring of the genetic material of interest, CNTs can be powerful therapeutic agents for future gene therapy treatments. In this regard, the wrapping immobilization of the acid nucleic on these CNTs through the ppAA deposition by PECVD, or the payload loading *via* the protein corona formation are arisen as key determinant chemical functionalization approaches to produce these type of delivery systems. Hopefully, this study can encourage further investigations to bring us closer towards determining the limitations and benefits that the CNT-based carrier vectors may offer.

What seems certain, as far as we can see, is that nanoparticles with non-spherical shapes as evaluated in this thesis open up a wide range of possibilities for the design of carrying materials for therapeutic drugs and genes. Hopefully, in the course of the coming years, nanotechnology will allow us the development of nanotubes made of other bulk materials that, by tuning their physicochemical properties, can give rise to new gene delivery strategies taking advantage of their tubular shape. Now, we are more concerned about the effect that the rigidity of the newly-developed nanotube will have on its behavior in the cell culture medium, or how its length will be a crucial factor to achieve the appropriate biocompatibility. All these parameters, combined with a suitable chemical functionalization, can bring us closer to a whole new world of opportunities for gene therapy treatments.

5.5. References

- 1 Walczyk, D., Bombelli, F. B., Monopoli, M. P., Lynch, I. & Dawson, K. A. What the Cell "Sees" in Bionanoscience. *Journal of the American Chemical Society* **132**, 5761-5768 (2010).
- 2 Walkey, C. D., Olsen, J. B., Guo, H., Emili, A. & Chan, W. C. W. Nanoparticle Size and Surface Chemistry Determine Serum Protein Adsorption and Macrophage Uptake. *Journal of the American Chemical Society* **134**, 2139-2147 (2012).
- 3 Salvati, A. *et al.* Transferrin-functionalized nanoparticles lose their targeting capabilities when a biomolecule corona adsorbs on the surface. **8**, 137-143 (2013).
- 4 Mirshafiee, V., Mahmoudi, M., Lou, K., Cheng, J. & Kraft, M. Protein corona significantly reduces active targeting yield. *Chemical Communications* **49**, 2557-2559, (2013).
- 5 Cavadas, M., González-Fernández, Á. & Franco, R. Pathogen-mimetic stealth nanocarriers for drug delivery: a future possibility. **7**, 730-743 (2011).
- 6 Walkey, C. D. & Chan, W. C. W. Understanding and controlling the interaction of nanomaterials with proteins in a physiological environment. *Chemical Society Reviews* **41**, 2780-2799 (2012).
- 7 Monopoli, M. P. *et al.* Physical-Chemical Aspects of Protein Corona: Relevance to *in Vitro* and *in Vivo* Biological Impacts of Nanoparticles. *Journal of the American Chemical Society* **133**, 2525-2534 (2011).
- 8 Liu, W. *et al.* Protein corona formation for nanomaterials and proteins of a similar size: hard or soft corona? *Nanoscale* **5**, 1658-1668, (2013).
- 9 Milani, S., Bombelli, F., Pitek, A., Dawson, K. & Radler, J. Reversible *versus* Irreversible Binding of Transferrin to Polystyrene Nanoparticles: Soft and Hard Corona. *Acs Nano* **6**, 2532-2541, (2012).
- 10 Casals, E., Pfaller, T., Duschl, A., Oostingh, G. J. & Puntès, V. Time Evolution of the Nanoparticle Protein Corona. *ACS Nano* **4**, 3623-3632, (2010).
- 11 Arvizo, R. R. *et al.* Identifying New Therapeutic Targets *via* Modulation of Protein Corona Formation by Engineered Nanoparticles. *PLoS ONE* **7**, e33650 (2012).
- 12 Dell'Orco, D., Lundqvist, M., Oslakovic, C., Cedervall, T. & Linse, S. Modeling the Time Evolution of the Nanoparticle-Protein Corona in a Body Fluid. *Plos One* **5**, (2010).
- 13 Lundqvist, M. *et al.* The Evolution of the Protein Corona around Nanoparticles: A Test Study. *ACS Nano* **5**, 7503-7509 (2011).
- 14 Prapainop, K., Witter, D. P. & Wentworth, P. A Chemical Approach for Cell-Specific Targeting of Nanomaterials: Small-Molecule-Initiated Misfolding of Nanoparticle Corona Proteins. *Journal of the American Chemical Society* **134**, 4100-4103 (2012).
- 15 Kah, J. C. Y., Chen, J., Zubieta, A. & Hamad-Schifferli, K. Exploiting the Protein Corona around Gold Nanorods for Loading and Triggered Release. *ACS Nano* **6**, 6730-6740 (2012).
- 16 Ge, C. *et al.* Binding of blood proteins to carbon nanotubes reduces cytotoxicity. *Proceedings of the National Academy of Sciences of the United States of America* **108**, 16968-16973, (2011).
- 17 Qiu, Y. *et al.* Surface chemistry and aspect ratio mediated cellular uptake of Au nanorods. *Biomaterials* **31**, 7606-7619 (2010).
- 18 Wijaya, A., Schaffer, S. B., Pallares, I. G. & Hamad-Schifferli, K. Selective Release of Multiple DNA Oligonucleotides from Gold Nanorods. *ACS Nano* **3**, 80-86 (2009).
- 19 Chen, C.-C. *et al.* DNA-Gold Nanorod Conjugates for Remote Control of Localized Gene Expression by near Infrared Irradiation. *Journal of the American Chemical Society* **128**, 3709-3715 (2006).
- 20 Park, S. & Hamad-Schifferli, K. Enhancement of *In Vitro* Translation by Gold Nanoparticle-DNA Conjugates. *ACS Nano* **4**, 2555-2560 (2010).
- 21 Lundqvist, M. *et al.* Nanoparticle size and surface properties determine the protein corona with possible implications for biological impacts. *Proceedings of the National Academy of Sciences* **105**, 14265-14270 (2008).
- 22 Huang, X., Jain, P. K., El-Sayed, I. H. & El-Sayed, M. A. Plasmonic photothermal therapy (PPTT) using gold nanoparticles. *Lasers in Medical Science* **23**, 217-228 (2008).

- 23 Jain, P. K., Qian, W. & El-Sayed, M. A. Ultrafast Cooling of Photoexcited Electrons in Gold Nanoparticle, à Thiolated DNA Conjugates Involves the Dissociation of the Gold, à Thiol Bond. *Journal of the American Chemical Society* **128**, 2426-2433 (2006).
- 24 de Puig, H., Cifuentes Rius, A., Flemister, D., Baxamusa, S. H. & Hamad-Schifferli, K. Selective light-triggered release of DNA from gold nanorods switches blood clotting on and off. *PLOS ONE*, (2013).
- 25 Sau, T. K. & Murphy, C. J. Seeded high yield synthesis of short Au nanorods in aqueous solution. *Langmuir* **20**, 6414-6420 (2004).
- 26 Dell'Orco, D., Lundqvist, M., Oslakovic, C., Cedervall, T. & Linse, S. Modeling the Time Evolution of the Nanoparticle-Protein Corona in a Body Fluid. *PLoS ONE* **5**, e10949 (2010).
- 27 Treuel, L. *et al.* Quantifying the influence of polymer coatings on the serum albumin corona formation around silver and gold nanoparticles. *Journal of Nanoparticle Research* **14**, 1-12 (2012).
- 28 Lacerda, S. H. D. *et al.* Interaction of Gold Nanoparticles with Common Human Blood Proteins. *ACS Nano* **4**, 365-379, (2010).
- 29 You, C. C., Verma, A. & Rotello, V. M. Engineering the nanoparticle-biomacromolecule interface. *Soft Matter* **2**, 190-204, (2006).
- 30 Afrooz, A. R. M. N. *et al.* Spheres vs. rods: The shape of gold nanoparticles influences aggregation and deposition behavior. **91**, 93-98 (2013).
- 31 Bahri, M. A. *et al.* Investigation of SDS, DTAB and CTAB micelle microviscosities by electron spin resonance. *Colloids and Surfaces A: Physicochemical and Engineering Aspects* **290**, 206 (2006).
- 32 Majhi, P. R. & Moulik, S. P. Energetics of Micellization: Reassessment by a High-Sensitivity Titration Microcalorimeter. *Langmuir* **14**, 3986-3990 (1998).
- 33 Alper, J., Crespo, M. & Hamad-Schifferli, K. Release Mechanism of Octadecyl Rhodamine B Chloride from Au Nanorods by Ultrafast Laser Pulses. *The Journal of Physical Chemistry C* **113**, 5967-5973, (2009).
- 34 Kah, J., Zubieta, A., Saavedra, R. & Hamad-Schifferli, K. Stability of Gold Nanorods Passivated with Amphiphilic Ligands. *Langmuir* **28**, 8834-8844, (2012).
- 35 Barhoumi, A., Huschka, R., Bardhan, R., Knight, M. W. & Halas, N. J. Light-induced release of DNA from plasmon-resonant nanoparticles: Towards light-controlled gene therapy. *Chemical Physics Letters* **482**, 171-179 (2009).
- 36 Lee, S. E. *et al.* Photonic Gene Circuits by Optically Addressable siRNA-Au Nanoantennas. *ACS Nano* **6**, 7770-7780 (2012).
- 37 Yamashita, S. *et al.* Controlled-release system of single-stranded DNA triggered by the photothermal effect of gold nanorods and its in vivo application. *Bioorganic & Medicinal Chemistry* **19**, 2130-2135 (2011).
- 38 Huschka, R. *et al.* Light-Induced Release of DNA from Gold Nanoparticles: Nanoshells and Nanorods. *J. Am. Chem. Soc.* **133**, 12247-12255 (2011).
- 39 Gou, L. F. & Murphy, C. J. Fine-tuning the shape of gold nanorods. *Chemistry of Materials* **17**, 3668-3672 (2005).
- 40 Jana, N. R. Gram-Scale Synthesis of Soluble, Near-Monodisperse Gold Nanorods and Other Anisotropic Nanoparticles. *Small* **1**, 875-882 (2005).
- 41 Link, S., Burda, C., Nikoobakht, B. & El-Sayed, M. A. Laser-Induced Shape Changes of Colloidal Gold Nanorods Using Femtosecond and Nanosecond Laser Pulses. *Journal of Physical Chemistry B* **104**, 6152-6163 (2000).
- 42 Tenzer, S. *et al.* Nanoparticle Size Is a Critical Physicochemical Determinant of the Human Blood Plasma Corona: A Comprehensive Quantitative Proteomic Analysis. *ACS Nano* **5**, 7155-7167 (2011).
- 43 Kim, Y., Phillips, J. A., Liu, H., Kang, H. & Tan, W. Using photons to manipulate enzyme inhibition by an azobenzene-modified nucleic acid probe. *Proceedings of the National Academy of Sciences* **106**, 6489-6494 (2009).
- 44 Lefkowitz, J. & Topol, E. J. Direct thrombin inhibitors in cardiovascular medicine. *Circulation* **90**, 1522-1536 (1994)

Chapter VI.
Conclusions

Stable and highly reactive surfaces with the ability to immobilize different kind of biologically active species have been developed, optimized and characterized.

- Surface modification by plasma techniques has been demonstrated as a gentle method for the polymerization PFM on a surface, allowing the covalent anchoring of molecules through the high specificity of this ester group towards primary amines. Two different approaches have been assessed in order to create smart, bioactive surfaces. Both techniques, PECVD and plasma grafting, have been proved to immobilize BSA although their final properties have been found to be different, causing also differences in the resulting functionalized surfaces.
- The formation of a hydrophobic ppPFM layer by PECVD and the capacity of anchoring higher amounts of protein have been confirmed. However, a greater conformational change in the BSA structure due to its strong binding and high hydrophobicity has been observed. ppPFM coating is preferred if full coverage of the surface is needed and the activity of the anchored molecule lack of importance
- Plasma grafting has been demonstrated to form PFM polymer brushes homogeneously distributed on the surface but without covering its totality, and thus providing less and more spread out reactive sites for the binding of biomolecules. Such phenomenon has been confirmed to cause the hydrophilization of the typically hydrophobic ppPFM-modified surfaces. Thus, the anchoring of the protein without remarkable structural changes has been corroborated for plasma-grafted substrates. In this regard, an enzyme and a gene delivery vector has been successfully immobilized on gPFM-modified substrates maintaining most part of its activity, or even enhancing it as it is the case for the cell reprogramming surfaces with an anchored virus particle.

CNTs have been satisfactorily modified by PECVD with a homogeneous and reactive coating in order to employ them as delivery vectors.

- The ppPFM-coated CNTs have been proved to bind QDs allowing the *in vitro* tracking in macrophages. The positive cellular uptake of the QD-functionalized CNTs into macrophages cells has been evidenced. The immobilization of TPA on these systems has been also demonstrated.

- Carbon nanotubes have also been successfully modified with ppAA. The resulting ppAA-deposited on the CNTs has been provides a positively charged surface, enabling the DNA binding through electrostatic interaction. Complexes of ppAA-modified CNTs and pGFP have been successfully prepared and their transfection efficiency in macrophages cells has been assessed. Despite the positive transfection achieved, large aggregates of nanotubes has been noticed, complicating their cell viability.

The effect of the physicochemical properties of the CNTs in term of dispersibility, cell viability and biodistribution has been assessed.

- Two different CNTs have been analyzed: thicker, rigid MWNT and thinner, flexible MWNT. An oxidation procedure in order to cut these two types of CNTs has been optimized, producing shorter and more hydrophilic CNTs but without affecting their morphology.
- The functionalization of these four kinds of CNTs with non-covalent stabilizing agents (CTAB, pHPMA and HS) and ppAA deposition have been explored, alongside with their resulting dispersibility in aqueous media and *in vitro* toxicology. Basically, it has been demonstrated that thick and thinner CNTs behave differently in aqueous and biologic milieu. Flexible tubes have been found to be more prone to tangle forming large aggregates, whereas rigid CNTs can remain stable in solution causing a lower impact on the cell viability.
- Differences in the *in vivo* biodistribution of these complexes have been also evidenced. Their behavior inside the body of a mouse has been elucidated after label the ppAA-modified CNTs with an IR dye. *In vivo* fluorescence semi-quantification has demonstrated the accumulation of these systems in a similar maner throughout the main organs 24 h post-injection. However, a major uptake has been detected in the lungs of the mice injected with the flexible tubes due to its higher aggregation tendency.
- All types of CNTs previously modified with ppAA have been proved to load DNA and, in fact, the lower the size of the tube, the higher the loading capacity observed. However, cell transfection experiments have revealed that the flexible tubes cannot release the pGFP in the conditions studied. Additionally, CNTs have been found to maintain the cell viability only when low dosages are administered and thus, low amounts of DNA have to be added to the cells avoiding high transfection efficiencies.

Protein coronas have been presented as the alternative to achieve higher loadings on the CNTs surface and its properties have been manipulated and optimized.

- The HS protein corona ability to load and hold nucleic acids has been mainly optimized for gold nanorods, given their advanced optical properties, and it has been subsequently extended to gold nanobones and CNTs.
- It has been demonstrated that the passive release rates of DNA payloads can be manipulated by varying the corona composition, exhibiting high loading capacities while holding the payload and thus slow the release rate. Such phenomenon has been proved to be especially beneficial for triggered release experiments *via* laser excitation of a mixture of NR/NB-coronas. Moreover, these corona properties have been demonstrated to play an important role in passive release, and concentrations of CTAB, HS, and phosphate buffer used in the corona formation have been proved to tune the payload release profiles.
- Despite being able to form a corona, HSA (soft protein) have been found not to load DNA and thus, the loading capacity of the HS corona has been evidenced to be due to other species present in the HS (hard proteins). Because HSA is a soft corona and binds weakly to the NP surface, it can be used as a blocking agent, providing a means to control payload release. These advances in understanding the protein corona properties have become a step forward towards developing a set of basic design rules that enable their manipulation and optimization for particular biological applications.

List of Publications and Presentations

Publications and Patents

A. Cifuentes-Rius, H. de Puig, J. Kah, S. Borros, K. Hamad-Schifferli. (2013) **Optimizing the Properties of the Protein Corona Surrounding Nanoparticles for Payload Release**. *ACS Nano (article ASAP)*

A. Cifuentes-Rius, A. de Pablo, V. Ramos-Perez, S. Borros. (2013) **Plasma Modification of Carbon Nanotubes for Gene Delivery Vectors**. *Plasma Processes and Polymers (Submitted)*

A. Cifuentes and Salvador Borrós. (2013) **Comparison of Two Different Plasma Surface Modification Techniques for Covalent Immobilization of Protein Monolayers**. *Langmuir*, 29 (22), 6645–6651

H. de Puig, A. Cifuentes Rius, D. Flemister and K. Hamad-Schifferli. (2013) **Switching On and Off Blood Clotting with Light Using Nanorod Protein Coronas**. *PLoS ONE*, 8(7), e68511

V. Ramos-Perez, A. Cifuentes, N. Coronas, A. de Pablo, S. Borrós. (2013). **Modification of Carbon Nanotubes for Gene Delivery Vectors**. In: K. Hamad-Schifferli, P. Bergese, *Nanomaterial Interfaces in Biology: Methods and Protocols*. Boston: Springer. 302.

D. Horna, J. C. Ramirez, A. Cifuentes, A. Bernad, S. Borrós and M. A. González. (2012) **Efficient Cell Reprogramming Using Bioengineered Surfaces**. *Advanced Healthcare Materials*, 1(2), 177-182.

M.A. González, J.C. Ramirez, A. Bernad, S. Borrós, D. Horna, A. Cifuentes. (2009) **Bioactive Surface Capable of Genetically Modifying Cells or Tissues and Use Thereof**. ES Patent 200931268, filed December 24, 2009 and issued July 13, 2011.

Seminars and Courses

11/2013 **The Royal Australian Chemical Institute Inc. (RACI) Polymer Student Symposium 2013**. Queensland University of Technology (QUT), Brisbane, Australia.
Oral Presentation: Covalent Immobilization of Enzymes on Polystyrene Substrates Modified by Plasma Grafting (Awarded with the Runner-Up Prize)

07/2011 **International Symposium on Plasma Chemistry (ISPC 20)**. Philadelphia, PA, USA.
Poster Presentation: Facile Surface Modification for Covalent Immobilization of Enzymes on Different Geometries

09/2010 **Gordon Research Conference (GRC)**. Biointerface Science. Les Diablerets Conference Center, Les Diablerets, Switzerland.
Poster Presentation: Enzyme Immobilization on Polymeric Surfaces Modified by Plasma-Grafting

03/2010 **NANOCHARM, 3rd Winter School on Ellipsometry**. Bad Hofgastein, Salzburg, Austria.
Poster Presentation: Enzyme Immobilization on Plasma-Grafting Modified Surfaces

06/2009 **NSF-GEM⁴ Summer School**. University of Illinois at Urbana-Champaign, Urbana, IL, USA.
Poster Presentation: Density-Controlled Attachment of Peptides on Plasma-Modified Spherical Surfaces for Cell Expansion

05/2009 **Ceramics, Cells and Tissues**. Faenza, Italy. Poster Presentation: Density-Controlled Attachment of Peptides on Plasma-Modified Spherical Surfaces for Cell Expansion